Adi Kurniawan

Modelling and geometry optimisation of wave energy converters

Doctoral Thesis

Adi Kurniawan

NTNU
Norwegian University of Science and Technology
Thesis for the degree of Philosophiae Doctor
Faculty of Engineering Science and Technology
Department of Marine Technology

NTNU – Trondheim
Norwegian University of
Science and Technology

NTNU – Trondheim
Norwegian University of
Science and Technology

NTNU

Adi Kurniawan

Modelling and geometry optimisation of wave energy converters

Thesis for the degree of philosophiae doctor

Trondheim, April 2013

Norwegian University of Science and Technology
Faculty of Engineering Science and Technology
Department of Marine Technology

NTNU – Trondheim
Norwegian University of
Science and Technology

To Sethia and Hana,
who made my joy complete

Abstract

The ultimate goal of wave energy undertaking is to find a solution that minimises the cost of delivered energy. Not only should a device maximise its energy absorption, but also the costs associated with absorbing and converting that energy into useful forms should be minimised. Towards realising this goal, this thesis contributes in three main areas, namely, numerical modelling, geometry optimisation, and geometry control.

The highlights of numerical modelling include the use of bond graph—a domain-independent, graphical representation of dynamical systems—in developing numerical models of wave energy converters (WECs), and the use of state-space models to represent the wave radiation terms. It is shown that bond graph is well-suited for modelling WECs, which involve interactions between multiple energy domains, and that state-space models of the wave radiation terms are efficient and sufficiently accurate for use in time-domain simulations of WECs. Both bond graph and state-space models are used in the modelling of a floating oscillating water column device, which, from the point of view of hydrodynamics, is a complex device involving various hydrodynamic radiation terms.

The main contribution of geometry optimisation is the incorporation of the cost factor in the design problem through the use of a multi-objective optimisation scheme. Two simplified cost factors are considered, namely, the surface area of the device and the reaction force that the device must withstand. The scheme is applied to find optimum geometries of a class of oscillating-body WECs that oscillate about a fixed horizontal axis. It is shown that when the cost factor is taken into account, a design that maximises the absorbed power is not necessarily the most economical. It is found, for example, that an economical bottom-hinged device has its section spanning only part of the water depth instead of the whole water depth.

Informed by the results of the geometry optimisation study, a design is proposed of a device which allows its geometry to be varied from time to time depending on the prevailing wave condition. An investigation of the device characteristics and potential is reported under geometry control. It is shown that controlling the variation of the geometry has the potential of broadening the power absorption bandwidth and improving its capacity factor in extreme conditions.

Acknowledgements

Contents

List of appended papers

The following papers are included as part of this thesis:

A) A. Kurniawan, E. Pedersen, and T. Moan. (2012). Bond graph modelling of a wave energy conversion system with hydraulic power take-off. *Renewable Energy* 38, 234–244.

B) A. Kurniawan, J. Hals, and T. Moan. (2011). Modelling and simulation of a floating oscillating water column. *Proceedings of 30th International Conference on Ocean, Offshore and Arctic Engineering (OMAE 2011)*, Rotterdam, 19-24 June 2011, pp. 395–406.

C) A. Kurniawan, J. Hals, and T. Moan. (2011). Assessment of time-domain models of wave energy conversion systems. *Proceedings of 9th European Wave and Tidal Energy Conference (EWTEC 2011)*, Southampton, 5-9 September 2011.

D) A. Kurniawan and T. Moan. (2013). Optimal geometries for wave absorbers oscillating about a fixed axis. *IEEE Journal of Oceanic Engineering* 38, 117–130.

E) A. Kurniawan and T. Moan. (2012). Characteristics of a pitching wave absorber with rotatable flap. *Energy Procedia* 20, 134–147.

F) A. Kurniawan and T. Moan. (2012). Multi-objective optimization of a wave energy absorber geometry. *Proceedings of 27th International Workshop on Water Waves and Floating Bodies*, Copenhagen, 22-25 April 2012.

G) A. Kurniawan, E. Pedersen, and T. Moan. (2012). Modelling of wave energy converters using bond graph. *Proceedings of 10th International Conference on Bond Graph Modeling and Simulation*, Genoa, 8-11 July 2012.

The following papers were written in the course of the PhD studies but are not included as part of this thesis:

H) A. Babarit, J. Hals, A. Kurniawan, T. Moan, and J. Krokstad. (2011). Power absorption measures and comparisons of selected wave energy converters. *Proceedings of 30th International Conference on Ocean, Offshore and Arctic Engineering (OMAE 2011)*, Rotterdam, 19-24 June 2011, pp. 437–446.

I) A. Babarit, J. Hals, M. J. Muliawan, A. Kurniawan, T. Moan, J. Krokstad. (2012). Numerical benchmarking study of a selection of Wave Energy Converters. *Renewable Energy* 41, 44–63.

Declaration of authorship

This doctoral thesis is submitted to the Norwegian University of Science and Technology (NTNU) for the degree of Philosophiae Doctor (PhD). The work was carried out at the Centre for Ships and Ocean Structures (CeSOS) and the Department of Marine Technology at NTNU in Trondheim, Norway. The main supervisor has been Prof. Torgeir Moan (NTNU) and the co-supervisor has been Prof. em. Johannes Falnes (NTNU). The PhD program started in August 2009 and the thesis was completed for submission in December 2012.

The author, Adi Kurniawan, declares that the work presented in this thesis is his own and contains no material that was previously submitted for a degree at this university or any other institution. Any quotation or paraphrase from the published or unpublished work of another person has been duly acknowledged.

In all the appended papers, the author was primarily responsible for formulating the problems, planning and performing the analyses, as well as interpreting and reporting the results. The co-authors provided guidance, comments, and suggestions.

The PhD program was part of the Statkraft Ocean Energy Research Program, sponsored by Statkraft (`www.statkraft.no`).

Nomenclature

The following are lists of acronyms, symbols, and mathematical operators used in the introductory chapters (Chapters 1 to 6). For the appended papers, notations may differ slightly from one paper to another. The reader is always to consult the meaning of a particular notation from the proximate text.

ACRONYMS

BBDB	backward bent duct buoy
DOF	degree-of-freedom
EMEC	European Marine Energy Centre
EWTEC	European Wave and Tidal Energy Conference
FRF	frequency response function
IRF	impulse response function
IUTAM	International Union of Theoretical and Applied Mechanics
JONSWAP	Joint North Sea Wave Project
MARINET	Marine Renewables Infrastructure Network
MDOF	multi-degree-of-freedom
MEAD	Marine Energy Array Demonstrator
MOEA	multi-objective evolutionary algorithm
NEL	National Engineering Laboratory
NNMREC	Northwest National Marine Renewable Energy Center
NTH	Norwegian Institute of Technology
NTNU	Norwegian University of Science and Technology
OWC	oscillating water column
PTO	power take-off
SEA	Sea Energy Associates
UK	United Kingdom
WEC	wave energy converter
WET-NZ	Wave Energy Technology–New Zealand

ROMAN SYMBOLS

a	radius
a, b	preselected parameters
a_n, b_n	random values generated from a Gaussian distribution with variance $S_{F_e}(\omega_n)\Delta\omega$

A	complex incident wave amplitude at origin
A_i	internal water surface area
A_s	submerged surface area, total surface area
$A_{s,r}(\theta)$	far-field coefficient
A_w	water plane area
$\hat{\mathbf{A}}, \hat{\mathbf{B}}, \hat{\mathbf{C}}$	constant matrices
$B(\omega)$	radiation susceptance
c_i	centroid of cluster C_i
C	capacitor (bond graph element)
$C(\omega)$	real part of radiation coupling coefficient
$C(\infty)$	real part of radiation coupling coefficient at infinite frequency
d	draft, width
d_a	absorption width
$d_{a\,\mathrm{max}}$	maximum absorption width
$D_{i,j}$	distance between two clusters C_i and C_j in the objective space
$e(kz)$	relative variation of hydrodynamic pressure in z-direction, as given in (2.34)
$\vec{f}(\vec{x})$	objective function values
$f_e(\omega)$	complex excitation force per unit incident wave amplitude
F_e	wave excitation force
$F_{e,i}$	wave excitation force on oscillator i
$\mathbf{F}_e$	wave excitation force vector
F_{e1}	surge excitation force
F_{e3}	heave excitation force
$F_{\mathrm{ext}}(s(t), u(t), t)$	general nonlinear force including power take-off force
F_r	wave radiation force
$F_{R\,\mathrm{max}}$	constrained maximum dynamic reaction force at rotation axis
F_t	total wave force
$\mathbf{F}_t$	total wave force vector
F_u	power take-off force
g	acceleration due to gravity
G	generation number
G_{max}	maximum number of generations
$G(\omega)$	radiation conductance
$\mathbf{G}$	radiation conductance matrix
GY	gyrator (bond graph element)
h	water depth
$h(t)$	radiation coupling impulse response function
$H(x)$	Heaviside step function
$H(\omega)$	radiation coupling coefficient
$H_j(\theta), H_j^U(\theta)$	Kochin function corresponding to unit velocity of oscillator j
$H_k^p(\theta)$	Kochin function corresponding to unit pressure of chamber k
$H_{r\,\mathrm{opt}}(\theta)$	optimum Kochin function for radiated wave
H_s	significant wave height

$H_{s,r}(\theta)$	Kochin function
$\mathbf{H}^p(\theta)$	vector of $H_k^p(\theta)$
$\mathbf{H}^U(\theta)$	vector of $H_j^U(\theta)$
i	imaginary unit
I	inertia (bond graph element)
$\mathbf{I}$	identity matrix
$\mathcal{I}(\phi_i, \phi_j)$	integral defined in (2.28)
J	wave energy transport
$J(\omega)$	imaginary part of radiation coupling coefficient
$\mathbf{J}$	imaginary part of radiation-coupling matrix
k	wavenumber
$k(t)$	radiation impedance impulse response function
$K(\omega)$	frequency response function corresponding to radiation impedance
$\hat{K}(s)$	rational transfer function
l	rotation arm length
$L(\omega)$	frequency response function corresponding to radiation coupling
$\mathbb{L}$	lower triangular matrix
m	added inertia, dimension of objective vector
$m(\infty)$	infinite-frequency added inertia
$\mathbf{m}$	added inertia matrix
m_{15}	surge-pitch added inertia
m_{35}	heave-pitch added inertia
M	structural inertia
M_u	load inertia
n	dimension of decision variable vector
$\vec{n}$	unit normal vector pointing into the water
n_j	j-component of $\vec{n}$
N	number of oscillators, number of values in time series, population size
p	hydrodynamic pressure
$p(t)$	dynamic chamber pressure
p_i, q_i	rational transfer function coefficients
p_k	dynamic pressure in chamber k
$\mathbf{p}$	vector of dynamic pressures in oscillating water column chambers
P	mean absorbed power
P_e	excitation power
$P_{e\,\mathrm{opt}}$	optimum excitation power
$P_{\max}$	unconstrained maximum mean absorbed power, constrained maximum mean absorbed power, maximum mean power achievable by linear damper
P_r	radiation power

$P_{r\,\mathrm{opt}}$	optimum radiation power
P^*	Pareto optimal set
PF^*	Pareto front
$Q_c(t)$	volume flow due to air compressibility
Q_e	excitation volume flow
$\mathbf{Q}_e$	excitation volume flow vector
$Q_{\mathrm{ext}}(p(t), t)$	general nonlinear volume flow including volume flow through air turbine
Q_u	volume flow through air turbine
$Q_v(t)$	volume flow through relief valve
r	ratio of constrained to optimum velocity amplitudes, relative density
r, θ, z	cylindrical coordinates
R	radiation damping, resistor (bond graph element)
$\mathbf{R}$	radiation damping matrix
R_{15}	surge-pitch radiation damping
R_{35}	heave-pitch radiation damping
R_C	Coulomb damping
R_e	loss damping
R_q	quadratic damping
R_u	load resistance
$R_{u\,\mathrm{opt}}$	optimum load resistance
$s(t)$	body displacement
S	sum of all wave-generating surfaces, external stiffness
$S(\omega)$	incident wave spectrum
S_b	hydrostatic stiffness
$S_{F_e}(\omega)$	spectral density of wave excitation force
S_j	wetted surface of oscillator j
S_k	internal water surface of chamber k
S_u	load stiffness
Se	effort source (bond graph element)
Sf	flow source (bond graph element)
t	time
t_N	length of time series
T	wave period
T_0	natural period
T_p	peak period
TF	transformer (bond graph element)
$U, u(t)$	velocity
U_{opt}	optimum velocity
U_i	velocity of oscillator i
$U_{\mathrm{opt},i}$	optimum velocity of oscillator i
$\mathbf{U}$	velocity vector
$\mathbf{U}_{\mathrm{opt}}$	optimum velocity vector

$\tilde{\mathbf{U}}$	solution to $\mathbf{R}\tilde{\mathbf{U}} = \mathbf{F}_e/2$
$\mathbb{U}$	upper triangular matrix
v_g	group velocity
v_p	phase velocity
v_r	r-component of water velocity
x	ratio of total inertia, i.e. sum of structural and added inertias, to structural inertia
x, y, z	Cartesian coordinates
$\vec{x}$	vector of decision variables
x_i^L, x_i^U	lower and upper bounds of decision variable i
$\mathbf{x}(t)$	state vector
X_u	load reactance
$y(t)$	radiation admittance impulse response function
$Y(\omega)$	radiation admittance
Z	radiation impedance
$\mathbf{Z}$	radiation impedance matrix
Z_i	intrinsic mechanical impedance
Z_u	load impedance
$Z_{u\,\mathrm{opt}}$	optimum load impedance

GREEK SYMBOLS

β	incident wave heading angle
γ	peakedness parameter
$\boldsymbol{\delta}$	arbitrary vector
$\boldsymbol{\delta}_0$	solution to $\boldsymbol{\delta}^\dagger \mathbf{R} \boldsymbol{\delta} = 0$
$\boldsymbol{\Delta}$	matrix defined in (2.52)
Δt	time interval
$\Delta \omega$	frequency interval
$\boldsymbol{\kappa}$	excitation vector defined in (2.51)
λ	incident wavelength
ρ	water density
$\boldsymbol{\upsilon}$	response vector defined in (2.50)
$\boldsymbol{\upsilon}_{\mathrm{opt}}$	optimum response vector
$\tilde{\boldsymbol{\upsilon}}$	solution of $\boldsymbol{\Delta}\tilde{\boldsymbol{\upsilon}} = \boldsymbol{\kappa}/2$
ϕ	total velocity potential
ϕ_0	incident wave potential
ϕ_n	phase (in radians) of $f_e(\omega_n)$
ϕ_r	radiation potential
ϕ_s	scattered potential
φ_j, φ_j^U	radiation potential due to unit forced velocity of oscillator j
φ_k^p	radiation potential due to unit applied pressure at chamber k
φ_p	radiation potential due to unit applied chamber pressure
φ_r	radiation potential due to unit forced body velocity

ω	angular frequency
ω_0	natural frequency
$\omega_{\min}, \omega_{\max}$	specified minimum and maximum frequencies
ω_p	tuned frequency, peak frequency
Ω	feasible decision variable space

MATHEMATICAL OPERATORS

$\dot{f}$	time derivative of f
$f * g$	convolution of f and g
$\Im\{y\}$	imaginary part of complex quantity y
$\Re\{y\}$	real part of complex quantity y
y^*	complex conjugate of y
$y^\dagger$	complex conjugate transpose of y

1 Introduction

> To ignore [the waves] is a crime against nature.
>
> DAVID ROSS

1.1 BACKGROUND

The ocean is an abundant source of energy, a significant proportion of which still remains untapped. Ocean wave energy, in particular, has a relatively higher energy density than solar or wind energy, has persistent supply, and low environmental impact, making it attractive to utilise. The global wave-power input is estimated to be in the order of 10^{13} W, comparable to the world's present power consumption [51].

1.1.1 A brief historical account

THE EARLY DAYS   Although efforts to harness energy from ocean waves into practical use have been made before the 1970s—notably by Yoshio Masuda from Japan and Walton Bott from Mauritius [119]—it was not until then that the potential of wave energy was seriously considered. The 1973 oil crisis spurred academic research in many parts of the world, and quickly resulted in the publications of two landmark papers in the journal *Nature*. One of these papers was by Stephen Salter from the University of Edinburgh, who proposed a design which has since been famously known as the Salter Duck [120]. His narrow-tank tests revealed two-dimensional efficiencies in excess of 80%, effectively conveying the message that it is possible to extract a large fraction of energy from the waves that are incident on the device. The other paper was by Budal and Falnes [21] from the Norwegian Institute of Technology (NTH, now NTNU), who introduced the term 'point absorber' to classify devices with horizontal dimensions much smaller than the wavelength. They also introduced the parameter 'absorption length' (now better known as 'capture width')[1], defined as "the width of a wavefront across which passes an average amount of power equal to that converted by the point absorber," and went on to show the remarkable result that it is possible for a point absorber to have an absorption length greater than its dimension.

---

[1]In the original definitions, capture width was distinguished from absorption width in that the former corresponds to the useful power, which is the absorbed power minus the power lost by friction and other dissipative effects. Capture width is therefore smaller than absorption width [see 11]. Today, however, capture width is often used to mean absorption width.

Much of the fundamental theory of wave energy absorption was laid out in the period which spanned roughly from the mid 1970s to the mid 1980s. An early theoretical review was given by Evans [38]. The subject of wave energy even occupied the minds of some prominent scientists such as Longuet-Higgins [88] and Lighthill [86] at one time. During this period also a number of different devices were proposed and extensive tests up to 1:10 scale sea trials of some of the most promising devices, including the Salter Duck and the Norwegian wave power buoy, were carried out. This period even saw the construction of two full-scale shore-based prototype wave energy converter (WEC) units in Norway [47].

Several conferences of high quality were organised which reported the significant theoretical and experimental results gathered in this period. The first of these conferences was the Wave Energy Conference at London-Heathrow in 1978 [115], which summarised what had been achieved in the first four years of activities in the UK. Another conference was held at the University of Edinburgh in 1979, sponsored by the Institute of Mathematics and Its Applications [26]. The conference focused on the theoretical aspects and highlighted the needs to improve understanding of the ocean and to consider nonlinear problems. Later in the same year, the first Symposium on Ocean Wave Energy Utilization was held in Gothenburg, followed by the second in Trondheim in 1982 [17, 71]. Wave energy papers also appeared in a few other conferences held during this time, but the IUTAM Symposium in Lisbon in 1985 [42] was perhaps the last of these early conferences which were specifically dedicated to wave energy.

Looking at this collection of works, one can sense the ingenuity, thoroughness, and enthusiasm which have perhaps not been equaled since.

THE DORMANT PERIOD   As the oil price went down, the urgency for wave energy research faded. The UK programme was closed in 1982 [121] and this set the tone for other countries [104]. In Norway, for example, the annual funding declined drastically after 1981 [47]. An account of the UK programme was presented by Grove-Palmer [65] shortly before its closure. In it, he lamented over the prospect of immediate closure, calling it a 'criminal waste' to stop the programme when so much had been spent into it and a prototype was within months of realisation. The closure of the UK programme was a blow to wave energy research. Devices that had gone through painstaking process of refinements (some of these are shown in Fig. 1.1) were suddenly abandoned and then forgotten.

Looking back, we may attribute the failure of the early UK programme to two factors. The first was the premature push towards identifying a single concept for prototype testing when a number of potential concepts could well be the solutions, at least at that early stage of development. Clearly, funding was the issue. Instead of funding all the promising concepts, the government was only willing to fund a single concept for further testing and development. The second was the mistake of setting wave energy technology to compete with conventional technologies by specifying a cost target that was too demanding (about 5p/kWh at that time), although cost estimates in the range of 3 to 16p/kWh were shown to be possible [65]. Indeed, there
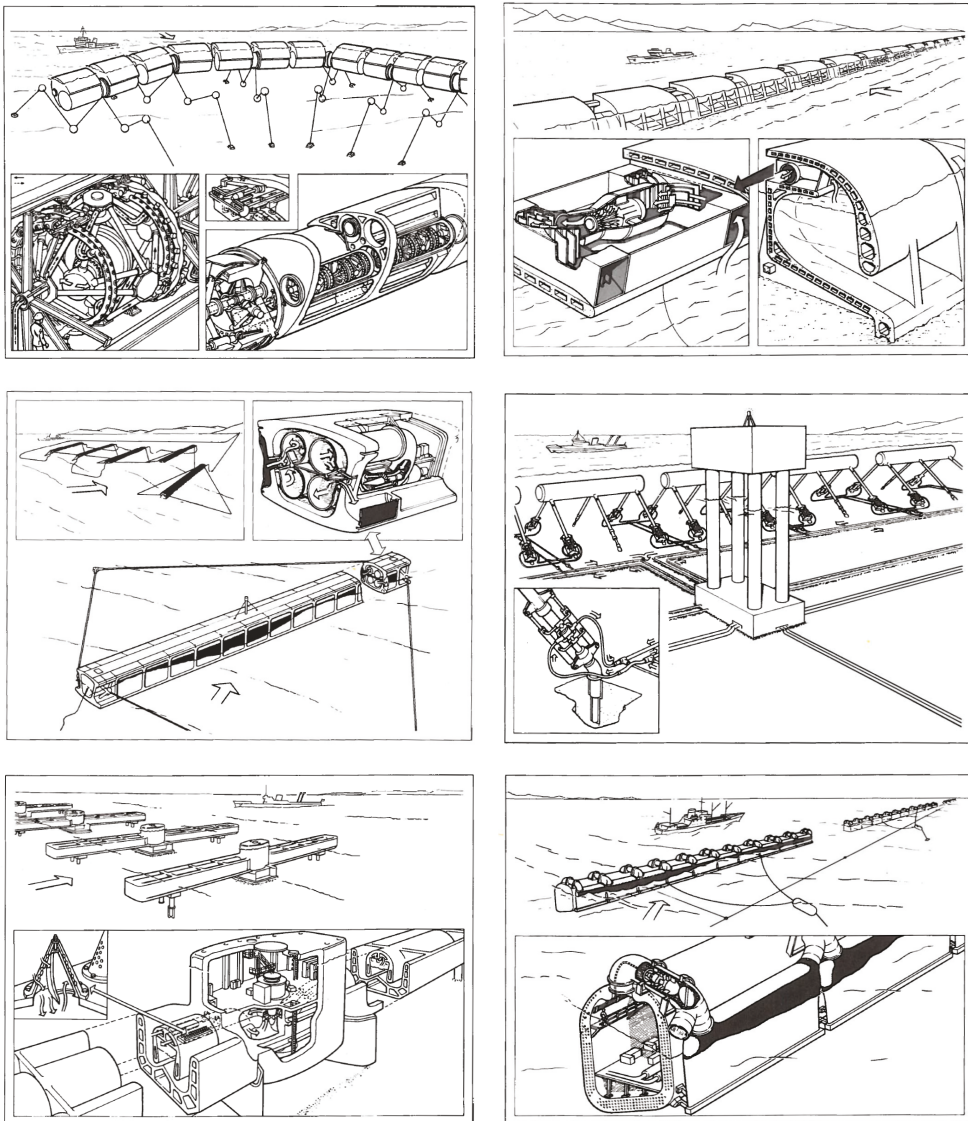
Figure 1.1: Artist impressions of some proposed UK devices from 1982 (reproduced from [65]). Clockwise from top left: Salter Duck, NEL oscillating water column, Bristol cylinder, SEA Clam, Vickers device, and Lancaster flexible bag. These devices are long—in the order of one wavelength—in contrast to the point absorber devices proposed in Norway and Sweden.

3

was much controversy surrounding the closure of the UK programme. Ross [119, p. 134], a journalist, suggested that already in 1978, the official policy had consigned wave energy to 2020 or later, in favour of nuclear energy.

The general feeling in this period was perhaps best exemplified in the following sentiments: "The main question mark which remains is how government departments and industrial organizations can be persuaded to invest in wave power" [87]. "It seems easier to make a start on projects concerned with more 'exotic' problems, such as fusion and star wars rather than every day phenomena. The fundamental reason for this may be the risk of failure—if an exotic process is involved, one can always blame the unknown features: where everyday phenomena is concerned, this is not so easy" [56].

It was a pity indeed that it took about 10 years before the next scientific meeting on wave energy was organised. Nevertheless, some work still continued in several countries, and some of the early workers persevered. At last, there were indications at the end of 1980s that the situation would change for the better. The main factors influencing this change were increasing public awareness of the damage to the environment from burning fossil fuel and of the radiation risks from nuclear power, as well as a change of attitude towards wave energy within the European Community [127]. These led to the first European Wave Energy Symposium in 1993 [34, 122], which was later to become the biannual European Wave and Tidal Energy Conference (EWTEC) series, which has continued up to now. Research activities from this time on continued to increase.

THE REVIVAL   The last decade, especially, has seen a revival of interest in wave energy. Wave energy has again engaged many research institutions in Europe [23], and also in other parts of the world [107, 137]. A scientific meeting was organised recently which brought together the world's experts on wave energy [see 58, and the other papers in the same issue].

A number of devices have been and are being tested at sea. Some of the devices now under active development include CETO [1], Oceanlinx [3], Oyster [4], Pelamis [5], PowerBuoy [2], Wavebob [8], WaveRoller [7], Wavestar [9], Wello Penguin [10], and WET-NZ [6].

Increasing support for wave energy comes from both governments and the private sector in the form of grants, incentives, and investments. One of the latest initiatives was the Danish Energy Agreement on 22 March 2012. As part of this agreement, over a period of four years a total of DKK 100 million will be committed to funding development and use of new renewable electricity production technologies, as well as DKK 25 million for wave power demonstration facilities alone [28]. The British government, likewise, on 5 April 2012 launched its £20 million Marine Energy Array Demonstrator scheme (MEAD), which will support up to two pre-commercial projects to demonstrate the operation of wave and/or tidal devices in array over a period of time [31]. Incentives are given for each unit of target energy delivered within a specified duration, as it has become accepted that the first goals for a device should be to meet the predicted output and to survive, despite its initial high cost. Test centres such as the European Marine Energy Centre (EMEC) in the UK and the Northwest

National Marine Renewable Energy Center (NNMREC) in the US, as well as initiatives such as Marine Renewables Infrastructure Network (MARINET), offer testing facilities and infrastructure to any device. Thus, every concept has equal opportunity to develop.

These are all encouraging developments, but much work still needs to be done, before the technology reaches a mature state [32, 45, 118].

1.1.2 The challenge

The preceding account has shown that probably the greatest challenge to harnessing energy from the waves came from the establishment. However, from the nature of ocean waves, a wave energy device faces two inherent challenges. First, a wave energy device must work with large forces and low velocities, in contrast to the current technology for electrical generation, which is more used to low force, high speed motions [25, 87]. Large forces are inconvenient and expensive to handle. Second, a wave energy device must deal with the stochastic nature of the waves. Ocean waves have variable directions, periods, and heights on all time scales. A wave energy device has to be able to absorb energy optimally from the most frequently occurring waves, and to survive the most extreme wave loads.

As stated by Evans [37], the abundant power that is available in the sea makes it certain that *any* device will deliver some energy. The problem, of course, is to do it economically. Put succinctly, the problem that wave energy research has to tackle may be stated as follows:

Problem. *Given the waves, design a device that minimises the cost per unit of delivered energy.*

Thus, it is clear that in addition to maximising the energy output, one also needs to minimise the cost. Each of these can be broken down still into a number of subobjectives. To maximise the energy output, one needs to maximise the power absorption, minimise the losses, maximise the capacity factor, and maximise the design life. On the other hand, to minimise cost, one needs to minimise both the capital expenditures and the operation expenses.

In the effort to solve this problem, a number of researchers have suggested directions for research [45, 63, 123, 125], pointed out challenges in developing a robust device [19, 23, 96], as well as outlined requirements for an economic device [62, 74, 133]. In addition, reports on ocean energy utilization published by international bodies [e.g., 70] gave a summary of the state of the art, highlighting areas which require further study. All these can be summarised in the following list, which is by no means exhaustive. As wave energy is a multidisciplinary subject, some overlaps between these areas are inevitably present:

(a) Geometric design of the primary interface
    A good wave absorber is a good wave maker [49]. The ratio of working area to size should be maximised for the device to be economic [62]. These, and

similar principles, should guide the design of the primary interface, i.e. the part of a WEC where hydrodynamic interactions with the wave field take place. Numerical optimisation methods could be useful to find optimum geometries [13, 94].

(b) Nonlinear wave/structure/current interactions
Although linear theory is useful, better predictions of power output and device response may require an understanding of the nonlinear interactions between the device and the waves. Some nonlinear effects such as slamming may be critical to the survivability of the device. The influence of currents should also be investigated as their effects on the wave field may be considerable and potentially dangerous for the device.

(c) Power take-off (PTO) and short-time energy storage
The PTO is usually modelled as a linear damper in theory. More realistic models, which include nonlinearities, should be considered. The design and efficiency of the PTO and short-time energy storage system itself need further study.

(d) Multi-degree-of-freedom (MDOF) systems
A MDOF WEC, having multiple resonances, has the potential of capturing energy from broader bandwidth.

(e) System design, modelling, and analysis
The wave energy conversion system should be designed, modelled, and analysed as a system, taking into account the interactions between its various components [74]. It has been suggested that short/direct load paths are preferable for an economic design [133]. Parametric optimisation which includes some economic constraints, and may have multiple competing objectives, could be useful to gain insights and may lead to unexpected solutions.

(f) Control and related means to improve power absorption
Various control strategies have been devised to push the power absorption curve closer to the maximum theoretical limit and covering a wider wave frequency bandwidth [50, 126]. More work is required for their practical implementation in real seas.

(g) Mooring design
The mooring philosophy for floating WECs differs from that for typical floating offshore structures used in the oil and gas industry. While for the latter any motion reductions would generally be considered beneficial, for floating WECs the moorings should not limit the motions if this implies a reduction of the power capture [61].

(h) Wave climate forecast and modelling
The availability of wave climate data is crucial for design purposes and for ac-

curate prediction of the available resource and of the device performance at potential sites.

(i) Survivability
Ocean wave is characterised with a very high ratio of peak to average loads (lower ratios may be found for ocean regions near the equator). Wave conditions that are most critical for different types of WECs are not fully understood. The highest waves do not necessarily create the highest loads [124]. Short waves with moderate heights can be most dangerous [74]. An economic WEC should have a stress-limiting mechanism to avoid loads higher than the design limit. The effects of this mechanism on the device performance should be understood [123].

(j) Availability and reliability
Novel components made of new combinations of materials which are suitable for use in marine environment need to be invented. To ensure that the whole system performs reliably in real sea environment, accelerated life tests of components are vital. A specialised test platform may be necessary to this end [124]. Test results and details of mistakes should be shared for progress to be made. While the understanding of the reliability of these components is still lacking, it is probably necessary to over-design initially [74].

(k) Model testing
Performance expectation at full scale can be made more accurately if more data from model tests at different scales are available. Model tests are also essential to understand nonlinear behaviour, discover unexpected effects [74], and to determine the validity limits of linear theory. Increased confidence in small-scale model testing will make it a valuable part in the development process of a WEC. Wave tanks with more advanced features need to be designed and built.

(l) Production, installation, serviceability, and removal
Cost-competitive WECs should make use of mass production advantages. Methods have to be devised for installing and removing devices and equipments efficiently at sea. Specialised installation and maintenance vessels should be designed.

(m) Arrays
WECs will likely be deployed in arrays of many units. We need to better understand the hydrodynamic interactions between WECs in arrays of various configurations. The mooring design for arrays of floating WECs is another challenge to be tackled.

(n) Environmental impacts
Effects on marine life and coastal processes such as due to the modified wave field at the site need to be investigated.

Fig. 1.2 illustrates how these areas are related in the bigger picture.
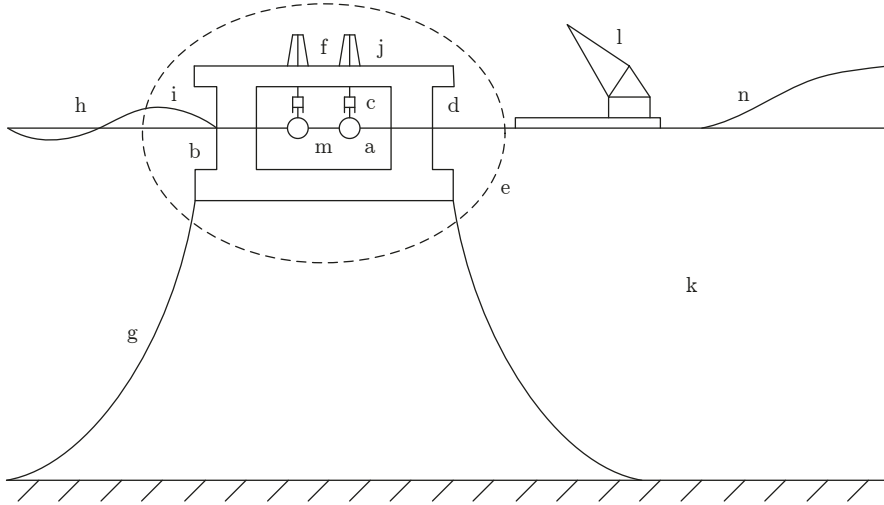
Figure 1.2: Areas of wave energy research: (a) geometric design of the primary interface, (b) nonlinear wave/structure/current interactions, (c) power take-off and short-time energy storage, (d) multi degree-of-freedom systems, (e) system design, modelling, and analysis, (f) control and related means to improve power absorption, (g) mooring design, (h) wave climate forecast and modelling, (i) survivability, (j) availability and reliability, (k) model testing, (l) production, installation, serviceability, and removal, (m) arrays, (n) environmental impacts.

1.2 OBJECTIVES AND SCOPE

A quick survey of the wave energy literature suggests that the amount of work of numerical nature is increasing along with the advance of hardware computing capabilities. We find more and more papers on topics which demand computer-intensive calculations, such as time-domain modelling and numerical optimisation. The former has enabled more realistic models of WECs to be developed which include representations of the whole PTO system, while the latter has enabled systematic assessment of design and/or operational variables in order to arrive at optimum solutions. The purpose of this thesis is to contribute to some of these areas. The questions we would like to address are as follows:

Question 1. *How can we develop more realistic models of WECs and at the same time reduce their simulation time?*

Question 2. *How can we incorporate the cost factor into the design problem and thus design a more economical WEC?*

We present our work under three main headings, namely, *numerical modelling*, *geometry optimisation*, and *geometry control*. Under these headings, the presented work may be seen as a journey towards identifying an economical WEC.

We address the first question under *numerical modelling*. We use the bond graph method and demonstrate its suitability for developing more realistic models of WECs.

Despite an allusion to the bond graph method by Jefferys [73] in his 1984 paper, the application of bond graph for modelling wave energy converters is otherwise relatively recent [15, 35, 66, 90, 105, 136]. We seek to complement these works by presenting bond graph models of two alternative hydraulic PTO systems, a floating oscillating water column (OWC), and generic models of oscillating-body and oscillating-water-column WECs. In the effort to reduce simulation time, we also look at different alternatives for modelling the wave radiation forces in time domain, and compare them in terms of their accuracy and efficiency. The work may be seen as a particular extension of [128] applied to WECs. A similar study has been reported recently by Ricci et al. [117]. The main difference between our study and theirs is that we consider more generic models with variable nonlinear terms, to allow for a more systematic study.

We deal with the second question under *geometry optimisation*. A multi-objective optimisation scheme is suggested as a way to incorporate the cost factor into the design problem. We consider specifically the geometric design problem, and pose the problem of finding an optimum, i.e. economic, geometry of a WEC as a multi-objective optimisation problem. A multi-objective optimisation framework is developed which makes use of the relational geometry approach to vary the geometry. We apply the method to find the optimum geometries for a class of WECs oscillating about a fixed horizontal axis. The work may be seen as a contribution to the areas of geometry optimisation [13, 93, 94] as well as applications of multi-objective optimisation in wave energy research [13]. Informed by the result of the geometry optimisation study, we propose a new WEC with variable geometry to further improve its economy. A numerical investigation of the potential of this WEC is presented under *geometry control*, making use of the tools from *numerical modelling*.

This thesis is supported by a collection of research papers. Under the suggested headings, papers A, B, C, and G fall under numerical modelling, papers D and F fall under geometry optimisation, and paper E falls under geometry control (see List of appended papers on p. ix). In papers A and G, the bond graph method is the main focus. Paper G concentrates on the modelling of the primary interface, while paper A mainly addresses the modelling of the PTO. Paper C addresses the comparison of alternative models of the wave radiation forces. Paper B looks at the modelling of a floating OWC in detail, where the bond graph method is applied. In papers D and F, the multi-objective optimisation framework is described and applied to find the optimum geometries of WECs oscillating about a fixed horizontal axis. In paper D, a number of different geometries are considered, where each has a uniform cross section, while in paper F, we deal with a cylinder composed of a central part and two ends having a larger diameter than the central part. Different combinations of objective functions are used in papers D and F. Finally, paper E contains a study of the proposed WEC. Referring to the previous list in §1.1.2, the papers touch upon items a, c, d, e, f, and i.

We adopt the classical linear wave theory in all the work presented. The validity of linear theory may be questioned in some of the considered problems, especially when small depth of submergence is involved. In these cases it could have been possible to

account for the hydrodynamic loss in a simplified manner, but to do so properly for all the considered geometric variations would merit a study on its own. In addition, the incident waves are assumed to propagate always in one direction. In other words, distribution of wave headings is not considered. Also, the water depth is assumed to be uniform everywhere.

1.3 OUTLINE

The papers are put together in the appendix. Several introductory chapters (Chapters 1 to 6) are written to summarise, provide theoretical background, and give an overall perspective of the work.

The purpose of the present chapter (Chapter 1) is to set the general context, in which this thesis falls.

Chapter 2 gathers some important theoretical results concerning wave power absorption. Expressions of maximum mean power that can be absorbed by a single body oscillating in one energy-absorbing mode and by a system of wave absorbers are derived using two different points of view. In the first point of view, the absorbed power is taken as the product of the wave forces on the bodies and their velocities. In the second point of view, the absorbed power is expressed as the product of the hydrodynamic pressure and the normal component of the water particle velocities over the surface of an envisaged vertical cylinder of infinite radius, spanning from the mean free surface to the bottom. The two results are equivalent and are related through reciprocity relations which exist between the near- and far-field quantities. These results are to be interpreted as the theoretical maximum that can be achieved by a given device, according to linear wave theory. It is possible to attain this theoretical maximum at all frequencies only if the system oscillates with optimum velocities at all frequencies. In practice, the mechanical parameters of the system are often set to constants tuned to one selected frequency. The power that can be absorbed by a system with constant load impedance is considered briefly at the end of Chapter 2.

Each of the three chapters thereafter (Chapters 3 to 5) deals with one of the three main headings mentioned earlier, namely, numerical modelling, geometry optimisation, and geometry control of WECs.

Chapter 3 deals with numerical modelling of WECs. It begins by presenting the equations of motion, in time domain, of an oscillating body, a fixed OWC, and a floating OWC. The bond graph method is then introduced, and generic bond graph models of the different WECs are presented. It is shown that a floating OWC is a combination of an oscillating body and a fixed OWC. The treatment of the wave excitation force/volume flow is considered next, followed by a discussion on the wave radiation force in the time domain and the alternative models to represent it, namely, the direct convolution integration, the constant-coefficient model, and the state-space model. The computations of hydrodynamic parameters and simulations are briefly discussed at the end of the chapter.

Chapter 4 deals with geometry optimisation of WECs. It begins with a motivation for considering the cost factor in addition to the power that can be absorbed

by a WEC. Several possible cost indicators are discussed, and a multi-objective optimisation scheme is suggested to be a useful tool for incorporating the cost factor into the design problem. The geometry optimisation framework is then introduced. The methodology is composed of three main elements. The first element is the multi-objective optimisation algorithm, the second one is the relational geometry approach for modelling the geometry, and the third one is the computation of the objective functions. Each is described in detail.

Chapter 5 deals with geometry control of WECs. It begins with a discussion of the natural resonant periods of heaving and bottom-hinged bodies. The natural period of a heaving body is governed by its size, while that of a bottom-hinged body is governed by the arm length and the relative density of the body. The need for controlling WECs to improve their economy is addressed next, with a discussion on geometry control, which is defined as any strategy that alters the excitation force (volume flow) and/or the intrinsic impedance (admittance) of the WEC. The chapter ends with a discussion of the proposed concept, which incorporates a geometry control strategy to improve its economy.

A summary of contributions and recommendations for future work is finally given in Chapter 6.

2 Wave power absorption

> To absorb a wave means to generate a wave.
>
> Kjell Budal

In terms of their hydrodynamic performance, many devices that appear to differ are in fact fundamentally similar [103]. In this chapter a review of some important results derived on the basis of linear wave theory is given. First we discuss the maximum mean power that can be absorbed by a single and many WECs. The case where the radiation damping matrix is singular is discussed in some details. Then we discuss the mean absorbed power for the case of a WEC with constant mechanical parameters tuned to a selected frequency.

2.1 MAXIMUM ABSORBED POWER

It is of theoretical interest to know how much power we can expect a given device to absorb from the waves.

We first consider a system of wave absorbers composed of rigid bodies oscillating in a total of N energy absorbing modes. A system which includes a number of oscillating water columns will be dealt with in §2.1.3. As in [46], we shall refer to a single mode of one body as an *oscillator*. Expressions for the maximum mean power that can be absorbed by a system of oscillators can be derived using different points of view. In all our derivation, we assume the wave amplitude to be so small that the design amplitude constraint need not be taken into consideration.

2.1.1 Wave excitation and radiation forces

In the first point of view, the absorbed power is taken as the product of the wave forces on the oscillators and their velocities.

SINGLE OSCILLATOR Consider first a single oscillator. The mean power P that can be absorbed by the oscillator may be expressed as the product of the wave force F_t on the oscillator and its velocity U:

$$P = \frac{1}{2}\Re\{F_t^* U\}, \tag{2.1}$$

where $\Re\{\ \}$ denotes the real part and * denotes complex conjugate. Both F_t and U are complex quantities, with the time-dependent factor $\exp(\mathrm{i}\omega t)$, where ω is the angular

wave frequency. The total wave force on the oscillator is the sum of the wave excitation F_e and radiation forces F_r:

$$
\begin{aligned}
F_t &= F_e + F_r \\
&= F_e - ZU,
\end{aligned}
\tag{2.2}
$$

where Z is the radiation impedance, which may be decomposed into

$$
Z = R + i\omega m,
\tag{2.3}
$$

where R is the radiation damping and m is the added inertia. Hence we may write the mean absorbed power as the excitation power minus the radiated power:

$$
\begin{aligned}
P &= P_e - P_r \\
&= \frac{1}{4}(F_e U^* + F_e^* U) - \frac{1}{2}R|U|^2,
\end{aligned}
\tag{2.4}
$$

which may be rewritten as [36]

$$
P = \frac{|F_e|^2}{8R} - \frac{1}{2}R\left|U - \frac{F_e}{2R}\right|^2.
\tag{2.5}
$$

It follows that the maximum mean power that can be absorbed by the oscillator is given by

$$
P_{\max} = \frac{|F_e|^2}{8R},
\tag{2.6}
$$

achieved when

$$
U = U_{\mathrm{opt}} = \frac{F_e}{2R}.
\tag{2.7}
$$

Equation (2.7) tells us that, for maximum power absorption, the single oscillator must move with a velocity in phase with the excitation force, and with an amplitude $|F_e|/2\omega R$. Furthermore, from (2.4) it can be seen that

$$
P_{\max} = P_{r\,\mathrm{opt}} = \frac{1}{2}P_{e\,\mathrm{opt}}.
\tag{2.8}
$$

The constrained versions of (2.6) and (2.7) are used in papers D and E.

The velocity and the excitation force are related through the equation of motion of the oscillator:

$$
(Z_i + Z_u)U = F_e,
\tag{2.9}
$$

where $Z_i = R + i\omega(M + m - S_b\omega^{-2})$ is the intrinsic mechanical impedance and $Z_u = R_u + iX_u$ is the load impedance. Here M is the structural inertia and S_b is the hydrostatic stiffness. The mean power absorbed by the load is given by

$$
P = \frac{1}{2}\Re\{Z_u\}|U|^2.
\tag{2.10}
$$

By substitution of (2.9) into (2.10) and some algebraic manipulation it can be shown that [41]

$$P = \frac{|F_e|^2}{8R}\left(1 - \frac{|Z_u - Z_i^*|^2}{|Z_u + Z_i|^2}\right). \tag{2.11}$$

Looking at the form of (2.11), we may see that maximum power absorption will be achieved when $Z_u = Z_{u\,\text{opt}} = Z_i^*$, or, equivalently, when both $R_u = R_{u\,\text{opt}} = R$ and the system is at resonance. This again yields (2.6) and (2.7).

The preceding analysis tells us that, in terms of maximising the power absorption, two things are needful. Firstly, the primary interface should be designed such that P_{max} is maximised over the range of frequently occurring wave frequencies. Secondly, the power take-off and control system should be designed and operated such that P approaches P_{max} most of the time. The problem of course is that both of these goals must be weighed against the cost of achieving them. When this is taken into account, it may be necessary to operate at suboptimal level of power absorption, as long as the overall cost per unit of delivered energy is minimised.

SYSTEM OF OSCILLATORS   For a system of oscillators, the mean absorbed power can be expressed as the product of the wave forces on the oscillators and their velocities:

$$P = \frac{1}{2}\Re\{\mathbf{F}_t^\dagger \mathbf{U}\}, \tag{2.12}$$

where now both $\mathbf{F}_t$ and $\mathbf{U}$ are column vectors of size $N \times 1$. The † symbol denotes complex conjugate transpose. The total wave force is the sum of the wave excitation and radiation forces:

$$\mathbf{F}_t = \mathbf{F}_e - \mathbf{Z}\mathbf{U}, \tag{2.13}$$

where $\mathbf{Z}$ is the radiation impedance matrix, which may be decomposed into

$$\mathbf{Z} = \mathbf{R} + i\omega\mathbf{m}, \tag{2.14}$$

where $\mathbf{R}$ is the radiation damping matrix and $\mathbf{m}$ is the added inertia matrix. By virtue of Green's second identity, it can be shown that the radiation impedance matrix $\mathbf{Z}$ is symmetric [101]. Hence we may write the mean absorbed power as the excitation power minus the radiated power:

$$\begin{aligned} P &= P_e - P_r \\ &= \frac{1}{4}(\mathbf{U}^\dagger\mathbf{F}_e + \mathbf{F}_e^\dagger\mathbf{U}) - \frac{1}{2}\mathbf{U}^\dagger\mathbf{R}\mathbf{U}. \end{aligned} \tag{2.15}$$

Equation (2.15) may be rewritten as [36]

$$P = \frac{1}{8}\mathbf{F}_e^\dagger\mathbf{R}^{-1}\mathbf{F}_e - \frac{1}{2}(\mathbf{U} - \frac{1}{2}\mathbf{R}^{-1}\mathbf{F}_e)^\dagger\mathbf{R}(\mathbf{U} - \frac{1}{2}\mathbf{R}^{-1}\mathbf{F}_e), \tag{2.16}$$

provided $\mathbf{R}^{-1}$ exists. It is often assumed that $\mathbf{R}$ is positive definite and $\mathbf{R}^{-1}$ exists. It then follows from (2.16) that the maximum mean power that can be absorbed by the system is

$$P_{\text{max}} = \frac{1}{8}\mathbf{F}_e^\dagger\mathbf{R}^{-1}\mathbf{F}_e, \tag{2.17}$$

15

achieved when

$$\mathbf{U} = \mathbf{U}_{\text{opt}} = \frac{1}{2}\mathbf{R}^{-1}\mathbf{F}_e. \tag{2.18}$$

In general, $\mathbf{R}$ is positive semidefinite and $\mathbf{R}$ may be singular [49, p. 213]. An alternative expression to (2.16) for the mean absorbed power may be obtained if we write

$$\mathbf{U} = \tilde{\mathbf{U}} + \boldsymbol{\delta}, \tag{2.19}$$

where $\boldsymbol{\delta}$ is an arbitrary vector and $\tilde{\mathbf{U}}$ is the solution of

$$\mathbf{R}\tilde{\mathbf{U}} = \frac{1}{2}\mathbf{F}_e. \tag{2.20}$$

Substituting (2.19) into (2.15) gives

$$P = \frac{1}{4}\mathbf{F}_e^{\dagger}\tilde{\mathbf{U}} - \frac{1}{2}\boldsymbol{\delta}^{\dagger}\mathbf{R}\boldsymbol{\delta}. \tag{2.21}$$

Since $\mathbf{R}$ is positive semidefinite, i.e. $\boldsymbol{\delta}^{\dagger}\mathbf{R}\boldsymbol{\delta} \geq 0$, the maximum mean absorbed power is given as

$$P_{\text{max}} = \frac{1}{4}\mathbf{F}_e^{\dagger}\tilde{\mathbf{U}} = \frac{1}{2}\tilde{\mathbf{U}}^{\dagger}\mathbf{R}\tilde{\mathbf{U}}, \tag{2.22}$$

This is a more general expression for the maximum mean absorbed power than (2.17). When $\mathbf{R}^{-1}$ exists, $\tilde{\mathbf{U}}$ is unique and is equal to $\mathbf{R}^{-1}\mathbf{F}_e/2$. This is then the (unique) optimum velocity of the oscillators, as shown in (2.18). When $\mathbf{R}$ is singular, $\tilde{\mathbf{U}}$ is not unique. However, P_{max} is always unique [46, 48]. This follows if we consider two different vectors $\tilde{\mathbf{U}}_1$ and $\tilde{\mathbf{U}}_2$, each satisfying (2.20) such that $\mathbf{R}(\tilde{\mathbf{U}}_1 - \tilde{\mathbf{U}}_2) = 0$. Hence, from (2.22), we have $P_{\text{max}\,1} - P_{\text{max}\,2} = 0$. Thus, P_{max} is unique even if $\tilde{\mathbf{U}}$ is not. From (2.15) it can be seen that, as in the single oscillator case, the identity (2.8) is valid, whether $\mathbf{R}$ is singular or not. Note that, unlike the case of a single oscillator, the optimal velocity $U_{\text{opt},i}$ of oscillator i is generally *not* in phase with the excitation force $F_{e,i}$ [46]. Even for a system of equal oscillators, the optimal amplitudes and phases of the oscillators may be different from each other [36].

Since $\boldsymbol{\delta}^{\dagger}\mathbf{R}\boldsymbol{\delta}$ may be zero for some nonzero $\boldsymbol{\delta} = \boldsymbol{\delta}_0$ when $\mathbf{R}$ is singular, the optimum velocity $\mathbf{U}_{\text{opt}}$ when $\mathbf{R}$ is singular may differ from $\tilde{\mathbf{U}}$ by some finite vector $\boldsymbol{\delta}_0$. Observe that the difference between any two vectors $\tilde{\mathbf{U}}_1$ and $\tilde{\mathbf{U}}_2$ which satisfy (2.20) is also a solution to $\boldsymbol{\delta}^{\dagger}\mathbf{R}\boldsymbol{\delta} = 0$. Referring to (2.15), we may note that $\boldsymbol{\delta}^{\dagger}\mathbf{R}\boldsymbol{\delta}/2$ is the radiated power corresponding to the velocity vector $\boldsymbol{\delta}$. This means that oscillations with velocity $\boldsymbol{\delta}_0$ do not radiate any waves in the far-field. As we shall see later in §2.1.2, the amount of power that can be absorbed from the waves is related to the far-field wave radiation pattern of the system of oscillators. It follows that any solution $\tilde{\mathbf{U}}$ to (2.20) will produce the same optimum radiated wave pattern in the far-field region, and adding such $\boldsymbol{\delta}_0$ to $\tilde{\mathbf{U}}$ will not change the optimum far-field radiated wave pattern.

Proceeding further, assuming that $\mathbf{R}^{-1}$ exists, Wolgamot et al. [134] showed that

$$\int_0^{2\pi} P_{\text{max}}(\beta)\mathrm{d}\beta = N\lambda J, \tag{2.23}$$

where λ is the incident wavelength, and

$$J = \frac{\rho g v_g}{2}|A|^2 = \frac{\rho g \pi v_p v_g}{\omega \lambda}|A|^2 \qquad (2.24)$$

is the wave energy transport, defined as the transported wave power per unit width of the wave front, of a plane harmonic wave with complex amplitude A and angular frequency ω [49]. Here, $v_g = \mathrm{d}\omega/\mathrm{d}k$ is the group velocity and $v_p = \omega/k$ is the phase velocity, where $k = 2\pi/\lambda$ is the wavenumber. Defining absorption width as

$$d_a = \frac{P}{J}, \qquad (2.25)$$

we may write (2.23) as

$$\int_0^{2\pi} d_{a\,\mathrm{max}}(\beta)\mathrm{d}\beta = N\lambda. \qquad (2.26)$$

The proof for identity (2.23) is given in Appendix 2.A.

It may appear from (2.23) that the amount of power that can be absorbed from the waves may be multiplied by increasing indefinitely the number of oscillators in the system. However, it should be noted that the identity (2.23) or (2.26) holds only when $\mathbf{R}^{-1}$ exists. As an example for which $\mathbf{R}$ is singular, consider a system of two concentric axisymmetric bodies, each absorbing energy in heave only. Thus, $N = 2$. It can be shown that $P_{\mathrm{max}} = \lambda J/2\pi$ in this case [49, pp. 217-218], equivalent to the maximum power that can be absorbed by a single heaving axisymmetric body. Hence, $\int_0^{2\pi} P_{\mathrm{max}}(\beta)\mathrm{d}\beta = \lambda J$, although $N = 2$. As another example, consider a single axisymmetric body absorbing energy in surge and pitch. In this case, it can be shown that $P_{\mathrm{max}}(\beta) = \lambda J \cos^2 \beta/\pi$. Again, $\int_0^{2\pi} P_{\mathrm{max}}(\beta)\mathrm{d}\beta = \lambda J$, although $N = 2$. It may thus be conjectured that a general form of identity (2.23) or (2.26) will have N replaced by the rank of the radiation damping matrix $\mathbf{R}$, which is equal to N if $\mathbf{R}$ is not singular, but less than N if $\mathbf{R}$ is singular [see 109, pp. 31-32] (In both examples with $N = 2$ above, the rank of $\mathbf{R}$ is equal to 1). Physically, this means that adding more oscillators in the system will increase the amount of power that can be absorbed from the waves only if it changes the optimum wave radiation pattern. This may have important implications for the design of WEC arrays.

2.1.2 Far-field theory

In the second point of view, we envisage a vertical cylinder from the sea bottom $z = -h$ to the mean free surface $z = 0$ with radius $r \to \infty$, containing all the wave absorbers. The absorbed power is taken as the net wave power that is transported from the outside to the inside of this cylinder. Thus

$$P = -\int_0^{2\pi}\int_{-h}^0 \frac{1}{2}\Re\{p v_r^*\}r\mathrm{d}\theta\mathrm{d}z, \qquad (2.27)$$

where $p = -\mathrm{i}\omega\rho\phi$ is the hydrodynamic pressure and $v_r = \partial\phi/\partial r$ is the r-component of the water velocity. Here ϕ is the total velocity potential, which is the sum of the incident wave potential ϕ_0, the scattered potential ϕ_s, and the radiation potential ϕ_r.

SYSTEM OF OSCILLATORS Consider first a system of oscillators. Budal [20] was the first to apply far-field theory to a system of oscillators. Let S be the sum of all the wave-generating surfaces and $\vec{n}$ a unit normal vector pointing into the water. If we define the integral

$$\mathcal{I}(\phi_i, \phi_j) \equiv \iint_S \left(\phi_i \frac{\partial \phi_j}{\partial n} - \frac{\partial \phi_i}{\partial n} \phi_j \right) \mathrm{d}S \tag{2.28}$$

for any two functions ϕ_i and ϕ_j which satisfy the Laplace equation in the water domain, and if, in addition, both ϕ_i and ϕ_j satisfy the linearised free-surface condition and the bottom boundary condition, then it can be shown by virtue of Green's second identity that the integral is equivalent to [101]

$$\mathcal{I}(\phi_i, \phi_j) = \int_{-h}^{0} \int_{0}^{2\pi} \left(\phi_i \frac{\partial \phi_j}{\partial r} - \frac{\partial \phi_i}{\partial r} \phi_j \right) r \mathrm{d}\theta \mathrm{d}z. \tag{2.29}$$

Therefore, (2.27) can be written as

$$P = \frac{\mathrm{i}\omega\rho}{4} \mathcal{I}(\phi, \phi^*) = \frac{\mathrm{i}\omega\rho}{4} \mathcal{I}(\phi_0 + \phi_s + \phi_r, \phi_0^* + \phi_s^* + \phi_r^*). \tag{2.30}$$

When all the oscillators are not moving, which means that $\phi_r = 0$, no power is absorbed from the waves. Hence

$$\mathcal{I}(\phi_0 + \phi_s, \phi_0^* + \phi_s^*) = 0. \tag{2.31}$$

Therefore, (2.30) reduces to

$$P = \frac{1}{2} \Re\{\mathrm{i}\omega\rho \mathcal{I}(\phi_0 + \phi_s, \phi_r^*)\} + \frac{\mathrm{i}\omega\rho}{4} \mathcal{I}(\phi_r, \phi_r^*). \tag{2.32}$$

The scattered and radiation potentials as $kr \to \infty$ can be written as [see 49, eq. (4.222)]

$$\phi_{s,r} = A_{s,r}(\theta) e(kz) (kr)^{-1/2} \exp(-\mathrm{i}kr), \tag{2.33}$$

where $A_{s,r}(\theta)$ is the far-field coefficient and

$$e(kz) = \frac{\cosh(kz + kh)}{\cosh(kh)}, \tag{2.34}$$

while the incident wave potential is given as [see 49, eq. (4.276)]

$$\phi_0 = \frac{\mathrm{i}g}{\omega} A e(kz) \exp(-\mathrm{i}kr \cos(\theta - \beta)), \tag{2.35}$$

where A is the complex incident wave amplitude at the origin and β is the angle of incidence.

There exists a non-trivial relationship between the far-field coefficient $A_{s,r}(\beta)$ and the so-called Kochin function $H_{s,r}(\beta)$, defined as

$$H_{s,r}(\beta) \equiv -\frac{g}{2v_p v_g} \mathcal{I}(e(kz) \exp(\mathrm{i}kr \cos(\theta - \beta)), \phi_{s,r}), \tag{2.36}$$

where v_p and v_g are the phase and group velocities, respectively. The relationship is given as [see e.g. 49, pp. 99-101, for a proof]:

$$H_{s,r}(\beta) = \sqrt{2\pi} A_{s,r}(\beta) \exp(i\pi/4). \tag{2.37}$$

We may write the radiation potential as $\phi_r = \sum_{j=1}^{N} \varphi_j U_j$, where φ_j is the radiation potential due to the forced motion of oscillator j with a unit velocity and U_j is the velocity of oscillator j. We may also write $H_r(\beta) = \sum_{j=1}^{N} H_j(\beta)U_j$, where $H_j(\beta) \equiv -\frac{g}{2v_p v_g}\mathcal{I}(e(kz)\exp(ikr\cos(\theta - \beta)), \varphi_j)$. The body boundary condition requires that $\partial\varphi_j/\partial n = n_j$ on S, where n_j is the j-component of $\vec{n}$. Since $\vec{n}$ is real in the case of rigid-body oscillations, $\partial\varphi_j^*/\partial n = \partial\varphi_j/\partial n$ on S. Also, $\partial(\phi_0 + \phi_s)/\partial n = 0$ on S. It follows that

$$\mathcal{I}(\phi_0 + \phi_s, \varphi_j^*) = \mathcal{I}(\phi_0 + \phi_s, \varphi_j) = \frac{2v_p v_g A}{i\omega}H_j(\beta \pm \pi), \tag{2.38}$$

where the last equality has been obtained from (2.35) and (2.36), and noting that $\mathcal{I}(\phi_s, \varphi_j) = 0$.

Therefore, in terms of the Kochin functions, the expression for the mean absorbed power (2.32) becomes

$$P = \rho v_p v_g \left(\Re\{A\bar{H}_r(\beta \pm \pi)\} - \frac{\omega}{4\pi g}\int_0^{2\pi} |H_r(\theta)|^2 d\theta \right), \tag{2.39}$$

where $\bar{H}_r(\beta) = \sum_{j=1}^{N} H_j(\beta)U_j^*$. The last term in (2.39) has been obtained using (2.33), (2.37), and (2.29).

Following [54], equation (2.39) may be written as

$$P = (AE^* + A^*E) - |D|^2 = \left|\frac{AE}{D}\right|^2 - \left|\frac{AE^*}{D^*} - D\right|^2, \tag{2.40}$$

with

$$E = \frac{\rho v_p v_g}{2}\bar{H}_r^*(\beta \pm \pi) \tag{2.41}$$

$$|D|^2 = \frac{\omega\rho v_p v_g}{4\pi g}\int_0^{2\pi} |H_r(\theta)|^2 d\theta. \tag{2.42}$$

From (2.40) we see that the maximum absorbed power is obtained when $AE^*/D^* = D$, or $AE^* = |D|^2 = A^*E$, from which we obtain the following condition for the optimum Kochin function:

$$A\bar{H}_{r\,\text{opt}}(\beta \pm \pi) = \frac{\omega}{2\pi g}\int_0^{2\pi} |H_{r\,\text{opt}}(\theta)|^2 d\theta. \tag{2.43}$$

The optimum Kochin function $H_{r\,\text{opt}}(\theta)$ is implicitly dependent on the incident wave direction β, since $\mathbf{F}_e$, and hence the optimum velocity vector $\mathbf{U}_{\text{opt}}$, depend on β [cf. 54, eq. (A 14)]. The maximum absorbed power is obtained as

$$P_{\text{max}} = \left|\frac{AE_{\text{opt}}}{D_{\text{opt}}}\right|^2 = \lambda J\frac{|\bar{H}_{r\,\text{opt}}(\beta \pm \pi)|^2}{\int_0^{2\pi} |H_{r\,\text{opt}}(\theta)|^2 d\theta}, \tag{2.44}$$

19

where J is defined in (2.24).

This final expression (2.44) relates the maximum absorbed power to the far-field pattern of the waves radiated by the system in the absence of incident waves. The denominator corresponds to the wave pattern that is radiated by the absorbers oscillating in optimum motions, while the numerator corresponds to the wave pattern that is radiated by the absorbers oscillating in *time-reversal* of the optimum motions [see 116, eq. (A 9)]. In the case of the Bristol cylinder [44], for example, if the incident waves are propagating from left to right, the denominator corresponds to the wave pattern radiated by the cylinder oscillating in optimum clockwise motion, while the numerator to the reverse, i.e., counter-clockwise motion. The expression (2.44) tells us that to maximise power absorption, a system of wave absorbers should produce waves mainly in the direction opposite to the incident wave direction, when each absorber is forced to oscillate in *time-reversal* of its optimum motion, in calm water. In other words, a good wave absorber has to be a good wavemaker.

It is also possible to arrive at the same result using (2.15) as the starting point and utilising some known relations between far-field and local terms. The wave excitation force can be expressed in terms of the Kochin function via the Haskind relation [see e.g. 49, eq. (5.200)]:

$$F_{ej} = 2\rho v_p v_g H_j(\beta \pm \pi)A, \tag{2.45}$$

and there is a relation between the radiation damping and the Kochin function [see e.g. 49, eq. (5.176)]:

$$R_{ij} = \frac{\omega \rho v_p v_g}{2\pi g} \int_0^{2\pi} H_i^*(\theta) H_j(\theta) \mathrm{d}\theta. \tag{2.46}$$

Hence,

$$\begin{aligned} P &= \frac{1}{4}(\mathbf{U}^\dagger \mathbf{F}_e + \mathbf{F}_e^\dagger \mathbf{U}) - \frac{1}{2}\mathbf{U}^\dagger \mathbf{R}\mathbf{U} \\ &= \frac{\rho v_p v_g}{2}\left(A\bar{H}_r(\beta \pm \pi) + A^*\bar{H}_r^*(\beta \pm \pi) - \frac{\omega}{2\pi g}\int_0^{2\pi} |H_r(\theta)|^2 \mathrm{d}\theta \right), \end{aligned} \tag{2.47}$$

exactly the same as (2.39).

SINGLE OSCILLATOR For a single oscillator, $|\bar{H}_r(\beta \pm \pi)| = |H_r(\beta \pm \pi)|$. Therefore

$$P_{\max} = \lambda J \frac{|H_{r\,\mathrm{opt}}(\beta \pm \pi)|^2}{\int_0^{2\pi} |H_{r\,\mathrm{opt}}(\theta)|^2 \mathrm{d}\theta}. \tag{2.48}$$

This result was derived independently by Evans [36] and Newman [102]. As in the many-oscillator case, it is possible to derive this result directly from (2.6) using the relations (2.45) and (2.46).

2.1.3 Oscillating bodies and water columns

If the system of wave absorbers include not only oscillating rigid bodies but also oscillating water columns, the mean absorbed power can be obtained using the first point of view as [49]

$$P = \frac{1}{4}(\boldsymbol{v}^\dagger\boldsymbol{\kappa} + \boldsymbol{\kappa}^\dagger\boldsymbol{v}) - \frac{1}{2}\boldsymbol{v}^\dagger\boldsymbol{\Delta}\boldsymbol{v}, \tag{2.49}$$

where

$$\boldsymbol{v} = \begin{pmatrix} \mathbf{U} \\ -\mathbf{p} \end{pmatrix}, \tag{2.50}$$

$$\boldsymbol{\kappa} = \begin{pmatrix} \mathbf{F}_e \\ -\mathbf{Q}_e \end{pmatrix}, \tag{2.51}$$

and

$$\boldsymbol{\Delta} = \begin{pmatrix} \mathbf{R} & -\mathrm{i}\mathbf{J} \\ \mathrm{i}\mathbf{J}^T & \mathbf{G} \end{pmatrix}. \tag{2.52}$$

Here, $\mathbf{p}$ is the vector of dynamic pressures in the oscillating water column chambers, $\mathbf{Q}_e$ is the excitation volume flow vector, $\mathbf{J}$ is the imaginary part of the radiation-coupling matrix, and $\mathbf{G}$ is the radiation conductance matrix. The radiation-coupling matrix relates the forces on the bodies, when held fixed, to the pressures in the chambers, or it relates the volume flow in the chambers, when open to the atmosphere, to the velocities of the bodies. The radiation-conductance matrix is the real part of the radiation-admittance matrix, which relates the volume flow in the chambers to the pressures in them.

If $\boldsymbol{\Delta}$ is non-singular, the maximum absorbed power is given as

$$P_{\mathrm{max}} = \frac{1}{8}\boldsymbol{\kappa}^\dagger\boldsymbol{\Delta}^{-1}\boldsymbol{\kappa}, \tag{2.53}$$

and the optimum response vector is

$$\boldsymbol{v}_{\mathrm{opt}} = \frac{1}{2}\boldsymbol{\Delta}^{-1}\boldsymbol{\kappa}. \tag{2.54}$$

The analogy with (2.17) and (2.18) is obvious. In general, $\boldsymbol{\Delta}$ is positive semidefinite and $\boldsymbol{\Delta}$ may be singular. Proceeding as in the case of a system of oscillating rigid bodies, a more general expression for the maximum absorbed power may be obtained as

$$P_{\mathrm{max}} = \frac{1}{4}\boldsymbol{\kappa}^\dagger\tilde{\boldsymbol{v}} = \frac{1}{2}\tilde{\boldsymbol{v}}^\dagger\boldsymbol{\Delta}\tilde{\boldsymbol{v}}, \tag{2.55}$$

where $\tilde{\boldsymbol{v}}$ is the solution of

$$\boldsymbol{\Delta}\tilde{\boldsymbol{v}} = \frac{1}{2}\boldsymbol{\kappa}. \tag{2.56}$$

Using the second point view, it can be shown (see Appendix 2.B) that (2.44) also applies for a system of oscillating rigid bodies and oscillating water columns, but with $\bar{H}_r(\theta) = \sum_{j=1}^{N} H_j^U(\theta)U_j + \sum_{k=1}^{M} H_k^p(\theta)p_k$ and $\bar{H}_r(\theta) = \sum_{j=1}^{N} H_j^U(\theta)U_j^* -$

$\sum_{k=1}^{M} H_k^p(\theta)p_k^*$, where M is the number of oscillating water columns and $H_j^U(\theta)$ and $H_k^p(\theta)$ are the Kochin functions associated with the unit velocity of oscillator j and the unit pressure of chamber k, respectively.

The same result can be obtained using (2.49) as the starting point and utilising the relations [49, eqs. (7.187) and (7.196)]

$$\boldsymbol{\kappa} = 2\rho v_p v_g \begin{pmatrix} \mathbf{H}^U(\beta \pm \pi) \\ \mathbf{H}^p(\beta \pm \pi) \end{pmatrix} A \tag{2.57}$$

$$\boldsymbol{\Delta} = \frac{\omega \rho v_p v_g}{2\pi g} \int_0^{2\pi} \begin{pmatrix} \mathbf{H}^U(\theta) \\ \mathbf{H}^p(\theta) \end{pmatrix} \begin{pmatrix} \mathbf{H}^U(\theta) \\ \mathbf{H}^p(\theta) \end{pmatrix}^{\dagger} \mathrm{d}\theta, \tag{2.58}$$

which are the generalisations of relations (2.45) and (2.46) for a system of oscillating rigid bodies and water columns. Here, $\mathbf{H}^U(\theta)$ is the vector of $H_j^U(\theta)$ and $\mathbf{H}^p(\theta)$ is the vector of $H_k^p(\theta)$.

2.2 Constant load impedance

To achieve the theoretical maximum power that can be absorbed from the waves at all frequencies requires that the optimum motions of the absorbers be sustained at all frequencies (cf. (2.7) and (2.18)). This is a difficult task. It is easier to set the load, or the PTO, impedance to a constant value, selected such that the absorbed power approaches the theoretical maximum over the range of predominant wave frequencies. In the following we consider the power than can be absorbed by a single oscillator when its load impedance is set to constant.

Assuming that the load impedance is composed of damping, inertia, and spring terms, we may write the equation of motion for the oscillator as (c.f. (2.9))

$$\left[R(\omega) + R_u + \mathrm{i}\omega \left(M + M_u + m(\omega) - (S_b + S_u)\omega^{-2} \right) \right] U(\omega) = F_e(\omega), \tag{2.59}$$

where we have distinguished frequency-dependent parameters (written as functions of ω) from constant parameters. The mean absorbed power is given as (c.f. (2.10))

$$P(\omega) = \frac{\frac{1}{2} R_u |F_e(\omega)|^2}{\left(R(\omega) + R_u\right)^2 + \omega^2 \left(M + M_u + m(\omega) - (S_b + S_u)\omega^{-2}\right)^2}. \tag{2.60}$$

The frequency-dependent parameters $m(\omega)$, $R(\omega)$, and $F_e(\omega)$ are governed by the body geometry.

If we aim to cancel the total reactance of the system at a particular frequency ω_p (a reasonable choice would be the peak frequency of the incident wave spectrum) by adjusting the (non-negative) load inertia M_u and (non-negative) restoring coefficient S_u such that

$$M + M_u - (S_b + S_u)\omega_p^{-2} = -m(\omega_p), \tag{2.61}$$

then we have

$$P(\omega) = \frac{\frac{1}{2} R_u |F_e(\omega)|^2}{(R(\omega) + R_u)^2 + |\Im\{Z_t\}|^2}, \tag{2.62}$$

where

$$\Im\{Z_t\} = \omega \left[m(\omega) - m(\omega_p) - (S_b + S_u)\omega^{-2} + (S_b + S_u)\omega_p^{-2} \right], \qquad (2.63)$$

or

$$\Im\{Z_t\} = \omega \left[M + M_u + m(\omega) - \omega_p^2 \omega^{-2} \left(M + M_u + m(\omega_p) \right) \right]. \qquad (2.64)$$

If we also make the substitution $R_u = R(\omega_p)$ in (2.62), it is easy to see that at $\omega = \omega_p$, the absorbed power $P(\omega_p)$ will be maximized and equal to $P_{\max}(\omega_p) = |F_e(\omega_p)|^2/8R(\omega_p)$. At $\omega \neq \omega_p$, the absorbed power $P(\omega)$ will be less than $P_{\max}(\omega)$ and its bandwidth will depend on the selections of M_u and S_u.

If we choose $R_u > R(\omega_p)$, then $P(\omega_p)$ will be less than $P_{\max}(\omega_p)$, but the resonance bandwidth will be larger [see 49, p. 53]. The optimum value of R_u may depend on the bandwidth of the incident wave spectrum.

As an illustration, Fig. 2.1 shows our computed results of typical variations of mean power absorbed by a heaving truncated vertical circular cylinder. If the load
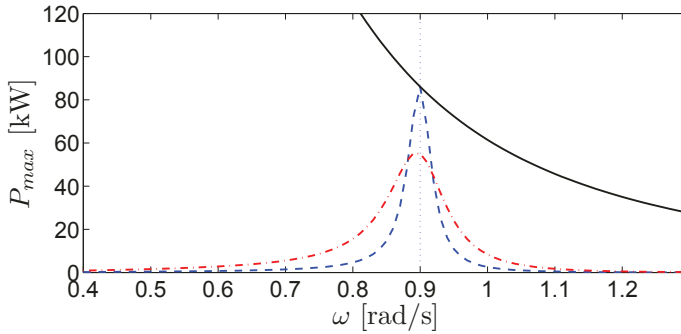

Figure 2.1: Mean absorbed power of a heaving truncated vertical circular cylinder with radius $a = 3.5$ m and draft $d = 7.91$ m in 30-m water depth, for 0.5-m incident wave amplitude. The natural frequency is 0.99 rad/s. Solid line: maximum power than can be absorbed by the cylinder, as given by (2.6); dashed line: absorbed power with $S_u = 0$, M_u selected such that (2.61) is satified at $\omega_p = 0.9$ rad/s, and $R_u = R(\omega_p)$; dash-dotted line: absorbed power with S_u and M_u as in the former, but with $R_u = 4R(\omega_p)$.

impedance is constant and tuned such that (2.61) is satisfied, then $P(\omega_p) = P_{\max}(\omega_p)$. Away from ω_p, the absorbed power $P(\omega)$ is less than $P_{\max}(\omega)$. By choosing a larger R_u, a larger bandwidth is obtained. In this example, the natural frequency of the cylinder is higher than the tuned frequency ω_p. Extra inertia M_u would then need to be added. A way to do this without changing the displacement of the cylinder is given, e.g., in [21].

As another example, we consider a submerged buoyant horizontal circular cylinder oscillating about an axis fixed at the sea bottom. Fig. 2.2 shows the variations of mean power absorbed by the cylinder. The maximum absorbed power is approximately twice that of the heaving vertical cylinder, in accordance with (2.48). Again, choosing a
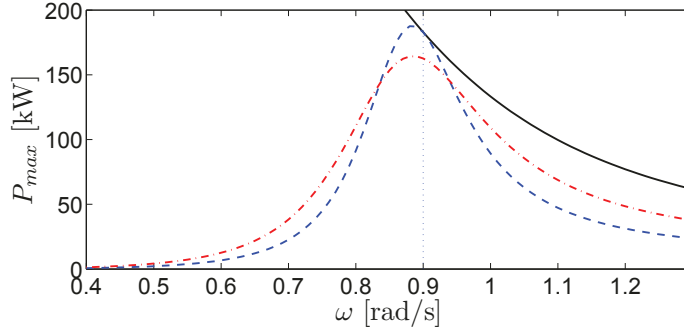
Figure 2.2: Mean absorbed power of a bottom-hinged submerged buoyant horizontal circular cylinder with radius $a = 3.5$ m and width $d = 15.83$ m in 20-m water depth, for 0.5-m incident wave amplitude. The distance from the seabed to the center of the cylinder is 15 m. The relative density of the cylinder is 0.3. The natural frequency is 0.6 rad/s. Solid line: maximum power than can be absorbed by the cylinder, as given by (2.6); dashed line: absorbed power with $M_u = 0$, S_u selected such that (2.61) is satified at $\omega_p = 0.9$ rad/s, and $R_u = R(\omega_p)$; dash-dotted line: absorbed power with S_u and M_u as in the former, but with $R_u = 2R(\omega_p)$.

larger R_u yields a larger bandwidth. In this example, the natural frequency of the cylinder is lower than the tuned frequency ω_p. Hence, an extra rotational spring S_u is needed.

In papers D and E, ballasting is considered as a means to tune M_u and S_u.

The proof for identity (2.23) follows via a well-known reciprocity relation which relates the radiation damping to the excitation force [100]:

$$\mathbf{R} = \frac{1}{8\lambda J} \int_0^{2\pi} \mathbf{F}_e(\beta)\mathbf{F}_e^\dagger(\beta)\mathrm{d}\beta. \tag{2.65}$$

We first write $\mathbf{R} = \mathbb{L}\mathbb{U}$, where $\mathbb{L}$ and $\mathbb{U}$ are lower and upper triangular matrices in an LU-factorisation. Therefore, from (2.17),

$$\int_0^{2\pi} P_{\max}(\beta)\mathrm{d}\beta = \int_0^{2\pi} \frac{1}{8}\mathbf{F}_e^\dagger(\beta)\mathbb{U}^{-1}\mathbb{L}^{-1}\mathbf{F}_e(\beta)\mathrm{d}\beta. \tag{2.66}$$

From (2.65),

$$\mathbb{L}^{-1}\mathbf{R}\mathbb{U}^{-1} = \frac{1}{8\lambda J} \int_0^{2\pi} \mathbb{L}^{-1}\mathbf{F}_e(\beta)\mathbf{F}_e^\dagger(\beta)\mathbb{U}^{-1}\mathrm{d}\beta = \mathbf{I}, \tag{2.67}$$

where $\mathbf{I}$ is the identity matrix. Defining $\mathbf{A}(\beta) = \mathbb{L}^{-1}\mathbf{F}_e(\beta)$ and $\mathbf{B}(\beta) = \mathbf{F}_e^\dagger(\beta)\mathbb{U}^{-1}$, then

$$\frac{1}{8\lambda J} \int_0^{2\pi} A_i(\beta)B_j(\beta)\mathrm{d}\beta = \begin{cases} 1, & i = j \\ 0, & i \neq j \end{cases}. \tag{2.68}$$

Returning to (2.66) and making use of (2.68), it follows that

$$\int_0^{2\pi} P_{\max}(\beta)\mathrm{d}\beta = \frac{1}{8} \int_0^{2\pi} \sum_{i=1}^{N} A_i(\beta)B_i(\beta)\mathrm{d}\beta = N\lambda J. \tag{2.69}$$

We shall show that (2.44) also applies for a system of oscillating rigid bodies and oscillating water columns, but with $H_r(\theta) = \sum_{j=1}^{N} H_j^U(\theta)U_j + \sum_{k=1}^{M} H_k^p(\theta)p_k$ and $\bar{H}_r(\theta) = \sum_{j=1}^{N} H_j^U(\theta)U_j^* - \sum_{k=1}^{M} H_k^p(\theta)p_k^*$, where M is the number of oscillating water columns and $H_j^U(\theta)$ and $H_k^p(\theta)$ are the Kochin functions associated with the unit velocity of oscillator j and the unit pressure of chamber k, respectively.

The derivation is the same as in the case of a system of oscillating rigid bodies without oscillating water columns, the only difference being the evaluation of the integral $\mathcal{I}(\phi_0 + \phi_s, \phi_r^*)$ in (2.32). Note that in the definition (2.28), the surface S now includes the internal water surfaces in the chambers. We may write

$$\phi_r = \sum_{j=1}^{N} \varphi_j^U U_j + \sum_{k=1}^{M} \varphi_k^p p_k, \tag{2.70}$$

where φ_k^p is the radiation potential due to a unit applied pressure at chamber k. Then

$$\mathcal{I}(\phi_0 + \phi_s, \phi_r^*) = \sum_{j=1}^{N} \mathcal{I}(\phi_0 + \phi_s, \varphi_j^{U*})U_j^* + \sum_{k=1}^{M} \mathcal{I}(\phi_0 + \phi_s, \varphi_k^{p*})p_k^*. \tag{2.71}$$

On the wetted body surfaces, it is required that

$$\frac{\partial \varphi_j^U}{\partial n} = \begin{cases} n_j, & \text{on } S_j \\ 0, & \text{elsewhere} \end{cases} \tag{2.72}$$

$$\frac{\partial \varphi_k^p}{\partial n} = 0 \tag{2.73}$$

$$\frac{\partial}{\partial n}(\phi_0 + \phi_s) = 0, \tag{2.74}$$

while on the internal water surfaces,

$$\left(\frac{\partial}{\partial z} - \frac{\omega^2}{g}\right)\varphi_k^p = \begin{cases} -\mathrm{i}\omega/\rho g, & \text{on } S_k \\ 0, & \text{elsewhere} \end{cases} \tag{2.75}$$

$$\left(\frac{\partial}{\partial z} - \frac{\omega^2}{g}\right)\varphi_j^U = 0 \tag{2.76}$$

$$\left(\frac{\partial}{\partial z} - \frac{\omega^2}{g}\right)(\phi_0 + \phi_s) = 0. \tag{2.77}$$

The part of the integral $\mathcal{I}(\phi_0 + \phi_s, \varphi_j^{U*})$ over the internal water surfaces vanishes due to (2.76) and (2.77), Furthermore, using (2.72) and (2.74),

$$\mathcal{I}(\phi_0 + \phi_s, \varphi_j^{U*}) = \iint_{S_j} (\phi_0 + \phi_s)\frac{\partial \varphi_j^{U*}}{\partial n}\,\mathrm{d}S. \tag{2.78}$$

Since n_j is real, then according to (2.72), $\partial\varphi_j^{U*}/\partial n = \partial\varphi_j^U/\partial n$ on S_j. Hence,

$$\mathcal{I}(\phi_0 + \phi_s, \varphi_j^{U*}) = \mathcal{I}(\phi_0 + \phi_s, \varphi_j^U). \tag{2.79}$$

The part of the integral $\mathcal{I}(\phi_0 + \phi_s, \varphi_k^{p*})$ over the wetted body surfaces vanishes due to (2.73) and (2.74). It remains to evaluate the part of the integral over the internal water surfaces. Using (2.75) and (2.77), the surface of integration further reduces to S_k. Thus,

$$\mathcal{I}(\phi_0 + \phi_s, \varphi_k^{p*}) = \iint_{S_k} \left[(\phi_0 + \phi_s)\frac{\partial\varphi_k^{p*}}{\partial n} - \frac{\partial}{\partial n}(\phi_0 + \phi_s)\varphi_k^{p*} \right] \mathrm{d}S. \tag{2.80}$$

Adding the term $\frac{g}{\omega^2}\frac{\partial}{\partial n}(\phi_0 + \phi_s)\frac{\partial\varphi_k^{p*}}{\partial n} - \frac{g}{\omega^2}\frac{\partial}{\partial n}(\phi_0 + \phi_s)\frac{\partial\varphi_k^{p*}}{\partial n} = 0$ to the integrand, we obtain

$$\begin{aligned} \mathcal{I}(\phi_0 + \phi_s, \varphi_k^{p*}) = \iint_{S_k} \Bigg[&\frac{\partial\varphi_k^{p*}}{\partial n}\left(1 + \frac{g}{\omega^2}\frac{\partial}{\partial n}\right)(\phi_0 + \phi_s) \\ &- \frac{\partial}{\partial n}(\phi_0 + \phi_s)\left(1 + \frac{g}{\omega^2}\frac{\partial}{\partial n}\right)\varphi_k^{p*} \Bigg]\mathrm{d}S. \end{aligned} \tag{2.81}$$

The first term in the integrand vanishes due to (2.77), while $\left(1 + \frac{g}{\omega^2}\frac{\partial}{\partial n}\right)\varphi_k^{p*} = -\left(1 + \frac{g}{\omega^2}\frac{\partial}{\partial n}\right)\varphi_k^{p}$ according to (2.75). It follows that

$$\mathcal{I}(\phi_0 + \phi_s, \varphi_k^{p*}) = -\mathcal{I}(\phi_0 + \phi_s, \varphi_k^{p}). \tag{2.82}$$

Therefore, equation (2.71) can be written as

$$\mathcal{I}(\phi_0 + \phi_s, \phi_r^*) = \sum_{j=1}^{N}\mathcal{I}(\phi_0 + \phi_s, \varphi_j^U)U_j^* - \sum_{k=1}^{M}\mathcal{I}(\phi_0 + \phi_s, \varphi_k^{p})p_k^*, \tag{2.83}$$

which, as in (2.38), reduces to $2v_p v_g A\bar{H}_r(\beta\pm\pi)/\mathrm{i}\omega$, with $\bar{H}_r(\theta) = \sum_{j=1}^{N}H_j^U(\theta)U_j^* - \sum_{k=1}^{M}H_k^p(\theta)p_k^*$. Following the rest of the derivation as in the case of a system of oscillating rigid bodies, we may arrive at the result (2.44).

3 Modelling

> The conflict between the theoretical desires and the practical limitations has created most of the problems in wave energy research and the importance of modelling realistic systems cannot be over emphasized.
>
> B. M. Count

With the notable exception of the Bristol cylinder [44], whose geometry permits ideal-fluid analytical results to be produced before any tank tests, many of the early devices were tested in the laboratory before mathematical models were developed for them. Today, the advance of numerical capabilities has allowed theoretical predictions to be made with increasing speed and confidence, saving the cost of preliminary model tests[1].

Essential for more realistic representations of WECs are time-domain models. They are necessary for taking into account nonlinearities which exist to a significant degree in WECs, arising mainly from the power take-off system and the control mechanism.

The purpose of this chapter is to summarize and introduce the work presented in papers A, B, C, and G. To develop a complete system model of a WEC is a tremendous task. Here, the bond graph method, which has found wide applications elsewhere but not as much used yet in wave energy, is introduced. It is shown to be a helpful tool for modelling WECs, complementing earlier works by Hals [66] and Yang [135], among a few others. Alternatives to model the wave radiation terms are also discussed, which are treated in more detail in paper C. But first, we present the equations of motion of some generic WECs.

3.1 EQUATIONS OF MOTION

A WEC is essentially a mechanical oscillator with frequency-dependent inertia and damping. The frequency dependency is due to the fact that the wave radiation force, which is classically decomposed into an added inertia term and a radiation damping term, depends on the oscillation frequency.

A common way to formulate the time-domain model of a body oscillating in water (a ship, a floating offshore structure, or a WEC) is by an integro-differential equation of motion which contains a convolution integral representing the wave radiation

---

[1]Model testing is still an indispensable part of the development process. It is especially useful to determine how far ideal-fluid and/or linear theory is applicable.

force [27, 106]. The convolution integral accounts for the system memory, signifying the fact that waves radiated by the body in the past continue to affect the body for all subsequent times [16, 64]. Mathematically, the convolution integral arises from applying an inverse Fourier transform to a product of two frequency-dependent functions. The kernel of the integral is an impulse response function (IRF)—also known as the retardation function when the IRF is causal and nonzero for $t > 0$—which is related to the frequency-dependent hydrodynamic radiation coefficients by Fourier transforms.

In terms of device hydrodynamics, two large categories of WECs may be identified, namely, the oscillating bodies and the oscillating water columns. Oscillating-body WECs utilise relative motion between a moving body and a fixed reference, such as the sea bed, or between several moving bodies, to absorb energy. Oscillating-water-column WECs utilise the motion of a partially enclosed mass of water relative to a fixed reference, or relative to a moving body, to absorb energy. Basic models of each category are presented in the following.

3.1.1 Oscillating bodies

The time-domain equation of motion for an oscillating-body WEC operating in a single mode can be written in general form as (c.f. (2.9) for the frequency-domain counterpart)

$$F_e(t) = [M + m(\infty)]\dot{u}(t) + k(t) * u(t) + S_b s(t) + F_{\text{ext}}(s(t), u(t), t). \quad (3.1)$$

Here, $F_e(t)$ is the wave excitation force, $F_{\text{ext}}(s(t), u(t), t)$ is a general nonlinear force which includes the PTO force, $s(t)$ is the body displacement, $u(t)$ is the body velocity, M is the structural inertia, $m(\infty)$ is the infinite-frequency added inertia, $k(t)$ is the radiation impedance IRF, and S_b is the hydrostatic stiffness.

The wave radiation force is seen as a sum of two terms $m(\infty)\dot{u}(t)$ and $k(t) * u(t)$. The latter is the convolution term which arises from the fact that the added inertia and radiation damping are frequency-dependent. The radiation impedance IRF, because it is causal, can be obtained from the frequency-domain radiation damping or added inertia terms as follows [27]:

$$k(t) = \frac{2}{\pi} \int_0^\infty R(\omega) \cos(\omega t) d\omega, \quad (3.2)$$

where $R(\omega)$ is the radiation damping, or, alternatively,

$$k(t) = -\frac{2}{\pi} \int_0^\infty \omega[m(\omega) - m(\infty)] \sin(\omega t) d\omega, \quad (3.3)$$

where $m(\omega)$ is the added inertia. In practice, the integrals are truncated at a sufficiently high frequency. Practical extrapolation methods to obtain added inertia and radiation damping values at high frequencies are detailed in paper C.

In paper C, we assume that the force $F_{\text{ext}}(s(t), u(t), t)$ is composed of nonlinear Coulomb and quadratic damping forces, an external restoring force, and the PTO

force. For simplicity, the PTO force is assumed to be applied by a linear damper with damping coefficient (or load resistance) R_u. In this case, the equation of motion becomes

$$
\begin{aligned}
F_e(t) = {}& [M + m(\infty)]\dot{u}(t) + k(t) * u(t) + (S_b + S)s(t) \\
& + R_C \operatorname{sgn} u(t) + R_q u(t)|u(t)| + R_u u(t),
\end{aligned}
\tag{3.4}
$$

where S is the external stiffness, R_C is the Coulomb damping coefficient, and R_q is the quadratic damping coefficient.

The instantaneous absorbed power can be evaluated from the product of the PTO force and the body velocity:

$$
P(t) = F_u(t)u(t).
\tag{3.5}
$$

If the PTO force is assumed to be applied by a linear damper with load resistance R_u, then

$$
P(t) = R_u u^2(t).
\tag{3.6}
$$

3.1.2 Oscillating water columns

FIXED OWC We first consider a fixed OWC. For a fixed OWC, the chamber body is fixed. The equation of motion can be written in general form as

$$
Q_e(t) = y(t) * p(t) + Q_{\text{ext}}(p(t), t).
\tag{3.7}
$$

Here, $Q_e(t)$ is the excitation volume flow, $Q_{\text{ext}}(p(t), t)$ is a general nonlinear volume flow which includes the volume flow through the PTO, i.e. an air turbine, $p(t)$ is the chamber pressure, and $y(t)$ is the radiation admittance IRF.

The radiation admittance IRF can be obtained from the frequency-domain counterpart as

$$
y(t) = \frac{2}{\pi} \int_0^\infty G(\omega) \cos(\omega t) \mathrm{d}\omega,
\tag{3.8}
$$

where $G(\omega) = \Re\{Y(\omega)\}$, or, alternatively,

$$
y(t) = -\frac{2}{\pi} \int_0^\infty B(\omega) \sin(\omega t) \mathrm{d}\omega,
\tag{3.9}
$$

where $B(\omega) = \Im\{Y(\omega)\}$. The radiation admittance $Y(\omega)$ is defined as

$$
Y(\omega) = -\iint_S \frac{\partial \varphi_p}{\partial z} \mathrm{d}S,
\tag{3.10}
$$

where φ_p is the radiation potential due to a unit pressure in the chamber. Further details on how to evaluate $Y(\omega)$ are given in papers B and C.

Unlike $k(t) * u(t)$, there is no analog to $m(\infty)$ that is related to $y(t) * p(t)$. While this has been confirmed by numerical computations (see paper B), a physical explanation is now given as follows. We consider first a rigid body harmonically oscillating

with finite velocity. As the oscillation frequency is increased to infinity, the acceleration also increases to infinity. The force required to move the body will necessarily also be infinite. There is therefore sufficient force to accelerate the fluid, which needs to move with the same velocity as the body on the wetted body surface. The added mass m is related to the difference between kinetic and potential energy of the fluid [95]. Since the potential energy is zero in this limiting case of infinite frequency (there is no radiated waves at infinite frequency), while the kinetic energy is nonzero, $m(\infty)$ is therefore nonzero. On the other hand, consider an oscillating finite pressure distribution on the free surface. As the oscillation frequency is increased to infinity, the force on the free surface remains finite since the pressure is finite. There is therefore insufficient force to accelerate the fluid, and hence the kinetic energy of the fluid is zero. Since the potential energy is also zero at infinite frequency, there is no analog to $m(\infty)$ that is related to $y(t) * p(t)$.

In paper C, we assume that the OWC is equipped with a relief valve, the air in the chamber is compressible, and there is some loss of volume flow. The volume flow $Q_{\text{ext}}(p(t), t)$ is thus composed of nonlinear volume flow through the relief valve, nonlinear volume flow due to air compressibility, the volume flow through the air turbine, and a volume flow loss term. The pressure-volume flow relationship of the turbine is assumed to be linear. In this case, the equation of motion becomes

$$Q_e(t) = y(t) * p(t) + Q_v(t) + Q_c(t) + (1/R_e + 1/R_u)\, p(t), \tag{3.11}$$

where $Q_v(t)$ is the volume flow through the relief valve, $Q_c(t)$ is the volume flow due to air compressibility, R_e is the damping coefficient related to the loss, and R_u is the pneumatic load resistance. Expressions for $Q_v(t)$ and $Q_c(t)$ are given in paper B, C, and G.

The instantaneous absorbed power is evaluated from the product of the chamber pressure and the volume flow through the turbine:

$$P(t) = p(t)Q_u(t). \tag{3.12}$$

If the volume flow through the turbine is assumed to be given by $Q_u(t) = p(t)/R_u$, then

$$P(t) = \frac{p^2(t)}{R_u}. \tag{3.13}$$

FLOATING OWC For a floating OWC, the chamber body is free to move. For a floating OWC constrained to move only in one degree of freedom, we then have two coupled equations of motion, which can be written as

$$
\begin{aligned}
F_e(t) &= [M + m(\infty)]\dot{u}(t) + k(t) * u(t) - C(\infty)p(t) \\
&\quad - h(t) * p(t) + S_b s(t) + F_{\text{ext}}(s(t), u(t), t) - A_i p(t)
\end{aligned}
\tag{3.14}
$$

$$
\begin{aligned}
Q_e(t) &= y(t) * p(t) + C(\infty)u(t) + h(t) * u(t) \\
&\quad + A_i u(t) + Q_{\text{ext}}(p(t), t).
\end{aligned}
\tag{3.15}
$$

Here, $C(\infty)$ is the real part of the radiation coupling coefficient $H(\omega)$ at infinite frequency [see 59], A_i is the internal water surface area, and $h(t)$ is the radiation coupling IRF.

The radiation coupling IRF can be obtained from the frequency-domain counterpart as

$$h(t) = -\frac{2}{\pi} \int_0^\infty J(\omega) \sin(\omega t) \mathrm{d}\omega, \tag{3.16}$$

where $J(\omega) = \Im\{H(\omega)\}$, or, alternatively,

$$h(t) = \frac{2}{\pi} \int_0^\infty (C(\omega) - C(\infty)) \cos(\omega t) \mathrm{d}\omega, \tag{3.17}$$

where $C(\omega) = \Re\{H(\omega)\}$. The radiation coupling coefficient $H(\omega)$ is defined as

$$H(\omega) = -\iint_S \frac{\partial \varphi_r}{\partial z} \mathrm{d}S, \tag{3.18}$$

where φ_r is the radiation potential due to a unit velocity of the body. Further details on how to evaluate $H(\omega)$ are given in paper B.

A physical explanation for the fact that $C(\infty)$ is nonzero is given as follows. As we have described in §2.1.3, the radiation coupling coefficient relates the body velocity to the resulting volume flow across the internal free surface, when the chamber is open to the atmosphere. Since the fluid is assumed to be incompressible, we cannot avoid creating a volume flow by moving the body, even at infinite frequency.

If $F_{\text{ext}}(s(t), u(t), t)$ is composed of the same terms as in the above oscillating body excluding the PTO force, and $Q_{\text{ext}}(p(t), t)$ is composed of the same terms as in the above fixed OWC, then the equations of motion become

$$\begin{aligned}
F_e(t) = {} & [M + m(\infty)]\dot{u}(t) + k(t) * u(t) - C(\infty)p(t) - h(t) * p(t) \\
& + (S_b + S)s(t) + R_C \operatorname{sgn} u(t) + R_q u(t)|u(t)| - A_i p(t)
\end{aligned} \tag{3.19}$$

$$\begin{aligned}
Q_e(t) = {} & y(t) * p(t) + C(\infty)u(t) + h(t) * u(t) + Q_v(t) + Q_c(t) \\
& + A_i u(t) + (1/R_e + 1/R_u)\, p(t).
\end{aligned} \tag{3.20}$$

The instantaneous absorbed power is given as in (3.12) and (3.13).

3.2 BOND GRAPH

As mentioned in Chapter 1, one great challenge for a WEC is to convert slow oscillating motion into one that is more suited for electrical generation. To do this, it is natural for a WEC to have several conversion stages involving various energy domains, as illustrated in Fig. 3.1 [cf. 32, 52].

As seen from the figure, several alternatives are available to convert energy from mechanical translational/rotational, hydraulic, or pneumatic domain to electrical domain. For a fixed OWC, energy is converted from pneumatic to electrical domains via an air turbine coupled to a rotational generator [cf. 73, Fig. 2]. For a floating OWC,
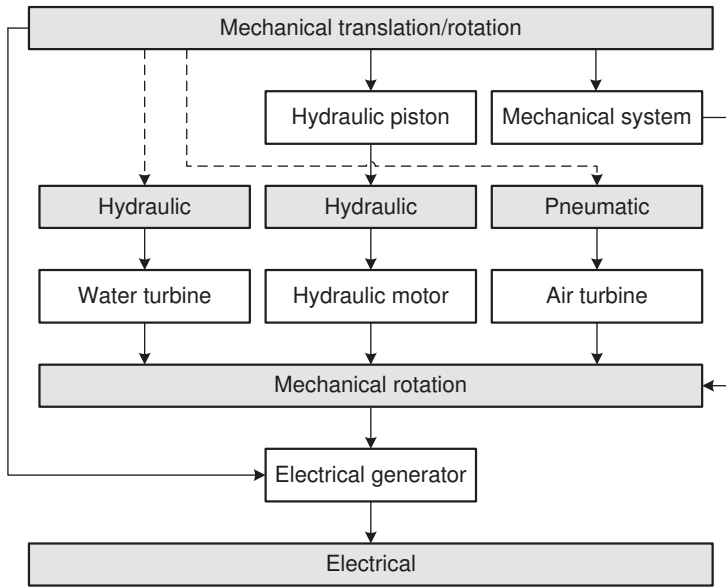
Figure 3.1: Typical alternative conversion stages in WECs (adapted from [82]). Shaded rectangles represent energy domains, while non-shaded rectangles represent primary components/subsystems.

the motions of the body contribute to the absorbed energy, hence the broken lines connecting mechanical translational/rotational domain to pneumatic domain. For a fixed overtopping WEC, energy is converted from hydraulic to electrical domains via a water turbine coupled to a rotational generator. For a floating overtopping WEC, the motions of the body contribute to the absorbed energy, hence the broken lines connecting mechanical translational/rotational domain to hydraulic domain. For an oscillating-body WEC, direct conversion from mechanical translational domain to electrical domain can be achieved by means of a linear generator. It is also possible to convert energy from mechanical translational/rotational domain to mechanical rotational domain via a mechanical system comprising of cables, rods, and/or wheels before converting it to electrical domain via a rotational generator. Another alternative is to convert energy from mechanical translational/rotational domain to hydraulic domain via a hydraulic piston before converting it to mechanical rotational domain via a hydraulic motor and then to electrical domain via a rotational generator. Due to the energy-production problem of wave grouping, it may be important to incorporate, early in the conversion chain, a short-time energy storage with a capacity of about 100 s times the rated power of the WEC, in each of these alternatives [121]. To build a realistic model of a WEC, it is necessary to include all components in the conversion chain in detail.

A modelling method that is particularly suited for modelling multidisciplinary engineering systems is the bond graph method, invented by Henry Paynter from Massachusetts Institute of Technology (MIT) in 1959 [108]. Apart from being a

graphical, port-based modelling approach, one virtue of bond graph lies in the fact that it is domain-independent; it uses common notations for elements and variables across various energy domains. Hence, it is capable of representing a complex system involving diverse energy domains in a unified manner. Also, due to the common notations, analogies between systems across energy domains are readily inferred, even if the components involved are physically different. This helps in providing insight into the behaviour of the system. Another important virtue of bond graph is that derivation of model equations can be done in a systematic manner, allowing for automated computer simulation.

Bond graph has been used in many applications, including vehicle dynamics, fluid networks, heat exchangers, diesel engines, electromagnetic actuators, and cardiovascular systems [18]. However, its application for modelling WECs is relatively new. An allusion to the bond graph method was made in 1984 by Jefferys [73], who presented a word bond graph of a fixed OWC device, although he did not explicitly mention the term 'bond graph.' Otherwise, it was only more recently that a number of works using bond graph started to appear in wave energy literature.

The first of these was an application of bond graph in the modelling of a PTO system for a hinged-barge WEC used to generate electricity and produce potable water [105]. The bond graph method was further introduced to the wave energy community by Engja and Hals [35], who described the modelling of a WEC consisting of a heaving buoy connected to a semi-submersible. Others have then followed by considering diverse applications and objectives [15, 136]. An overview of bond graph modelling of WECs was given by Hals [66], who also presented bond graph models for the mooring lines, power conditioning, and grid connection. The suitability of bond graph to model WECs is further demonstrated through the work presented in papers A, B, and G.

In bond graph terms, a WEC essentially performs a power transformation from one energy domain to another, usually from mechanical translational/rotational domain to electrical domain. In bond graph notation this is simply $\mathbf{Sf} \longmapsto \mathbf{TF} \longmapsto \mathbf{R}$ where Sf is the source of mechanical translation/rotation, R is the load of the system, and TF is the power transformation from mechanical to electrical domains. The power bonds (represented by half arrows) indicate the energy flow and signify flows in opposite directions of the power co-variables, namely, *effort* and *flow*. The causal stroke (a vertical line at one end of the bond and perpendicular to it) indicates the direction of the effort signal. As an example, in the above, flow is the input to the R element while effort is the output. In reality, the TF is made up of a number of subsystems depending on the PTO mechanism and the conversion stages employed, and these should be modelled in detail.

In total, nine basic elements are generally sufficient to model any physical system. Each of these represents an elementary behaviour, namely, storage (C and I elements), reversible transformation (TF and GY elements), irreversible transformation (R element), supply and demand (Se and Sf elements), and distribution (0- and 1-junctions).

Bond graph representations of the equations of motions presented earlier for an

oscillating-body WEC, a fixed OWC, and a floating OWC are shown respectively in Figs. 3.2, 3.3, and 3.4. For the oscillating body, the force balance on the body
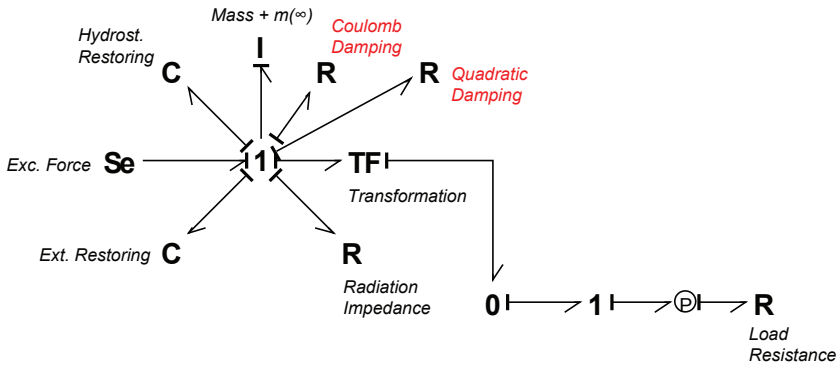

Figure 3.2: Bond graph model of an oscillating-body WEC constrained to move only in one degree of freedom (reproduced from [83]). The force balance on the body (3.4) is represented by the power bonds connected to the 1-junction on the left. In addition, a TF element is included to represent a general transformation, e.g. from rotational to linear motion. Nonlinear terms are labeled in red.
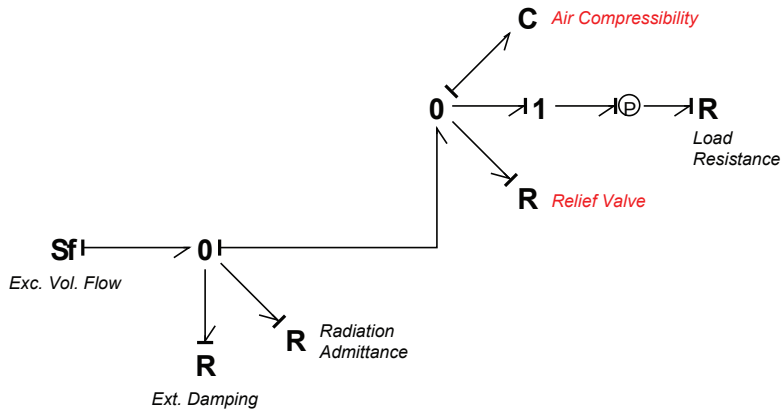
Figure 3.3: Bond graph model of a fixed OWC (reproduced from [83]). The volume flow balance in the chamber (3.11) is represented by the power bonds connected to the 0-junction. Nonlinear terms are labeled in red.

is represented by the power bonds connected to the 1-junction on the left, while for the fixed OWC, the volume flow balance in the chamber is represented by the power bonds connected to the 0-junction. It is clearly seen in the bond graph representation that a floating OWC is a combination of a fixed OWC and an oscillating body, connected at the 0-junction, signifying that it is the relative motion between the two that is utilised for power. The coupling term is represented by a TF element which connects the 1-junction representing the body velocity and the 0-junction representing the pressure in the chamber. A bond graph model of a self-reacting WEC composed

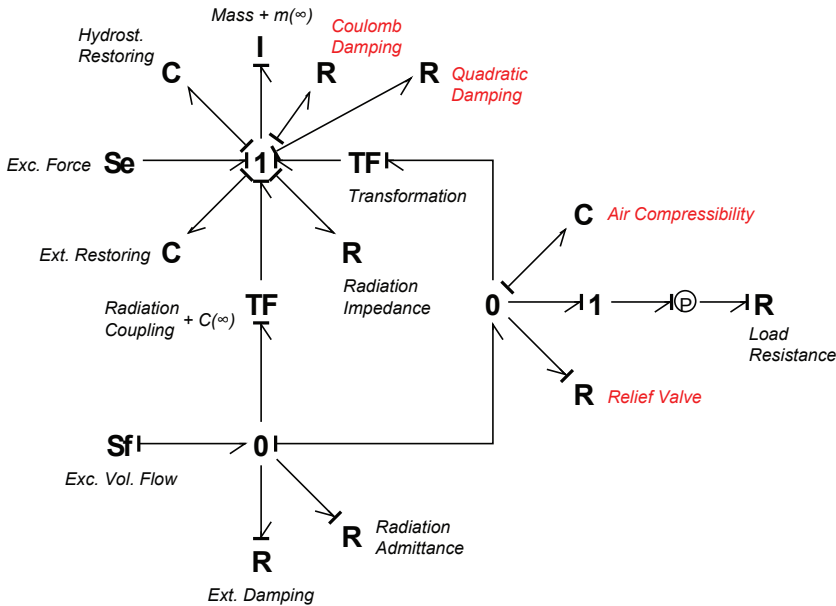Figure 3.4: Bond graph model of a floating OWC constrained to move only in one degree of freedom (reproduced from [83]). The force balance on the body (3.19) is represented by the power bonds connected to the 1-junction on the left. The volume flow balance in the chamber (3.20) is represented by the power bonds connected to the 0-junction. The radiation coupling term is represented by the TF element on the left. Nonlinear terms are labeled in red.

of two bodies moving relative to each other is also presented in paper G. In this case the self-reacting WEC is a combination of two oscillating bodies connected at the 0-junction.

More realistic WEC models are presented in papers A and B. In paper A, bond graph is used to model a WEC with hydraulic PTO. Two alternative hydraulic systems are considered. Each system consists of a hydraulic piston, a number of check valves, two accumulators, and a hydraulic motor. One system uses a single-acting piston and two check valves, and the other uses a double-acting piston and four check valves (see Fig. 3.5). The modularity of bond graph is demonstrated by first modelling the components/subsystems separately before assembling them together to form a complete system model. The hydraulic system models can be connected to bond graph models of various primary interface designs (single-body, multi-body, heaving, pitching, etc.) to form different models of WECs. In paper A, a hypothetical nearshore device is considered, the primary interface of which resembles the Salter Duck, and which can act at the same time as a breakwater. It is an oscillating body with one degree of freedom, i.e. pitch. The device, with the two alternative hydraulic PTO systems, is simulated in irregular incident waves. It is found that the 4-valve system is likely to be more expensive and have greater losses, but it has less pressure fluctuations compared to the 2-valve system.

In paper B, bond graph is used to model a backward bent duct buoy (BBDB), a
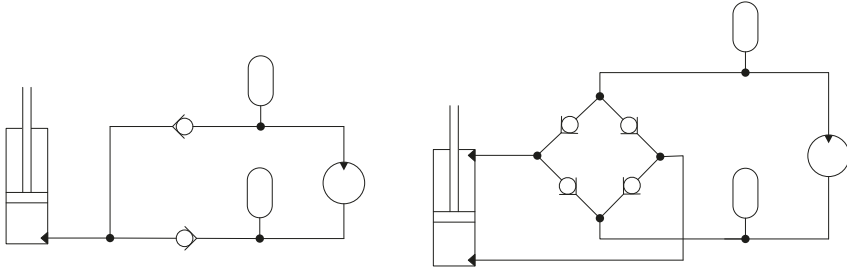
Figure 3.5: Hydraulic power take-off system with a single-acting piston and two check valves (left) and one with a double-acting system and four check valves (right) (reproduced from [82]).

particular type of floating OWCs proposed by Masuda et al. [91]. Its particular geometry was designed to broaden the power absorption bandwidth by coupling the heave and pitch motions of the floating body and the motion of the water column inside the body. It is therefore a multi-degree-of-freedom system, and its bond graph, as shown in Fig. 3.6, is more general than that of a floating OWC constrained to move in only one degree of freedom, as shown previously in Fig. 3.4. The main difference is in the use of multibonds to represent the force vectors on and the velocity vector of the floating body. Hydrodynamic parameters related to wave radiation due to applied pressure inside the chamber (the radiation admittance and radiation coupling terms) are evaluated by reciprocity relations [40, 57] from the parameters related to the conventional wave diffraction and radiation by a rigid body.

3.3 WAVE EXCITATION

The wave excitation is the input to the system. It is a force in the case of oscillating bodies and a volume flow in the case of OWCs.

The excitation force and/or the excitation volume flow time series are generated before the simulations and stored as data files to be read during the simulation. The generation of excitation force and/or excitation volume flow time series in monochromatic waves is straightforward. For polychromatic waves, the method is described as follows.

First, we obtain the spectral density of the excitation force (likewise for the excitation volume flow):

$$S_{F_e}(\omega) = |f_e(\omega)|^2 S(\omega), \tag{3.21}$$

where $f_e(\omega)$ is the complex excitation force per unit incident wave amplitude and $S(\omega)$ is the given wave spectrum. The excitation force is then given as

$$F_e(t) = \sum_{n=0}^{N/2} (a_n \cos \phi_n + b_n \sin \phi_n) \cos \omega_n t + \sum_{n=0}^{N/2} (-a_n \sin \phi_n + b_n \cos \phi_n) \sin \omega_n t, \tag{3.22}$$
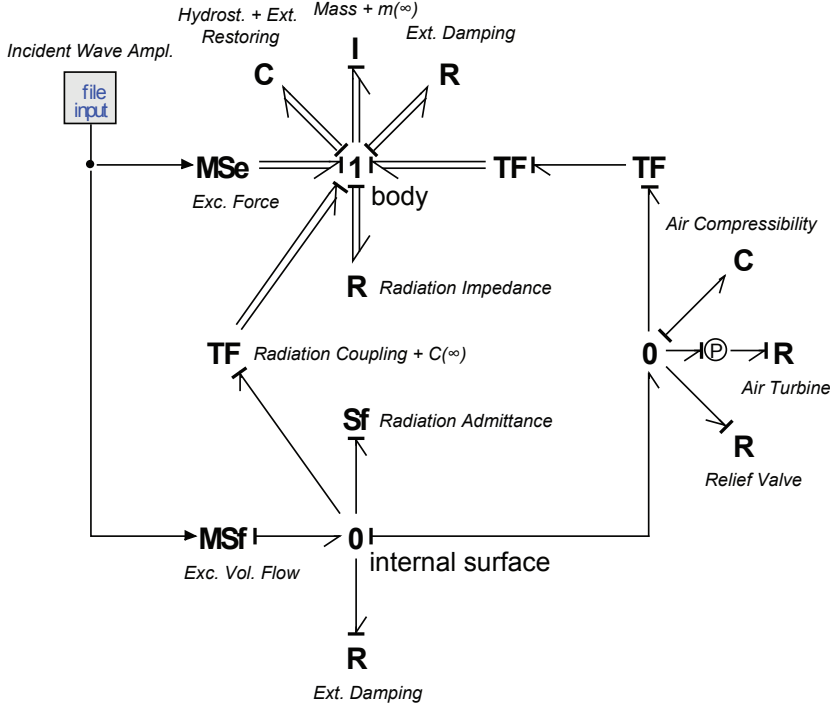
Figure 3.6: Bond graph model of a backward-bent duct buoy (reproduced from [83]). Multi-bonds are used for the 1-junction labeled 'body' since we are dealing with vectors and matrices instead of scalars.

where a_n and b_n are generated from a Gaussian distribution with variance $S_{F_e}(\omega_n)\Delta\omega$ [129]. Here, N is the number of values in the time series, determined by the required length of the series t_N and the time interval between values Δt. Also, $\omega_n = n\Delta\omega$, where $\Delta\omega = 2\pi/t_N$. In addition, ϕ_n is the phase (in radians) of $f_e(\omega_n)$.

Values of ω_n may be larger than the largest frequency for which f_e has been computed. The modulus and phase of f_e for these frequencies may therefore be extrapolated separately using fitting functions as in the extrapolation of the added inertia and radiation damping data. The necessity of having accurate f_e values for $\omega > 6$ rad/s, however, is of low importance because typical wave spectra have negligible values beyond 6 rad/s. Thus, it may be practical to assume zero values for f_e beyond 6 rad/s.

The sum in (3.22) may be alternatively evaluated by an inverse Fast Fourier Transform at a fraction of computer time. This is implemented in our simulations. The initial part of the resulting time series is filtered by a cosine taper window so as to avoid exciting any lightly damped modes in the system.

The JONSWAP model for the wave spectrum is used in our simulations. The model is given as [see, e.g. 98]

$$S(\omega) = \frac{\alpha g^2}{\omega^5} \exp\left(-1.25\frac{\omega_p^4}{\omega^4}\right) \gamma^{a(\omega)}, \tag{3.23}$$

where

$$a(\omega) = \exp\left(-\frac{(\omega - \omega_p)^2}{2\sigma^2\omega_p^2}\right) \tag{3.24}$$

$$\sigma = \begin{cases} 0.07 & \text{for } \omega \leq \omega_p \\ 0.09 & \text{for } \omega > \omega_p \end{cases} \tag{3.25}$$

$$\alpha = 5.058\frac{H_s^2}{T_p^4}(1 - 0.287\ln\gamma). \tag{3.26}$$

In the above, H_s is the significant wave height, $T_p = 2\pi/\omega_p$ is the peak period, and γ is the peakedness parameter.

3.4   RADIATION FORCE MODELS

The traditional representation of the hydrodynamic radiation force is in the form of a convolution [27]. In time-domain simulations, evaluation of the convolution integral is known to be time-consuming and difficult to carry out with standard adaptive time-stepping solvers. The reason is that one usually has to store discrete values of the IRF sampled at every simulation time step for the whole simulation time length or up to the point where the IRF value becomes negligible, and one has to re-evaluate the convolution integral at every time step. It is obvious that for a multi-degree-of-freedom system, which contains a number of these integrals, the computational effort can be tremendous.

To avoid this difficulty, a set of coupled linear ordinary differential equations has been proposed as an approximate replacement for the convolution integral, first probably by Jefferys [72] in wave energy context. This so-called state-space representation is more efficient due to its Markovian property: at any instant, the value of the state summarises all the past system information [111]. The need to store a large amount of data and re-evaluate the integral at every time step is therefore eliminated.

Different approaches have been proposed in the literature to identify this state-space radiation force model, and have been summarized recently in [111]. Each of these approaches belongs to either time-domain or frequency-domain identification. In time-domain identification the state-space model is obtained from the corresponding radiation IRF, whereas in frequency-domain identification the state-space model is obtained from the corresponding radiation data in frequency domain.

A comparative study of alternative models for the hydrodynamic radiation terms is presented in paper C. The compared models are the direct convolution integration, the state-space model, and the constant coefficient model. They are compared with regards to their efficiency and accuracy.

In the direct convolution integration the radiation convolution terms are not replaced by any approximations and are integrated directly at each time step. This requires, firstly, precomputation of the IRF values at specified time intervals, where linear interpolation is used if the simulation time step is shorter, and, secondly, storage of past response (velocity and/or pressure). With accurate IRFs and sufficiently

small simulation time step, a direct convolution integration model should give accurate simulation results despite the considerable computational burden involved.

In the constant coefficient model the frequency-dependent hydrodynamic coefficients are replaced by constant coefficients, whose values are taken to be those at the wave spectral peak frequency ω_p. The constant-coefficient model is the most efficient, but it is found to give reasonably accurate results only for certain cases where the radiation force is dominated by other terms in the equation of motion. Thus, it should be used with care.

In the state-space model, the radiation convolution term

$$\mu(t) = k(t) * u(t) = \int_0^t k(t - \tau)u(\tau)\mathrm{d}\tau \tag{3.27}$$

is approximated by $\hat{\mu}(t)$, which is obtained as [see, e.g. 112]

$$\dot{\mathbf{x}}(t) = \hat{\mathbf{A}}\mathbf{x}(t) + \hat{\mathbf{B}}u(t) \tag{3.28}$$

$$\hat{\mu}(t) = \hat{\mathbf{C}}\mathbf{x}(t), \tag{3.29}$$

where $\mathbf{x}(t)$ is the state vector, the number of components of which corresponds to the *order* of the state-space model, and $\hat{\mathbf{A}}$, $\hat{\mathbf{B}}$, $\hat{\mathbf{C}}$ are constant matrices to be determined. We use the frequency-domain identification approach following the algorithm detailed in [112, 113]. The method uses frequency-domain hydrodynamic data for identification. The approach is to fit a rational transfer function

$$\hat{K}(s) = \frac{P(s)}{Q(s)} = \frac{p_r s^r + p_{r-1}s^{r-1} + \ldots + p_0}{s^n + q_{n-1}s^{n-1} + \ldots + q_0}, \tag{3.30}$$

where $s = \mathrm{i}\omega$, to the frequency response functions (FRFs) $K(\omega)$, $Y(\omega)$, or $L(\omega)$, depending on the problem considered. The FRFs $K(\omega)$ and $L(\omega)$ are defined as follows [80]:

$$K(\omega) = R(\omega) + \mathrm{i}\omega(m(\omega) - m(\infty)) \tag{3.31}$$

$$L(\omega) = C(\omega) - C(\infty) + \mathrm{i}J(\omega). \tag{3.32}$$

Further constraints on the model have been derived in [111] based on the properties of the FRF and its corresponding IRF. A least-squares fitting method is applied to find the coefficients p_i and q_i, and once all coefficients p_i and q_i are obtained, the matrices $\hat{\mathbf{A}}$, $\hat{\mathbf{B}}$, and $\hat{\mathbf{C}}$ can be constructed using any of the standard canonical forms [128]. The state-space models, obtained according to the method presented in [112] for oscillating bodies, and extended to include oscillating water columns, are found in paper C to be efficient and accurate.

As an illustration, Fig. 3.7 shows a comparison of the error in body velocity obtained from state-space radiation models of various orders, for the case of a single-DOF oscillating-body WEC without any nonlinear terms. The error is measured relative to the body velocity obtained from frequency-domain model. It is shown that
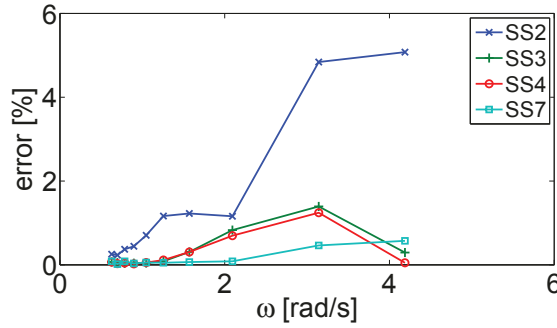
Figure 3.7: Comparison of error in body velocity obtained from state-space radiation models of various orders relative to that obtained from frequency-domain model, for an oscillating-body WEC without nonlinear terms (reproduced from [81]).
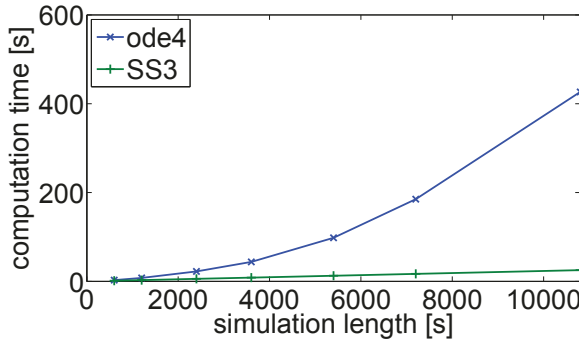
Figure 3.8: Computation time of state-space radiation model of order 3 (SS3) compared to that of direct convolution integration (ode4), for an oscillating-body WEC (reproduced from [81]). Both models are simulated using the same fixed-step Runge-Kutta 4 solver with the same time step. For the direct convolution integration, no truncation has been made on the radiation impedance IRF, hence the computation time varies quadratically with the simulation length.

increasing the model order improves the model accuracy for the range of wave frequencies considered. Fig. 3.8 shows a comparison of the computation time for the direct convolution integration and the state-space model with accuracy comparable to the direct convolution integration, for the same single-DOF oscillating-body WEC. The figure gives an idea of the time saved by replacing the radiation convolution terms with state-space models. To improve the efficiency of the direct convolution integration, the radiation impedance IRF may be truncated at the point where its values become negligible. Then the computation time will vary quadratically with the simulation length initially, but will vary linearly afterwards. More complete results are presented in paper C.

A bond graph model of a BBDB with the radiation terms approximated by state-space models is shown in Fig. 3.9.
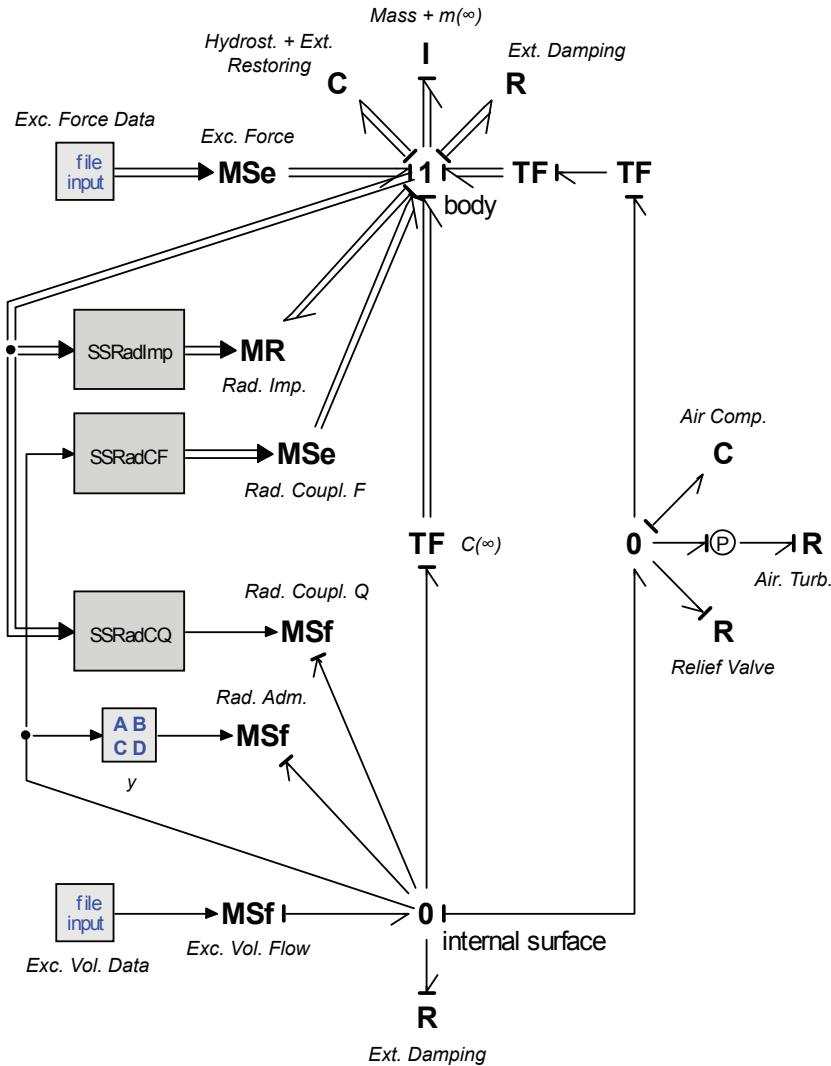
Figure 3.9: Bond graph model of a backward-bent duct buoy with state-space representations of the hydrodynamic radiation terms (reproduced from [83]). The state-space models are represented by the four blocks on the left.

3.5 COMPUTATIONS OF HYDRODYNAMIC PARAMETERS AND SIMULATIONS

The hydrodynamic parameters are computed using the radiation/diffraction program WAMIT [131], which is based on a three-dimensional panel method. Moreover, the geometric modelling program MultiSurf [97] is used to prepare the body geometry, where it is only necessary to model the submerged body surface. The higher-order panel method, with 'cosine spacing' for better accuracy close to the corners, is used instead of the low-order method. Low- and higher-order refer to the method for representation of the body surface and solution. In the low-order method the body

surface is discretized using flat quadrilateral elements, and the solutions for the velocity potential are approximated by piecewise constant values on each element. The higher-order method, on the other hand, is based on B-splines to represent the body surface, velocity potential, and pressure on the body surface. For surface-piercing bodies, the option for removal of irregular frequency effects is used.

The modelling and simulation package 20-sim [12] is used for developing the bond graph models and simulating the models. The mathematical package MATLAB [92] is used for certain simulation cases, for example when the direct convolution integration is used.

Before concluding this section, we shall make a brief note concerning the evaluation of the radiation admittance terms and the radiation coupling terms.

In paper B, we make use of known reciprocity relations [40, 57] to evaluate the radiation admittance and radiation coupling terms. Whereas we have used WAMIT 6.4 in our computations, hence the need of the reciprocity relations, the latest version of WAMIT (version 7) has the capability of directly evaluating hydrodynamic parameters due to applied surface pressure distributions.

In March 2012 an erratum was put up on the WAMIT website regarding the dimensioning of free-surface velocities for the radiation problem [132]. This was brought to the author's attention in April 2012 [22]. As the evaluation of the radiation coupling terms requires the computation of free-surface velocities on the internal free surface due to oscillations of the body with a unit velocity, the dimensioning of the radiation coupling terms in papers B, C, and G are incorrect, except at the limits of zero and infinite frequencies, for which a different dimensioning convention is adopted. As a consequence, in paper B, the absorbed power and the response amplitude operators would be affected. The overall conclusion, however, would remain essentially the same. In paper C, the computed values for the floating OWC case would be affected, but, again, the conclusion would be the same. In paper G, the same BBDB as that in paper B is considered as a case study. The model uses state-space representations for the wave radiation terms. Time-domain simulation results are presented and compared with those in paper B, which are obtained from direct convolution integration. Fair agreement is observed between the two. Since the correct radiation coupling terms have not been used, it is likely that the agreement would have been better had the correct terms been used.

4   Geometry optimisation

> Any properly designed system will generate electricity: the trick is to do it economically.
>
> C. O. J. Grove-Palmer

The motivation behind modern wave energy research was the prospects of escalating cost of conventional energy sources. So the cost issue has been the focus since the early days. A parameter that has been most commonly used to judge the economic potential of a WEC is the hydrodynamic "efficiency," also known as the capture width ratio or the capture factor. It is defined as the ratio of the power absorbed by the device to the incident wave power which passes through the horizontal extent of the device. Its prevalent use has been due to the fact that early wave energy experiments were done in narrow tanks.

Despite its popularity, it can be misleading to judge the economic potential of a WEC based on this parameter alone, because a more hydrodynamically "efficient" device does not necessarily deliver cheaper energy. Thus Falnes and Hals [54] have reminded us recently:

> ... a most important and urgent challenge is to develop a feasible single unit of a WEC, a unit that maximises the power output, not with respect to the free wave power that is available in the ocean, but with respect to parameters related more directly to the WEC itself (size, cost of investment and maintenance, etc.).

Too much emphasis on "efficiency" while neglecting costs could be a hindrance to realizing an economic solution to capturing energy from the waves.

To incorporate the cost factor in the design of a WEC, however, has proven to be a nontrivial task. The problem is that the total cost of a WEC depends on many factors which are intricately interrelated, making it inconvenient to analyse. Nevertheless, it is possible to relate the cost of a WEC to some measurable quantities, such as surface area, volume, mass, PTO force, and reaction force. For arrays, another relevant quantity is the separation distances between the WECs.

A set of parameters has recently been used as a basis for comparison of several different WEC concepts [14]. They were the absorbed annual energy per unit mass, the absorbed annual energy per unit surface area, and the absorbed annual energy per unit root mean square of the PTO force. Although they cannot be equated with

energy per unit cost, still they are better measures of the economic potential of a WEC than hydrodynamic "efficiency."

The purpose of this chapter is to give a summary of and an introduction to the work presented in papers D and F, which deals with finding optimal geometries for a class of WECs which oscillate about a horizontal axis. In addition to maximising the absorbed power, we seek to minimise some parameters related to the cost of the WEC. The essential feature is the use of multi-objective optimisation approach to finding economic WEC designs. This approach will be described in the following.

4.1 MULTI-OBJECTIVE OPTIMISATION

Many design problems have multiple objectives which are generally in conflict with one another. Consider a classical example of designing a bridge. We want the bridge to carry as much load as possible and to be as light as possible. The two objectives are in conflict. For the bridge to have a higher load-carrying capacity, the members should be made thicker, which means a heavier bridge. On the other hand, for the bridge to be lighter, the members should be made thinner, which means a lower load-carrying capacity. The problem of designing a WEC is the same. We want to maximise the power absorption, with as low cost as possible. What characterises these problems is that the optimal solution of one objective is not necessarily the optimum for the other objectives. Such problems do not have a single optimal solution, but many optimal solutions, out of which a compromise solution is to be chosen.

Multi-objective optimisation deals with multiple conflicting objectives. It is not restricted to find a unique single solution, but a set of solutions called *non-dominated solutions*. Each solution in this set is said to be *Pareto optimal*, and when these solutions are plotted in the objective space they are collectively known as the *Pareto front*.

In the following some definitions of these terms are given, following [30, 99]. Without losing generality, we assume the minimisation of all the objective function values.

Definition 1 (Multi-objective optimisation problem). *Find a vector of n decision variables $\vec{x}^* = (x_1^*, x_2^*, \ldots, x_n^*)$ which satisfies the k inequality constraints $g_i(\vec{x}) \geq 0$, $i = 1, 2, \ldots, k$, the p equality constraints $h_i(\vec{x}) = 0$, $i = 1, 2, \ldots, p$, the variable bounds $x_i^L \leq x_i \leq x_i^U$, $i = 1, 2, \ldots, n$, and which minimises the vector of m objective function values $\vec{f}(\vec{x}) = (f_1(\vec{x}), f_2(\vec{x}), \ldots, f_m(\vec{x}))$.*

The set of all values satisfying the constraints and variable bounds defines the *feasible decision variable space* Ω. Any point $\vec{x} \in \Omega$ is a *feasible solution*. For each $\vec{x} \in \Omega$, there exists a point $\vec{f}(\vec{x}) = (f_1(\vec{x}), f_2(\vec{x}), \ldots, f_m(\vec{x}))$ in the objective space. A mapping exists between an n-dimensional decision variable vector and an m-dimensional objective vector through the objective function, constraints, and variable bounds.

Definition 2 (Pareto Optimality). *A point $\vec{x}^* \in \Omega$ is Pareto optimal if for every $\vec{x} \in \Omega$ and $I = \{1, 2, \ldots, m\}$ either $(\forall i \in I) f_i(\vec{x}) = f_i(\vec{x}^*)$ or $(\exists i \in I) f_i(\vec{x}) > f_i(\vec{x}^*)$.*

The above definition states that $\vec{x}^*$ is Pareto optimal if there is no feasible vector $\vec{x}$ which would decrease some function values without simultaneously increasing at least one other function value. Other important definitions associated with Pareto optimality are the following:

Definition 3 (Pareto Dominance). *A vector $\vec{u} = (u_1, \ldots, u_m)$ is said to dominate $\vec{v} = (v_1, \ldots, v_m)$ (denoted by $\vec{u} \preceq \vec{v}$) if and only if $\vec{u}$ is partially less than $\vec{v}$, that is, $(\forall i \in \{1, \ldots, m\}) u_i \leq v_i \land (\exists i \in \{1, \ldots, m\}) u_i < v_i$.*

Definition 4 (Pareto Optimal Set). *For a given multi-objective optimisation problem, the Pareto optimal set is defined as $P^* = \{\vec{x} \in \Omega \mid (\neg\exists \vec{x}' \in \Omega) \, \vec{f}(\vec{x}') \preceq \vec{f}(\vec{x})\}$.*

Definition 5 (Pareto Front). *For a given multi-objective optimisation problem and its Pareto optimal set P^*, the Pareto front is defined as $PF^* = \{\vec{f}(\vec{x}) \mid \vec{x} \in P^*\}$.*

Obtaining the Pareto front and the Pareto optimal set is the main goal of multi-objective optimisation. However, since a Pareto front can contain a large number of points, a good solution must contain a limited number of them. These should be as close as possible to the true Pareto front and well distributed over the entire Pareto front. Otherwise, they would not be very useful to the decision maker.

It is possible to cast a multi-objective optimisation problem into a single-objective problem by combining the objective functions into one aggregate function, a popular approach being the weighted sum approach. However, there are difficulties associated with this approach, such as the need to know beforehand the relative importance of the objectives. Another disadvantage of a single-objective approach is that it returns a single optimal solution, whereas a multi-objective approach returns a set of alternative optimal solutions. Identifying optimal solutions in the multi-objective sense can shed some light into the behavior of the Pareto optimal solutions.

4.2 METHODOLOGY

4.2.1 Algorithm

In the following we will describe in detail the optimisation algorithm used in papers D and F. The algorithm we use is a multi-objective evolutionary algorithm (MOEA) [see, e.g., 29, for an overview of MOEA]. The ability of MOEA to find multiple solutions in a single run and the fact that it can incorporate any number of objectives makes it well-suited to tackle the problem at hand. The algorithm is adapted from [76]. Although in papers D and F we deal with optimising the geometry of a WEC, the algorithm is also applicable for optimising other design parameters, such as the PTO parameters.

The first step in the algorithm is to create an N-sized set of solutions, P. This set is generated randomly from a uniform distribution, taking into account the constraints and variable bounds. A solution j is defined by a vector $(x_1^j, \ldots, x_n^j)$ in the decision variable space and its map $(f_1(\vec{x}^j), \ldots, f_m(\vec{x}^j))$ in the objective space. n is the total

number of decision variables and m is the number of objective functions. The mapping is from an n-dimensional vector $\vec{x}^j$ to an m-dimensional vector $\vec{f}(\vec{x}^j)$.

The next step is *selection*. This operation is made up of two tasks: (1) the selection of non-dominated solutions, and (2) the discard of crowded solutions from those obtained from (1). By (1) we want to keep the solutions closest to the true Pareto optimal solutions, and by (2) we want to maximise the spread of solutions. In addition, with (2) the number of solutions are kept within a specified limit, since a large number of solutions slows down the iteration process.

The first task is described as follows:

1. Create two empty sets of temporary non-dominated solutions, P_t and $P_{t'}$.
2. Mark the solution in P having the least $f_1(\vec{x})$ and put its copy into P_t.
3. Put into $P_{t'}$ the solutions in P with $f_2(\vec{x})$ smaller than that of the solution we have previously marked. Keep the remaining solutions in P.
4. Repeat step 3 for the rest of the objective functions up to f_m, or until there is only one solution in P.
5. Update $P = P_{t'}$ and then empty $P_{t'}$.
6. Repeat steps 2 to 5 until there are no more solutions in $P_{t'}$.

At the end of this task, we have temporary non-dominated solutions in P_t.

The second task is performed only if the number of solutions in P_t is larger than N, which can only happen after the first iteration/generation. To reduce the size of P_t to N, we apply the clustering algorithm. The idea is to group solutions close to each other into one cluster, keep one solution in the cluster, and discard the other solutions in the cluster. This is achieved as follows:

1. Calculate the distance in the objective space, $D_{i,j}$, between two clusters C_i and C_j for all pairs of clusters in P_t. A cluster is defined as a set of points. Thus, initially, each point belongs to a distinct cluster. The distance $D_{i,j}$ is given as

$$D_{i,j} = \frac{1}{|C_i||C_j|} \sum_{i \in C_i,\, j \in C_j} \sqrt{\sum_{k=1}^{m} \left(\frac{f_k(\vec{x}^i) - f_k(\vec{x}^j)}{f_k^{\max}(\vec{x}) - f_k^{\min}(\vec{x})} \right)^2}. \qquad (4.1)$$

   The superscripts max and min denote the maximum and minimum function values, while $|\ \ |$ denotes the size of the cluster. The expression with the square root is the normalized distance between any two clusters i and j in P_t.

2. Find two clusters, among all the clusters in P_t, which have the minimum $D_{i,j}$. These clusters are combined to form one bigger cluster. The number of clusters in P_t is now reduced by one.

3. Repeat steps 1 to 2 until the number of clusters in P_t is reduced to N.

4. Calculate the centroid of each cluster. The centroid c_i of a cluster C_i is the average coordinate in the objective space of all the points in the cluster. It is calculated as

$$c_i = \frac{1}{|C_i|} \sum_{j \in C_i} \left(f_1(\vec{x}^j), \ldots, f_m(\vec{x}^j) \right). \qquad (4.2)$$

5. In each cluster, keep the point with the minimum distance to the centroid and discard all the other points.

At the end of this task we have N temporary non-dominated solutions in P_t.

After performing the selection operation we have $q \leq N$ solutions. These solutions are called the parent solutions and are labelled 1 to q. The next step is to generate $(2N - q)$ offspring solutions labelled $q + 1$ to $2N$ via a *variation* operator. This is described as follows:

1. Set $j = 1$ and $k = q + 1$.
2. Calculate the coordinate in the decision variable space of the offspring solution k as

$$x_i^k = x_i^j + \frac{a}{G^b} R, \quad \text{for } i = 1, \dots, n, \tag{4.3}$$

   where R is a random value drawn from the standard normal distribution, i.e. the normal distribution with zero mean and standard deviation equal to one, G is the generation number, while a and b are preselected parameters.
3. If $x_i^k < x_i^L$, then $x_i^k = x_i^L$. If $x_i^k > x_i^U$, then $x_i^k = x_i^U$.
4. Update $k = k + 1$.
5. If $j = q$, then $j = 1$. Else, $j = j + 1$.
6. Repeat steps 2 to 5 while $k \leq 2N$.
7. Compute $(f_1(\vec{x}^k), \dots, f_m(\vec{x}^k))$, for $k = q + 1, \dots, 2N$.

At the end of the variation operation we have a population of $2N$ solutions made up of the q parent solutions and the $(2N - q)$ offspring solutions. This becomes the new population for the next generation.

The selection and variation operations are carried out iteratively up to a specified number of generations, $G_{\max}$. At $G = G_{\max}$ we stop after the selection operation; we do not carry out the variation operation. The final solutions contained in P_t are regarded as the optimum solutions.

The algorithm can be summarized as follows:

1. Create a random population of solutions of size N. Denote this set of solutions by P. Set $G = 1$.
2. Perform selection of non-dominated solutions from P. Keep these non-dominated solutions in P_t. If $|P_t| > N$, then reduce it to N by discarding crowded solutions from P_t using the clustering algorithm. Otherwise, proceed to step 3. At the end of step 2 we have $q \leq N$ solutions.
3. Generate $(2N - q)$ offspring solutions by variation. At the end of this step we have a total of $2N$ solutions.
4. Denote this set of solutions by P. Set $G = G + 1$.
5. Repeat steps 2 to 4 while $G \leq G_{\max}$. When $G = G_{\max}$, stop at step 2.
6. The final solutions in P_t are the optimum solutions.

4.2.2 Relational geometric modelling

Essential to modelling the geometry is the relational geometry approach, which captures and retains dependency relationships between objects (points, lines, surfaces, etc.) [85]. It is then possible to create parametrically variable geometric models suited for optimisation.
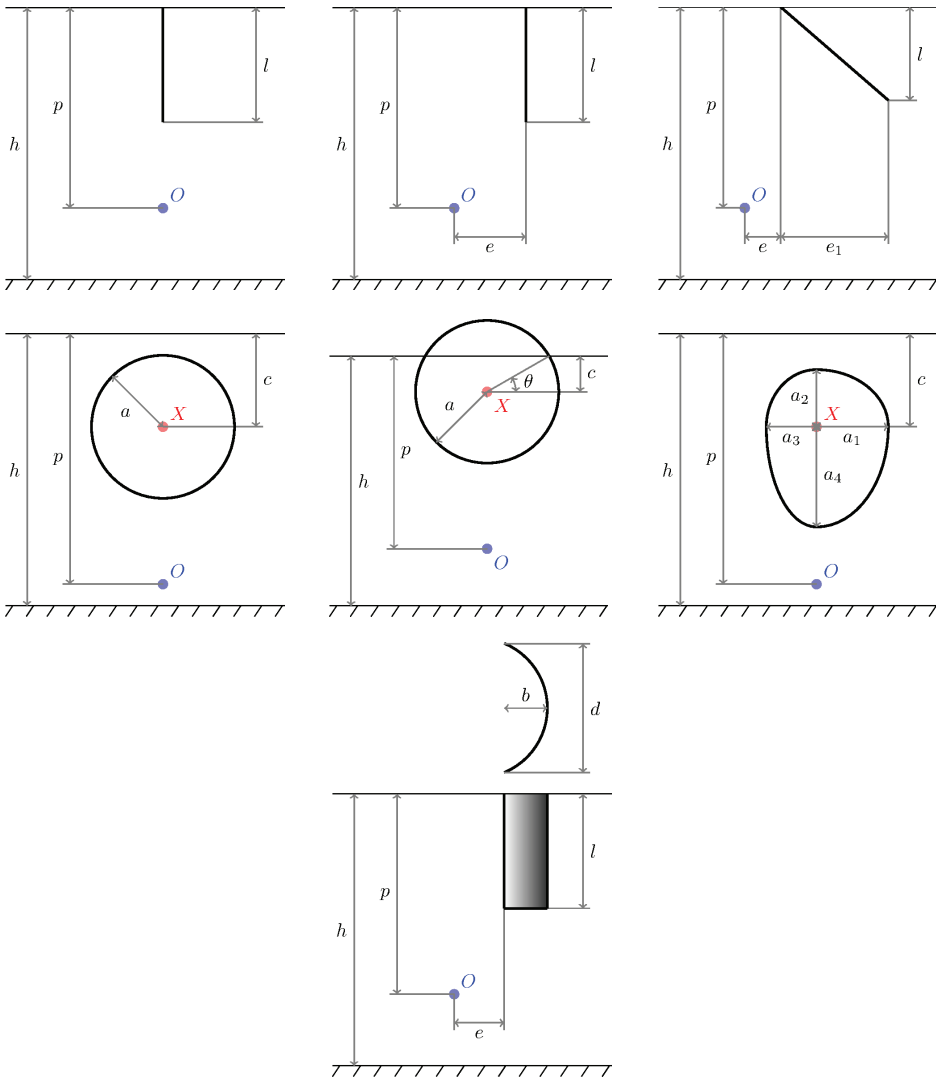
Figure 4.1: Geometric configurations considered in paper D (reproduced from [77]). Top row: thin vertical flap, thin vertical flap with eccentricity of rotation axis, thin inclined flap; middle row: submerged circular cylinder, surface-piercing circular cylinder, submerged elliptical cylinder; bottom row: thin curved vertical flap.

In papers D and F, a class of WECs oscillating about fixed horizontal axes of rotation is considered. The geometric variables are the depth of submergence of the rotational axis, total width, etc. depending on the complexity of the geometry. A solution in the decision variable space is defined by a vector of these variables, whose values are to be optimised within specified bounds. Fig. 4.1 shows the various geometries considered in paper D. Fig. 4.2 shows the composite cylinder geometry considered in paper F.

The geometry is first prepared using MultiSurf, a relational geometric model-
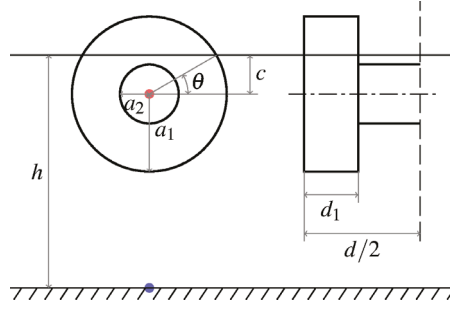
Figure 4.2: Geometric configuration considered in paper F (reproduced from [78]).

ing software. Care is taken to ensure that the desired dependency relationships are maintained between the objects. Two files of importance are output by MultiSurf: a geometry file, which stores the object dependency relationships, and a geometric data file, which is a standard WAMIT [131] input file. By virtue of the link between WAMIT and the Relational Geometry Kernel of MultiSurf, a geometry can be varied only by modifying a few lines in the geometric data file, without having to construct a new geometry in MultiSurf [84]. In paper D, one of the variables to be optimised is the depth of submergence of the rotation axis. Thus, another WAMIT input file needs to be modified for each new geometry, i.e. the potential control file, which contains a line specifying the depth of submergence of the rotation axis.

4.2.3 Computation of objective functions

Two different sets of objective functions are used in papers D and F. In paper D, the objective functions are

$$f_1(\vec{x}) = \int_{\omega_{\min}}^{\omega_{\max}} A_s/P_{\max}(\omega)\mathrm{d}\omega \tag{4.4}$$

$$f_2(\vec{x}) = \int_{\omega_{\min}}^{\omega_{\max}} F_{R\max}(\omega)/P_{\max}(\omega)\mathrm{d}\omega, \tag{4.5}$$

where $\omega_{\min}$ and $\omega_{\max}$ are the specified minimum and maximum frequencies, A_s is the submerged surface area, $P_{\max}$ is the constrained maximum mean absorbed power, and $F_{R\max}$ is the constrained maximum dynamic reaction force at the rotation axis. The expression for $P_{\max}$ is given as [39]

$$P_{\max} = [1 - (1-r)^2 H(1-r)]\frac{|F_e|^2}{8R}, \tag{4.6}$$

where r is the ratio of the constrained to the optimum velocity amplitudes of the body and $H(x)$ is the Heaviside step function. The expression for $F_{R\max}$ is given as [77]

$$F_{R\max} = \sqrt{\frac{1}{2}\left(|F_{R1}^2 + F_{R3}^2| + |F_{R1}|^2 + |F_{R3}|^2\right)}, \tag{4.7}$$

51

where

$$F_{R1} = F_{e1} - (\mathrm{i}\omega m_{15} + R_{15})U \qquad (4.8)$$

and

$$F_{R3} = \begin{cases} F_{e3}, \ \text{for symmetrical bodies} \\ F_{e3} - (\mathrm{i}\omega m_{35} + R_{35})U, \\ \qquad \text{for submerged asymmetrical bodies} \\ F_{e3} - \left(\mathrm{i}\omega m_{35} + R_{35} + \frac{\mathrm{i}}{\omega}\rho g \int_{A_w} x\mathrm{d}A\right)U, \\ \qquad \text{for surface-piercing asymmetrical bodies.} \end{cases} \qquad (4.9)$$

Here, F_{e1} and F_{e3} are the surge and heave excitation forces, m_{15} and R_{15} are the added inertia and radiation damping in the horizontal direction due to the oscillation of the body about the rotation axis, m_{35} and R_{35} are the added inertia and radiation damping in the vertical direction due to the oscillation of the body, A_w is the water plane area, and U is the constrained velocity of the body, given as

$$U = F_e[1 - (1 - r)H(1 - r)]/2R. \qquad (4.10)$$

In paper F, the objective functions are

$$f_1(\vec{x}) = \int_{\omega_{\min}}^{\omega_{\max}} P_{\max}(\omega)\mathrm{d}\omega \qquad (4.11)$$

$$f_2(\vec{x}) = A_s, \qquad (4.12)$$

where A_s is now the total surface area, not just the submerged surface area, and $P_{\max}$ is the maximum mean power achievable by a linear damper, given as [41]

$$P_{\max} = \frac{|F_e|^2}{4(R + |Z_i|)}, \qquad (4.13)$$

where Z_i is the intrinsic impedance, defined previously in Chapter 2.

Computations of the excitation forces, added inertia, and radiation damping necessary for the evaluation of the maximum absorbed power and reaction force are carried out using WAMIT. The surface areas, on the other hand, are evaluated from the geometry using known formulas.

Different combinations of objective functions can be considered, and while we have used two objective functions, it is possible to consider three or more objective functions. For example, the two objective functions in paper D may be decomposed into three functions: the absorbed power, the surface area, and the reaction force.

4.2.4 Framework

The geometry optimisation framework is summarised in Fig. 4.3. The whole scheme is programmed in MATLAB [92], which needs to perform repeated calls of WAMIT to compute the required hydrodynamic parameters for the evaluation of the objective functions. As described earlier, geometry preparation using MultiSurf is done only
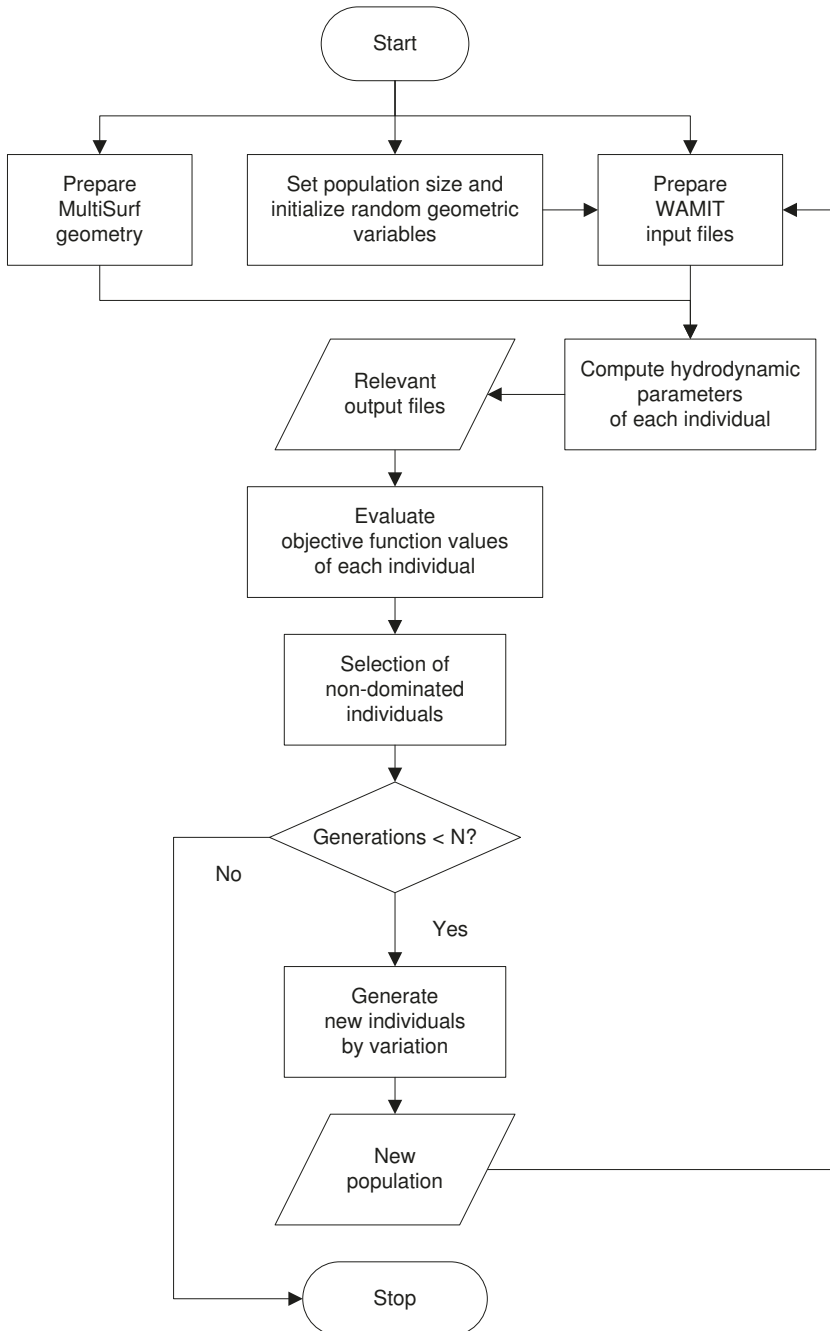
Figure 4.3: Geometry optimisation flowchart (reproduced from [77]).

at the start of the optimisation process. A geometry can be varied only by modifying a few lines in the geometric data file, which is a WAMIT input file, without having to reconstruct it in MultiSurf. Another WAMIT input file which may need to be

modified for each new geometry is the potential control file, which contains a line specifying the depth of submergence of the rotation axis. The rest of the WAMIT input files do not change throughout the optimisation process. The bulk of the computation time is for computing the required hydrodynamic parameters for each new geometry. The computation time taken for the selection and variation operations is minor compared to the computation of the hydrodynamic parameters.

5 Geometry control

> If we make wave devices with the brute strength to stand up to the very worst loads they will be heavy and expensive because infinity is such a big number.
>
> Stephen Salter

For a single WEC operating in one mode, two conditions must be satisfied for maximum power absorption, namely, the optimum phase condition, or the resonance condition, and the optimum amplitude condition [49, §3.5]. The first is achieved when the imaginary part of the system impedance, i.e. the reactance, cancels, while the second is achieved by choosing the right value of the load resistance. This chapter is concerned mainly with the first condition. A discussion of the natural periods and resonance bandwidths of typical WECs will first be given as a motivation for the need to include control strategies to improve the economy of WECs[1]. A summary will then be given for the new WEC with geometry control proposed in paper E.

5.1 NATURAL RESONANCE

In general, the natural period of a WEC can be expressed as

$$T_0 = 2\pi \sqrt{\frac{M + m}{S_b}}, \tag{5.1}$$

where M is the structural inertia, m is the (frequency-dependent) added inertia, and S_b is the linearised hydrostatic stiffness. When the incident wave period T equals T_0, the system is in resonance. We first consider three examples to give an idea of the typical natural periods of oscillating-body WECs and how one can engineer them to match the prevailing wave periods.

First consider a heaving hemisphere with radius a. Then $M = 2\rho\pi a^3/3$ and $S_b = \rho g\pi a^2$, where ρ is the water density. Thus,

$$T_0 = 2\pi \sqrt{\frac{2\rho\pi a^3 x}{3\rho g\pi a^2}} = 2\pi\sqrt{\frac{2ax}{3g}}, \tag{5.2}$$

---

[1]That resonance does not necessarily result in optimum phase for WEC arrays, is another motivation for motion control.

where x is a factor such that $M + m = Mx$. The added mass of a heaving hemisphere in deep water for wave frequencies typically occurring at sea is approximately $M/2$ [68]. Therefore,

$$T_0 \approx (2 \, \mathrm{sm}^{-1/2})\sqrt{a}. \tag{5.3}$$

For a hemisphere with radius $a = 5$ m, then, $T_0 \approx 4.5$ s.

Next, consider a heaving truncated cylinder with radius a and draft d. Then $M = \rho\pi a^2 d$ and S_b is the same as the heaving hemisphere. Thus,

$$T_0 = 2\pi\sqrt{\frac{\rho\pi a^2 dx}{\rho g \pi a^2}} = 2\pi\sqrt{\frac{dx}{g}}. \tag{5.4}$$

The added mass of a heaving truncated cylinder in deep water may be approximated as $2aM/3d$ for wave frequencies typically occurring at sea [33]. Therefore,

$$T_0 \approx (2 \, \mathrm{sm}^{-1/2})\sqrt{d + 2a/3}. \tag{5.5}$$

For a cylinder with radius $a = 5$ m and $d = 10$ m, then $T_0 \approx 7$ s, but the resonance bandwidth is disappointingly small (c.f. Fig. 2.1).

Finally, we consider a submerged buoyant horizontal cylinder oscillating about an axis fixed at the sea bottom. The cylinder has radius a, width d, rotation arm length l, and we assume that $a \ll l$. Then $M = \rho\pi a^2 d l^2 r$ and $S_b = \rho g \pi a^2 d l(1-r)$, where r is the relative density of the cylinder. Thus,

$$T_0 \approx 2\pi\sqrt{\frac{\rho\pi a^2 d l^2 rx}{\rho g \pi a^2 d l(1-r)}} \approx 2\pi\sqrt{\frac{lrx}{g(1-r)}} \approx (2 \, \mathrm{sm}^{-1/2})\sqrt{\frac{lrx}{1-r}}. \tag{5.6}$$

Assuming that the added inertia of a bottom-hinged submerged horizontal cylinder is in the order of its structural inertia, i.e., $x \approx 2$, then for a cylinder with $l = 10$ m and $r = 0.3$, $T_0 \approx 6$ s.

We observe that the natural period of a heaving WEC is governed by its size whereas for a bottom-hinged submerged buoyant WEC the governing parameters are the arm length and the relative density. Unless some means of phase control is used, a heaving WEC should be large enough to resonate with offshore waves, which usually have large periods. To have $T_0 = 8$ s, for example, a heaving hemisphere of radius $a = 16$ m is required. On the other hand, a bottom-hinged submerged WEC can be made sufficiently small. For a fixed arm length, the natural period of a bottom-hinged submerged WEC can be made indefinitely large in theory by increasing its relative density. It is, however, more difficult to tune a bottom-hinged WEC to low resonant periods.

5.2   THE NEED FOR CONTROL

In reality, the periods of ocean waves keep changing. A WEC then should have a broad natural resonance bandwidth or otherwise be able to adapt itself from time to

time to keep resonating with the waves. The problem with small WECs is that they generally have a relatively narrow bandwidth. A small heaving WEC, in addition to having a relatively narrow bandwidth, has a natural period that is lower than the prevailing wave periods (c.f. Fig. 2.1). To make a WEC large, however, does not seem to be an economic option.

Another option is to design a WEC such that it has more than one natural periods. That it is possible for a WEC to have more than one natural periods may be seen by writing (5.1) as

$$m(\omega_0) = \frac{S_b}{\omega_0^2} - M, \qquad (5.7)$$

where $\omega_0 = 2\pi/T_0$. The function $S_b/\omega^2 - M$ is monotonically decreasing with ω, while the behaviour of $m(\omega)$ depends on the geometry. If both functions can be made to intersect at more than one frequency by a suitable choice of geometric configuration, then we have multiple resonances. For example, multiple resonances have been shown to exist for a bottom-hinged submerged WEC having a small depth of submergence [43]. It is of course important that the natural periods fall within the range of the prevailing wave periods and that the bandwidths are sufficiently large.

For other geometries and modes of motion, the remaining option is to adapt the WEC from time to time to resonate with the waves. A well-known strategy is latching [53, 55], by which the motion of the WEC, at every half wave cycle, is stopped upon reaching its maximum excursion and then released, ideally, about a quarter of its natural period before the wave excitation force reaches maximum. By latching, a small WEC having natural period lower than the wave period will move in approximately the same way as a larger WEC with larger natural period and larger bandwidth. This strategy belongs to the category of wave-by-wave or discrete control [24, 50].

Another strategy which is not new but has not received much academic attention so far is geometry control. It was defined by Price et al. [114] as anything that alters the excitation force and/or the intrinsic impedance of the WEC (or the excitation volume flow and/or the intrinsic admittance, in the case of fixed OWCs, or a combination of the four, in the case of floating OWCs). Changing the orientation of a WEC relative to the incident wave direction, changing the inertia or inertia distribution of a WEC by ballasting [60, 89], or changing the freeboard of an overtopping WEC [130] are all examples of geometry control. In these examples, geometry control is used mainly to improve power absorption.

In addition to their periods, the amplitudes of real ocean waves are also changing. A WEC therefore must be able to survive the worst wave loading scenarios. Geometry control may also be used to achieve survivability. For example, the WaveStar, which consists of many floats oscillating about an axis above the water level, is designed with a mechanism which allows the floats to be lifted out of reach of the waves in storm conditions. Two recent concepts, WEPTOS [110], which consists of ducks mounted on two horizontal arms connected at a hinge, and WaveCat [69], an oblique overtopping device consisting of two rows of tanks joined at a hinge, have different primary conversion principles but share similar survival strategies. The angle between the two rows of ducks/tanks can be controlled, and made smaller in survival mode.
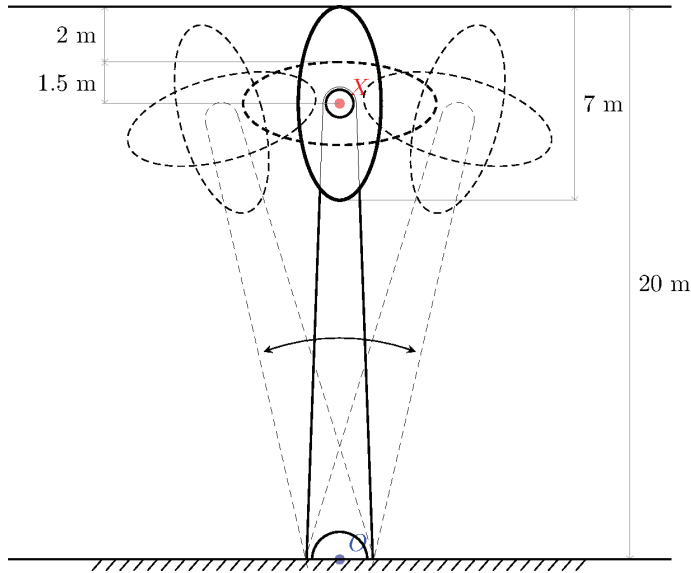
Figure 5.1: Two-dimensional sketch of the proposed WEC (reproduced from [79]). The device oscillates about the bottom hinge O upon wave action. The upper hinge X enables the flap to be aligned at variable angle relative to the arm.

5.3 A PROPOSAL FOR AN ECONOMIC WAVE ENERGY CONVERTER

In paper E, a novel WEC is proposed, which makes use of a geometry control strategy to improve its economy. The geometry consists of a submerged buoyant flap with elliptical cross-section, supported by an arm hinged at the sea bottom. The novelty is in the provision of another hinge at the upper end of the arm. The extra hinge allows the flap to be fixed at variable angles relative to the arm. Since changing the flap angle changes the dynamic characteristics of the WEC and its hydrodynamic properties, the angle of the flap can be controlled from time to time, depending on the wave conditions, so as to broaden the overall power absorption bandwidth and to avoid excessive loadings. In paper E, the potential of this WEC is investigated by considering two possible orientations of the flap: parallel or perpendicular to the arm. The absorbed power and reaction force for the case where the flap is fixed for all sea states are compared with those for the case where the best orientation of the flap is used for each sea state. Ballasting the flap is also considered at the same time.

6   *Conclusion*

We began this thesis by looking back some thirty years ago, when harnessing energy from ocean waves looked more like science fiction to most people. Today, harnessing wave energy in an economical way and a major scale is still a dream, but with increasing support from governments and the public, as we have seen in recent years, we may confidently say that it will not be too long until this dream becomes a reality. Meanwhile, many areas still require further research, and this thesis is a small contribution to that effort.

The underlying motivation for the work presented in this thesis has been the necessity to lower the cost of useful energy from the waves. We have argued, as did Falnes and Hals [54], that our objective should be to maximise the absorbed energy, not with respect to the available wave energy resource, but with respect to the cost of the WEC itself. The first part of the thesis (Chapter 3) concerns the application of useful tools to help develop more realistic, yet efficient, numerical models of WECs. The second part (Chapter 4) deals with the incorporation of the cost factor into the problem of designing economical WEC geometries. The final part (Chapter 5) looks at geometry control as a means to improve the economy of a WEC.

6.1   SUMMARY OF CONTRIBUTIONS

In summary, we have shown that

1. Bond graph is well-suited for developing comprehensive models of WECs, which involve interactions between multiple energy domains. In particular, we have developed bond graph models of

   a) two alternative hydraulic PTO systems connected to a bottom-standing WEC resembling the Salter Duck, and

   b) a floating OWC in the form of a BBDB,

   as well as presented generic bond graph models of oscillating-body and oscillating-water-column WECs.

2. State-space models for wave radiation terms are efficient and accurate for use in time-domain simulations of WECs, while constant-parameter models may be useful to give quick estimates of the desired outputs when the radiation terms are relatively smaller than the other terms in the system. These findings

were obtained from a systematic assessment of three alternative models for the wave radiation terms (constant-parameter, state-space, and direct convolution integration models) applied to oscillating-body and oscillating-water-column WECs.

3. Multi-objective optimisation is a useful approach to incorporate the cost factor into the problem of finding economical WEC designs. An optimisation framework has been developed which makes use of relational geometry to parametrically vary the geometry. The methodology has been applied to find optimum geometries of WECs oscillating about fixed horizontal axes. Among the findings was that it is generally more economical for a bottom-hinged pitching WEC to have its flap spanning only the upper part of the water depth instead of the whole water depth.

4. Geometry control has the potential for improving the economy of WECs. A WEC with variable flap angle has been proposed and shown to have the potential of broadening the power absorption bandwidth and avoiding excessive forces.

6.2 RECOMMENDATIONS FOR FUTURE WORK

The following topics are suggested as direct extensions of the work presented in this thesis:

1. *Bond graph modelling of other types of WECs, such as overtopping and flexible WECs*
   Bond graph models of oscillating-body and oscillating-water-column WECs have been developed. A subsequent task in the modelling of WECs using bond graph would be to develop bond graph models of other types of WECs, such as overtopping [e.g. 75] and flexible WECs [e.g. 58].

2. *Optimisation of BBDB and other floating OWCs*
   The BBDB is an interesting device in that it uses the heave and pitch motions of the body to broaden the bandwidth of the motion of the water column relative to the body. A device with similar working principle has been proposed recently which consists of a vessel with two OWCs, one at the bow and the other at the stern [67]. It would be interesting to optimise the geometry of this class of WECs. The optimisation objectives could be to maximise power absorption and minimise drift forces to be resisted by the mooring lines, over a range of wave frequencies.

3. *Bottom-hinged device with variable flap angle*
   As a further step in the study of the WEC proposed in paper E, the dimensions of the proposed WEC need to be optimised. Furthermore, the performance of the device was studied in paper E by assuming that the flap angle was fixed in each sea state. Further refinement to the study would include evaluating the performance of the device when the flap angle is allowed to vary within

a sea state. Only two different flap angles were considered in paper E. The characteristics of the WEC for other flap angles are yet to be studied. It may also be worthwhile to investigate a survival strategy of letting the flap move freely relative to the arm. The effect of variation in water depth due to tides should also be investigated. Ultimately, a series of model tests will be essential to validate the numerical predictions made under the assumption of linear wave theory.

4. *Bottom-hinged horizontal cylinders*
   In paper F, we optimised the geometry of a bottom-hinged horizontal cylinder composed of a submerged central part and two surface-piercing ends. It would be interesting to compare the composite cylinder with submerged and surface-piercing uniform cylinders.

5. *Optimisation of PTO parameters in addition to geometrical parameters*
   So far we have dealt with geometry optimisation, where the maximum absorbed power, as given by (4.6) or (4.13), has been used as one of the objective functions. If the PTO parameters are set to constants, where the absorbed power is given by (2.60), the PTO parameters become additional design variables to be optimised apart from the geometrical parameters.

6. *Formulations of objective functions*
   Another interesting study is to compare various combinations and formulations of the objective functions and their effects on the resulting optimal designs. This would include studying the effects of the wave climate at a given site.

7. *Multi-objective optimisation of other classes of WECs, such as heaving bodies and self-reacting multiple bodies*
   The goal is to obtain general ideas on the relative cost-effectiveness of various classes of WECs, cost-effective design principles for WECs, and general understanding of the relationship between geometry and PTO parameters on one hand, and absorbed power, PTO force, and reaction force on the other, for different classes of WECs.

8. *Array optimisation*
   For WECs in an array, the positioning of the WECs in the array is an additional variable to be optimised. A relevant objective function would be related to the separation distances between the WEC units.

9. *WECs with adaptive geometries*
   The first step of the study would be to explore the possibilities of varying the geometries of existing WECs, as well as proposing other novel WECs with variable geometries. From these, the most promising concepts may be identified, and they will be subjected to further study to determine the optimal operation of the control strategy.

References

[1]   http://www.carnegiewave.com.

[2]   http://www.oceanpowertechnologies.com.

[3]   http://www.oceanlinx.com.

[4]   http://www.aquamarinepower.com.

[5]   http://www.pelamiswave.com.

[6]   http://www.wavenergy.co.nz.

[7]   http://www.aw-energy.com.

[8]   http://www.wavebob.com.

[9]   http://www.wavestarenergy.com.

[10]   http://www.wello.fi.

[11]   "Appendix 5 Glossary of wave energy terms," in *Wave Energy Conversion*, J. Brooke, Ed.   Elsevier, 2003, pp. 169–175.

[12]   20-sim, Controllab Products B. V., Enschede, The Netherlands, 2011, version 4.2.

[13]   A. Babarit, A. H. Clément, and J.-C. Gilloteaux, "Optimization and time-domain simulation of the SEAREV wave energy converter," in *Proceedings of the 24th International Conference on Offshore Mechanics and Arctic Engineering (OMAE)*, vol. 2, Halkidiki, Greece, 2005, pp. 703–712.

[14]   A. Babarit, J. Hals, M. J. Muliawan, A. Kurniawan, T. Moan, and J. Krokstad, "Numerical benchmarking study of a selection of wave energy converters," *Renewable Energy*, vol. 41, no. 0, pp. 44–63, 2012.

[15]   G. Bacelli, J.-C. Gilloteaux, and J. Ringwood, "State space model of a hydraulic power take off unit for wave energy conversion employing bondgraphs," in *Proceedings of World Renewable Energy Conference*, 2008, pp. 1–4.

[16] G. Bennet and M. Greenhow, "Nonlinear dynamics of a floating body," in *Proceedings of the 7th International Workshop on Water Waves and Floating Bodies*, R. Cointe, Ed., Val de Reuil, France, 1992, pp. 11–14.

[17] H. Berge, Ed., *Proceedings of the 2nd International Symposium on Wave Energy Utilization*, Trondheim, Norway, 1982.

[18] P. C. Breedveld, R. C. Rosenberg, and T. Zhou, "Bibliography of bond graph theory and application," *Journal of the Franklin Institute*, vol. 328, no. 5-6, pp. 1067–1109, 1991.

[19] I. Bryden, "The marine energy resource, constraints and opportunities," *Proceedings of the Institution of Civil Engineers: Maritime Engineering*, vol. 159, no. 2, pp. 55–65, 2006.

[20] K. Budal, "Theory for absorption of wave power by a system of interacting bodies," *Journal of Ship Research*, vol. 21, no. 4, pp. 248–253, 1977.

[21] K. Budal and J. Falnes, "A resonant point absorber of ocean-wave power," *Nature*, vol. 256, pp. 478–479, 1975.

[22] D. Bull, 2012, private communication.

[23] A. Clément, P. McCullen, A. F. d. O. Falcão, A. Fiorentino, F. Gardner, K. Hammarlund, G. Lemonis, T. Lewis, K. Nielsen, S. Petroncini, M. Pontes, P. Schild, B. Sjöström, H. C. Sørensen, and T. Thorpe, "Wave energy in Europe: Current status and perspectives," *Renewable and Sustainable Energy Reviews*, vol. 6, no. 5, pp. 405–431, 2002.

[24] A. H. Clément and A. Babarit, "Discrete control of resonant wave energy devices," *Philosophical Transactions of the Royal Society A: Mathematical, Physical and Engineering Sciences*, vol. 370, no. 1959, pp. 288–314, 2012.

[25] B. M. Count, "Wave power: A problem searching for a solution," in *Power from Sea Waves*, B. M. Count, Ed.   Academic Press, 1980, pp. 11–27.

[26] B. M. Count, Ed., *Power from Sea Waves*.   Academic Press, 1980.

[27] W. E. Cummins, "The impulse response function and ship motions," David Taylor Model Basin, Tech. Rep., October 1962.

[28] Danish Ministry of Climate, Energy and Building, "DK Energy Agreement, March 22 2012," http://www.kemin.dk/Documents/Presse/2012/Energiaftale/FAKTAUK1.pdf, 2012.

[29] K. Deb, *Multi-Objective Optimization Using Evolutionary Algorithms*, 1st ed. Wiley, 2001.

[30]   ——, "Evolutionary multi-objective optimization without additional param-
        eters," in *Parameter Setting in Evolutionary Algorithms*, ser. Studies in Com-
        putational Intelligence, F. G. Lobo, C. F. Lima, and Z. Michalewicz, Eds.
        Springer, 2007, pp. 241–257.

[31]   Department of Energy and Climate Change, "£20million marine scheme
        now open," http://www.decc.gov.uk/en/content/cms/news/pn12_043/pn12_
        043.aspx, 2012.

[32]   S. Drew, A. R. Plummer, and M. N. Sahinkaya, "A review of wave energy
        converter technology," *Proc. IMechE Part A: J. Power and Energy*, vol. 223, pp.
        887–902, 2009.

[33]   H. Eidsmoen, "Hydrodynamic parameters for a two-body axisymmetric sys-
        tem," *Applied Ocean Research*, vol. 17, no. 2, pp. 103–115, 1995.

[34]   G. Elliot and G. Caratti, Eds., *European Wave Energy Symposium*, Edinburgh,
        1993.

[35]   H. Engja and J. Hals, "Modelling and simulation of sea wave power conversion
        systems," in *Proceedings of the 7th European Wave and Tidal Energy Conference*,
        Porto, Portugal, 2007, pp. 1–7.

[36]   D. V. Evans, "Some theoretical aspects of three-dimensional wave energy ab-
        sorbers," in *Proceedings of the First Symposium on Wave Energy Utilization*, K.-
        G. Jansson, J. K. Lunde, and T. Rindby, Eds., Gothenburg, 1979, pp. 77–113.

[37]   ——, "Some analytic results for two- and three-dimensional wave-energy ab-
        sorbers," in *Power from Sea Waves*, B. M. Count, Ed.   Academic Press, 1980,
        pp. 213–249.

[38]   ——, "Power from water waves," *Annual Review of Fluid Mechanics*, vol. 13,
        pp. 157–187, 1981.

[39]   ——, "Maximum wave-power absorption under motion constraints," *Applied
        Ocean Research*, vol. 3, no. 4, pp. 200–203, 1981.

[40]   ——, "Wave-power absorption by systems of oscillating surface pressure dis-
        tributions," *Journal of Fluid Mechanics*, vol. 114, pp. 481–499, 1982.

[41]   ——, "The hydrodynamic efficiency of wave-energy devices," in *Hydrodynamics
        of ocean wave-energy utilization*, D. V. Evans and A. F. de O. Falcão, Eds.
        Springer-Verlag, 1985, pp. 1–34.

[42]   D. V. Evans and A. F. d. O. Falcão, Eds., *Hydrodynamics of ocean wave-energy
        utilization*.   Springer-Verlag, 1986.

[43]   D. V. Evans and R. Porter, "Wave energy extraction by coupled resonant ab-
        sorbers," *Phil. Trans. R. Soc. A*, vol. 370, no. 1959, pp. 315–344, 2012.

[44] D. V. Evans, D. C. Jeffrey, S. H. Salter, and J. R. M. Taylor, "Submerged cylinder wave energy device: theory and experiment," *Applied Ocean Research*, vol. 1, no. 1, pp. 3–12, 1979.

[45] A. F. d. O. Falcão, "Wave energy utilization: A review of the technologies," *Renewable and Sustainable Energy Reviews*, vol. 14, pp. 899–918, 2010.

[46] J. Falnes, "Radiation impedance matrix and optimum power absorption for interacting oscillators in surface waves," *Applied Ocean Research*, vol. 2, no. 2, pp. 75–80, 1980.

[47] ——, "Research and development in ocean-wave energy in Norway," in *Proceedings of International Symposium on Ocean Energy Development*, H. Kondo, Ed., Muroran, Hokkaido, Japan, August 1993, pp. 27–39.

[48] ——, "Maximum wave-energy absorption by oscillating systems consisting of bodies and water columns with restricted or unrestricted amplitudes," in *Proceedings of the International Offshore and Polar Engineering Conference*, vol. 1, 2000, pp. 420–426.

[49] ——, *Ocean Waves and Oscillating Systems*. Cambridge, UK: Cambridge University Press, 2002.

[50] ——, "Optimum control of oscillation of wave-energy converters," *International Journal of Offshore and Polar Engineering*, vol. 12, no. 2, pp. 147–155, 2002.

[51] ——, "A review of wave-energy extraction," *Marine Structures*, vol. 20, pp. 185–201, 2007.

[52] ——, "Ocean wave energy: Introductory lectures," 2009. [Online]. Available: http://folk.ntnu.no/falnes/teach/wave/TFY4300/index.html

[53] J. Falnes and K. Budal, "Wave-power conversion by point absorbers," *Norwegian Maritime Research*, vol. 6, no. 4, pp. 2–11, 1978.

[54] J. Falnes and J. Hals, "Heaving buoys, point absorbers and arrays," *Philosophical Transactions of the Royal Society A: Mathematical, Physical and Engineering Sciences*, vol. 370, no. 1959, pp. 246–277, 2012.

[55] J. Falnes and P. M. Lillebekken, "Budal's latching-controlled-buoy type wave-power plant," in *Proc. 5th European Wave Energy Conference*, 2003, pp. 233–244.

[56] J. Falnes and J. Løvseth, "Ocean wave energy," *Energy Policy*, vol. 19, no. 8, pp. 768–775, 1991.

[57] J. Falnes and P. McIver, "Surface wave interactions with systems of oscillating bodies and pressure distributions," *Applied Ocean Research*, vol. 7, no. 4, pp. 225–234, 1985.

[58] F. J. M. Farley, R. C. T. Rainey, and J. R. Chaplin, "Rubber tubes in the sea," *Philosophical Transactions of the Royal Society A: Mathematical, Physical and Engineering Sciences*, vol. 370, no. 1959, pp. 381–402, 2012.

[59] A. C. Fernandes, "Analysis of an axisymmetric pneumatic buoy by reciprocity relations and a ring-source method," Ph.D. dissertation, Department of Ocean Engineering, MIT, Cambridge, Massachusetts, 1983.

[60] F. Flocard and T. D. Finnigan, "Increasing power capture of a wave energy device by inertia adjustment," *Applied Ocean Research*, vol. 34, pp. 126–134, 2012.

[61] J.-M. Forestier, B. Holmes, S. Barrett, and A. W. Lewis, "Value and validation of small scale physical model tests of floating wave energy converters," in *Proceedings of the 7th European Wave and Tidal Energy Conference*, Porto, Portugal, 2007.

[62] M. J. French, "On the difficulty of inventing an economical sea wave energy converter: A personal view," *Proceedings of the Institution of Mechanical Engineers Part M: Journal of Engineering for the Maritime Environment*, vol. 220, no. 3, pp. 149–155, 2006.

[63] A. Garrad, "The lessons learned from the development of the wind energy industry that might be applied to marine industry renewables," *Philosophical Transactions of the Royal Society A: Mathematical, Physical and Engineering Sciences*, vol. 370, no. 1959, pp. 451–471, 2012.

[64] M. Greenhow and S. P. White, "Optimal heave motion of some axisymmetric wave energy devices in sinusoidal waves," *Applied Ocean Research*, vol. 19, no. 3-4, pp. 141–159, 1997.

[65] C. O. J. Grove-Palmer, "Wave energy in the United Kingdom: A review of the programme June 1975 - March 1982," in *Proceedings of the 2nd International Symposium on Wave Energy Utilization*, Trondheim, Norway, 1982, pp. 23–54.

[66] J. Hals, "Modelling and phase control of wave-energy converters," Ph.D. dissertation, Department of Marine Technology, Norwegian University of Science and Technology, Trondheim, 2010.

[67] J. A. Helder, C. Schmittner, and B. Buchner, "On the further optimization of the 'green water concept' for wave energy conversion," in *Proceedings of the 31st International Conference on Ocean, Offshore and Arctic Engineering*, Rio de Janeiro, Brazil, 2012.

[68] A. Hulme, "The wave forces acting on a floating hemisphere undergoing forced periodic oscillations," *Journal of Fluid Mechanics*, vol. 121, pp. 443–463, 1982.

[69] G. Iglesias, H. Fernandez, R. Carballo, A. Castro, and F. Taveira-Pinto, "The WaveCat – development of a new wave energy converter," in *Proc World Renewable Energy Congress 2011*, 2011.

[70] ISSC, "Ocean, wind and wave energy utilization," 17th International Ship and Offshore Structures Congress, Seoul, Korea, Tech. Rep., August 2009.

[71] K.-G. Jansson, J. K. Lunde, and T. Rindby, Eds., *Proceedings of the First Symposium on Wave Energy Utilization*, Gothenburg, 1979.

[72] E. R. Jefferys, "Device characterisation," in *Power from Sea Waves*, B. M. Count, Ed. Academic Press, 1980, pp. 413–438.

[73] ——, "Simulation of wave power devices," *Applied Ocean Research*, vol. 6, no. 1, pp. 31–39, 1984.

[74] ——, "What can wave energy learn from offshore oil and gas?" *Philosophical Transactions of the Royal Society A: Mathematical, Physical and Engineering Sciences*, vol. 370, no. 1959, pp. 439–450, 2012.

[75] J. P. Kofoed, P. Frigaard, E. Friis-Madsen, and H. C. Sørensen, "Prototype testing of the wave energy converter Wave Dragon," *Renewable Energy*, vol. 31, no. 2, pp. 181–189, 2006.

[76] A. Kurniawan and G. Ma, "Optimization of ballast plan in launch jacket loadout," *Structural and Multidisciplinary Optimization*, vol. 38, pp. 267–288, 2009.

[77] A. Kurniawan and T. Moan, "Optimal geometries for wave absorbers oscillating about a fixed axis," *Oceanic Engineering, IEEE Journal of*, vol. 38, no. 1, pp. 117–130, 2013.

[78] ——, "Multi-objective optimization of a wave energy absorber geometry," in *Proceedings of the 27th International Workshop on Water Waves and Floating Bodies*, Copenhagen, 2012.

[79] ——, "Characteristics of a pitching wave absorber with rotatable flap," *Energy Procedia*, vol. 20, pp. 134–147, 2012.

[80] A. Kurniawan, J. Hals, and T. Moan, "Modelling and simulation of a floating oscillating water column," in *Proceedings of the 30th International Conference on Ocean, Offshore and Arctic Engineering*, Rotterdam, The Netherlands, 2011.

[81] ——, "Assessment of time-domain models of wave energy conversion systems," in *Proceedings of the 9th European Wave and Tidal Energy Conference*, Southampton, 2011.

[82] A. Kurniawan, E. Pedersen, and T. Moan, "Bond graph modelling of a wave energy conversion system with hydraulic power take-off," *Renewable Energy*, vol. 38, no. 1, pp. 234–244, 2012.

[83] ——, "Modelling of wave energy converters using bond graph," in *Proceedings of the 10th International Conference on Bond Graph Modeling and Simulation*, Genoa, 2012.

[84] C.-H. Lee, J. S. Letcher Jr., R. G. Mack II, J. N. Newman, D. M. Shook, and E. Stanley, "Integration of geometry definition and wave analysis software," in *Proc. 21st Int. Conf. Offshore Mech. Arctic Eng.*, Oslo, Norway, 2002, pp. 721–733.

[85] J. S. Letcher Jr., D. M. Shook, and S. G. Shepherd, "Relational geometric synthesis: Part 1-framework," *Computer–Aided Design*, vol. 27, no. 11, pp. 821–832, 1995.

[86] J. Lighthill, "Two-dimensional analyses related to wave-energy extraction by submerged resonant ducts," *Journal of Fluid Mechanics*, vol. 91, no. 2, pp. 253–317, 1979.

[87] A. E. Long and T. J. T. Whittaker, "Wave power–a challenge to engineers." *Proceedings of the Institution of Civil Engineers*, vol. 84, pp. 355–374, 1988.

[88] M. S. Longuet-Higgins, "The mean forces exerted by waves on floating or submerged bodies with applications to sand bars and wave power machines," *Proceedings of the Royal Society of London. A. Mathematical and Physical Sciences*, vol. 352, no. 1671, pp. 463–480, 1977.

[89] J. Lucas, S. Salter, J. Cruz, J. Taylor, and I. Bryden, "Performance optimisation of a modified Duck through optimal mass distribution," in *Proceedings of the 8th European Wave and Tidal Energy Conference*, Uppsala, Sweden, 2009, pp. 270–279.

[90] I. R. Marré, "Modelling and simulation of a wave energy converter using a bond graph approach," Master's thesis, Norwegian University of Science and Technology, June 2006.

[91] Y. Masuda, H. Kimura, X. Liang, X. Gao, R. M. Mogensen, and T. Anderson, "Regarding BBDB wave power generating plant," in *Proceedings of the 2nd European Wave Power Conference*, G. Elliot and K. Diamantaras, Eds., Lisbon, Portugal, 1996, pp. 69–76.

[92] MATLAB, The MathWorks, Inc., Natick, Massachusetts, 2010, version 7.10.0 (R2010a).

[93] A. P. McCabe, "Constrained optimization of the shape of a wave energy collector by genetic algorithm," *Renewable Energy*, vol. 51, pp. 274–284, 2013.

[94] A. P. McCabe, G. A. Aggidis, and M. B. Widden, "Optimizing the shape of a surge-and-pitch wave energy collector using a genetic algorithm," *Renewable Energy*, vol. 35, no. 12, pp. 2767–2775, 2010.

[95] P. McIver and D. V. Evans, "The occurrence of negative added mass in free-surface problems involving submerged oscillating bodies," *Journal of Engineering Mathematics*, vol. 18, no. 1, pp. 7–22, 1984.

[96] M. Mueller and R. Wallace, "Enabling science and technology for marine renewable energy," *Energy Policy*, vol. 36, no. 12, pp. 4376–4382, 2008.

[97] MultiSurf, AeroHydro, Inc., Southwest Harbor, Maine, 2009, version 7.0.

[98] A. Naess and T. Moan, *Stochastic Dynamics of Marine Structures*. Cambridge University Press, 2012.

[99] A. J. Nebro, J. J. Durillo, F. Luna, B. Dorronsoro, and E. Alba, "A cellular genetic algorithm for multiobjective optimization," in *Proceedings of the Workshop on Nature Inspired Cooperative Strategies for Optimization (NICSO 2006)*, 2006, pp. 25–36.

[100] J. N. Newman, "The exciting forces on fixed bodies in waves," *Journal of Ship Research*, vol. 6, no. 3, pp. 10–17, 1962.

[101] ——, "The interaction of stationary vessels with regular waves," in *Eleventh Symposium on Naval Hydrodynamics*, London, 1976, pp. 491–501.

[102] ——, "Absorption of wave energy by elongated bodies," *Applied Ocean Research*, vol. 1, no. 4, pp. 189–196, 1979.

[103] ——, "Power from ocean waves," *Oceanus*, vol. 22, no. 4, pp. 39–45, 1979.

[104] ——, "Power from ocean waves," *Technology Review*, July 1983.

[105] G. Nolan, M. O'Catháin, J. Murtagh, and J. V. Ringwood, "Modelling, simulation and validation of the PTO system for a hinge-barge wave-energy converter," in *Proc. 5th European Wave Energy Conf.*, 2003, pp. 1–8.

[106] T. F. Ogilvie, "Recent progress toward the understanding and prediction of ship motions," in *Proceedings of the 5th Symposium on Naval Hydrodynamics*, Bergen, Norway, 1964, pp. 3–128.

[107] R. Paasch, K. Ruehl, J. Hovland, and S. Meicke, "Wave energy: A Pacific perspective," *Philosophical Transactions of the Royal Society A: Mathematical, Physical and Engineering Sciences*, vol. 370, no. 1959, pp. 481–501, 2012.

[108] H. M. Paynter, "An epistemic prehistory of bond graphs," in *Bond Graphs for Engineers*, P. C. Breedveld and G. Dauphin-Tanguy, Eds. Elsevier Science Publishers, 1992, pp. 3–17.

[109] M. C. Pease, *Methods of matrix algebra*. Academic Press, 1965.

[110] A. Pecher, J. P. Kofoed, and T. Larsen, "Design specifications for the Hanstholm WEPTOS wave energy converter," *Energies*, vol. 5, no. 4, pp. 1001–1017, 2012.

[111] T. Perez and T. I. Fossen, "Time- vs. frequency-domain identification of parametric radiation force models for marine structures at zero speed," *Modeling, Identification and Control*, vol. 29, no. 1, pp. 1–19, 2008.

[112] ——, "A Matlab toolbox for parametric identification of radiation-force models of ships and offshore structures," *Modeling, Identification and Control*, vol. 30, no. 1, pp. 1–15, 2009.

[113] ——, "Practical aspects of frequency-domain identification of dynamic models of marine structures from hydrodynamic data," *Ocean Engineering*, vol. 38, no. 2-3, pp. 426–435, 2011.

[114] A. A. E. Price, C. J. Dent, and A. R. Wallace, "On the capture width of wave energy converters," *Applied Ocean Research*, vol. 31, no. 4, pp. 251–259, 2009.

[115] P. Quarrel, Ed., *Proceedings of the Wave Energy Conference*, London-Heathrow, November 1978.

[116] R. C. T. Rainey, "Key features of wave energy," *Philosophical Transactions of the Royal Society A: Mathematical, Physical and Engineering Sciences*, vol. 370, no. 1959, pp. 425–438, 2012.

[117] P. Ricci, J.-B. Saulnier, A. F. d. O. Falcão, and M. T. Pontes, "Time-domain models and wave energy converters performance assessment," in *Proceedings of the 27th International Conference on Offshore Mechanics and Arctic Engineering*, Estoril, Portugal, 2008, pp. 1–10.

[118] J. Ringwood, "Practical challenges in harvesting wave energy," in *Proc. ECOR Symposium*, St. John's, Newfoundland, Canada, October 2008.

[119] D. Ross, *Power from the Waves*. Oxford University Press, 1995.

[120] S. H. Salter, "Wave power," *Nature*, vol. 249, pp. 720–724, 1974.

[121] ——, "World progress in wave energy - 1988," *International Journal of Ambient Energy*, vol. 10, no. 1, pp. 3–24, 1989.

[122] ——, "European wave energy symposium Edinburgh July 1993," in *Proceedings of the 2nd International Conference on Advances in Power System Control, Operation and Management*, vol. 1, Hong Kong, 1993, pp. 425–431.

[123] ——, "Research requirements for fourth generation wave energy devices," in *European Community, Results from the work of the European Thematic Network on Wave Energy (WaveNet)*, 2003, pp. 194–224.

[124] ——, "A personal view of renewable marine energy," in *Wave and Tidal Technologies Symposium*, Aberdeen, UK, 2005.

[125] ——, "Looking back," in *Ocean Wave Energy: Current Status and Future Perspectives*, J. Cruz, Ed.   Springer, 2008.

[126] S. H. Salter, J. R. M. Taylor, and N. J. Caldwell, "Power conversion mechanisms for wave energy," *Proc. IMechE Part M: J Engineering for the Maritime Environment*, vol. 216, pp. 1–27, 2002.

[127] G. Senior, "Recent wave energy developments in the United Kingdom," in *Proceedings of OCEANS '91. 'Ocean Technologies and Opportunities in the Pacific for the 90's'*, vol. 1, 1991, pp. 371 –374.

[128] R. Taghipour, T. Perez, and T. Moan, "Hybrid frequency-time domain models for dynamic response analysis of marine structures," *Ocean Engineering*, vol. 35, no. 7, pp. 685–705, 2008.

[129] M. J. Tucker, P. G. Challenor, and D. J. T. Carter, "Numerical simulation of a random sea: A common error and its effect upon wave group statistics," *Applied Ocean Research*, vol. 6, no. 2, pp. 118–122, 1984.

[130] L. Victor, P. Troch, and J. P. Kofoed, "On the effects of geometry control on the performance of overtopping wave energy converters," *Energies*, vol. 4, no. 10, pp. 1574–1600, 2011.

[131] WAMIT, WAMIT, Inc., Chestnut Hill, MA, 2008, version 6.4.

[132] ——, *USER MANUAL – WAMIT Version 7.0: List of Updates and Revisions*, WAMIT, Inc., Chestnut Hill, MA, 2012.

[133] T. Whittaker and M. Folley, "Optimisation of wave power devices towards economic wave power systems," in *World Renewable Energy Congress*, Aberdeen, UK, 2005.

[134] H. A. Wolgamot, P. H. Taylor, and R. E. Taylor, "The interaction factor and directionality in wave energy arrays," *Ocean Engineering*, vol. 47, pp. 65–73, 2012.

[135] L. Yang, "Stochastic dynamic system analysis of wave energy converter with hydraulic power take-off, with particular reference to wear damage analysis," Ph.D. dissertation, Department of Marine Technology, Norwegian University of Science and Technology, Trondheim, 2011.

[136] L. Yang, J. Hals, and T. Moan, "A wear model for assessing the reliability of wave energy converter in heave with hydraulic power take-off," in *Proceedings of the 8th European Wave and Tidal Energy Conference*, Uppsala, Sweden, 2009, pp. 874–881.

[137] Y. You, S. Sheng, B. Wu, and Y. He, "Wave energy technology in China," *Philosophical Transactions of the Royal Society A: Mathematical, Physical and Engineering Sciences*, vol. 370, no. 1959, pp. 472–480, 2012.

Paper A

Bond graph modelling of a wave energy conversion system with hydraulic power take-off

A. Kurniawan, E. Pedersen, and T. Moan
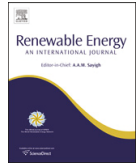
Bond graph modelling of a wave energy conversion system with hydraulic power take-off☆

Adi Kurniawan [a,*], Eilif Pedersen [b], Torgeir Moan [a]

[a] Centre for Ships and Ocean Structures, Trondheim, Norway
[b] Department of Marine Technology, Norwegian University of Science and Technology, Trondheim, Norway

ARTICLE INFO

ABSTRACT

A system viewpoint is essential in the study of wave energy converters, since several different energy domains are involved in such devices. In this regard, bond graph, a graphical, port-based approach to modelling engineering systems, serves as a useful tool. This article presents a study of a wave energy conversion system with hydraulic power take-off. With the aid of bond graph, two alternative hydraulic system designs are modelled by assembling hydraulic subsystems/components in different manners. A shallow-water pitching wave energy conversion system is considered as a case study, and selected simulation results using the two alternative hydraulic system designs are presented. In addition, this article suggests how to model by bond graph the dynamics of a multi-body wave energy conversion system.

© 2011 Elsevier Ltd. All rights reserved.

1. Introduction

Ocean wave is characterized by its high energy density, low-frequency oscillatory motions, and randomness. Thus, a wave energy conversion system (WECS) generally has to have some means for converting the low-frequency oscillatory motions into fast unidirectional motion, as well as some strategies to yield steady power output despite the random input, in order to produce some form of energy for practical use. A WECS typically consists of [1], (1) a primary interface, where hydrodynamic interactions with the surrounding waves take place, resulting in a relative motion, (2) a power take-off (PTO) mechanism, which could be some combination of mechanical, hydraulic, pneumatic, and electrical subsystems, (3) a mechanism for securing the primary interface at sea, such as mooring lines, (4) a control mechanism to maximize power capture, and (5) cable connection to electricity grid. It is natural for a WECS to have several conversion stages beginning in the mechanical translational/rotational domain and ending in electrical domain. Inside as well as outside the conversion chain, different energy domains interact with one another. Such complexities are apparent from recent reviews by Falnes [2], Drew et al. [3], and Falcão [4], for example.

Research on WECSs to date has generally been diverse, focusing on different parts or aspects of the system rather than the totality of the whole system. Granted, there is value in studying individual parts of the system in order to have accurate understanding of the constitutive behaviour of a single part. However, as the parts or subsystems in a WECS are intimately related, one should carefully note that if interactions between the different domains are taken into account, modelling assumptions that appear justifiable on one engineering domain may become a problem on the others. Having a good understanding of the whole system is therefore important if the fruitfulness of different wave energy conversion concepts is to be assessed, and when improvements are sought. In other words, a system viewpoint is essential in the study of WECSs. This has been identified as one crucial area to be addressed in wave energy research [3].

In this regard, bond graph, a graphical, port-based approach to modelling engineering systems, may serve as a useful tool [for a general introduction to bond graph, see, e.g., 5,6]. The first allusion to the bond graph method for modelling WECSs was perhaps in an article by Jefferys [7], although the term bond graph was not mentioned. However, not until recently did works using bond graph start to appear in wave energy literature [8–14]. Apart from being a graphical, port-based modelling approach, one virtue of bond graph lies in the fact that it is domain-independent; it uses common notations for elements and variables across various energy domains, hence capable of representing a complex system involving diverse energy domains, such as a WECS, in a unified manner. Also, due to the common notations, analogies between

☆ Poster presented at Renewable Energy Research Conference, Trondheim, 7–8 June 2010.
* Corresponding author.
E-mail addresses: adi.kurniawan@ntnu.no (A. Kurniawan), eilif.pedersen@ntnu.no (E. Pedersen), torgeir.moan@ntnu.no (T. Moan).

systems across energy domains are readily inferred, even if the components involved are physically different. This helps in providing insight into the behaviour of a WECS, and in assessing various wave energy conversion concepts. The same feature could also be useful in small-scale model testing of WECSs, where the dynamics of the PTO mechanism, controller, moorings, and connection to the electricity grid may not be realisable in small scale. Based on the bond graph representation, a simulator could be devised to mimic the expected dynamic behaviour in a laboratory setup. Another important virtue of bond graph is that derivation of model equations can be done in a systematic manner, allowing for automated computer simulation.

This article looks into a class of WECSs which utilize oscillating body (or bodies) as their working principle, and in particular, those with hydraulic PTO mechanism. This choice is motivated by the fact that a large number of WECSs belong into this class. Hydraulic PTO is thought to be suited for wave energy conversion in that it can capture power from slowly varying large forces which characterize ocean waves [15] and that it is highly controllable [16]. A bond graph model of the WECS is constructed by first considering the separate subsystems/components before assembling them together. This is illustrated in Section 2. Two alternative hydraulic system designs are studied, which result from assembling the subsystems/components differently. In passing, Section 2 also suggests how one can use bond graph to model the dynamics of a WECS consisting of a platform and several point absorbers. Finally, in Section 3, a shallow-water pitching WECS is considered where the primary interface resembles the Edinburgh duck [17]. Each of the two hydraulic PTO systems is connected to the primary interface and selected simulation results under irregular wave excitation are presented and discussed.

2. Bond graph model

In bond graph terms, a WECS essentially performs a power transformation from one energy domain to another, usually from mechanical translational/rotational domain to electrical domain. In bond graph notation this is simply

$$Sf \longmapsto TF \longmapsto R$$

where *Sf* is the source of mechanical translation/rotation, *R* is the load of the system, and *TF* the power transformation from mechanical to electrical domains. The power bonds (represented by half arrows) indicate the energy flow and signify flows in opposite directions of the power co-variables, namely effort and flow. The causal stroke (a vertical line at one end of the bond and perpendicular to it) indicates the direction of the effort signal. As an example, in the above, flow is the input to the *R* element while effort is the output. In reality, the *TF* is made up of a number of subsystems depending on the PTO mechanism and the conversion stages employed, and these should be modelled in detail.

Typical conversion stages in a WECS is illustrated in Fig. 1 [cf. 3,18]. As seen from the figure, several alternatives are available to convert energy from mechanical translational/rotational, hydraulic, or pneumatic domain to electrical domain. For an oscillating water column (OWC), energy is converted from pneumatic to electrical domains via an air turbine [cf. 7, Fig. 2] while for an overtopping WECS, energy is converted from hydraulic to electrical domains via a water turbine. For an oscillating-body WECS, direct conversion from mechanical translational/rotational to electrical domains can be achieved by means of a direct-drive electrical generator. The second alternative is to have a hydraulic piston convert energy from mechanical translational/rotational to hydraulic domains before converting it to mechanical rotational domain via a hydraulic motor. This article concentrates on the latter alternative.
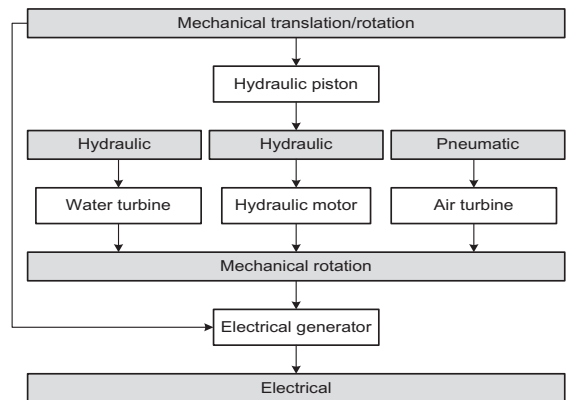

Fig. 1. Typical conversion stages in a wave energy conversion system. Shaded rectangles represent energy domains, while non-shaded rectangles represent primary components/subsystems.

An initial bond graph model of such hydraulic PTO, showing the primary conversion stages, is shown in Fig. 2. In the figure, the two *TF* elements represent the hydraulic piston and hydraulic motor, respectively, and the labels above and below the power bonds represent the effort-flow pair or the power co-variables in each energy domain. In mechanical translational domain, these are force (F) and velocity (v), in hydraulic domain, pressure (p) and volume flow rate (Q), while in mechanical rotational domain, these are torque (τ) and angular velocity (ω). The resemblance of the bond graph model to the chart in Fig. 1 is readily seen. Fig. 1 can in fact be conceived as a word bond graph for different classes of WECS.

Clearly, in a realistic model, energy losses in between successive conversion stages have to be accounted for. In a hydraulic system, these losses are mainly due to pressure drops along the pipes, leakages, and frictions. In bond graph, each of these is modelled by an *R* element, which serves to dissipate energy. These have to be added into the model. Apart from *Sf*, *TF*, and *R*, additional elements are also required in order to develop a bond graph model with sufficient details. In total, nine basic elements are generally sufficient to model any physical system. Each of these represents an elementary behaviour, viz. storage (*C* and *I* elements), reversible transformation (*TF* and *GY* elements), irreversible transformation (*R* element), supply and demand (*Se* and *Sf* elements), and distribution (0- and 1-junctions). They are introduced in the following.

2.1. Subsystems and components

The hydraulic PTO system in this study consists of the following subsystems and components [for a more detailed overview of hydraulic components, see e.g. 19].

2.1.1. Hydraulic piston

Energy from translational/rotational motion of the WEC primary interface is converted into hydraulic pressure by one or more

Fig. 2. An initial bond graph model of a hydraulic PTO, showing the major conversion stages.

hydraulic pistons. These pistons can be either single or double acting. A bond graph model of the single-acting piston is shown in Fig. 3. The model has two ports: the first port connects to a source, which in the case of a WEC could be a flow source representing the relative velocity of the primary interface, whereas the second port transfers the pressurized fluid to the next conversion stage or to pipes and valves.

It is seen that the model is built up using *TF, R, I, C* elements, as well as 0- and 1-junctions. The primary function of a hydraulic piston is to convert energy from mechanical translational domain to hydraulic domain. This is represented by the *TF* element, with the following constitutive relation:

$$F_p = A_p p_c \tag{1}$$

$$Q_c = A_p v_p, \tag{2}$$

where F_p is the force applied to the piston, A_p is the piston area, p_c is the chamber pressure relative to the initial chamber pressure, Q_c is the volume flow rate, and v_p is the velocity of the piston.

The *R* elements are used to represent energy losses due to damping and friction. The cylinder friction F_f can be modelled according to the static plus Coulomb plus viscous plus Stribeck model [20]:

$$F_f = F_n \left\{ \left[\mu_c + (\mu_{st} |\tanh(sv_p)| - \mu_c) \exp\left(-\frac{v_p^2}{v_{st}^2}\right) \right] \text{sgn}(v_p) + \mu_v v_p \right\}, \tag{3}$$

where F_n is the normal force, μ_c is the Coulomb friction coefficient, μ_{st} is the static friction coefficient, μ_v is the viscous friction coefficient, v_{st} is the characteristic Stribeck velocity, and s is the steepness of Coulomb friction curve. Also, since the stroke length of the piston is limited, a conditional damping model is used to represent energy loss whenever the piston collides with the cylinder heads. This is modelled as a linear damping with a large damping coefficient which is applied whenever the piston displacement exceeds the stroke limit. Similarly, the damping of the piston rod is modelled as a linear damping with a large damping coefficient.

Some of the force applied to the piston will accelerate the piston mass. This is represented as an *I* element. The mass of the piston relates its momentum and velocity.

The *C* elements are used to represent, firstly, the stiffness applied whenever the piston displacement exceeds the stroke limit, secondly, the stiffness of the piston rod, and thirdly, the compressibility of the fluid in the chamber. The latter is modelled by the following equation which relates the chamber pressure p_c and the change in chamber volume ΔV_c [21]:

Fig. 4. Bond graph model of a double-acting hydraulic piston.

$$p_c = B \frac{\Delta V_c}{V_{c0} - \Delta V_c}, \tag{4}$$

where B is the bulk modulus of the fluid and V_{c0} is the initial chamber volume.

A double-acting piston, as opposed to the single acting, has two flow outlets (represented by the two ports at the right hand side), and as such, has two *TF* elements in the bond graph model (see Fig. 4). Eqs. (1) and (2) are used for each *TF*, but it should be noted that the area of one side of the piston is not necessarily equal to the area of the other side, due to the presence of the piston rod. Also, compared to the single-acting piston (Fig. 3), an additional *C* element is needed to model fluid compressibility in the other chamber. An additional *R* element is used to model internal leakage across the cylinder chambers.

2.1.2. Pipes

Pipes transfer hydraulic fluid from one point to another. These can be thought of as transmission lines in the case of electrical systems. As the fluid flows along the pipes, energy is dissipated resulting in pressure drops. Pressure drops Δp_p along the pipes are modelled according to the following equation [22]:

Fig. 3. Bond graph model of a single-acting hydraulic piston.

Fig. 5. Bond graph model of a hydraulic motor.

Fig. 6. Hydraulic system design with a single-acting hydraulic piston and two check valves.

$$\Delta p_p = \frac{128 L \rho \nu Q}{\pi D^4}, \tag{5}$$

where L is the pipe length, ρ is the fluid density, ν is the kinematic viscosity of the fluid, Q is the volume flow rate, and D is the pipe diameter. This can be represented by an R element. Also, as the fluid in the pipe is accelerated, inertial force arises. The fluid inertance, which is modelled by an I element, is given as [22]

$$I = \frac{4 \rho L}{\pi D^2}. \tag{6}$$

2.1.3. Check valves

A check valve or no-flow valve resembles a diode in electrical systems. It allows flow in only one direction. Such behaviour can be modelled in bond graph using an R element with conditional equations which determine the flow Q_v through the valve depending on the pressure difference across it. One such model is given as follows [c.f. 21]:

$$Q_v = \begin{cases} \dfrac{\Delta p_v}{p_{cl}} Q_{cl} & \text{if } \Delta p_v < p_{cl} \\[2mm] Q_{cl} + \dfrac{\Delta p_v - p_{cl}}{p_{op} - p_{cl}} (Q_{op} - Q_{cl}) & \text{if } p_{cl} \leq \Delta p_v \leq p_{op} \\[2mm] C_d A_{max} \sqrt{\dfrac{2}{\rho} \Delta p_v} & \text{if } \Delta p_v > p_{op}, \end{cases} \tag{7}$$
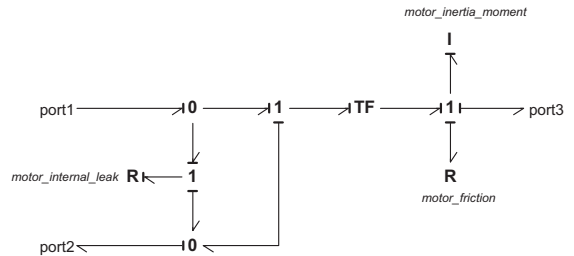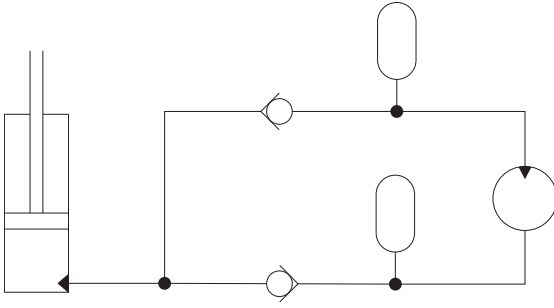
where

$$Q_{cl} = C_d A_{min} \sqrt{\frac{2}{\rho} p_{cl}} \tag{8}$$

$$Q_{op} = C_d A_{max} \sqrt{\frac{2}{\rho} p_{op}}. \tag{9}$$

In the above, C_d is the discharge coefficient, A_{min} is the leakage area, while A_{max} is the fully open flow area. The pressures p_{cl} and p_{op} are reference pressures for the closing and opening of the valve. The valve is closed if the pressure difference across the valve Δp_v is lower than p_{cl}, and is fully open if Δp_v is higher than p_{op}. The leakage area A_{min} is introduced to model leakage when the valve is closed.

2.1.4. Accumulators

An accumulator, which behaves as a capacitor in electrical systems, provides means for energy storage. It has the effect of smoothing out pressure and flow fluctuations in the system. A common type is the gas-charged accumulator, which uses a gas-filled bladder in a chamber. The expansion and compression of the gas follows the following relation [22]:

$$p_0 + \Delta p = p_0 \left(\frac{V_0}{V_0 - \Delta V} \right)^k, \tag{10}$$

where p_0 is the initial gas pressure and V_0 is the initial gas volume. The volume of fluid entering the accumulator is denoted by ΔV and the corresponding increase in pressure by Δp. The value of the specific heat ratio k depends on whether the expansion and compression occur rapidly or slowly. Such relation between pressure and volume can be modelled by a C element.

2.1.5. Hydraulic motor

A hydraulic motor transforms energy from hydraulic into mechanical rotational domains. A bond graph model of the hydraulic motor is shown in Fig. 5. The model has three ports: the first port represents the inflow into the motor, the second represents the outflow, and the third represents the connection to the next conversion stage, i.e. an electric generator. The transformation from hydraulic into mechanical rotational domains is carried out according to the following equation for the TF element [21]:

$$T = V_r p \tan \alpha \tag{11}$$

$$Q = V_r \omega \tan \alpha, \tag{12}$$

where T is the motor torque, V_r the motor displacement per radian, p the hydraulic pressure, α the inclination angle, Q the volume flow rate, and ω the motor rotational velocity. Internal leakage is included in the model using an R element in the same way as in the double-acting piston (c.f. Fig. 4). In addition, the inertia of the rotating part is modelled as an I element and friction is included using an R element.
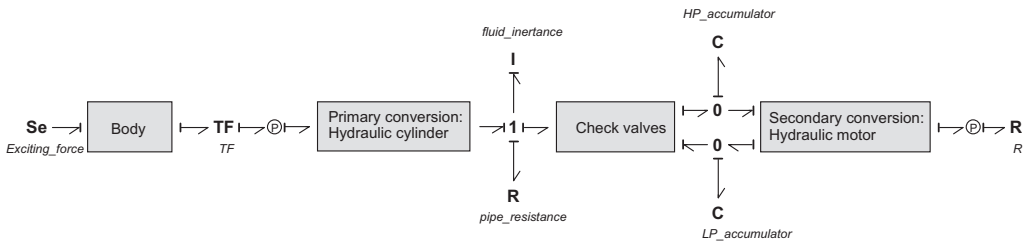

Fig. 7. Bond graph model of a WECS with hydraulic PTO using a single-acting hydraulic piston and two check valves.

Fig. 8. Bond graph model of a 2-check-valve system.

2.2. Assembled subsystems and components

The various subsystems/components having been described, one is now ready to assemble them together. One possible hydraulic PTO design for use in a WECS is shown in Fig. 6. This system has a single-acting hydraulic piston at one end, two check valves, two accumulators, and a hydraulic motor. Relative motion of the primary interface due to the waves drives the piston up and down. Referring to the figure, as the piston moves down, hydraulic fluid is forced to flow through the upper pipe into the high-pressure accumulator and through the hydraulic motor. As the piston moves up, the fluid flows through the lower pipe from the hydraulic motor and the low-pressure accumulator back into the cylinder. Throughout this cycle, the fluid always flows in one direction as it

drives the hydraulic motor. The motor in turn drives an electric generator, which applies load into the system.

A bond graph model of such system is shown in Fig. 7. One can see that the model resembles the schematic in Fig. 6 and that it is build up from the subsystems/components described previously. Here, the details of the hydraulic cylinder and the hydraulic motor are just as shown in Figs. 3 and 5. The detail of the 2-check-valve system is shown in Fig. 8. Due to the nature of the check valve, its causality has to be fixed. As a consequence, one has to introduce a C element connected to the 0-junction to avoid differential causality in the model. The electric generator is modelled using a linear R element.

As an illustration, an oscillating body has been included as a primary interface, constrained to move in one degree of freedom (DOF). A bond graph of the body consists of an I element representing its structural mass and added mass, a C element representing its hydrostatic restoring force, and an R element representing its hydrodynamic damping. The motion of the body drives the hydraulic piston. A TF element representing some transformation relation, such as between mechanical rotational and translational domain, connects the body and the hydraulic PTO. Exciting force from the waves is represented by Se element.

It is possible to assemble the subsystems/components differently. An alternative hydraulic PTO design utilizing a double-acting hydraulic piston and four check valves is described in Section 3.

2.3. Dynamics of a multi-body primary interface

In passing, we shall now suggest how to model the dynamics of the primary interface of a multi-body WECS and how to implement it in bond graph. Consider a particular WECS in the form of a floating platform with multiple buoys hanging underneath, such

Fig. 9. Bond graph model of a floating platform with multiple buoys.
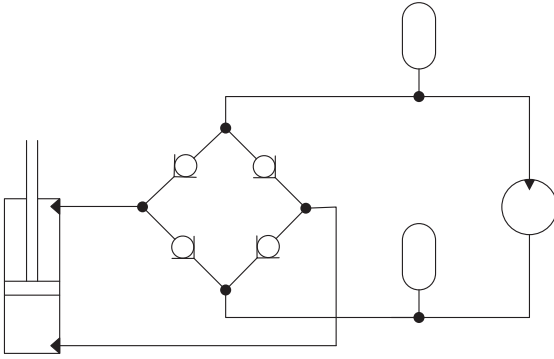
Fig. 10. Hydraulic system design with a double-acting hydraulic piston and four check valves.

as the concept studied in [10] and [23]. Each buoy is constrained to move only in vertical direction relative to the platform. This relative motion is in turn converted by a hydraulic PTO into electricity. A floating platform generally has 6 DOFs. Each buoy introduces one extra DOF to the system. For n buoys, there will be a total of n extra DOFs. Assuming that the motion of the platform is not affected by the motion of the buoys, Marré [10] modelled the platform as a flow source. In the following a more realistic bond graph model of the interaction between the platform and the buoys shall be developed.

Consider a floating rectangular platform in head sea. A right-handed coordinate system (x, y, z) lies on the mean water surface with x-axis pointing in the incident wave propagation direction and z-axis pointing upwards. For simplicity, the centre of gravity of the platform at rest is assumed to coincide with the origin of the coordinate system, and the incident wave is assumed to propagate in the direction normal to the side of the platform. Let the platform displacements along the x-, z-, and about the y-axes be $\eta_1(t)$, $\eta_3(t)$, and $\eta_5(t)$, respectively, the displacements of buoy i along the x-, z-, and about the y-axes be $\eta_{1i}(t)$, $\eta_{3i}(t)$, and $\eta_{5i}(t)$, respectively, the x-coordinate of buoy i be x_i, and the vertical displacement of buoy i relative to the platform be $r_i(t)$. Assuming small $\eta_5(t)$, the following relations hold:

$$\eta_{1i}(t) = \eta_1(t) + r_i(t)\eta_5(t) \tag{13}$$

$$\eta_{3i}(t) = \eta_3(t) - x_i\eta_5(t) + r_i(t) \tag{14}$$

$$\eta_{5i}(t) = \eta_5(t). \tag{15}$$

Taking time derivatives gives the following relations between the velocities:

$$\dot{\eta}_{1i}(t) = \dot{\eta}_1(t) + r_i(t)\dot{\eta}_5(t) + \dot{r}_i(t)\eta_5(t) \tag{16}$$

$$\dot{\eta}_{3i}(t) = \dot{\eta}_3(t) - x_i\dot{\eta}_5(t) + \dot{r}_i(t) \tag{17}$$

$$\dot{\eta}_{5i}(t) = \dot{\eta}_5(t). \tag{18}$$

Following [21], the equation of motions for the system can be expressed as

$$\frac{d}{dt}\left(\frac{\partial T}{\partial \dot{q}_j}\right) - \left(\frac{\partial T}{\partial q_j} - \frac{\partial V}{\partial q_j}\right) = E_j, \tag{19}$$

where q_j is the j-th generalized displacement, T and V are the kinetic and potential energy expressions as functions of the generalized displacements, and E_j the generalized forces for the j-th coordinate including forces which can be derived from dissipation terms. $\mathbf{q} = (\eta_1, \eta_3, \eta_5, r_i | i = 1, ..., n)^T$ is chosen as the generalized displacement vector. An alternative choice of generalized displacements was considered by Taghipour and Moan [23].

Without contributions from added masses, the kinetic energy T can be expressed in terms of the generalized displacements as

$$T = \frac{1}{2}\left[m_1\dot{\eta}_1^2 + m_3\dot{\eta}_3^2 + m_5\dot{\eta}_5^2 + \sum_{i=1}^{n}m_{1i}(\dot{\eta}_1 + r_i\dot{\eta}_5 + \dot{r}_i\eta_5)^2\right]$$
$$+ \frac{1}{2}\sum_{i=1}^{n}\left[m_{3i}(\dot{\eta}_3 - x_i\dot{\eta}_5 + \dot{r}_i)^2 + m_{5i}\dot{\eta}_5^2\right], \tag{20}$$

where m_1, m_3, and m_5 denote the platform inertias associated with η_1, η_3, and η_5, respectively, while m_{1i}, m_{3i}, and m_{5i} denote the inertias of buoy i associated with η_{1i}, η_{3i}, and η_{5i}. Considering only the hydrostatic restoring forces, the potential energy V can be expressed as

$$V = \frac{1}{2}\left(C_{33}\eta_3^2 + C_{55}\eta_5^2\right) + \frac{1}{2}\sum_{i=1}^{n}\left\{C_{33i}(\eta_3 - x_i\eta_5 + r_i)^2 + C_{55i}\eta_5^2\right\}, \tag{21}$$

where C_{33}, C_{55}, C_{33i}, and C_{55i} are the hydrostatic restoring coefficients. Taking the required derivatives and substituting into Eq. (19) yields a system of equations which can be implemented in bond graph using an IC field, a special bond graph element.

A bond graph model of the platform-buoy dynamics, where bonds for only one buoy have been drawn, is shown in Fig. 9. The IC field is shown on the top. The three 1-junctions on the upper left represent the platform velocities, while the three 1-junctions on the lower right represent the buoy velocities, all in the inertial coordinate system. The 1-junction on the upper right represents the buoy velocity relative to the platform, $\dot{r}_i$. External restoring forces such as from moorings have been included in the model

Fig. 11. Bond graph model of a WECS with hydraulic PTO using a double-acting hydraulic piston and four check valves.
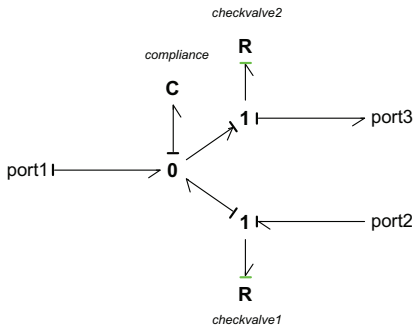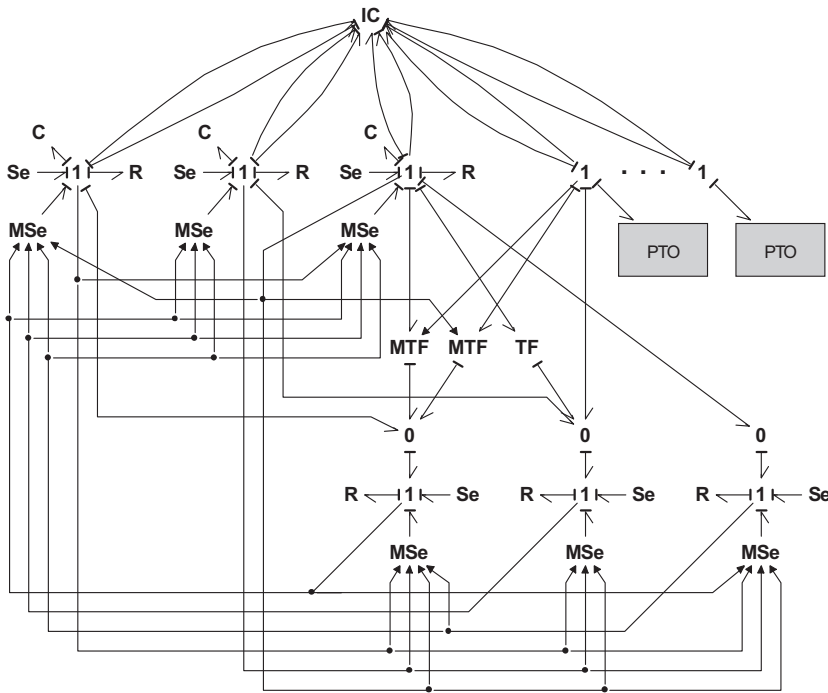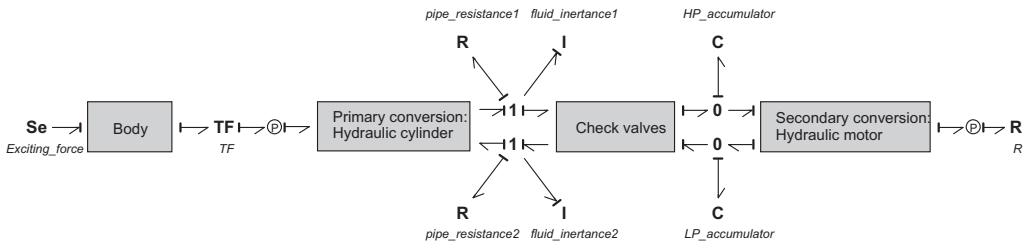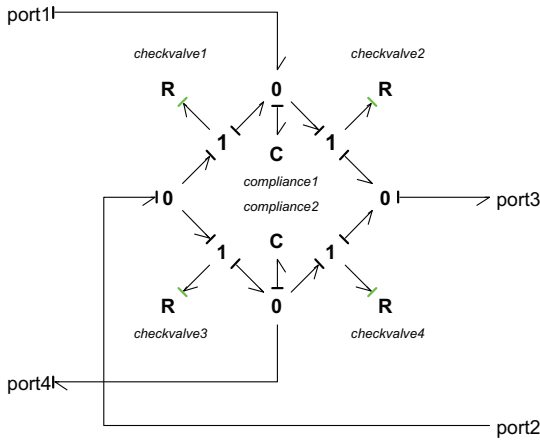
Fig. 12. Bond graph model of a 4-check-valve system.

using C elements, while external damping forces such as from viscous damping have been included using R elements. The wave exciting forces are effort sources, and therefore are represented by Se elements. The magnitudes of the wave radiation forces depend on the body velocities, and therefore are represented by MSe (modulated effort source) elements, which take the velocities of the bodies as input signals. Alternatively, the radiation forces can be decomposed into added mass and radiation damping forces, and included using I and R fields connected to the 1-junctions, respectively. The wave exciting and radiation forces on the buoy are given in the inertial coordinate system, and thus MTF and TF elements are needed to relate the velocities and forces in this coordinate system to those along r_i. The rectangle labelled PTO contains bond graph of the hydraulic system considered earlier.

Simulation of this multi-body dynamic model is not pursued in this article. Instead, in the next section we shall consider a shallow-water pitching WECS.

3. Simulations of a shallow-water pitching WECS with alternative hydraulic PTO systems

Alternative designs of hydraulic PTO can be conceived by assembling the various subsystems and components described in Section 2 in different manners. Two designs are considered here. The first, with a single-acting hydraulic piston and two check valves, is similar to that studied in [11,24], and has been described

above in Section 2.2. The second, with a double-acting hydraulic piston and four check valves, is similar to that studied in [12,13,25]. This second design resembles a full-wave rectifier in electrical systems (see Fig. 10). As the piston moves down, hydraulic fluid from the lower cylinder chamber is forced to flow into the high-pressure accumulator, through the hydraulic motor, into the low-pressure accumulator, and into the upper chamber of the cylinder. As the piston moves up, hydraulic fluid from the upper cylinder chamber is again forced to flow into the high-pressure accumulator, through the hydraulic motor, into the low-pressure accumulator, and into the lower chamber of the cylinder. Throughout the cycle, the fluid always flows in one direction as it drives the hydraulic motor. The motor in turn drives an electric generator, which applies load into the system. A bond graph representation of the system is shown in Fig. 11. At a glance, the system looks similar to the first design (see Fig. 7). The differences are in the details of the hydraulic cylinder and the check valve system, as well as the connection between the cylinder and the check valve system. The detail of the hydraulic cylinder is shown in Fig. 4 while the detail of the check valve system is shown in Fig. 12. In the following, the design with a single-acting hydraulic piston and two check valves is referred as the *2-valve system* and the design with a double-acting piston and four valves as the *4-valve system*.

Selected simulation results from the two alternative hydraulic PTO designs connected to a primary interface shall now be presented. Consider a shallow-water pitching WECS as shown in Fig. 13, where the primary interface resembles the Edinburgh Duck [17]. The cross section of the primary interface is formed by an arc of radius 5 m and two straight lines of equal length, each tangent to the arc. The width of the primary interface is 10 m and its draft is 7.5 m. A supporting structure constrains the primary interface to move only in pitch. The pitch motion under wave action activates the hydraulic piston, which drives the fluid flow in the hydraulic system. The device is set to operate in 10-m water depth. It can be shown that the wave energy transport J, defined as the transported wave power per unit width of the wave front, for plane progressive irregular wave in finite water depth is

$$J = \rho g \int_0^\infty S(\omega) v_g \mathrm{d}\omega, \tag{22}$$

where ρ is the water density, g is the acceleration of gravity, $S(\omega)$ is the (one-sided) wave spectrum, and v_g is the group velocity, which is a function of wave frequency ω and water depth h [c.f. 26, Eq. (29), where a two-sided spectrum was used instead of the more common one-sided one. The expression differs by a factor of 2]. The wave energy transport in 10-m water depth is plotted in Fig. 14,
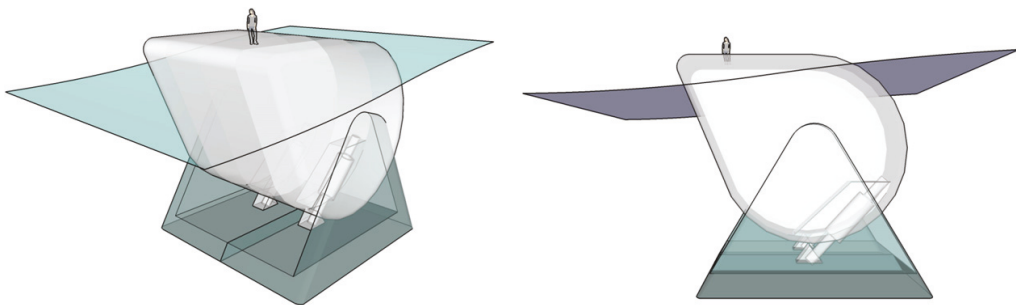

Fig. 13. Artist impression of the pitching WECS: isometric view (left) and side view (right).
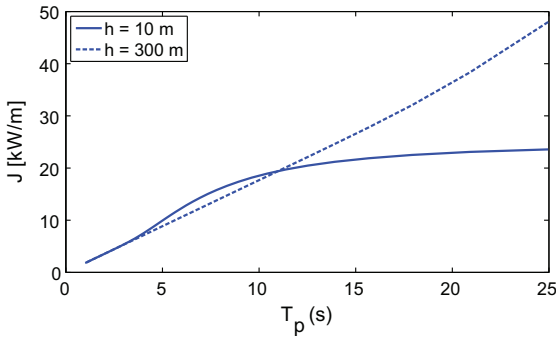
Fig. 14. Wave energy transport for irregular plane progressive waves according to JONSWAP spectrum with $H_s = 2$ m in shallow and deep waters.

Fig. 16. Bond graph model of the pitching WECS primary interface.

together with that in 300-m water depth. A JONSWAP spectrum with peakedness parameter of 3 and significant wave height $H_s = 2$ m is used as the wave spectrum model. It can be seen that, for the same H_s, the 10-m-water-depth wave transports more energy than the 300-m-water-depth wave in the range of spectral peak period $T_p \approx 3$ to 11 s. This constitutes one motivation for pursuing WECS development in shallow water.

Hydrodynamic parameters of the primary interface are computed using a higher-order panel method [27]. Wave diffraction due to the support structure is neglected and the water depth is assumed to be uniform. Referring to Fig. 13 (right), the incident wave is assumed to propagate from left to right.

In addition to tuning the linear generator load R, the possibility of tuning the inertia moment of the primary interface in order to maximise the energy capture is considered. This may be achieved in practice by transferring some mass in the primary interface along the radial direction. In the mathematical model, the same effect is obtained by allowing the radius of gyration r_{55} to be varied. Fig. 15 shows the pitch velocity amplitudes of the primary interface when it is not connected to the hydraulic system, for 1-m incident harmonic wave amplitude and for different realistic radii of gyration. The figure illustrates that depending on the frequency content of the incident wave, there is an optimum radius of gyration which maximises the energy capture.

A bond graph model of the primary interface is shown in Fig. 16. This constitutes the detail of the body in Figs. 7 and 11. A state-space model is used to approximate the radiation convolution term. The state-space model is represented by the element $ABCD$ in

Fig. 16. It takes the body velocity as input and outputs the corresponding radiation force. Identification of the state-space model is done in the frequency domain following the algorithm detailed in [28]. It has been shown that the model is highly efficient and accurate [see, e.g. 29]. The I element represents the sum of the structural inertia and the infinite-frequency added mass. The C element represents the hydrostatic restoring force.

Simulations are carried out using a modelling and simulation package [20]. The implicit Backward Euler method, which is suited

Fig. 15. Pitch velocity amplitudes of the primary interface without the hydraulic system for 1-m incident harmonic wave amplitude and for different radii of gyration.

Table 1
Parameters used in numerical simulations.

Parameter	Symbol	Value	Unit
Primary interface			
Displaced volume	Vol	681.374	m³
Infinite-frequency added mass	$m(\infty)$	9.8×10^5	kgm²
Hydrostatic restoring coefficient	S_b	2.4×10^7	Nm
Hydraulic piston			
Piston mass	m_p	8.0	kg
Piston diameter	D_p	0.3	m
Rod diameter	D_r	0.05	m
Coulomb friction coefficient	μ_c	0.04	–
Static friction coefficient	μ_{st}	0.04	–
Viscous friction coefficient	μ_v	5.0	m⁻¹s
Characteristic Stribeck velocity	v_{st}	0.002	ms⁻¹
Steepness of Coulomb friction curve	s	1000	m⁻¹s
Normal force	F_n	10	N
Bulk modulus of hydraulic fluid	B	1.6×10^9	Nm⁻²
Initial length of chamber 1	L_{c01}	3.0	m
Initial length of chamber 2	L_{c02}	3.0	m
Initial chamber pressure	p_{c0}	2.0×10^7	Nm⁻²
Pipes			
Pipe total length	L	2.0	m
Pipe diameter	D	0.03	m
Fluid density	ρ	865.0	kgm⁻³
Kinematic viscosity	ν	5.0×10^{-5}	m²s⁻¹
Check valves			
Discharge coefficient	C_d	0.9	–
Leakage area	A_{min}	1.0×10^{-8}	m²
Fully open area	A_{max}	2.0×10^{-3}	m²
Reference closed pressure	p_{cl}	1.0	Nm⁻²
Reference fully open pressure	p_{op}	8.0×10^4	Nm⁻²
High-pressure accumulator			
Initial gas pressure	p_{h0}	3.0×10^7	Nm⁻²
Initial gas volume	V_{h0}	9.0	m³
Specific heat ratio	k	1.4	–
Low-pressure accumulator			
Initial gas pressure	p_{l0}	1.0×10^7	Nm⁻²
Initial gas volume	V_{l0}	3.0	m³
Hydraulic motor			
Displacement per radian	V_r	0.3	m³
Inclination angle	α	30.0	deg
Inertia	m_m	10.0	kgm²
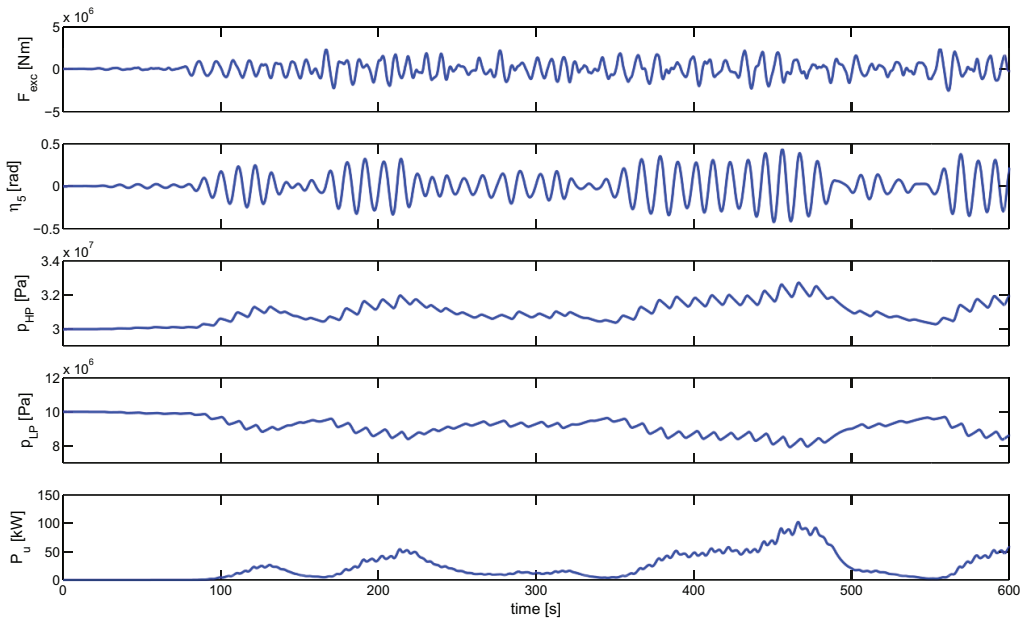
Fig. 17. Excitation force, primary interface displacement, high-pressure accumulator pressure, low-pressure accumulator pressure, and converted power of the pitching WECS with 2-valve system, for optimised set of linear generator load R and radius of gyration r_{55}, for $T_p = 11$ s and $H_s = 2$ m.

for stiff systems, is used as the numerical integration method, with a relative tolerance of 1.0×10^{-7}. Step sizes of 2×10^{-3} s and 1×10^{-3} s are used for the 2-valve and the 4-valve systems, respectively. The parameters used in the numerical simulations are listed in Table 1. The same set of parameters are used for the two

hydraulic PTO designs to show how the two systems behave under similar circumstances. The excitation force time series are generated before the simulation and stored as data files to be read during the simulation. The excitation force time series are generated following the method described in [29].
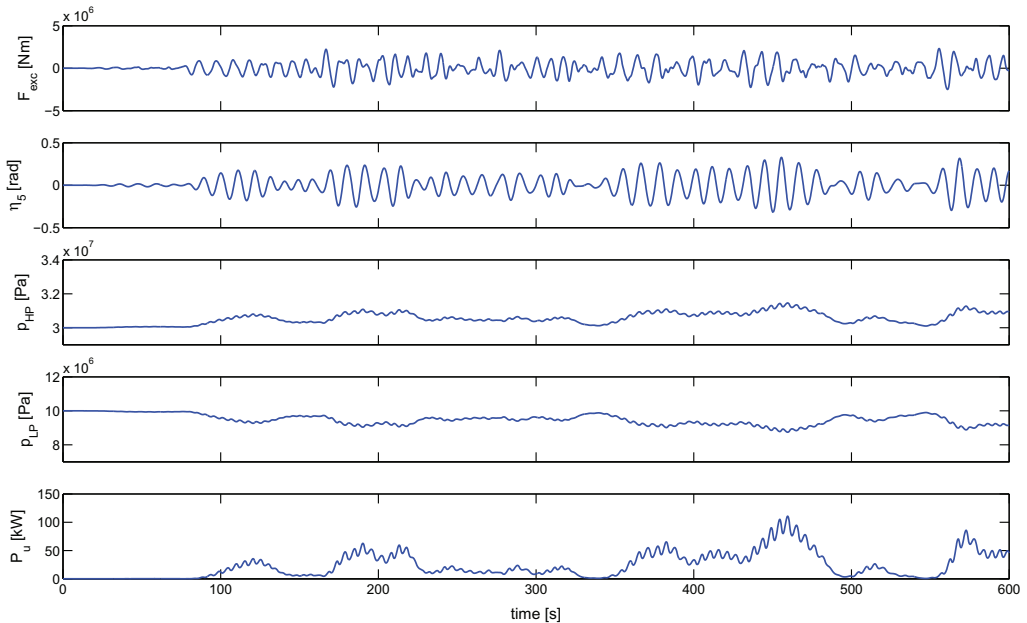
Fig. 18. As in Fig. 17, of the pitching WECS with 4-valve system.

Table 2
Optimised values of the linear generator load R and radius of gyration of the primary interface r_{55} together with the amount of converted energy E_u for the pitching WECS with 2-valve system.

T_p [s]	R_{opt} [Nms]	r_{55opt} [m]	E_u [kWh]
7	1464	6.0	5.1
9	1477	8.5	2.8
11	1414	10.2	4.0

Table 3
As in Tab. 2, for the pitching WECS with 4-valve system.

T_p [s]	R_{opt} [Nms]	r_{55opt} [m]	E_u [kWh]
7	484	5.9	4.9
9	509	8.2	2.8
11	516	10.1	3.9

Selected results from 600-s simulation of the pitching WECS are presented in Fig. 17 for the 2-valve system and in Fig. 18 for the 4-valve system. The wave parameters are $T_p = 11$ s and $H_s = 2$ m. The same wave realisation is used for both systems. The results are for optimised linear generator load R and radius of gyration of the primary interface r_{55} which give the largest amount of converted energy during the 600 s. These optimised values together with the amount of converted energy for $T_p = 7, 9$, and 11 s and $H_s = 2$ m are listed in Table 2 for the 2-valve system and in Table 3 for the 4-valve system. It should be noted that for a given case the amount of converted energy obtained using different wave realisations may differ, but they should converge for a sufficiently long simulation. The 600-s duration is not sufficiently long to give reliable estimates of the converted energy; it is selected for comparison purposes only.

From the close agreement between the optimum amount of converted energy obtained from the two systems (see Tables 2 and 3), the following is deduced. Given that the two systems have equal losses, the amount of optimum converted energy obtained by the two systems will be equal when the same optimising strategy is used even if the details of the two systems are different. In the present case, the parameters of the two systems have been set to give approximately the same amount of major losses. The lower amount of converted energy obtained by the 4-valve system is likely due to larger minor losses arising for instance from valve leakages. It is also interesting to note that while the optimum values of r_{55} are similar for the two systems, the optimum values of R are lower for the 4-valve system than those for the 2-valve system.

Referring again to Figs. 17 and 18, the distinct feature of the 4-valve system as opposed to the 2-valve system is noticeable from the plots of the accumulator pressures. For the 4-valve system there are two oscillations of the accumulator pressure for each oscillation of the primary interface, whereas for the 2-valve system there is one oscillation of the accumulator pressure for each oscillation of the primary interface. It is also apparent that pressure fluctuations are larger for the 2-valve system than those for the 4-valve system. The 4-valve system is probably the better option if minimising pressure fluctuations is one of the primary interests. Numerical experimentations also reveal that further smoothing of the converted power may be obtained by increasing the accumulator volumes and/or the motor inertia.

4. Conclusions

This article demonstrates the virtue of bond graph modelling as being graphical, modular, and domain-independent, by considering two alternative hydraulic PTO system designs obtained by first considering the subsystems/components separately and then

assembling them in different manners. The first design uses a single-acting hydraulic piston and two check valves. The second uses a double-acting hydraulic piston and four check valves. These hydraulic system models can then be connected to bond graph models of various primary interface designs (single-body or multi-body in terms of configuration, or heaving, pitching, etc. in terms of modes of motion) to form different models of wave energy conversion systems with hydraulic PTO.

Illustrative numerical results of the two hydraulic PTO designs have been presented for a shallow-water device where the primary interface resembles the Edinburgh Duck, constrained to move in pitch about a fixed axis. These results include the variations with time of body displacements, accumulator pressures, and converted power in irregular waves, for optimised generator load and radius of gyration of the primary interface. In addition, we have suggested how to model in terms of bond graph the dynamics of a platform and multiple buoys, each connected to a hydraulic PTO system.

It is our belief that in view of the multidisciplinary nature of wave energy research, bond graph could serve as a valuable tool in assessing the system behaviour of various wave energy conversion concepts. Furthermore, bond graph could be helpful in devising small-scale PTO simulators for the purpose of small-scale model testing.

References

[1] Salter SH, Taylor JRM, Caldwell NJ. Power conversion mechanisms for wave energy. Proc IMechE Part M: J Engineering for the Maritime Environment 2002;216:1–27.
[2] Falnes J. A review of wave-energy extraction. Marine Structures 2007;20:185–201.
[3] Drew S, Plummer AR, Sahinkaya MN. A review of wave energy converter technology. Proc IMechE Part A: J Power and Energy 2009;223:887–902.
[4] Falcão AFdO. Wave energy utilization: a review of the technologies. Renewable and Sustainable Energy Reviews 2010;14:899–918.
[5] Rosenberg RC. Reflections on engineering systems and bond graphs. Journal of Dynamic Systems, Measurement and Control, Transactions of the ASME 1993; 115(2 B):242–51.
[6] Breedveld PC. Port-based modeling of mechatronic systems. Mathematics and Computers in Simulation 2004;66:99–127.
[7] Jefferys ER. Simulation of wave power devices. Applied Ocean Research 1984; 6(1):31–9.
[8] Nolan G, O'Catháin M, Murtagh J, Ringwood JV. Modelling, simulation and validation of the PTO system for a hinge-barge wave-energy converter. In: Proc. 5th European Wave Energy Conf. 2003, 1–8.
[9] Nolan G, Ringwood JV. Design and control considerations for a wave energy converter. In: Proc. Irish Signals and Systems Conf. 2004, 1–6.
[10] Marré IR. Modelling and simulation of a wave energy converter using a bond graph approach. Master's thesis; Norwegian University of Science and Technology; 2006.
[11] Engja H, Hals J. Modelling and simulation of sea wave power conversion systems. In: Proceedings of the 7th European Wave and Tidal Energy Conference. Porto, Portugal; 2007, 1–7.
[12] Bacelli G, Gilloteaux, JC, Ringwood J. State space model of a hydraulic power take off unit for wave energy conversion employing bondgraphs. In: Proceedings of World Renewable Energy Conference. 2008, 1–4.
[13] Yang LM, Hals J, Moan, T. A wear model for assessing the reliability of wave energy converter in heave with hydraulic power take-off. In: Proceedings of the 8th European Wave and Tidal Energy Conference. Uppsala, Sweden; 2009, 874–881.
[14] Hals, J. Modelling and phase control of wave-energy converters. Ph.D. thesis; Department of Marine Technology, Norwegian University of Science and Technology; Trondheim; 2010.
[15] Taylor J. Power take-off systems: hydraulics. In: Cruz J, editor. Ocean wave energy: current status and future perspectives. Springer; 2008. p. 241–60.
[16] Plummer AR, Schlotter M. Investigating the performance of a hydraulic power take-off. In: Proceedings of the 8th European Wave and Tidal Energy Conference. Uppsala, Sweden; 2009, 729–735.
[17] Salter SH. Wave power. Nature 1974;249:720–4.
[18] Falnes J. Ocean wave energy: introductory lectures. URL http://folk.ntnu.no/falnes/teach/wave/TFY4300/index.html; 2009.

[19] Parr A. Hydraulics and pneumatics: a technician's and engineer's guide. Butterworth-Heinemann; 1999.

[20] Kleijn C. 20-sim 4.1 reference manual. URL http://www.20sim.com; 2009.

[21] Pedersen E, Engja H. Mathematical modelling and simulation of physical systems. Department of Marine Technology, Norwegian University of Science and Technology; 2008.

[22] Karnopp DC, Margolis DL, Rosenberg RC. System dynamics: modeling and simulation of mechatronic systems. 4 ed. John Wiley & Sons; 2006.

[23] Taghipour R, Moan T. Efficient frequency-domain analysis of dynamic response for the multi-body wave energy converter in multi-directional waves. In: Proceedings of the 18th International Offshore and Polar Engineering Conference. Vancouver, Canada; 2008, 357–365.

[24] Hals J, Taghipour R, Moan T. Dynamics of a force-compensated two-body wave energy converter in heave with hydraulic power take-off subject to phase control. In: Proceedings of the 7th European Wave and Tidal Energy Conference. Porto, Portugal; 2007, 1–10.

[25] Ricci P, Lopez J, Santos M, Villate JL, Ruiz-Minguela P, Salcedo F, et al. Control strategies for a simple point-absorber connected to a hydraulic power take-off. In: Proceedings of the 8th European Wave and Tidal Energy Conference. Uppsala, Sweden; 2009, 746–755.

[26] Falcão AFdO, Rodrigues RJA. Stochastic modelling of OWC wave power plant performance. Applied Ocean Research 2002;24:59–71.

[27] WAMIT. Version 6.4. Chestnut Hill, MA: WAMIT, Inc., URL http://www.wamit.com; 2008.

[28] Perez T, Fossen TIA. Matlab toolbox for parametric identification of radiation-force models of ships and offshore structures. Modeling, Identification and Control 2009;30(1):1–15.

[29] Kurniawan A, Hals J, Moan T. Assessment of time-domain models of wave energy conversion systems, in press.

Paper B

Modelling and simulation of a floating oscillating water column

A. Kurniawan, J. Hals, and T. Moan

Paper C

Assessment of time–domain models of wave energy conversion systems

A. Kurniawan, J. Hals, and T. Moan

Assessment of Time-Domain Models of Wave Energy Conversion Systems

Adi Kurniawan, Jørgen Hals, Torgeir Moan

Centre for Ships and Ocean Structures, Norwegian University of Science and Technology (NTNU)

NO-7491 Trondheim, Norway

E-mail: adi.kurniawan@ntnu.no, jorgen.hals@ntnu.no, torgeir.moan@ntnu.no

Abstract—**Time-domain models are necessary for the analysis of wave energy conversion systems, due to the presence of nonlinearities which may not be neglected for accurate prediction of their performance and behaviour. Such nonlinearities are contributed in varying degrees by drag, Coulomb friction, fluid compressibility, and also control mechanism. In time-domain, the equations of motion for the system will contain hydrodynamic radiation terms expressed as convolution integrals due to the frequency dependence of the radiation coefficients. The evaluation of the convolution integral is time-consuming and is difficult to carry out by standard adaptive solvers. Hence, various approximations to the convolution integral have been proposed to avoid these problems. The purpose of this study is to systematically assess the quality of some selected time-domain models. Generic models of wave energy conversion systems will be developed, with the possibility of varying the relative importance of the nonlinear terms. The time-domain models are categorised according to the convolution approximation and the numerical integration method used. Selected assessment criteria include computation time as well as the statistics of device motions and converted power. A model is always a trade-off between efficiency and accuracy. It is hoped that this study will provide some guidelines in the choice of time-domain models suitable for simulation of wave energy conversion systems.**

Index Terms—**wave energy, time-domain simulation, bond graph**

I. INTRODUCTION

The need for time-domain models for the simulation of wave energy conversion systems (WECSs) has been recognised as early as late 1970s [1]. Time-domain approach is necessary because WECSs contain substantial degree of nonlinearities, arising mainly from the power take-off system and control mechanism. The common way to formulate a time-domain model is to use integro-differential equations of motion which contain convolution integrals representing the wave radiation force [2], [3]. The convolution integral account for the system memory, signifying the fact that waves radiated by the body in the past continue to affect the body force for all subsequent times [4], [5]. The kernel of the integral is an impulse response function (IRF) also known as the retardation function, which is related to the frequency-dependent hydrodynamic radiation coefficients by Fourier transforms. When the system is nonlinear, this integral is necessary even when the incident waves are monochromatic, as shown in [4].

In time-domain simulations, evaluation of the convolution integral is known to be time-consuming and difficult to carry out with standard adaptive time-stepping solvers. The reason is

that one usually has to store discrete values of the IRF sampled at every simulation time step for the whole simulation time length, and one has to re-evaluate the convolution integral at every time step. It is obvious that for a multiple-degree-of-freedom system, which contains a number of these integrals, the computational effort can be tremendous. To avoid this difficulty, a set of coupled linear ordinary differential equations has been proposed as an approximate replacement for the convolution integral, first probably by Jefferys [1] in wave energy context. This so-called state-space representation is more efficient due to its Markovian property: at any instant, the value of the state summarises all the past system information [6]. The need to store a large amount of data and re-evaluate the integral at every time step is therefore eliminated.

Different approaches have been proposed in the literature to identify this state-space radiation force model, and have been summarized recently in [6]. Each of these approaches belongs to either time-domain or frequency-domain identification. In time-domain identification the state-space model is obtained from the corresponding radiation IRF, whereas in frequency-domain identification the state-space model is obtained from the corresponding radiation data in frequency domain.

To assess the quality of these state-space models, one may compare the steady-state responses of a linear system obtained from such models against those from a frequency-domain model. This was done by Jefferys [7], who compared the velocity and power obtained from a state-space model by frequency-domain identification with those from a frequency-domain model, over a range of wave periods. Taghipour et al. [8] compared the displacements from two state-space models, one by time-domain identification and the other by frequency-domain identification, with those from a frequency-domain model. Perez and Fossen [6] later made similar comparisons of the force-displacement frequency response functions (FRFs) obtained from the three models. One may also compare the transient responses obtained from the state-space models with those from a direct convolution integration (without convolution replacement). Considering a linear system, Taghipour et al. [8] compared the displacements in calm water after an initial displacement obtained from the two state-space models and from direct convolution integration. Also, considering a nonlinear system, Jefferys [7] compared the mean power and mean square velocity in a given sea state obtained from a state-space model by frequency-domain
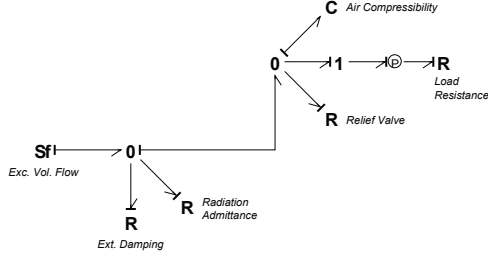
identification, with those obtained from direct convolution integration. Common to all these studies was the considerable saving of computation time resulting from the use of state-space model as opposed to direct convolution integration.

The purpose of this study is to complement those previous works by supplying a more systematic comparison of some selected time-domain models of WECSs. To achieve this purpose, generic models of WECSs are developed, with the possibility of varying the relative importance of their nonlinear terms. Hydrodynamic data are computed from some simple geometries. The time-domain models to be compared are categorised according to the convolution approximation and the numerical integration method used. For the state-space approximations, we will focus on state-space models obtained by frequency-domain identification, with different orders of approximation. Comparisons will be made of response in monochromatic waves and response in polychromatic waves. The assessment criteria include computation time, statistics of device motions, and statistics of converted power. A similar study with relevant discussions has been presented by Ricci et al. [9]. The main difference between our study and theirs is that we consider more generic models with variable nonlinear terms, to allow for a more systematic study of the various effects. Moreover, they considered time-domain identification whereas we consider frequency-domain identification for the state-space models.

II. GENERIC MODELS OF WAVE ENERGY CONVERSION SYSTEMS

We first develop generic models of a selection of WECSs in the bond graph framework [10]. These are thought to represent most wave energy conversion concepts available to date. For all these models, we assume a linear load resistance. Each model contains nonlinear terms. The effects of varying the degrees of nonlinearity of these nonlinear terms will be examined for each model.

A. Floating oscillating water column

We consider firstly a floating oscillating water column (OWC) wave energy device, restricted to move only in one degree of freedom. A bond graph model of such system is shown in Fig. 1, with the following main characteristics. The force balance on the OWC body is represented by the bonds connected to the 1-junction on the upper left. The volume flow balance in the OWC chamber is represented by the bonds connected to the 0-junction on the bottom left. The coupling between the body velocity and the chamber pressure is represented by the TF element connecting the 0-junction to the 1-junction. The TF element to the right of the first 1-junction carries out the transformation between force-velocity and pressure-volume flow. The 0-junction on the right connects 1- and 0-junctions on the left, signifying that the volume flow relative to the body is utilised for power absorption. The circle labelled P connected to the load resistance is a power sensor. The nonlinear terms in the model are the Coulomb and quadratic damping forces on the body, the volume flow

Fig. 1. Bond graph model of a floating oscillating water column wave energy device restricted to move only in one degree of freedom.

due to air compressibility in the chamber, and the volume flow through the relief valve. All other terms are assumed to be linear. The coupled equations of motion for this device in time domain can be written as

$$
\begin{aligned}
F_e(t) = {}& [m_m + m(\infty)]\dot{u}(t) + k(t) * u(t) - C(\infty)p(t) \\
& - h(t) * p(t) + (S_b + S)s(t) + R_C \operatorname{sgn} u(t) \\
& + R_q u(t)|u(t)| - rp(t)
\end{aligned} \tag{1}
$$

$$
\begin{aligned}
Q_e(t) = {}& y(t) * p(t) + C(\infty)u(t) + h(t) * u(t) \\
& + Q_v(t) + Q_c(t) + ru(t) + (R_e + 1/R_u)\,p(t),
\end{aligned} \tag{2}
$$

where $F_e(t)$ is the wave excitation force, m_m is the inertia of the body, $m(\infty)$ is the infinite-frequency added mass, $u(t)$ is the body velocity, $k(t)$ is the radiation IRF, $C(\infty)$ is the real part of the radiation coupling coefficient $H(\omega)$ at infinite frequency (see [11]), $h(t)$ is the radiation coupling IRF, $p(t)$ is the chamber pressure, S_b is the hydrostatic stiffness, S is the external stiffness, $s(t)$ is the body displacement, R_C is the Coulomb damping coefficient, R_q is the quadratic damping coefficient, r is some transformation factor, $Q_e(t)$ is the excitation volume flow, $y(t)$ is the radiation admittance IRF, $Q_v(t)$ is the volume flow through the relief valve, $Q_c(t)$ is the volume flow due to air compressibility, R_e is the external damping coefficient, and R_u is the load resistance.

The flow $Q_v(t)$ through the relief valve depends on the pressure difference across the valve:

$$
Q_v(t) = \begin{cases}
\dfrac{p(t)}{p_{cl}}Q_{cl} & \text{if } |p(t)| < p_{cl} \\[2ex]
\operatorname{sgn} p(t)\left[Q_{cl} + \dfrac{|p(t)| - p_{cl}}{p_{op} - p_{cl}}(Q_{op} - Q_{cl})\right] \\[1ex]
\hspace{3em} \text{if } p_{cl} \leq |p(t)| \leq p_{op} \\[2ex]
C_d A_{\max}\sqrt{\dfrac{2}{\rho_a}|p(t)|}\,\operatorname{sgn} p(t) & \text{if } |p(t)| > p_{op},
\end{cases} \tag{3}
$$

Fig. 2.   Bond graph model of a fixed oscillating water column wave energy device.

Fig. 3.   Bond graph model of an oscillating single-body wave energy device restricted to move only in one degree of freedom.

where

$$Q_{cl} = C_d A_{\min} \sqrt{\frac{2}{\rho_a} p_{cl}} \qquad (4)$$

$$Q_{op} = C_d A_{\max} \sqrt{\frac{2}{\rho_a} p_{op}}. \qquad (5)$$

In the above, C_d is the discharge coefficient, ρ_a is the air density, $A_{\min}$ is the leakage area, while $A_{\max}$ is the fully open flow area. The pressures p_{cl} and p_{op} are reference pressures for the closing and opening of the valve. The valve is closed if $|p| < p_{cl}$, and is fully open if $|p| > p_{op}$. To be realistic, the leakage area $A_{\min}$ is introduced to allow possible leakage when the valve is closed.

The air compressibility in the chamber can be modelled according to this nonlinear relationship:

$$p_0 + p = p_0 \left(\frac{V_0}{V_0 - \Delta V}\right)^\gamma, \qquad (6)$$

where p_0 is the atmospheric pressure and V_0 is the average air volume in the chamber. The volume change due to compressibility is denoted by $\Delta V = \int_0^t Q_c(t)\mathrm{d}t$. The specific heat ratio γ depends on whether the expansion and compression occur rapidly or slowly. The value $\gamma = 1.4$ is usually adopted.

B. Fixed oscillating water column

The second device we consider is a fixed OWC. A bond graph of this type of device is shown in Fig. 2. We have intentionally maintained the layout of the bond graph for the floating OWC in Fig. 1 to show that the bond graph for a fixed OWC is a subset of the former. Since there is no coupling with the body motions, the bond graph structure representing the body dynamics is removed. The nonlinear terms in the model are the volume flow due to air compressibility and the volume flow through the relief valve. The equation of motion for this device can be written as

$$Q_e(t) = y(t)*p(t) + Q_v(t) + Q_c(t) + (R_e + 1/R_u)\, p(t), \quad (7)$$

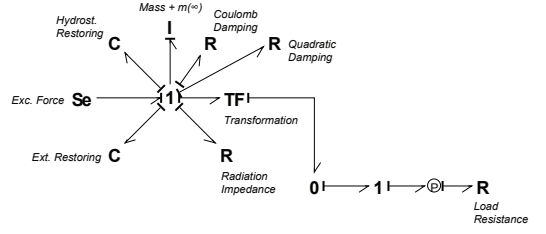using the same notations as for the floating OWC (Section II-A).

C. Oscillating single body

Lastly, we consider an oscillating single-body wave energy device, restricted to move only in one degree of freedom. A bond graph of this type of device is shown in Fig. 3. Again, we have shown that the bond graph for an oscillating single-body wave energy device is a subset of that for the floating OWC. The TF element in the model is some transformation from one energy domain to another. The nonlinear terms in the model are the Coulomb and quadratic damping forces. The equation of motion for this device can be written as

$$F_e(t) = [m_m + m(\infty)]\dot{u}(t) + k(t)*u(t) + (S_b + S)s(t) \\ + R_C \operatorname{sgn} u(t) + R_q u(t)|u(t)| + r R_u u(t). \tag{8}$$

III. Computation of hydrodynamic parameters

A. Body geometries

For the fixed and floating OWC device we consider a vertical square cylinder with a square moonpool in the centre. The cylinder is 10 m by 10 m, the moonpool is 5 m by 5 m, and the draft is 5 m. For the floating OWC, the cylinder is restricted to move only in heave. The incident wave is assumed to propagate in the direction normal to any of the cylinder side walls.

For the oscillating single-body device we consider a geometry similar to the Edinburgh duck [12]. It is a horizontal cylindrical body with a cross section formed by a combination of a semicircle and a right triangle meeting at 30 degree angle. The body is free to move only in rotation about the axis passing through the centre of the arc. The arc centre is located 1.5 m below the water line and the arc radius is 3 m, making a draft of 4.5 m, while its length (measured along the rotation axis) is 8 m. The incident wave is assumed to propagate in the direction perpendicular to the rotation axis.

Three-dimensional views of the submerged body geometries are shown in Fig. 4.

B. Computation in frequency domain

The computation of the frequency-domain hydrodynamic parameters is carried out using a three-dimensional higher-order panel method [13]. For all computations, infinite water
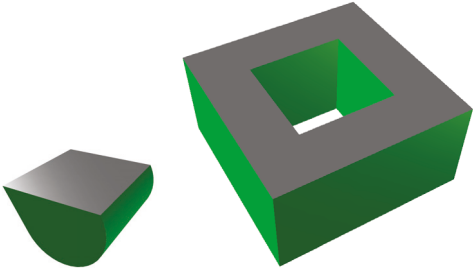
Fig. 4. Three-dimensional views of the submerged body geometries of the oscillating single-body device (left) and the OWC device (right).

depth is assumed. Computations are performed for wave frequencies from 0 to 6 rad/s, in interval of 0.05 rad/s, and also for the infinite-frequency limit. As the wave frequency increases, greater number of panels is required for convergence, and the computational burden at the same time increases. A panel subdivision is chosen which gives converged results up to a certain cut-off frequency. Beyond the cut-off frequency, the computed hydrodynamic parameters start to fluctuate around the correct values. For accurate evaluation of the radiation impulse response function (to be discussed in the next section), there is a need to have hydrodynamic data for high frequencies. For this purpose, the values for wave frequencies above the cut-off frequency are approximated by extrapolation using a fitting function fitted to the tail of the data. Given the fact that fitting is done in the least-squares sense, although values computed beyond the cut-off frequency for the chosen panel subdivision are inaccurate, but since they fluctuate around the correct values, they are useful for the fitting. Several fitting functions are tested, and exponential function in the form of $a\exp(b\omega)+c\exp(d\omega)$ is found to yield the best fit. Fig. 5 shows the added mass and radiation damping of the oscillating body. Fig. 6 shows the added mass, radiation damping, and the parameters $G(\omega) = \Re\{Y(\omega)\}$, $B(\omega) = \Im\{Y(\omega)\}$, $C(\omega) = \Re\{H(\omega)\}$, and $J(\omega) = \Im\{H(\omega)\}$ of the OWC. Definitions of the parameters G, B, C, J and the procedures to derive them are given in [14]. However, instead of using relation (11) in [14], here we use the following relation to derive $B(\omega)$:

$$B(\omega) = -\int_0^\infty y(t)\sin(\omega t)\mathrm{d}t, \qquad (9)$$

where

$$y(t) = \frac{2}{\pi}\int_0^\infty G(\omega)\cos(\omega t)\mathrm{d}\omega. \qquad (10)$$

Also, $C(\omega)$ is obtained as follows:

$$C(\omega) = C(\infty) + \int_0^\infty h(t)\cos(\omega t)\mathrm{d}t, \qquad (11)$$

where

$$h(t) = -\frac{2}{\pi}\int_0^\infty J(\omega)\sin(\omega t)\mathrm{d}\omega. \qquad (12)$$
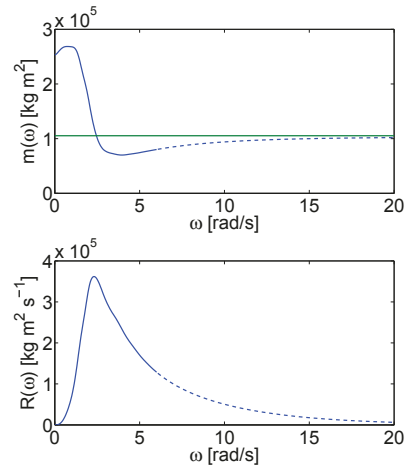

Fig. 5. Added mass (top) and radiation damping (bottom) of the oscillating body in pitch. The dashed lines are the extrapolated data. The horizontal line in the added mass plot is the infinite-frequency added mass.

Here any integration over the interior free surface is approximated by a sum over 100 field points with uniform spacings on the interior free surface. Any integration from $\beta = 0$ to 2π, where β is the incident wave propagation angle, is approximated by a sum over a discrete set of incident wave propagation angles with uniform interval of 5 degrees.

C. Impulse response functions

For direct convolution integration, which is described in Section IV-A, it is essential to have an accurate IRF for each mode of motion. The IRFs can be evaluated directly by solving the time-domain boundary value problem or indirectly from the frequency-domain data. Here we will discuss the latter option since softwares which solve the boundary value problem in time domain are less widely known than those which solve the problem in frequency domain.

For an oscillating body, the radiation IRF for a given degree of freedom can be obtained from the corresponding frequency-domain data as follows (see, e.g. [15]):

$$k(t) = \frac{2}{\pi}\int_0^\infty R(\omega)\cos(\omega t)\mathrm{d}\omega, \qquad (13)$$

where $R(\omega)$ is the radiation damping, or, alternatively,

$$k(t) = -\frac{2}{\pi}\int_0^\infty \omega[m(\omega) - m(\infty)]\sin(\omega t)\mathrm{d}\omega, \qquad (14)$$

where $m(\omega)$ is the added mass. For an OWC, the radiation admittance IRF $y(t)$ and the radiation coupling IRF $h(t)$ can be obtained similarly (see (10) and (12)).

For most body geometries, the hydrodynamic data are not available in analytical forms, and are normally evaluated by a numerical panel method. The integration in (13) or (14) then has to be evaluated numerically over a finite frequency range. This presents a challenge for accurate evaluation of IRF
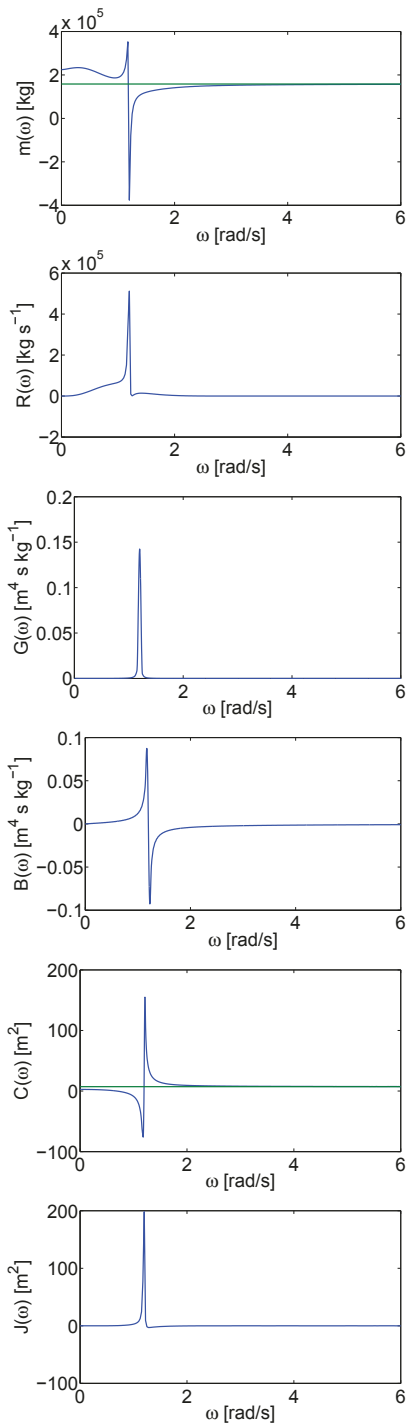
Fig. 6. Top to bottom: added mass, radiation damping, and parameters G, B, C, J of the OWC. Horizontal lines are infinite-frequency values.

from frequency-domain data. The necessity of a high enough upper truncation limit of integration has been highlighted by several authors [5]–[7], [16], [17]. Low truncation frequency is known to result in inaccuracies in the evaluated IRF. To obtain hydrodynamic data at high frequencies by panel methods, however, would require very small panels, which is not practical. High-frequency values should be obtained by other means. One way to do this is by extrapolation using a fitting function to fit the tail of the data. We use this approach in our study, where an exponential function is used for the fitting. Trapezoidal integration method is used to evaluate the integral, where finer frequency resolution is obtained by interpolation.

The radiation IRF of the oscillating body evaluated using (13), the radiation admittance IRF $y(t)$ of the OWC, and the radiation coupling IRF $h(t)$ of the floating OWC are shown in Fig. 7. In contrast to the radiation IRF of the oscillating body, the radiation IRFs of the OWC decay very slowly due to the narrow bandwidth of the corresponding frequency-domain parameters. This behaviour has been reported, e.g. in [18]. Fig. 8 shows comparisons of the convolution terms $k(t) * u(t)$ of the oscillating body, $k(t) * u(t)$, $y(t) * p(t)$, and $h(t) * u(t)$ of the OWC with their respective frequency-domain equivalents for given $u(t)$ and $p(t)$. The very good agreement verifies the accuracy of our method. Improved agreement may be obtained by using finer frequency resolution for the computation of the hydrodynamic parameters.

IV. TIME-DOMAIN MODELS

We compare three categories of time-domain models, namely the direct convolution integration model, the constant hydrodynamic parameter model, and the state-space model.

A. Direct convolution integration

In the direct convolution integration model the convolution terms in the equations of motion are not replaced by any approximations and are integrated directly at each time step. This requires, firstly, precomputation of the IRF values at specified time intervals, where linear interpolation is used if the simulation time step is shorter, and, secondly, storage of past response (velocity and/or pressure). With accurate IRFs and sufficiently small simulation time step, a direct convolution integration model should give accurate simulation results despite the considerable computational burden involved.

B. Constant hydrodynamic coefficients

In the constant hydrodynamic coefficient model the frequency-dependent coefficients are replaced by constant coefficients, whose values are taken to be those at the wave spectral peak frequency ω_p.

The equation of motion for the oscillating single body then becomes

$$
\begin{aligned}
F_e(t) = &[m_m + m(\omega_p)]\dot{u}(t) + R(\omega_p)u(t) \\
&+ (S_b + S)s(t) + R_C \operatorname{sgn} u(t) + R_q u(t)|u(t)| \\
&+ rR_u u(t),
\end{aligned} \tag{15}
$$
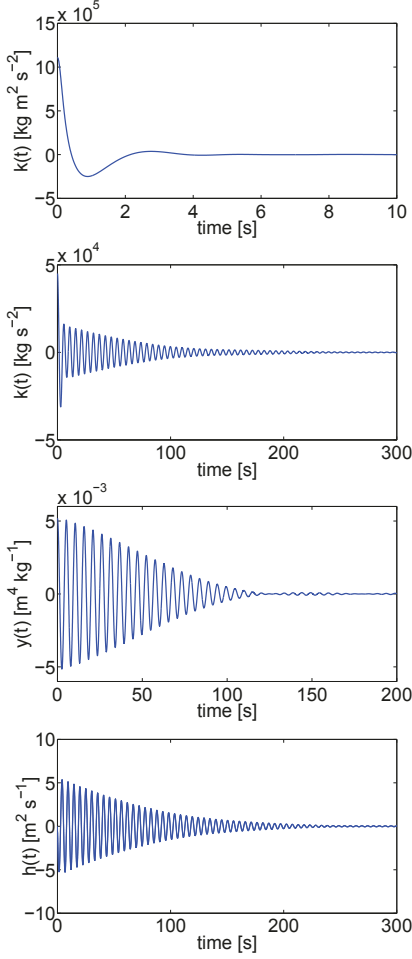
Fig. 7. Top to bottom: radiation IRF of the oscillating body, and radiation IRF, radiation admittance IRF, and radiation coupling IRF of the OWC.
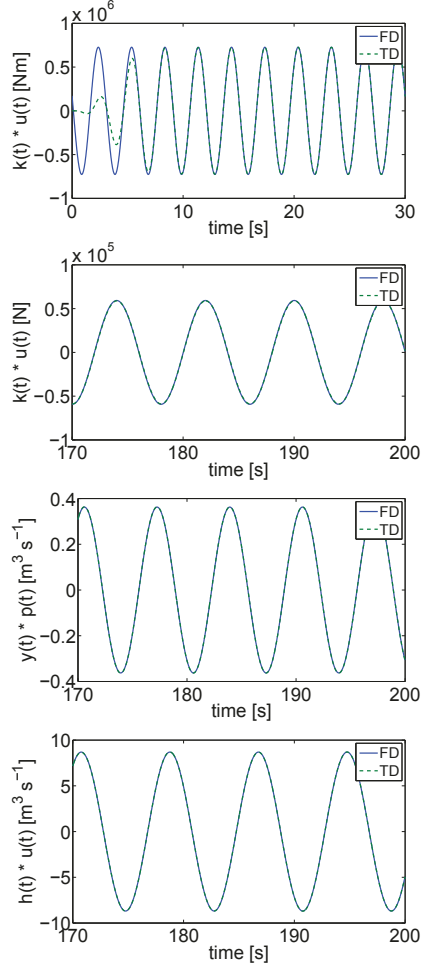

Fig. 8. Top to bottom: frequency domain (FD) and time domain (TD) comparison of $k(t) * u(t)$ of the oscillating body, $k(t) * u(t)$, $y(t) * p(t)$, and $h(t) * u(t)$ of the OWC. For the OWC, the early, transient, parts have been removed for clarity.

the equation of motion for the fixed OWC becomes

$$Q_e(t) = G(\omega_p)p(t) + B'(\omega_p) \int_0^t p(t)\mathrm{d}t \\ + Q_v(t) + Q_c(t) + (R_e + 1/R_u)\,p(t), \quad (16)$$

and the equations of motion for the floating OWC become

$$F_e(t) = [m_m + m(\omega_p)]\dot{u}(t) + R(\omega_p)u(t) \\ - C(\omega_p)p(t) - J'(\omega_p)\dot{p}(t) + (S_b + S)s(t) \\ + R_C\,\mathrm{sgn}\,u(t) + R_q u(t)|u(t)| - rp(t) \quad (17)$$

$$Q_e(t) = G(\omega_p)p(t) + B'(\omega_p) \int_0^t p(t)\mathrm{d}t \\ + C(\omega_p)u(t) + J'(\omega_p)\dot{u}(t) + Q_v(t) + Q_c(t) \\ + ru(t) + (R_e + 1/R_u)\,p(t). \quad (18)$$

In the above, $J' = J/\omega$ and $B' = -\omega B$.

C. State-space representation

In the state-space model the convolution term

$$\mu(t) = k(t) * u(t) = \int_0^t k(t - \tau)u(\tau)\mathrm{d}\tau \quad (19)$$

is replaced by a set of coupled linear ordinary differential equations, which may be expressed in matrix form (see, e.g. [19]):

$$\dot{\mathbf{x}}(t) = \hat{\mathbf{A}}\mathbf{x}(t) + \hat{\mathbf{B}}u(t) \quad (20)$$

$$\hat{\mu}(t) = \hat{\mathbf{C}}\mathbf{x}(t) \quad (21)$$

where $\mathbf{x}(t)$ is the state vector, the number of components of which corresponds to the *order* of the state-space model,

and $\hat{\mathbf{A}}$, $\hat{\mathbf{B}}$, $\hat{\mathbf{C}}$ are constant matrices. We use the frequency-domain identification approach following the algorithm detailed in [19], [20]. As mentioned earlier, the method uses frequency-domain hydrodynamic data for identification. The approach is to fit a rational transfer function

$$\hat{K}(s) = \frac{P(s)}{Q(s)} = \frac{p_r s^r + p_{r-1} s^{r-1} + \ldots + p_0}{s^n + q_{n-1} s^{n-1} + \ldots + q_0}, \quad (22)$$

where $s = i\omega$, to the FRF $K(\omega)$, $Y(\omega)$, or $H(\omega)$ depending on the problem considered. Further constraints on the model have been derived in [6] based on the properties of the FRF and its corresponding IRF. A least-squares fitting method is applied to find the coefficients p_i and q_i, and once the coefficients p_i and q_i are obtained, the matrices $\hat{\mathbf{A}}$, $\hat{\mathbf{B}}$, and $\hat{\mathbf{C}}$ can be constructed using any of the standard canonical forms. We will examine the use of different model orders, starting from a minimum order of 2.

V. SIMULATION

A. Excitation force and excitation volume flow

Comparisons will be made of the different models under both monochromatic wave and polychromatic wave excitations. The excitation force and/or excitation volume flow time series are generated before the simulation and stored as data files to be read during the simulation. The generation of excitation force and/or excitation volume flow time series in monochromatic waves is straightforward. For polychromatic waves, the method is described as follows.

First, we obtain the spectral density of the excitation force (likewise for the excitation volume flow):

$$S_{F_e}(\omega) = |f_e(\omega)|^2 S(\omega), \quad (23)$$

where $f_e(\omega)$ is the computed complex excitation force for a unit incident wave and $S(\omega)$ is the given wave spectrum. We use a JONSWAP spectrum with peakedness parameter of 3 in our simulations. The excitation force is then given as

$$\begin{aligned} F_e(t) = &\sum_{n=0}^{N/2} (a_n \cos\phi_n + b_n \sin\phi_n) \cos\omega_n t \\ &+ \sum_{n=0}^{N/2} (-a_n \sin\phi_n + b_n \cos\phi_n) \sin\omega_n t, \end{aligned} \quad (24)$$

where a_n and b_n are generated from a Gaussian distribution with variance $S_{F_e}(\omega_n)\Delta\omega$ [21]. Here, N is the number of values in the time series, determined by the required length of the series T and the time interval between values Δt. Also, $\omega_n = n\Delta\omega$, where $\Delta\omega = 2\pi/T$. In addition, ϕ_n is the phase (in radians) of $f_e(\omega_n)$. Values of ω_n may be larger than the largest frequency for which f_e is computed. Modulus and phase of f_e for these frequencies may therefore be extrapolated separately using fitting functions as in the extrapolation of added mass and radiation damping data. For the modulus, an exponential function in the form of $a\exp(b\omega) + c\exp(d\omega)$ is used, while for the phase, a power function in the form of $a\omega^b$ is used. The necessity of having accurate f_e values beyond 6

rad/s, however, is of lower importance in this case because typical wave spectra have negligible values beyond 6 rad/s. Thus, it may be practical to even assume zero values for f_e beyond 6 rad/s.

The sum in Eqn. (24) may be identically evaluated by an inverse Fast Fourier Transform at a fraction of computer time. This is implemented in our simulation. The initial part of the resulting time series is filtered by a cosine taper window so as to avoid exciting any lightly damped modes in the system.

B. Integration methods

For the direct convolution integration model, simulations are carried out with fixed time step. We compare different time integration methods and examine the effect of different time steps on accuracy and efficiency. The methods compared are the Euler's method (ode1), the improved Euler's (Heun's) method (ode2), Runge-Kutta 3 (ode3), and Runge-Kutta 4 (ode4) methods. Simulations for the direct convolution integration model are carried out using a computing package [22].

For the constant coefficient and the state-space models, an adaptive Runge-Kutta-Fehlberg solver is used for the oscillating body device, while an adaptive Vode Adams solver is used for the OWC device. Whenever the adaptive methods are not successful, the fixed step solvers are used. Both the absolute and relative integration error tolerances are set to 1×10^{-7}. Simulations for the constant coefficient and state-space models are carried out using a modelling and simulation package [23].

All simulations are run in a 2.53 GHz, 2.96 GB RAM CPU.

C. Treatment of Coulomb damping

In the simulations, Coulomb damping force is modelled as follows:

$$F_C(t_i) = \begin{cases} \dfrac{R_C}{u_C} u(t_i) & \text{if } -u_C < u(t_i) < u_C \\ R_C \operatorname{sgn} u(t_i) & \text{otherwise} \end{cases}, \quad (25)$$

where u_C is a small velocity threshold. We choose $u_C = 4 \times 10^{-4}$ rad/s for the oscillating body and $u_C = 4 \times 10^{-4}$ m/s for the floating OWC.

VI. RESULTS AND DISCUSSIONS

For each device, we compare responses obtained from the different time-domain models under monochromatic and polychromatic wave excitations. We compare both the case where all nonlinear terms are set to zero and the case where the nonlinear terms are varied. For the former, responses are compared to those from the frequency-domain model, and we measure the error (in %) which is defined as

$$e_{FD} = 100 \frac{|\hat{u} - u_{FD}|}{|u_{FD}|}, \quad (26)$$

where $\hat{u}$ is the complex body velocity obtained from state-space or direct convolution model and u_{FD} is the complex body velocity obtained from frequency-domain model.

For the latter, the assessed response is compared to the 'true' response, and we assess the error (in %) which is defined as

$$e = \frac{100}{N} \sum_{i=1}^{N} \frac{|\hat{q}(t_i) - q(t_i)|}{|\max q(t_i)|}, \qquad (27)$$

where $\hat{q}(t_i)$ and $q(t_i)$ are the instantaneous assessed response and the 'true' response, respectively, at time i. The response $q(t)$ can be the converted power, the body velocity for the oscillating body device, or the chamber pressure for OWC devices. The 'true' response is defined as the converged response obtained from direct convolution integration using sufficiently small simulation time step. When nonlinear terms are zero, expression (27) is approximately equivalent to (26).

For comparisons in polychromatic waves, in addition to comparing instantaneous values of power, velocity, and/or pressure, we also compare the maximum and mean values of converted power, as well as the root mean square velocity and/or pressure.

A. Oscillating single body

Fig. 9 compares the body velocity obtained from state-space and frequency-domain models of the oscillating single-body device when the external stiffness S is set to 100 Nm, the transformation factor r is set to 1, the load resistance R_u is set to 6×10^5 kg m^2 s^{-1}, and the nonlinear terms are set to zero. The wave amplitude is 1 m. Four different state-space model orders are compared: 2, 3, 4, and 7. From the figures we see that increasing model order improves the model accuracy for the range of wave frequencies considered. For this particular case, however, a model order even as low as 3 keeps the error within 2% and increasing the model order up to 7 does not improve the accuracy significantly. It should be noted that the error for a given model order is dependent on the specified tolerance in the adaptive solver. The purpose of the comparison is to give an indication of how the different model orders perform relative to one another.

Fig. 10 compares the performance of different time integration methods in the direct convolution integration model of the oscillating single-body device for the same set of parameters. The top figure compares the time step required for each time-integration method to keep the error defined in (26) within 2%. Our assumption is that the error increases with time step length. The bottom figure compares the computation time (averaged from three runs) required for 200-second simulation using the time steps of the top figure. In general, shorter time steps are required for smaller wave periods to keep the same degree of accuracy. The Euler's (ode1) method requires much longer computation time than that of the other methods for smaller wave periods. The performance of the improved Euler's (Heun's) method (ode2), Runge-Kutta 3 (ode3), and Runge-Kutta 4 (ode4) methods are comparable, with ode4 being the best performing method for smaller wave periods and ode3 for larger wave periods.

To give an idea of how a state-space model compares with the direct convolution integration model in terms of efficiency,
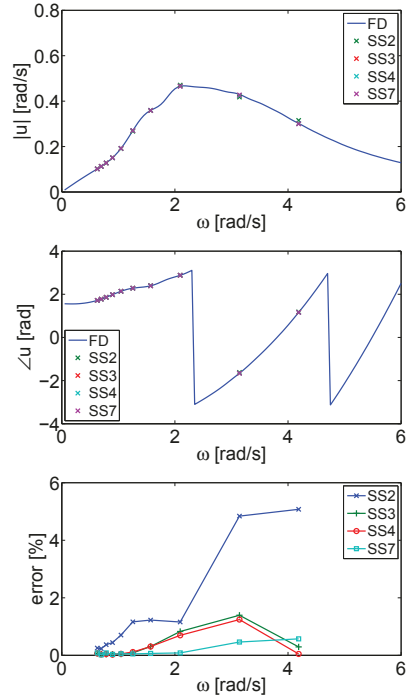

Fig. 9. Comparison of state-space (SS) models of different orders against frequency domain (FD) model of the oscillating body for $R_u = 6 \times 10^5$ kg m^2 s^{-1}: velocity amplitude (top), velocity phase (middle), and error (bottom).
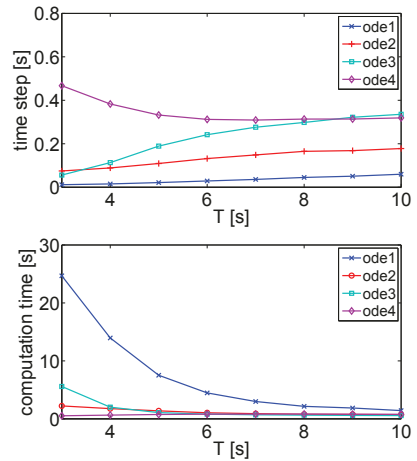

Fig. 10. Comparison of time integration methods in the direct convolution integration model of the oscillating body for $R_u = 6 \times 10^5$ kg m^2 s^{-1}: time step (top) and computation time (bottom) required for 2% error.
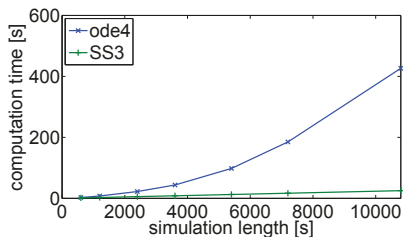
Fig. 11. Comparison of third order state-space model (SS3) and direct convolution integration model using a Runge-Kutta 4 (ode4) solver for the oscillating body for $R_u = 6 \times 10^5$ kg m^2 s^{-1}.

we perform simulations of both models—still with nonlinear terms set to zero—using the same fixed step solver (Runge-Kutta 4) with the same time step and implemented in the same computing package [22]. An order of 3 is used for the state-space model. The result is shown in Fig. 11. We see that the computation time for the state-space model varies linearly with the simulation length, while for the direct convolution integration model it varies as a quadratic function of the simulation length. A simple explanation to this is the fact that for a direct convolution integration model the number of computations to be performed at every time step corresponds to the simulation length or the number of time steps up to that time. This means that the number of computations to be performed at every time step grows as an arithmetic progression. The total computation time then is proportional to the sum of this series. On the other hand, for a state-space model the number of computations to be performed at every time step is constant so that the total computation time is just proportional to the number of time steps or the simulation length.

Now we consider cases where nonlinearities are introduced. We first present results from monochromatic wave excitations, and then from polychromatic wave excitations. For the monochromatic case, we consider a wave period T of 8 s. The load resistance R_u is set to 5×10^4 kg m^2 s^{-1}. The simulation length is 100 s. For the oscillating body, the nonlinear terms we have included in the model are the Coulomb and quadratic damping forces. Table I compares the error in velocity and power (according to (27)) from the direct convolution integration model with different time integration methods (ode2, ode3, and ode4), for different values of Coulomb damping, while the quadratic damping R_q is set to zero. We see that the larger the Coulomb damping, the larger is the error for a given integration method and time step. This implies that the introduction of Coulomb damping carries with it a requirement for shorter time step to achieve the same degree of accuracy. Also, all the three integration methods exhibit similar order of accuracy, with ode4 generally being the most accurate, followed by ode3 and ode2. It should be noted however that for the same time step, ode4 requires a longer computation time than the other two methods. For instance, for the same time step of 0.01 s, we note that ode4 requires approximately

TABLE I
VELOCITY (POWER) ERROR IN % FOR THE DIRECT CONVOLUTION INTEGRATION MODEL OF THE OSCILLATING SINGLE-BODY DEVICE. $T = 8$ s, $R_u = 5 \times 10^4$ KG M^2 S^{-1}, $R_q = 0$

		R_C [kg m^2 s^{-1}]		
	time step [s]	2×10^4	8×10^4	15×10^4
ode2	0.01	0.06 (0.07)	0.27 (0.09)	0.68 (0.16)
	0.05	0.38 (0.35)	1.92 (0.99)	3.99 (1.32)
	0.1	0.95 (0.87)	2.89 (0.67)	8.15 (3.15)
ode3	0.01	0.06 (0.08)	0.25 (0.18)	0.45 (0.19)
	0.05	0.38 (0.40)	1.28 (0.65)	2.97 (1.23)
	0.1	0.80 (0.77)	1.93 (0.87)	7.14 (3.86)
ode4	0.01	0.04 (0.06)	0.19 (0.09)	0.40 (0.12)
	0.05	0.26 (0.28)	1.00 (0.35)	2.91 (1.17)
	0.1	0.60 (0.53)	2.12 (0.96)	5.80 (2.39)

35 s to complete a 100-second simulation length, while ode3 requires approximately 25 s and ode2 requires only 17 s.

With state-space model, simulation using adaptive time step solvers can be done with ease. The performance of state-space and constant-coefficient models simulated with adaptive time step solver (see Section V-B above) for the same set of parameters is summarized in Table II. For the state-space models, increasing the model order improves the accuracy of the solutions although the lowest model order of 2 already gives very good accuracy. The low percentage of errors also confirms the excellent agreement between state-space and direct convolution integration models when Coulomb damping is introduced. Moreover, we note the following: (1) longer computation time is required for larger Coulomb damping to meet the same error tolerance, (2) increasing the model order improves the accuracy and has little effect on the computation time, and (3) overall, the required computation time is much less than that required by the direct convolution models to achieve similar degree of accuracy.

The constant-coefficient model, on the other hand, requires the least computation time—although still comparable to that of the state-space model—but has larger errors. And this is so even for monochromatic wave excitation considered here, as already pointed out in [4]. With larger Coulomb damping, however, the error reduces. This may be surprising at first, but it can be explained by the fact that as other forces begin to dominate, the radiation force becomes relatively less important so that a constant-coefficient model of the radiation force provides an acceptable approximation [24].

The effect of quadratic damping, as it turns out, is not as significant as that of Coulomb damping, as shown in Table III, where now $R_C = 0$. For the direct convolution integration models we use a time step of 0.1 s as this is comparable with the state-space and constant coefficient models in terms of computation time. Compared to the previous case of increasing Coulomb damping, increasing quadratic damping does not introduce significantly larger errors. Also, the errors for the

	R_C [kg m^2 s^{-1}]		
	2×10^4	8×10^4	15×10^4
SS2	0.48 (0.47)	0.34 (0.26)	0.22 (0.18)
SS3	0.10 (0.12)	0.20 (0.19)	0.14 (0.13)
SS4	0.08 (0.11)	0.19 (0.19)	0.14 (0.13)
SS7	0.03 (0.04)	0.03 (0.04)	0.03 (0.04)
constant coeffs.	19.04 (22.68)	10.72 (11.80)	6.52 (7.88)

	R_q [kg m^2]		
	2×10^4	15×10^4	5×10^5
ode2 $\Delta t = 0.1$ s	0.58 (0.57)	0.58 (0.57)	0.59 (0.58)
ode3 $\Delta t = 0.1$ s	0.11 (0.11)	0.11 (0.11)	0.11 (0.12)
ode4 $\Delta t = 0.1$ s	0.14 (0.17)	0.15 (0.18)	0.16 (0.20)
SS3	0.03 (0.03)	0.03 (0.03)	0.03 (0.03)
constant coeffs.	0.27 (0.29)	1.07 (1.34)	2.31 (3.04)

constant-coefficient model are shown to be small.

We shall now move on to polychromatic wave excitations. We consider two spectral peak periods $T_p = 5$ and 8 s, and significant wave height $H_s = 2$ m. The simulation length is 100 s. The load resistance R_u is set to 5×10^4 kg m^2 s^{-1}. The result is shown in Table IV. Two combinations of R_C and R_q are considered. We compare the velocity and power errors calculated according to (27), as well as the errors in mean power, maximum power, and root mean square velocity. These are listed in sequence in the table. For the direct convolution integration model, a time step of 0.1 s is used for all the fixed step solvers (ode 2 to 4). From the table we see that among the fixed step solvers, ode4 is generally the most accurate for the same time step, followed by ode2 and ode3. It is worth noting that this is somewhat different from the monochromatic case, with ode2 generally being the least accurate. As in the monochromatic case, the state-space model proves to be superior both in terms of accuracy and efficiency. The performance of constant-coefficient model is significantly poorer than the other models. For cases with higher load resistance (not shown here), however, the constant-coefficient model has smaller errors for the reason given previously.

B. Fixed oscillating water column

For the fixed OWC, the nonlinear terms we have included are the terms associated with air compressibility and relief valve charateristics. For brevity, we only present comparisons for polychromatic case, with $T_p = 5$ and 8 s, and significant wave height $H_s = 2$ m. We set $R_u = 0.9$ kg m^{-4} s^{-1} and $R_e = 1$ m^4 s kg^{-1}. The result is shown in Table V. Two combinations of parameters p_{cl}, p_{op}, and V_0 are considered, as shown in the table. We compare the pressure and power errors calculated from (27), and also the errors in mean power, maximum power, and root mean square pressure.

The fixed OWC model exhibits stiff dynamics arising mainly from the air compressibility relationship (6). Thus, for the direct convolution integration model, very small time step is necessary to achieve stability of the numerical solution. Even smaller time step is required for the second combination of p_{cl}, p_{op}, and V_0 as the response exhibits Coulomb-type nonlinearity due to the operation of the relief valve. For this reason we do not investigate the effects of step size for the direct convolution integration model. It may be possible to use more sophisticated implicit fixed step solvers more suited for stiff problems, but this is beyond the scope of this study.

From the table we see that the state-space models give very good results. Nearly perfect accuracy is obtained by a model order of 4, whereas a model order of 2 already gives excellent accuracy. The constant-coefficient model is shown to have relatively good performance, probably because the radiation admittance has small values relative to $1/R_u$ and R_e. We may expect poorer accuracy for larger R_u and smaller R_e.

C. Floating oscillating water column

When the floating OWC is considered, four convolution terms are present (see (1) and (2)). Thus we expect the computational burden to be multiplied. For the state-space model, different orders are used for the various convolution terms. We consider two set of model orders, one with model orders of 4, 2, and 3 for the radiation, radiation admittance, and radiation coupling terms, respectively, and the other with model orders of 6, 4, and 5. We call the former SSlow and the latter SShigh. In addition, all four nonlinear terms are present, namely the Coulomb and quadratic damping terms, as well as the terms related to air compressibility and relief valve operation. As in the fixed OWC, we only consider the polychromatic case, with $T_p = 5$ and 8 s, and significant wave height $H_s = 2$ m. We set $R_u = 0.9$ kg m^{-4} s^{-1}, $R_e = 1$ m^4 s kg^{-1}, $p_{cl} = 40$ Pa, $p_{op} = 41$ Pa, $V_0 = 500$ m^3, $R_C = 3 \times 10^5$ kg m^2 s^{-1}, and $R_q = 8 \times 10^3$ kg m^2. Thus, we only vary the spectral peak period T_p. We compare the velocity, pressure, and power errors calculated from (27), and also the errors in mean power, maximum power, root mean square velocity, and root mean square pressure. Table VI summarizes the result.

As in the fixed OWC, the floating OWC model also exhibits stiff dynamics. Therefore we do not investigate the effects of step size for the direct convolution integration model. Similar to the fixed OWC case, the state-space models give very good results, with the higher-order model giving better accuracy than the lower-order one. The constant-coefficient model performs poorer than the state-space models, but the errors are seen to be acceptable. This is again dependent on the relative magnitude of the radiation terms compared to the other terms.

TABLE IV

ERRORS (IN %) IN VELOCITY, POWER, MEAN POWER, MAXIMUM POWER, AND ROOT MEAN SQUARE VELOCITY FOR THE OSCILLATING SINGLE-BODY DEVICE. $R_u = 5 \times 10^4$ KG M^2 S^{-1}, $H_s = 2$ M

| | $R_C = 15 \times 10^4$ kg m^2 s^{-1}, $R_q = 0$ | | $R_C = 0$, $R_q = 5 \times 10^5$ kg m^2 | |
	$T_p = 5$ s	$T_p = 8$ s	$T_p = 5$ s	$T_p = 8$ s
ode2	2.16, 0.57, 0.98, 1.63, 0.45	4.09, 0.76, 1.28, 4.19, 0.60	0.95, 0.56, 1.31, 0.14, 0.70	0.91, 0.45, 1.53, 0.78, 0.81
ode3	1.92, 0.67, 5.90, 0.71, 2.95	3.56, 0.93, 7.73, 17.06, 3.90	0.92, 0.58, 2.62, 2.86, 1.27	0.88, 0.45, 2.45, 2.47, 1.18
ode4	1.53, 0.48, 3.65, 2.41, 1.80	3.03, 0.58, 2.28, 0.90, 1.10	0.61, 0.35, 0.45, 0.91, 0.18	0.60, 0.29, 0.36, 0.63, 0.13
SS3	0.12, 0.07, 0.05, 0.51, 0.00	0.06, 0.03, 0.26, 0.03, 0.11	0.20, 0.13, 0.05, 0.64, 0.01	0.18, 0.09, 0.28, 0.41, 0.12
SS7	0.03, 0.02, 0.05, 0.25, 0.00	0.02, 0.01, 0.01, 0.15, 0.03	0.04, 0.03, 0.09, 0.03, 0.03	0.04, 0.02, 0.07, 0.09, 0.02
cc	5.41, 2.89, 13.78, 3.90, 6.65	4.59, 2.24, 36.12, 9.5, 16.64	11.57, 7.58, 33.83, 25.81, 15.66	18.37, 11.60, 98.88, 42.03, 40.99

TABLE V

ERRORS (IN %) IN PRESSURE, POWER, MEAN POWER, MAXIMUM POWER, AND ROOT MEAN SQUARE PRESSURE FOR THE FIXED OWC DEVICE. $R_u = 0.9$ KG M^{-4} S^{-1}, $R_e = 1$ M^4 S KG^{-1}, $H_s = 2$ M

| | $p_{cl} = 40$ Pa, $p_{op} = 41$ Pa, $V_0 = 150$ m^3 | | $p_{cl} = 20$ Pa, $p_{op} = 21$ Pa, $V_0 = 500$ m^3 | |
	$T_p = 5$ s	$T_p = 8$ s	$T_p = 5$ s	$T_p = 8$ s
SS2	0.08, 0.05, 0.24, 0.23, 0.12	0.04, 0.03, 0.02, 0.14, 0.01	0.06, 0.05, 0.04, 0.02, 0.02	0.03, 0.03, 0.08, 0.01, 0.04
SS4	0.01, 0.00, 0.00, 0.00, 0.00	0.01, 0.00, 0.00, 0.00, 0.00	0.01, 0.00, 0.00, 0.00, 0.00	0.01, 0.00, 0.00, 0.00, 0.00
cc	1.01, 0.68, 3.91, 3.89, 1.94	0.98, 1.01, 5.74, 3.36, 2.83	0.99, 0.86, 3.04, 0.38, 1.51	0.75, 0.79, 3.12, 0.31, 1.55

TABLE VI

ERRORS (IN %) IN VELOCITY, PRESSURE, POWER, MEAN POWER, MAXIMUM POWER, ROOT MEAN SQUARE VELOCITY, AND ROOT MEAN SQUARE PRESSURE FOR THE FLOATING OWC DEVICE. $R_u = 0.9$ KG M^{-4} S^{-1}, $R_e = 1$ M^4 S KG^{-1}, $p_{cl} = 40$ PA, $p_{op} = 41$ PA, $V_0 = 500$ M^3, $R_C = 3 \times 10^5$ KG M^2 S^{-1}, $R_q = 8 \times 10^3$ KG M^2, $H_s = 2$ M

	$T_p = 5$ s	$T_p = 8$ s
SSlow	0.03, 0.03, 0.03, 0.18, 0.01, 0.01, 0.09	0.02, 0.09, 0.09, 0.40, 1.83, 0.30, 0.20
SShigh	0.00, 0.00, 0.00, 0.01, 0.00, 0.00, 0.01	0.01, 0.03, 0.03, 0.19, 0.68, 0.15, 0.10
cc	0.58, 0.64, 0.48, 1.42, 0.16, 0.96, 0.71	0.55, 1.11, 1.02, 3.20, 2.07, 6.82, 1.55

VII. CONCLUSIONS

Different time-domain models according to their convolution approximations have been compared. The direct convolution integration model numerically integrates the convolution without any approximations. The simulation error is largely controlled by the simulation time step used. The state-space model approximates the convolution term by a set of coupled linear ordinary differential equations. The state-space model can be simulated using an adaptive solver with ease, and the simulation error is largely controlled by the model order corresponding to the number of extra state variables introduced. The constant-coefficient model replaces the frequency-dependent hydrodynamic parameters by constants assuming the values of the parameters at the incident wave spectral peak frequency. Three generic models of wave energy devices have been used to represent major features of WECSs. The fixed OWC and the oscillating single body have distinct features both in terms of hydrodynamics and the nonlinearities involved. The floating OWC can be seen as a combination of a fixed OWC and

an oscillating body, coupled through additional hydrodynamic coupling parameters.

A direct convolution integration model is slow, but its accuracy is guaranteed for sufficiently small integration time step provided that the IRFs are accurate. When evaluating the IRFs from frequency-domain data, extrapolation to high frequencies and interpolation for finer frequency resolution are practical ways to ensure accuracy of the IRFs. Some fixed step solvers have been compared. The improved Euler's (Heun's) method may be a good choice for a balance between accuracy and efficiency. A fixed time step of 0.1 s for the improved Euler's and Runge-Kutta 3 and 4 methods is acceptable for most cases with oscillating body devices. Smaller time step is necessary when Coulomb-type nonlinearities are present or when the model exhibits stiff dynamics due to fluid compressibility.

A state-space model is shown to be highly accurate and offer significant saving in computation time. Even a model order as low as 2 has good performance for most cases.

A constant-coefficient model is useful to give a quick approximation of the desired outputs for cases when the

radiation force is relatively smaller than the other forces in the system.

References

[1] E. R. Jefferys, "Device characterisation," in *Power from Sea Waves*, 1980, pp. 413–438.

[2] W. E. Cummins, "The impulse response function and ship motions," David Taylor Model Basin, Tech. Rep., October 1962.

[3] T. F. Ogilvie, "Recent progress toward the understanding and prediction of ship motions," in *Proceedings of the 5th Symposium on Naval Hydrodynamics*, Bergen, Norway, 1964, pp. 3–128.

[4] G. Bennet and M. Greenhow, "Nonlinear dynamics of a floating body," in *Proceedings of the 7th International Workshop on Water Waves and Floating Bodies*, R. Cointe, Ed., Val de Reuil, France, 1992, pp. 11–14.

[5] M. Greenhow and S. P. White, "Optimal heave motion of some axisymmetric wave energy devices in sinusoidal waves," *Applied Ocean Research*, vol. 19, no. 3-4, pp. 141–159, 1997.

[6] T. Perez and T. I. Fossen, "Time- vs. frequency-domain identification of parametric radiation force models for marine structures at zero speed," *Modeling, Identification and Control*, vol. 29, no. 1, pp. 1–19, 2008.

[7] E. R. Jefferys, "Simulation of wave power devices," *Applied Ocean Research*, vol. 6, no. 1, pp. 31–39, 1984.

[8] R. Taghipour, T. Perez, and T. Moan, "Hybrid frequency-time domain models for dynamic response analysis of marine structures," *Ocean Engineering*, vol. 35, no. 7, pp. 685–705, 2008.

[9] P. Ricci, J.-B. Saulnier, A. F. de O. Falcão, and M. T. Pontes, "Time-domain models and wave energy converters performance assessment," in *Proceedings of the 27th International Conference on Offshore Mechanics and Arctic Engineering*, Estoril, Portugal, 2008, pp. 1–10.

[10] D. C. Karnopp, D. L. Margolis, and R. C. Rosenberg, *System Dynamics: Modeling and Simulation of Mechatronic Systems*, 4th ed. John Wiley & Sons, 2006.

[11] A. C. Fernandes, "Analysis of an axisymmetric pneumatic buoy by reciprocity relations and a ring-source method," Ph.D. dissertation, Department of Ocean Engineering, MIT, Cambridge, Massachusetts, 1983.

[12] S. H. Salter, "Wave power," *Nature*, vol. 249, pp. 720–724, 1974.

[13] WAMIT, WAMIT, Inc., Chestnut Hill, MA, 2008, version 6.4. [Online]. Available: http://www.wamit.com

[14] A. Kurniawan, J. Hals, and T. Moan, "Modelling and simulation of a floating oscillating water column," in *Proceedings of the 30th International Conference on Ocean, Offshore and Arctic Engineering*, Rotterdam, The Netherlands, 2011.

[15] J. Falnes, *Ocean Waves and Oscillating Systems*. Cambridge University Press, 2002.

[16] M. Greenhow, J. Rosen, and M. Reed, "Control strategies for the clam wave energy device," *Applied Ocean Research*, vol. 6, no. 4, pp. 197–206, 1984.

[17] Z. Yu and J. Falnes, "State-space modelling of a vertical cylinder in heave," *Applied Ocean Research*, vol. 17, no. 5, pp. 265–275, 1995.

[18] G. Oltedal, "Pneumatic wave-power conversion by a phase-controlled buoy," Ph.D. dissertation, Department of Experimental Physics, NTH (now NTNU), Trondheim, 1985.

[19] T. Perez and T. I. Fossen, "A Matlab toolbox for parametric identification of radiation-force models of ships and offshore structures," *Modeling, Identification and Control*, vol. 30, no. 1, pp. 1–15, 2009.

[20] ——, "Practical aspects of frequency-domain identification of dynamic models of marine structures from hydrodynamic data," *Ocean Engineering*, vol. 38, pp. 426–435, 2011.

[21] M. J. Tucker, P. G. Challenor, and D. J. T. Carter, "Numerical simulation of a random sea: a common error and its effect upon wave group statistics," *Applied Ocean Research*, vol. 6, no. 2, pp. 118–122, 1984.

[22] MATLAB, The MathWorks, Inc., Natick, Massachusetts, 2010, version 7.10.0 (R2010a). [Online]. Available: http://www.matlab.com

[23] 20-sim, Controllab Products B. V., Enschede, The Netherlands, 2009, version 4.1. [Online]. Available: http://www.20sim.com

[24] J. Hals, "Modelling and phase control of wave-energy converters," Ph.D. dissertation, Department of Marine Technology, Norwegian University of Science and Technology, Trondheim, 2010.

Optimal geometries for wave absorbers oscillating about a fixed axis

A. Kurniawan and T. Moan
IEEE Journal of Oceanic Engineering 38, 117–130, 2013

Paper E

Characteristics of a pitching wave absorber with rotatable flap

A. Kurniawan and T. Moan

Technoport RERC Research 2012

Characteristics of a pitching wave absorber with rotatable flap

Adi Kurniawan[*], Torgeir Moan[*]

Centre for Ships and Ocean Structures, Trondheim, Norway

Abstract

A bottom-fixed flap-type pitching wave energy absorber which operates near-shore is studied. The design consists of an arm hinged on the sea bed and supporting a flap. The flap has an elliptical cross section spanning vertically from the free surface to about one third of the water depth. A mechanism is provided which allows the flap to be fixed at a variable angle relative to the supporting arm. Such mechanism is here proposed as a means of broadening the absorption bandwidth and avoiding large forces while still absorbing power. The variations of maximum absorbed power and reaction force with wave frequency are obtained for different flap widths and angles and for different angular displacement limits, on the basis of linear potential theory. Further analysis on the absorber with a selected flap width is then presented and its performance is shown to be promising.

Keywords: wave energy, pitch, flap, near-shore

1. Introduction

An earlier optimization study by the authors [1] suggested that an elliptical section could be an optimal section for a bottom-fixed flap-type pitching wave energy absorber, whose power take-off is located at the bottom hinge. To maximize power to surface area ratio the section should be elongated vertically and span from the free surface to no more than approximately one third of the water depth. Furthermore, it was found that having the section elongated horizontally and submerged at a certain depth would reduce the reaction force to power ratio.

Based on these findings, we propose a wave absorber design consisting of a bottom-hinged arm supporting a flap whose cross section is an ellipse (see Fig. 1). The design resembles the EB Frond [2] except that another hinge is provided at the upper end of the arm which allows the flap to be aligned at variable angles relative to the arm. We shall show that aligning the flap at different angles may quite significantly alter the power absorption, reaction force, and resonant characteristics of the absorber. This, together with ballasting the flap, can be used to good effect for maximizing power absorption and minimizing reaction forces. Such strategy has recently been termed geometry control to distinguish it from power take-off control [3].

_____

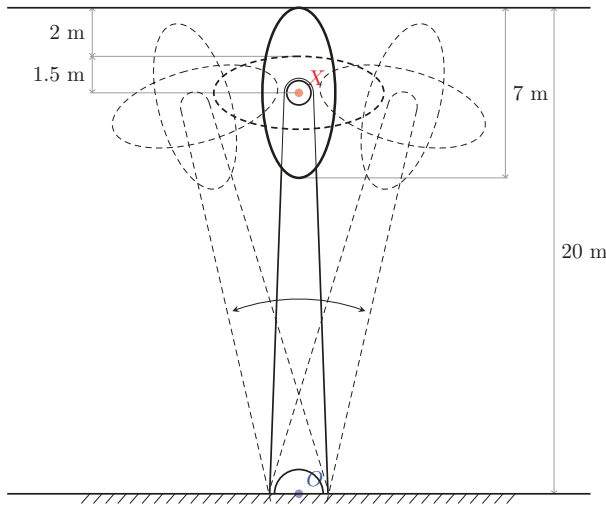[*] Corresponding author. E-mail address: adi.kurniawan@ntnu.no

Fig. 1. Two-dimensional sketch of the wave absorber. The arm oscillates about the bottom hinge *O* upon wave action. The upper hinge *X* enables the flap to be aligned parallel or perpendicular to the arm.
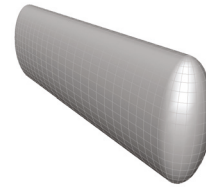

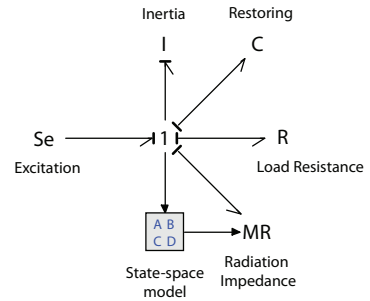Fig. 2. Panel model of the flap (shown in parallel orientation).

Fig. 3. Bond graph model of the absorber.

The wave absorber is designed to operate in water depth of 20 m. The flap height, that is the major axis of the ellipse, is 7 m and the flap thickness, that is the minor axis of the ellipse, is 3 m. The upper hinge is centred at the centroid of the flap. The arm length is thus 16.5 m, and when the flap is perpendicular to the arm, there will be a clearance of 2 m from the flap to the free surface. The two ends of the flap are rounded (in the form of half prolate spheroids) in order to minimize viscous losses (see Fig. 2). The incident waves are assumed to propagate normal to the flap axis.

In the following the characteristics of this wave absorber are studied. The added inertia and radiation damping for both the parallel and perpendicular flap orientations are first presented, followed by the absorbed power and the reaction force. The performance of the absorber is then assessed based on its absorbed power and reaction force at a given near-shore site.

2. Methodology

2.1. Maximum absorbed power and reaction force

We assume that the angular displacement of the arm is limited to a maximum of α by an increased linear load resistance. Let r be the ratio of the limited to the optimum angular velocity amplitudes of the absorber, or

$$r = 2\omega\alpha R_{55}/|X_{e5}|, \tag{1}$$

where R_{55} is the pitch radiation damping and X_{e5} is the pitch excitation moment. Then the maximum absorbed power is given as [4]

$$P_{\max} = \frac{|X_{e5}|^2}{8R_{55}}\left[1 - (1 - r)^2 H(1 - r)\right], \tag{2}$$

where $H(x)$ is the Heaviside step function.

Neglecting centrifugal force, we may write the dynamic horizontal and vertical reaction forces as

$$X_{R1} = X_{e1} - (i\omega m_{15} + R_{15})\,U \tag{3}$$

$$X_{R3} = X_{e3}, \tag{4}$$

where X_{e1} and X_{e3} are the horizontal and vertical excitation forces, m_{15} and R_{15} are the added inertia and radiation damping in the horizontal direction due to the absorber's pitch oscillation, and U is the pitch velocity:

$$U = \frac{X_{e5}}{2R_{55}} \left[1 - (1 - r)H(1 - r) \right]. \tag{5}$$

The maximum dynamic reaction force can be obtained as

$$F_{R\max} = \left[\frac{1}{2} \left(|X_{R1}^2 + X_{R3}^2| + |X_{R1}|^2 + |X_{R3}|^2 \right) \right]^{\frac{1}{2}}. \tag{6}$$

2.2. Tuned absorbed power and reaction force

To achieve the maximum absorbed power (2), the dynamic properties of the absorber must be varied with frequency. When the dynamic properties of the absorber are fixed and tuned to a single frequency ω_p by adjusting the body inertia M, hydrostatic restoring coefficient S, and load resistance R_u such that

$$M - S\omega_p^{-2} = -m_{55}(\omega_p) \tag{7}$$

$$R_u = R_{55}(\omega_p) \left[1 + \frac{2(1 - r(\omega_p))}{r(\omega_p)} H(1 - r(\omega_p)) \right], \tag{8}$$

where m_{55} is the pitch added inertia, the mean absorbed power is given as

$$P(\omega) = \frac{\frac{1}{2} R_u |X_{e5}(\omega)|^2}{(R_{55}(\omega) + R_u)^2 + |\Im\{Z\}|^2}, \tag{9}$$

where

$$\Im\{Z\} = \omega \left(m_{55}(\omega) - m_{55}(\omega_p) - S\omega^{-2} + S\omega_p^{-2} \right), \tag{10}$$

or

$$\Im\{Z\} = \omega \left[M + m_{55}(\omega) - \omega_p^2 \omega^{-2} \left(M + m_{55}(\omega_p) \right) \right]. \tag{11}$$

It is clear that $P(\omega_p) = P_{\max}(\omega_p) = |X_{e5}(\omega_p)|^2 [1 - (1 - r(\omega_p))^2 H(1 - r(\omega_p))]/8R_{55}(\omega_p)$, and that $P(\omega) < P_{\max}(\omega)$ for $\omega \neq \omega_p$.

The maximum reaction force in this case is given by (6), with (3) replaced by

$$X_{R1} = X_{e1} - (i\omega m_{15} + R_{15}) \frac{X_{e5}}{R_{55} + R_u + i\Im\{Z\}}. \tag{12}$$

2.3. Absorbed power and reaction force for a given sea state

If we assume that R_u, M, and S are fixed for a given sea state, the absorbed power for a given sea state can be obtained from

$$P = R_u \int_0^\infty \left| \frac{f_{e5}(\omega)}{R_{55}(\omega) + R_u + i\omega \left(M + m_{55}(\omega) - S\omega^{-2} \right)} \right|^2 S_\zeta(\omega) d\omega, \tag{13}$$

where f_{e5} is the pitch excitation force coefficient and $S_\zeta(\omega)$ is the wave spectrum. The choice of R_u, M, and S may be obtained from (7) and (8) with ω_p taken to be the spectral peak frequency, or from numerical optimization. The reaction force, however, must be obtained from time-domain simulations.

2.4. Time-domain model

The equation of motion for the absorber in time domain can be written as

$$F_{e5}(t) = [M + m_{55}(\infty)]\,\dot{u}(t) + k(t) * u(t) + S\,s(t) + R_u u(t), \tag{14}$$

where $m_{55}(\infty)$ is the infinite-frequency value of the pitch added inertia m_{55}, $s(t)$ is the angular displacement of the arm, and $k(t)$ is the radiation impulse response function, which is the inverse Fourier transform of the frequency response function $K(\omega) \equiv R_{55}(\omega) + i\omega\,[m_{55}(\omega) - m_{55}(\infty)]$.

To accelerate simulation, we replace the convolution term $\mu(t) \equiv k(t) * u(t) = \int_0^t k(t-\tau)u(\tau)d\tau$ by a state-space approximation. This amounts to replacing the term by a set of coupled linear ordinary differential equations, which may be expressed in matrix form (see, e.g. [5]):

$$\dot{\mathbf{x}}(t) = \hat{\mathbf{A}}\mathbf{x}(t) + \hat{\mathbf{B}}u(t) \tag{15}$$

$$\hat{\mu}(t) = \hat{\mathbf{C}}\mathbf{x}(t) \tag{16}$$

where $\mathbf{x}(t)$ is the state vector, the number of components of which corresponds to the *order* of the state-space model, and $\hat{\mathbf{A}}$, $\hat{\mathbf{B}}$, $\hat{\mathbf{C}}$ are constant matrices. We use the frequency-domain identification approach following the algorithm detailed in [5, 6]. The method uses frequency-domain hydrodynamic data for identification. The approach is to fit a rational transfer function

$$\hat{K}(s) = \frac{P(s)}{Q(s)} = \frac{p_r s^r + p_{r-1} s^{r-1} + \ldots + p_0}{s^n + q_{n-1} s^{n-1} + \ldots + q_0}, \tag{17}$$

where $s = i\omega$, to the frequency response function $K(\omega)$. Further constraints on the model have been derived in [7] based on the properties of the frequency response function and its corresponding impulse response function. A least-squares fitting method is applied to find the coefficients p_i and q_i, and once these are obtained, the matrices $\hat{\mathbf{A}}$, $\hat{\mathbf{B}}$, and $\hat{\mathbf{C}}$ can be constructed using any of the standard canonical forms.

The time series of the excitation moment $F_{e5}(t)$ are generated prior to the simulation and stored as data files to be read during the simulation. First, we obtain the spectral density of $F_{e5}(t)$:

$$S_{F_{e5}}(\omega) = |f_{e5}(\omega)|^2 S_\zeta(\omega). \tag{18}$$

The excitation moment $F_{e5}(t)$ is then given as

$$F_{e5}(t) = \sum_{n=0}^{N/2} [(a_n \cos\phi_n + b_n \sin\phi_n)\cos\omega_n t - (a_n \sin\phi_n - b_n \cos\phi_n)\sin\omega_n t], \tag{19}$$

where a_n and b_n are generated from a Gaussian distribution with variance $S_{F_{e5}}(\omega_n)\Delta\omega$ [8]. Here, N is the number of values in the time series, determined by the required length of the series T and the time interval between values Δt. Also, $\omega_n = n\Delta\omega$, where $\Delta\omega = 2\pi/T$. In addition, ϕ_n is the phase (in radians) of $f_{e5}(\omega_n)$. For ω_n larger than the largest frequency for which f_{e5} is computed, f_{e5} is assumed to be zero as typical wave spectra have negligible values at the high-frequency tail. The sum in (19) may be identically evaluated by an inverse Fast Fourier Transform at a fraction of computer time. The initial part of the resulting time series (the first 20 seconds) is filtered by a cosine taper window.

Having evaluated the angular velocity $u(t)$, we may obtain the instantaneous absorbed power $P(t) = R_u u^2(t)$. The instantaneous horizontal and vertical reaction forces are given as (c.f. (3) and (4))

$$F_{R1}(t) = F_{e1}(t) - m_{15}(\infty)\dot{u}(t) - k_{15}(t) * u(t) \tag{20}$$

$$F_{R3}(t) = F_{e3}(t), \tag{21}$$

where $m_{15}(\infty)$ is the infinite-frequency value of m_{15}, and $k_{15}(t)$ is the radiation impulse response function corresponding to $K_{15}(\omega) \equiv R_{15}(\omega) + i\omega\,[m_{15}(\omega) - m_{15}(\infty)]$. The instantaneous resultant reaction force can then be obtained as

$$F_R(t) = \left[F_{R1}^2(t) + F_{R3}^2(t)\right]^{\frac{1}{2}}. \tag{22}$$

The time-domain model is implemented using bond graph as a tool. A bond graph representation of the equation of motion (14) incorporating the state-space radiation force model is shown in Fig. 3.
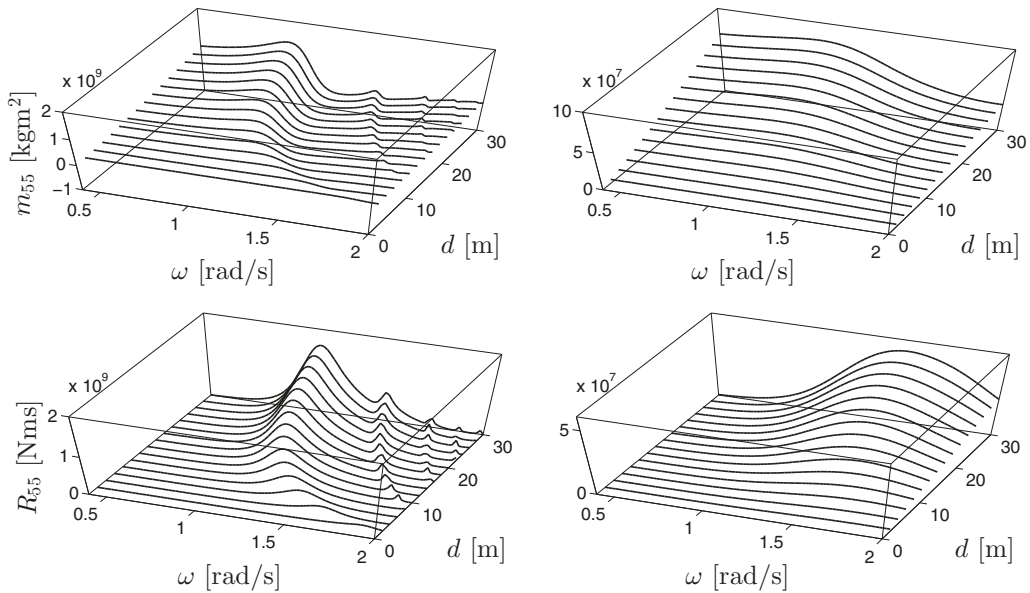
Fig. 4. Added inertia and radiation damping for $\theta = 0°$ (left) and $\theta = 90°$ (right).

2.5. Computation of hydrodynamic parameters

The hydrodynamic parameters are computed by a three-dimensional higher-order panel method [9] for every 0.02 rad/s. The panel model is shown in Fig. 2. The supporting arm is assumed to be transparent to the waves. Convergence studies are first carried out to decide on the panel size which gives the desired accuracy and computing efficiency.

The geometric variables are the flap width d (2 to 30 m in intervals of 2 m, making a total of 15 discrete widths), measured excluding the rounded ends, and the flap angle θ (0° and 90°, which correspond to parallel and perpendicular flap orientations, respectively). Different angular displacement limits (10° and 20°) are imposed.

3. Results and discussions

3.1. Added inertia and radiation damping

The added inertia and radiation damping for the two flap angles are plotted in Fig. 4. In general, the added inertia and radiation damping values increase, while their peak frequencies decrease, with flap width. The added inertia and radiation damping for the parallel flap orientation ($\theta = 0°$) are of larger magnitudes compared to those for the perpendicular flap orientation ($\theta = 90°$). However, the radiation damping for $\theta = 90°$ is more broad-banded. Compared to the parallel flap, the perpendicular flap is also less sensitive to the variation of flap width.

For $\theta = 0°$, negative added inertia are observed for all the flap widths considered. Negative added inertia occurs when the mean potential energy of the fluid exceeds the mean kinetic energy, which for a submerged body happens when the depth of submergence is small and free-surface effects are important [10]. No negative added inertia are observed for $\theta = 90°$.

3.2. Maximum absorbed power and reaction force

The maximum absorbed power and reaction force for different flap angles and angular displacement limits are plotted in Fig. 5. The absorbed power and reaction force increase with flap width. Limiting the
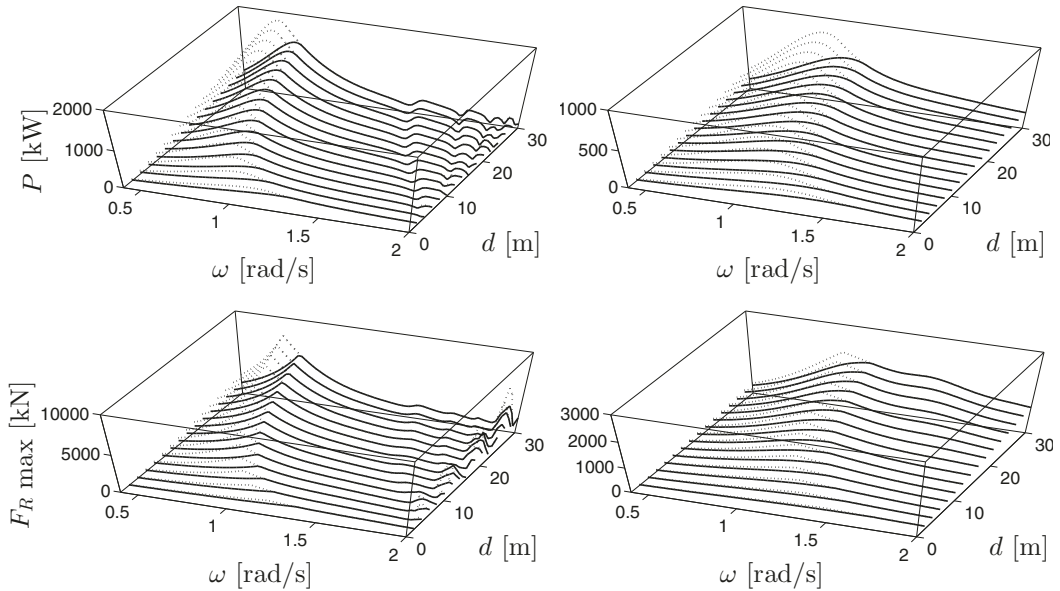
Fig. 5. Maximum absorbed power and maximum reaction force for 1-m amplitude waves for $\theta = 0°$ (left) and $\theta = 90°$ (right): $\alpha = \pi/18$ rad/s (solid), $\alpha = \pi/9$ rad/s (dotted).

angular displacements has the effect such that both the maximum absorbed power and reaction force curves fall off in the low-frequency range. Increasing the angular displacement limit simply shifts the onset of this fall to a lower frequency. It can be seen that although aligning the flap perpendicular to the arm reduces the amount of absorbed power possible, the absorber is subjected to lower reaction forces compared to the parallel flap orientation.

3.3. Tuned absorbed power and reaction force

We envisage that the body inertia M and hydrostatic restoring coefficient S can be adjusted by ballasting the flap with sea water. If we assume that the ballast centroid is fixed and coincides with the centroid of the flap, we may write (7) as

$$M_w l_{arm}^2 + \frac{g}{\omega_p^2} M_w l_{arm} = -m_{55}(\omega_p) - M_s + \frac{S_s}{\omega_p^2}, \tag{23}$$

where M_w is the ballast mass, l_{arm} is the arm length, g is the acceleration due to gravity, while M_s and S_s are the body inertia and restoring coefficient without the effect of ballast. Let $M_{w\,max}$ be the maximum ballast mass that can be put into the flap. If the right-hand side of (23) is denoted as $C(\omega_p)$, the condition that $0 \le M_w \le M_{w\,max}$ is then equivalent to

$$0 \le C(\omega_p) \le M_{w\,max}\left(l_{arm}^2 + \frac{g}{\omega_p^2} l_{arm}\right). \tag{24}$$

This sets the range of tunable frequencies ω_p for which $P(\omega_p) = P_{\max}(\omega_p)$. Fig. 6 shows the variations of $C(\omega)$ for different flap widths and angles, for some chosen realistic values of M_s, S_s, and $M_{w\,max}$. Ranges of tunable frequencies ω_p may be identified from the figure. For $\theta = 0°$ and $d = 10$ m, for example, perfect tuning is possible for $1.32 \le \omega_p \le 1.34$ and $1.65 \le \omega_p \le 1.79$ rad/s.

We may gain understanding of the characteristics of the absorber from the function $C(\omega)$. The natural frequencies of the unballasted system are the frequencies for which $C(\omega) = 0$. For frequencies where
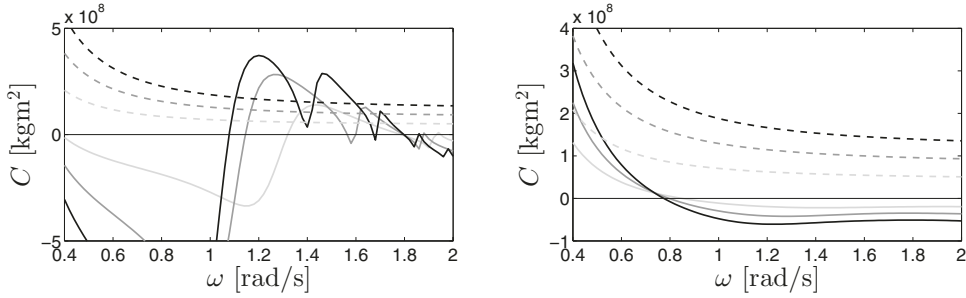
Fig. 6. Variations of $C(\omega)$ for $\theta = 0°$ (left) and $\theta = 90°$ (right). Upper bounds corresponding to a maximum ballast volume of 80% the total flap volume are drawn in dashed lines. Different shades of grey represent different flap widths: $d = 30$ m (black), $d = 20$ m (grey), $d = 10$ m (light grey). Ranges of tunable frequencies ω_p may be identified as the frequencies for which $0 \leq C(\omega) \leq$ upper bound.

$C(\omega) > 0$ the system is too stiff, while for frequencies where $C(\omega) < 0$ the system is too soft. Since ballasting the flap always has the effect of softening the system, perfect tuning is only possible for frequencies where $C(\omega) > 0$, subject to the limitations of the maximum ballast mass that can be put into the system. For frequencies where $C(\omega) < 0$ perfect tuning would require additional spring, while heavier ballast would be needed to achieve perfect tuning for frequencies where $C(\omega) > M_{w\max}\left(l_{arm}^2 + \frac{g}{\omega_p^2}l_{arm}\right)$.

Where perfect tuning is not possible, equation (23) is not satisfied. In this case, it is best to keep the difference between the left- and right-hand sides of (23) as small as possible (c.f. [11], §3.5). It follows that the absorber should be unballasted for frequencies where $C(\omega) < 0$ and ballasted to the maximum for frequencies where $C(\omega) > M_{w\max}\left(l_{arm}^2 + \frac{g}{\omega_p^2}l_{arm}\right)$. It can be shown that a choice of R_u which would maximize the absorbed power in this case is given as

$$R_u = [1 + xH(1 - r_r)]\,|Z_i(\omega_p)|, \tag{25}$$

where

$$x = \frac{\left[\frac{1}{r_r^2}\left(|Z_i(\omega_p)| + R_{55}(\omega_p)\right)^2 + \Im^2\{Z_i(\omega_p)\}\left(\frac{1}{r_r^2} - 1\right)\right]^{\frac{1}{2}} - R_{55}(\omega_p)}{|Z_i(\omega_p)|} - 1 \tag{26}$$

$$r_r = \frac{\omega_p \alpha}{|U_{r\,\mathrm{opt}}(\omega_p)|} \tag{27}$$

$$U_{r\,\mathrm{opt}}(\omega_p) = \frac{X_{e5}(\omega_p)}{|Z_i(\omega_p)| + Z_i(\omega_p)} \tag{28}$$

$$Z_i(\omega_p) = \begin{cases} R_{55}(\omega_p) - i\omega_p C(\omega_p), & \text{for } C(\omega_p) < 0 \\ R_{55}(\omega_p) + i\omega_p\left[M_{w\max}\left(l_{arm}^2 + \frac{g}{\omega_p^2}l_{arm}\right) - C(\omega_p)\right], & \text{for } C(\omega_p) > M_{w\max}\left(l_{arm}^2 + \frac{g}{\omega_p^2}l_{arm}\right). \end{cases} \tag{29}$$

Looking again at Fig. 6, we may observe different regions of tunable frequencies each for the different flap orientations. For $\theta = 0°$, the tunable frequencies lie on the higher-frequency side of the considered range, while for $\theta = 90°$, they lie on the lower-frequency side. This shows how varying the flap angle may result in quite different resonant characteristics, and adjusting the flap angle may be used as a means to broaden the absorption bandwidth, as illustrated in the following.

Fig. 7 shows the variations of the absorbed power and the corresponding maximum reaction force for the two flap angles, for an absorber with $d = 10$ m. The incident wave amplitude A is 0.5 m and the angular displacement amplitude is limited to 20°. The first set of lines (dashed) represents the maximum attainable absorbed power and the corresponding maximum reaction force required to attain this maximum

power. These are the same lines in Fig. 5 for $d = 10$ m. The maximum attainable power is relatively large, especially for $\theta = 0°$, but much of this potential, say for $\omega = 0.4$ to 1.3 rad/s, can be realised only if additional restoring force is supplied. The maximum reaction force required to attain this potential is also relatively large. The second set of lines (dotted) represents the maximum absorbed power that can be attained using a fixed ballast (tuned to four different frequencies $\omega_p = 0.6, 0.8, 1.0$, and 1.2 rad/s), and the corresponding maximum reaction force. These lines represent the more realistic upper bounds of the absorbed power attainable if we use ballasting as a means of tuning. The third set of lines (solid) represents the absorbed power and the corresponding maximum reaction force when both the ballast and the load resistance are fixed and tuned to each ω_p.

From Fig. 7 we see that depending on the incident wave frequency, changing the flap angle may improve the power absorption. In this case, for $0.5 < \omega < 1$ rad/s more power will be absorbed by aligning the flap to $\theta = 90°$, while for $1 < \omega < 1.7$ rad/s it is better to align the flap to $\theta = 0°$.

Now suppose that the design limit of the reaction force is 1000 kN. We expect the reaction force to exceed this limit when the incident wave amplitudes get higher. As an example, consider an incident wave amplitude of 1.6 m. Again we see that depending on the incident wave frequency, changing the flap angle may improve the power absorption (see Fig. 8). In this case, it is clearly better to align the flap to $\theta = 90°$ for $0.6 < \omega < 1$ rad/s. But now the design limit of the reaction force must be taken into account. For $\theta = 90°$, the maximum reaction force is just below this limit for all the different tuning frequencies. In fact, the maximum reaction force changes only slightly with the change of tuning frequency. For $\theta = 0°$, however, we see that this limit is exceeded when the absorber is tuned to $\omega_p = 1$ and 1.2 rad/s. To reduce the reaction force, the system may be tuned to higher or lower frequencies (see Fig. 8, top, where reductions of both the absorbed power and the maximum reaction force are clearly seen around $\omega_p = 1$ and 1.2 rad/s). Alternatively, the reaction force can be reduced by changing the flap angle with the same consequence of reducing the absorbed power (see Fig. 8, bottom).

Before we move on to the performance of the absorber in irregular waves, it may be noted that the tuned absorbed power of the $\theta = 90°$ configuration (Fig. 8, bottom left, grey solid line) exceeds the maximum attainable absorbed power for the given angular displacement limit (grey dashed line) at a small range of frequencies around $\omega = 0.85$ rad/s. The reason for this is that equation (25) ensures that the angular displacement does not exceed the given limit only at ω_p. If it is desired that the angular displacement be less than the given limit at all frequencies, then a larger load resistance must be applied with the consequence of reducing the absorbed power at around $\omega = 0.85$ rad/s.

3.4. Performance in irregular waves

Using the same absorber ($d = 10$ m) as an example, we assess the performance of the absorber at a given site characterized by a set of sea states and their probability of occurrence. The characteristic sea states are based on wave measurements at a site on the German Continental Shelf reported in [12] and are reproduced in Table 1. The average annual available wave power at this location is reported to be 11.6 kW/m, although a deep-water approximation (see, e.g. [13]) based on the data given in Table 1 gives a smaller value of 8.0 kW/m.

We use the JONSWAP spectrum relevant for the North Sea environment as the wave spectrum $S_\zeta(\omega)$ model for each sea state:

$$S_\zeta(\omega) = \frac{\alpha g^2}{\omega^5} \exp\left(-1.25\frac{\omega_p^4}{\omega^4}\right)\gamma^{a(\omega)},\tag{30}$$

Table 1. Characteristic sea states (reproduced from [12])

Sea state	H_s [m]	T_e [s]	Prob. [%]
1	0.25	4.15	9.14
2	0.75	4.67	27.31
3	1.25	5.53	22.62
4	1.75	5.95	18.55
5	2.25	6.21	10.25
6	2.75	6.59	5.08
7	3.25	7.55	3.35
8	3.75	8.16	1.63

Table 2. Load resistance R_u, maximum displacement s_{max}, maximum reaction force $F_{R\,max}$, and mean absorbed power P for an absorber with $d = 10$ m and $\theta = 0°$, for the sea states listed in Table 1. The ballast mass $M_w = 0$ for all sea states. The values in parentheses are obtained from (13).

Sea state	R_u [Nms]	s_{max} [rad]	$F_{R\,max}$ [kN]	P [kW]
1	5.9×10^8	0.004	175	1.0 (1.1)
2	4.8×10^8	0.013	473	13.5 (12.0)
3	2.6×10^8	0.038	708	31.2 (32.0)
4	2.0×10^8	0.059	753	63.7 (59.2)
5	1.8×10^8	0.087	918	90.3 (94.2)
6	1.6×10^8	0.115	1198	133.6 (134.4)
7	1.2×10^8	0.173	1058	142.8 (169.0)
8	9.4×10^7	0.255	1141	210.4 (213.4)
			P_{ann} [kW]	46.9 (47.2)

where

$$a(\omega) = \exp\left(-\frac{(\omega - \omega_p)^2}{2\sigma^2\omega_p^2}\right) \tag{31}$$

$$\sigma = \begin{cases} 0.07 & \text{for } \omega \le \omega_p \\ 0.09 & \text{for } \omega > \omega_p \end{cases} \tag{32}$$

$$\alpha = 5.058 \frac{H_s^2}{T_p^4}(1 - 0.287\ln\gamma). \tag{33}$$

The peakedness parameter γ is chosen to be 3.3. The peak period T_p and the energy period T_e is related by $T_e = 0.857T_p$ [13]. For each sea state we generate two 1220-second length excitation moment time series, one for $\theta = 0°$ and the other for $\theta = 90°$, according to the method outlined in § 2.4. The same wave realization is used for both.

The simulations are carried out using a modelling and simulation software [14]. For simplicity the load resistance R_u and ballast mass M_w used for each sea state are the optimum R_u and M_w assuming regular incident wave with frequency $1/T_p$ and amplitude $H_s/2$. A typical simulation result is shown in Fig. 9, where the first 20 seconds have been discarded.

A summary of the result if the parallel flap orientation ($\theta = 0°$) is used for all sea states (case A) is tabulated in Table 2. The mean annual power P_{ann} in this case is 46.9 kW. If the perpendicular flap orientation ($\theta = 90°$) is used for all sea states (case B), a larger P_{ann} is obtained, i.e. 55.6 kW (Table 3). Using the best configuration for each sea state (case C), we have $P_{ann} = 57.2$ kW (Table 4). Also presented are the mean absorbed power values obtained using (13). The results are similar.

The fact that larger P_{ann} is obtained for case B than case A is because the most resourceful sea states in a year, i.e. sea states 4 to 7 ($\omega_p = 0.9$ to 0.7 rad/s), are more favourable to the $\theta = 90°$ configuration than $\theta = 0°$, if no additional restoring force is supplied (see again Fig. 6, where it is shown that for $\theta = 0°$ perfect tuning is not possible at these frequencies without additional restoring force). The $\theta = 0°$ configuration will be capable of absorbing more power at these frequencies if additional restoring force is provided. This, however, entails greater reaction force, as noted previously in the discussion of Fig. 7. The $\theta = 0°$ configuration gives higher absorbed power than $\theta = 90°$ for sea states 1 to 3 and 8. These sea states, however, have relatively smaller resource. Sea state 2 ($\omega_p = 1.2$ rad/s), for example, has the highest probability of occurrence but the amount of power available for this sea state is small. On the other hand, sea state 8 is the most energetic but has the least probability of occurrence, and so it contributes little to the total mean annual power. This explains why the improvement of case C over case B is not so significant.

If for $\theta = 0°$ we now supply an additional restoring force of 1.0×10^8 Nm (the value is not optimized, but chosen just for the sake of comparison) for sea states 4 to 7 (case D), the mean annual power is increased

Table 3. As in Table 2, for $\theta = 90°$. The ballast mass M_w for each sea state is given in the table.

Sea state	R_u [Nms]	M_w [10^3 kg]	s_{max} [rad]	$F_{R\,max}$ [kN]	P [kW]
1	2.9×10^7	0	0.016	121	0.6 (0.7)
2	2.2×10^7	0	0.052	337	8.8 (8.0)
3	1.0×10^7	0	0.197	620	30.9 (33.3)
4	5.9×10^6	0	0.459	750	90.6 (84.4)
5	9.5×10^6	0	0.429	952	125.9 (133.7)
6	1.2×10^7	5.5	0.512	1204	166.3 (173.4)
7	1.5×10^7	26	0.511	1007	144.4 (179.5)
8	1.7×10^7	39	0.570	1134	190.8 (191.0)
				P_{ann} [kW]	55.6 (57.1)

Table 4. As in Table 3, with $\theta = 90°$ for sea states 4 to 7, and $\theta = 0°$ for the rest of the sea states.

Sea state	R_u [Nms]	M_w [10^3 kg]	s_{max} [rad]	$F_{R\,max}$ [kN]	P [kW]
1	5.9×10^8	0	0.004	175	1.0 (1.1)
2	4.8×10^8	0	0.013	473	13.5 (12.0)
3	2.6×10^8	0	0.038	708	31.2 (33.3)
4	5.9×10^6	0	0.459	750	90.6 (84.4)
5	9.5×10^6	0	0.429	952	125.9 (133.7)
6	1.2×10^7	5.5	0.512	1204	166.3 (173.4)
7	1.5×10^7	26	0.511	1007	144.4 (179.5)
8	9.4×10^7	0	0.255	1141	210.4 (213.4)
				P_{ann} [kW]	57.2 (58.6)

to 62.2 kW. The maximum reaction forces for these sea states, however, are also higher, especially for sea states 6 and 7. The benefit of changing the flap angle to $\theta = 90°$ for these sea states (case C) with the accompanying reduction of the reaction forces is therefore obvious.

4. Conclusion

The characteristics of a pitching wave absorber with variable flap angle relative to the supporting arm has been presented in this article. It has been shown that changing the flap angle may alter the resonant characteristics of the absorber and can be used to good effect in broadening the absorption bandwidth. Furthermore, having the flap aligned perpendicularly to the arm is characterised by a low reaction force, and can be used as a means to avoid large forces associated with large waves.

There is a pressing need to lower the cost of ocean wave power. Such means of geometry control should be explored further in order to meet this need.

Acknowledgements

References

[1] A. Kurniawan, T. Moan, Optimal geometries for wave absorbers oscillating about a fixed axis (submitted) (2011).

[2] The Engineering Business Ltd, EB Frond wave energy converter - phase 2, Tech. rep., DTI (2005).

[3] A. Price, C. Dent, A. Wallace, On the capture width of wave energy converters, Applied Ocean Research 31 (4) (2009) 251 – 259. doi:10.1016/j.apor.2010.04.001.

[4] D. V. Evans, Maximum wave-power absorption under motion constraints, Applied Ocean Research 3 (4) (1981) 200–203. doi:10.1016/0141-1187(81)90063-8.

[5] T. Perez, T. I. Fossen, A Matlab Toolbox for Parametric Identification of Radiation-Force Models of Ships and Offshore Structures, Modeling, Identification and Control 30 (1) (2009) 1–15. doi:10.4173/mic.2009.1.1.

[6] T. Perez, T. I. Fossen, Practical aspects of frequency-domain identification of dynamic models of marine structures from hydrodynamic data, Ocean Engineering 38 (2-3) (2011) 426–435. doi:10.1016/j.oceaneng.2010.11.004.

[7] T. Perez, T. I. Fossen, Time- vs. Frequency-domain Identification of Parametric Radiation Force Models for Marine Structures at Zero Speed, Modeling, Identification and Control 29 (1) (2008) 1–19. doi:10.4173/mic.2008.1.1.

[8] M. J. Tucker, P. G. Challenor, D. J. T. Carter, Numerical simulation of a random sea: a common error and its effect upon wave group statistics, Applied Ocean Research 6 (2) (1984) 118–122. doi:10.1016/0141-1187(84)90050-6.

[9] WAMIT, WAMIT, Inc., Chestnut Hill, MA, version 6.4 (2008).

[10] P. McIver, D. V. Evans, The occurrence of negative added mass in free-surface problems involving submerged oscillating bodies, Journal of Engineering Mathematics 18 (1) (1984) 7–22. doi:10.1007/BF00042895.

[11] J. Falnes, Ocean Waves and Oscillating Systems, Cambridge University Press, 2002.
[12] C. Beels, J. C. C. Henriques, J. De Rouck, M. T. Pontes, G. De Backer, H. Verhaeghe, Wave energy resource in the North Sea, in: Proceedings of the 7th European Wave and Tidal Energy Conference, Porto, Portugal, 2007.
[13] K. Nielsen, T. Pontes, Annex II Task 1.1 Generic and site-related wave energy data, Tech. Rep. T02-1.1, OES IA (September 2010).
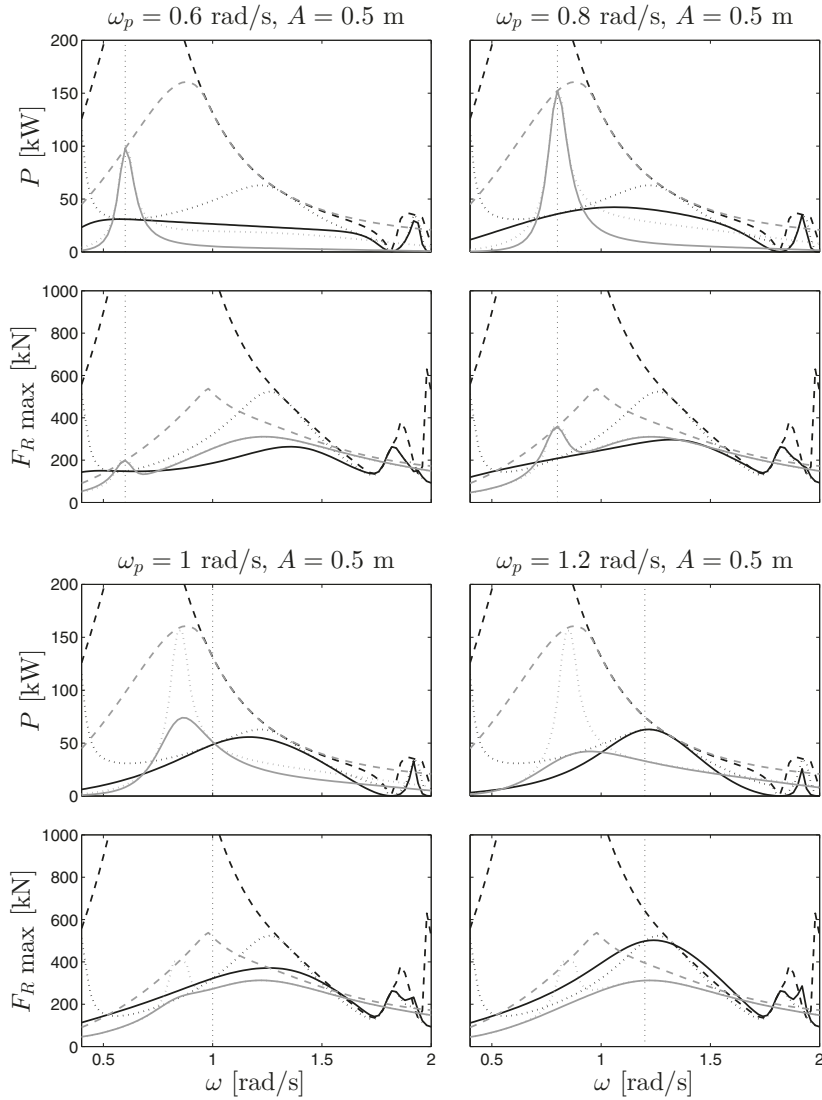[14] 20-sim, Controllab Products B. V., Enschede, The Netherlands, version 4.1 (2009).

Fig. 7. Absorbed power and maximum reaction force of the absorber with $d = 10$ m for $\theta = 0°$ (black) and $\theta = 90°$ (grey). The wave amplitude A is 0.5 m. Solid lines represent the absorbed power for fixed ballast mass and load resistance (tuned at ω_p) and the corresponding maximum reaction force. Dashed lines represent the maximum achievable absorbed power and the corresponding maximum reaction force. Dotted lines represent the maximum absorbed power for a fixed ballast mass (tuned at ω_p) and the corresponding maximum reaction force.
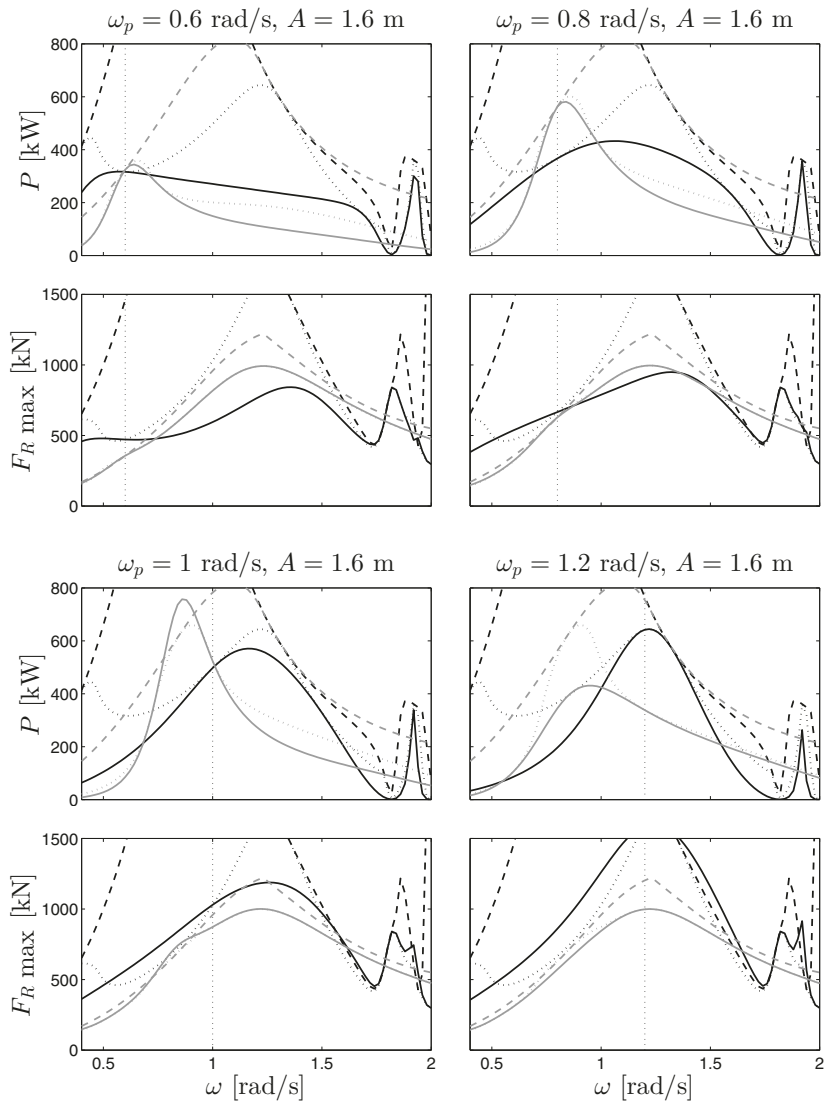
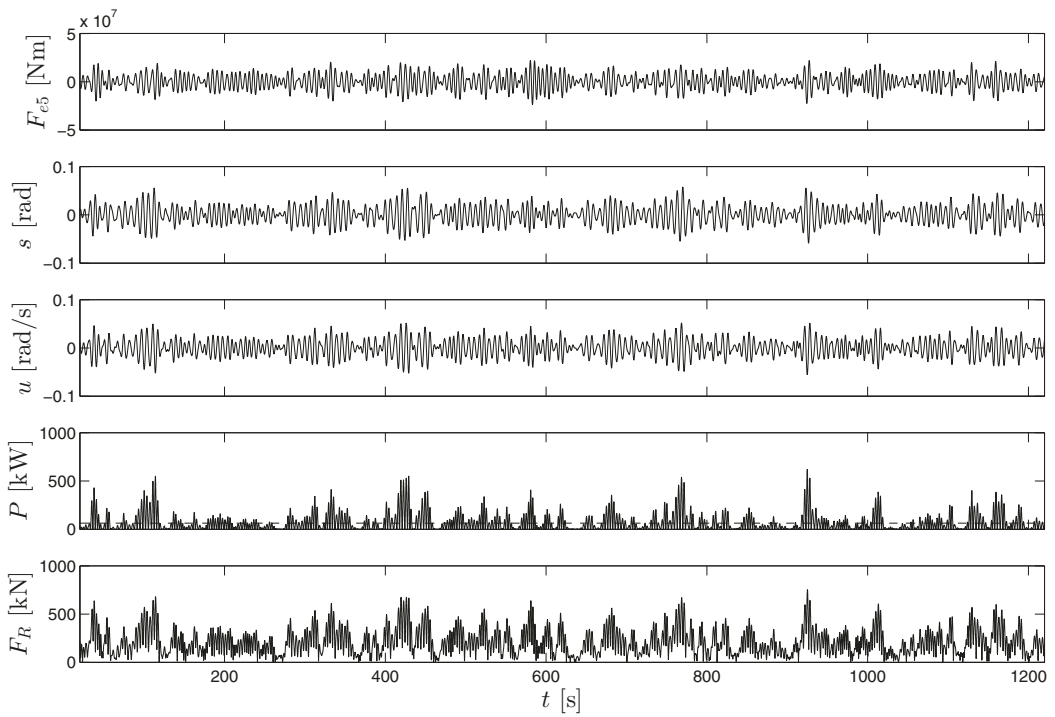Fig. 8. As in Fig. 7, for *A* = 1.6 m.

Fig. 9. Excitation moment, displacement, velocity, absorbed power (mean in dashed line), and reaction force for an absorber with $d = 10$ m and $\theta = 0°$, for sea state 4. The ballast mass $M_w = 0$ and the load resistance $R_u = 2.0 \times 10^8$ Nms.

Paper F

Multi–objective optimization of a wave energy absorber geometry

A. Kurniawan and T. Moan

Multi-objective optimization of a wave energy absorber geometry

Adi Kurniawan **Torgeir Moan**

adi.kurniawan@ntnu.no torgeir.moan@ntnu.no

Centre for Ships and Ocean Structures, Trondheim, Norway

1   Introduction

In terms of power performance, it is desirable for a wave energy absorber to have not only high levels of power absorption but also a broad absorption bandwidth. However, it may be the case that superior power performance is achieved at the expense of a high structural cost. Therefore, apart from maximizing the power absorption, we also need to minimize the cost of the absorber. The two objectives are, in general, conflicting, and it is not obvious what constitutes the best trade-off solution. In this study we pose this problem as a multi-objective optimization problem. An optimization algorithm is used to optimize the geometry of a wave energy absorber, with the objectives of maximizing the maximum mean absorbed power and minimizing the surface area of the absorber. The latter is supposed to be indicative of the structural cost.

2   Formulation of the problem

Consider a wave energy absorber which oscillates in one degree of freedom in response to incident regular plane waves of angular frequency ω. We assume that the power take-off is effected by a linear damper with coefficient R_u. Let M be the inertia of the absorber, m the added inertia, R the radiation damping coefficient, and S the restoring coefficient. The absorber velocity U and the wave exciting force X_e are related through the equation of motion of the absorber:

$$X_e = (R_u + Z)U, \tag{1}$$

where $Z = R + i\omega\left(M + m - S\omega^{-2}\right)$. The maximum mean power that can be absorbed by the linear damper is given as

$$P_{\max} = \frac{|X_e|^2}{4(R + |Z|)}, \tag{2}$$

obtained when $R_u = |Z|$. On the other hand, the maximum theoretical limit of achievable mean power is

$$P_{\lim} = \frac{|X_e|^2}{8R}. \tag{3}$$

Comparing (2) and (3), we see that $P_{\max} = P_{\lim}$ when

$$M + m - S\omega^{-2} = 0. \tag{4}$$

In this case the velocity U is in phase with the exciting force X_e, and the system is at resonance. When (4) is not satisfied, $P_{\max} < P_{\lim}$. Multiple resonances (Evans and Porter, 2012) are achieved if (4) is satisfied for more than one frequency. If it is possible to have these frequencies lie within the range of typical wave frequencies occurring at sea, we have a good wave energy absorber in terms of its power performance.

To have a cost-effective wave energy absorber, however, we also need to minimize its cost. A number of cost indicators may be identified for a wave energy absorber (see, e.g. Babarit et al., 2012), but for simplicity, in this study we consider only one cost indicator, namely the surface area A_s. Thus $P_{\max}$ is to be maximized for a given range of frequencies while A_s is to be minimized. This is a multi-objective optimization problem with two objectives. Since the objectives are, in general, conflicting, instead of a single optimum, there are multiple optimum solutions. The task is to identify these optimum solutions.

The problem can be formulated as follows: for $V_{\min} \leq V \leq V_{\max}$, where V is a set of geometric variables, find V which maximize $f_1^{\mathrm{obj}}(V) = \int_{\omega_{\min}}^{\omega_{\max}} P_{\max}(\omega)\,d\omega$ and minimize $f_2^{\mathrm{obj}}(V) = A_s$. Here, $\omega_{\min}$ and $\omega_{\max}$ are the specified minimum and maximum frequencies.

3   Methodology

A multi-objective optimization algorithm is used to solve the above problem. The algorithm works by generating successive (random) *populations* through *selection* and *variation* operations. A population is defined as a collection of *individuals*, where an individual is a set of design variables. Selection consists of retaining the 'best' individuals in the population and ensuring the spread of these individuals. The 'best' set of individuals are identified from the population by sorting their objective function values such that in this set there is no individual which improves an objective without worsening another one. The spread of individuals is ensured by grouping individuals with objective function values close to each other, retaining just one individual in this group, and discarding the rest. Variation consists of generating new individuals to be added to the set of individuals which survive the selec-
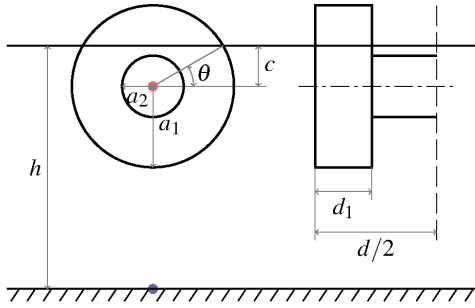
Figure 1: Two-dimensional sketch (side and front views).

Table 1: Variables of the cylinder

Geometric variable	min [m]	max [m]
Total width (d)	4	20
Thickness of larger cylinders (d_1)	1	$d/2 - 1$
Radius of larger cylinders (a_1)	2	7
Radius of smaller cylinder (a_2)	1	$0.95c$

tion process, to make up a new population. The new population is again subjected to selection and variation operations, and the process is repeated for a number of *generations*, or iterations, until convergence is observed. The final population is taken as the optimum set of solutions.

For each individual, $P_{\max}$ is obtained according to (2), where the hydrodynamic parameters X_e, m, and R are computed using the higher-order panel method of WAMIT, whereas A_s is calculated from known formulas. Here, A_s is taken as the total surface area and not the submerged surface area. The whole optimization routine is programmed in MATLAB, which then needs to perform repeated calls of WAMIT. The basic geometry is modelled using MultiSurf, and by virtue of the link between WAMIT and the Relational Geometry Kernel of MultiSurf (Lee et al., 2002), any variations in dimensions may be imposed only by modifying a few lines in the Geometric Data File. Further, it is convenient to minimize both objective functions instead of maximizing one and minimizing the other. Thus, the first objective function is recast into $f_1^{\text{obj}} = k / \int_{\omega_{\min}}^{\omega_{\max}} P_{\max}(\omega)\, d\omega$, where k is a scale factor which is used so that the values of f_1^{obj} is comparable to those of f_2^{obj}.

4   Case study

We consider a wave energy absorber in the form of a horizontal composite circular cylinder oscillating about a horizontal axis fixed at the bottom, where the power take-off is located. The geometry of the cylinder consists of a central part and two surface-piercing ends. The central part, which is submerged close to the water surface, has the purpose of introducing multiple resonances. The two ends, which are of a larger diameter, have the purpose of supplying additional buoyancy. A sketch of the cylinder is shown in Fig. 1.

The variables to be optimized are the radii of the larger cylinders and the smaller cylinder, a_1 and a_2, as well as the thickness of the larger cylinders d_1 and the total width d (see Table 1 for the specified limits). The ratio of the depth of submergence of the cylinder axis c to the radius of the larger cylinder a_1 is fixed. For this geometric configuration, $S = (M_w - M)g(h - c) + 4\rho g d_1 a_1^3 \cos^3\theta/3$, where M_w is the mass of the displaced water and h is the water depth.

Results are obtained for $h = 15$ m, incident wave amplitude $A = 1$ m, $c/a_1 = 0.6$, $M/M_w = 0.4$, $\omega_{\min} = 0.4$ rad/s, and $\omega_{\max} = 1.3$ rad/s. The hydrodynamic parameters are computed for every 0.02 rad/s. Interpolation is used to refine this resolution by a factor of 3. A population size of 10 is chosen, and the maximum number of generations is 4. The total time taken to complete the optimization in this case was less than 3 hours on a 2.50 GHz, 2.96 GB RAM PC.

The evolution of the 'best' solutions at the end of each generation is shown in Fig. 2 (top). The optimum geometries at the end of generation 4 are shown in Fig. 3, and the corresponding objective function values are plotted in Fig. 2 (middle). It is clear that among the optimum geometries, more power can be absorbed only by increasing the surface area. Further, it is observed that the radii of the central cylinder tend to the maximum limit. This could be explained by the fact that more energy is available close to the water surface. On the other hand, the radii of the larger cylinders are not maximized. In fact, for geometries 6 to 10, $a_1 = 2$ m, the minimum limit.

The maximum mean absorbed power is plotted in Fig. 4 (right) for some selected optimum geometries, while Fig. 4 (left) shows the behaviour of the added inertia and the function $S\omega^{-2} - M$. It is shown that the frequencies for which the added inertia intersects the function $S\omega^{-2} - M$ correspond to the frequencies where $P_{\max} = P_{\lim}$. A case of multiple resonances is seen for geometry 1.

The next step after identifying the set of optimum solutions is to choose one solution from it. Further information is required for this purpose, but for the present, let us say that the optimum should minimize the ratio of A_s to $\int_{\omega_{\min}}^{\omega_{\max}} P_{\max}(\omega)\, d\omega$. Then, according to Fig. 2 (bottom), geometry 6 should be chosen.
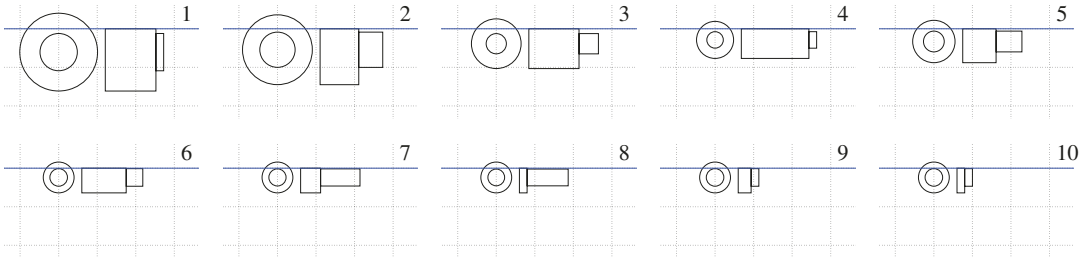
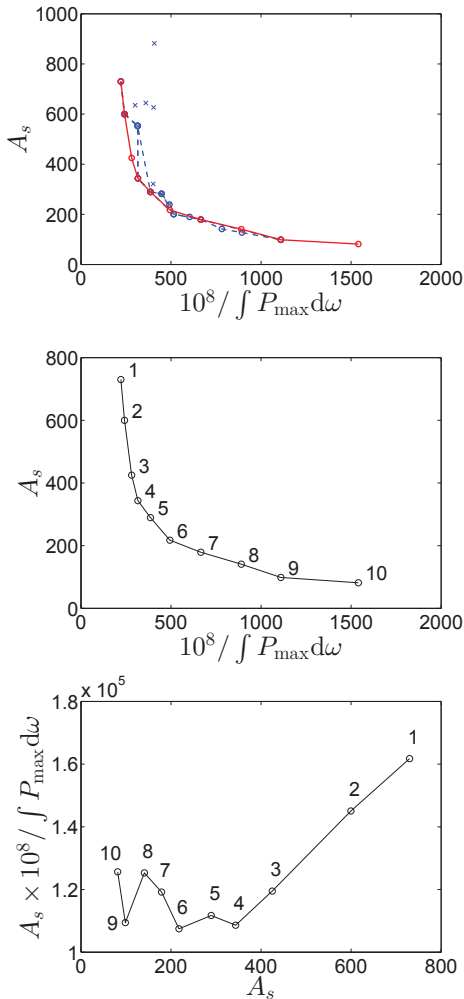Figure 3: Optimum geometries. One grid is 5×5 m^2.

Figure 2: Top: Initial population (crosses) and 'best' solutions at the end of each generation (circles), plotted in the objective function space. The final solutions are identified in red. Middle: Final objective function values. Bottom: f_2^{obj} versus $f_1^{\mathrm{obj}} f_2^{\mathrm{obj}}$.

5 Conclusion

The increasing efficiency of today's computers has permitted intensive numerical optimizations to be carried out within a reasonable time. We have illustrated this by presenting an example of how a multi-objective optimization algorithm may be used to optimize the geometry of a wave energy absorber in the form of a composite circular cylinder. While we have used simple expressions as the optimization objectives in this example, the importance of considering other objectives besides maximizing power absorption is evident.

The present formulation of the problem appears to favour smaller geometries over larger ones. This, however, is likely to be dependent on the selected range of wave frequencies. Further information such as the wave climate, if available, should preferably be included, and more than two objectives may be considered.

The method may be applied to optimize other geometric configurations. It may be worthwhile to compare the present results to those of a uniform circular cylinder. Perhaps more interestingly, the method may be applied to find optimum configurations of arrays of wave energy absorbers, which are not quite practical to study experimentally.

References

A. Babarit, J. Hals, M. J. Muliawan, A. Kurniawan, T. Moan, and J. Krokstad. Numerical benchmarking study of a selection of wave energy converters. *Renewable Energy*, 41(0):44–63, 2012.

D. V. Evans and R. Porter. Wave energy extraction by coupled resonant absorbers. *Phil. Trans. R. Soc. A*, 370(1959):315–344, 2012.

C.-H. Lee, J. S. Letcher Jr., R. G. Mack II, J. N. Newman, D. M. Shook, and E. Stanley. Integration of geometry definition and wave analysis software. In *Proc. 21st Int. Conf. Offshore Mech. Arctic Eng.*, pages 721–733, Oslo, Norway, 2002.
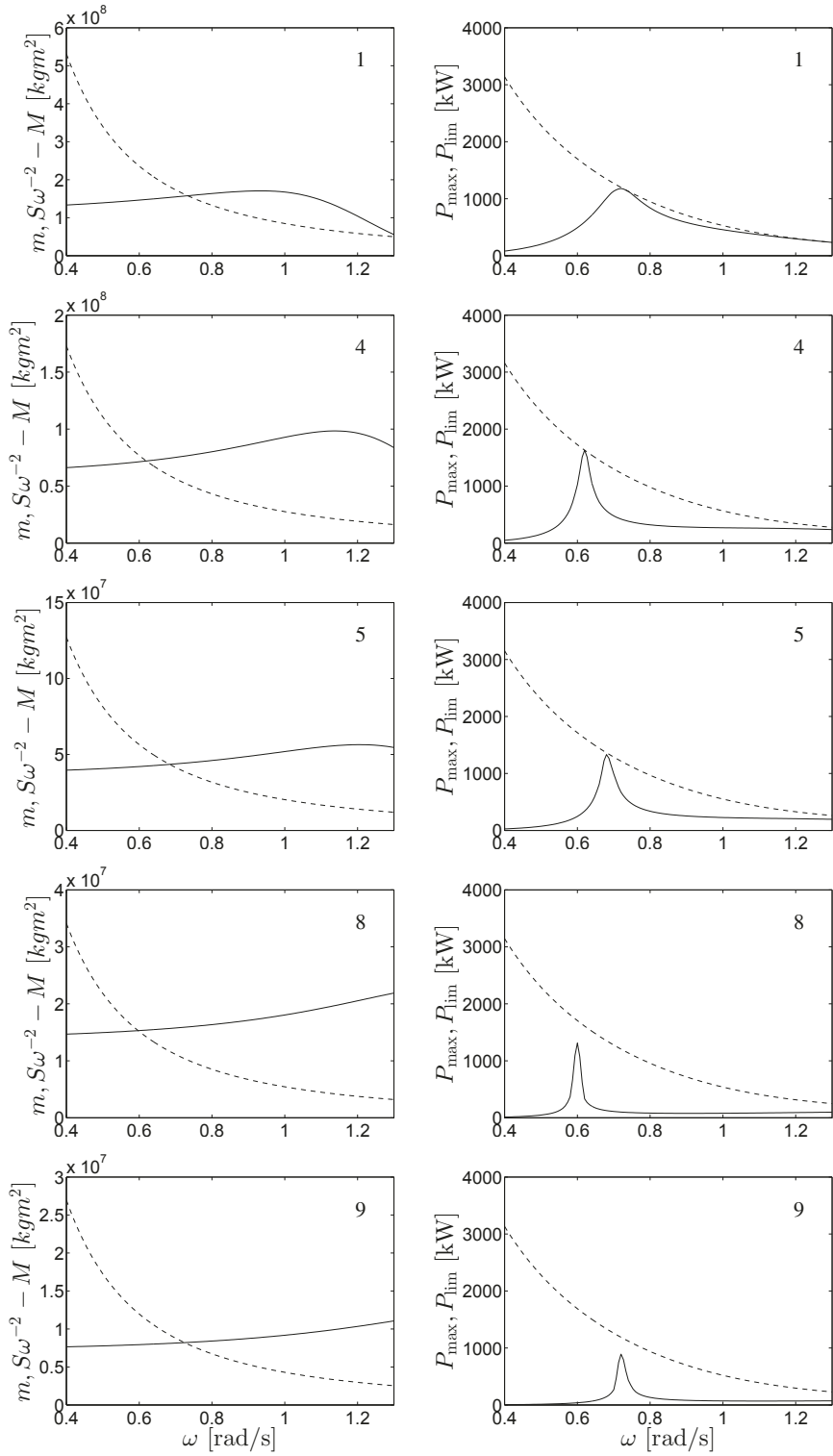
Figure 4: Added inertia and $S\omega^{-2} - M$ (left), and maximum mean absorbed power and the theoretical limit (right), corresponding to optimum geometries 1, 4, 5, 8, and 9.

Paper G

Modelling of wave energy converters using bond graph

A. Kurniawan, E. Pedersen, and T. Moan
Proceedings of 10th International Conference on Bond Graph Modeling and Simulation,
Genoa, 8-11 July 2012

Modelling of Wave Energy Converters Using Bond Graph

Adi Kurniawan[1], Eilif Pedersen[2], and Torgeir Moan[1]

[1]Centre for Ships and Ocean Structures
[2]Department of Marine Technology
Norwegian University of Science and Technology, NO-7491 Trondheim, Norway
{adi.kurniawan, eilif.pedersen, torgeir.moan}@ntnu.no

Abstract

This article summarizes recent works by the authors on the modelling of wave energy converters (WECs) using the bond graph method. Generic models for two categories of WECs, viz. oscillating bodies and oscillating water columns (OWCs), are presented. Oscillating-body WECs utilise relative motion between a moving body and a fixed reference, such as the sea bed, or between several moving bodies. On the other hand, oscillating-water-column WECs utilise the motion of a mass of water relative to a fixed reference, or relative to a moving body. A generic model of self-reacting multibody WECs, one subcategory of the former, is presented here for the first time. Finally, as a case study, we model a particular type of floating OWCs known as the backward-bent duct buoy, and present some simulation results. To accelerate simulations, the wave radiation forces are modelled using state-space approximations, instead of convolutions used in an earlier work.

1. INTRODUCTION

Ocean waves constitute an abundant source of renewable energy. Man has been seeking to exploit this potential for many years, but it was the oil crisis in the early 1970s that spurred modern wave energy research activities worldwide. During this period, interesting concepts were proposed and tested, and fundamental theories were laid out. Sadly, with the decline of oil price, funding for wave energy research was drastically reduced in the 1980s. Recently, however, there has been a renewed global interest in wave energy [1]. A scientific meeting was organised very recently which brought together the world's experts on wave energy. A special issue has been published which contains the papers presented at the meeting (see [2] and the accompanying papers in the same issue). Together they serve as the latest summary available of the state-of-the-art of wave energy research.

The use of bond graph for modelling wave energy converters (WECs) is relatively new. An allusion to the bond graph method was made in an article from 1984 by Jefferys [3], who presented a word bond graph of a fixed oscillating water column (OWC) device, although he did not explicitly use the term 'bond graph.' Otherwise it was only more recently that a number of works using bond graph started to appear in wave energy literature.

The first of these was a paper presented at a conference dedicated to wave energy, which contained an application of bond graph in the modelling of a power take-off (PTO) system for a hinged-barge WEC used to generate electricity and produce potable water [4]. The bond graph method was further introduced to the wave energy community by Engja and Hals [5], who described the modelling of a WEC consisting of a floating buoy connected to a semi-submersible. Others have then followed by considering diverse applications and objectives [6–9]. An overview of bond graph modelling of WECs was given by Hals [10], who also presented bond graph models for the mooring lines, power conditioning, and grid connection.

The purpose of this article is to summarize our recent works on bond graph modelling of WECs. Our emphasis is on the modelling of the primary interface, where hydrodynamic interactions of the device with the waves take place. We will focus on the oscillating-body and the oscillating-water-column WECs.

2. GENERIC WAVE ENERGY CONVERTERS

In terms of device hydrodynamics, two large categories of WECs may be identified, viz. the oscillating bodies and the oscillating water columns. Oscillating-body WECs utilise relative motion between a moving body and a fixed reference, such as the sea bed, or between several moving bodies. Oscillating-water-column WECs utilise the motion of an enclosed mass of water relative to a fixed reference, or relative to a moving body. For oscillating bodies, the absorbed power is evaluated from the product of body force and velocity, while for oscillating water columns, it is evaluated from the product of air pressure and volume flow.

Basic models of each category are presented in the following. Time-domain formulation is assumed. For simplicity and as is common in theory, a linear damper is used to represent the PTO. Various nonlinearities which are typically present are included. Also, incident plane waves are assumed.

2.1. Oscillating Bodies

The first subcategory we consider is a WEC comprising a rigid body oscillating against a fixed reference. We assume that the body is constrained to oscillate in only *one* degree of freedom. The body could be sliding along a fixed guide, for example, or oscillating about a fixed axis. The oscillation of the body upon wave action drives the PTO.

The equation of motion for this device can be written as

$$F_e(t) = [m_m + m(\infty)]\dot{u}(t) + k(t) * u(t) + (S_b + S)s(t) \\ + R_C \operatorname{sgn} u(t) + R_q u(t)|u(t)| + rR_u u(t), \tag{1}$$

where $F_e(t)$ is the wave excitation force, m_m is the inertia of the body, $m(\infty)$ is the infinite-frequency added inertia, $u(t)$ is the body velocity, $k(t)$ is the radiation impedance impulse response function (IRF), S_b is the hydrostatic stiffness, S is the external stiffness, if any, $s(t)$ is the body displacement, R_C is the Coulomb damping coefficient, R_q is the quadratic damping coefficient, r is some transformation factor, and R_u is the load resistance (PTO damping). Linear hydrodynamics is usually assumed and thus the hydrodynamic forces (wave exciting force, added inertia, and radiation damping) may be computed from programs employing linear panel method such as WAMIT [11].

A bond graph model of this WEC is shown in Fig. 1. The force balance on the body is represented by the bonds connected to the left 1-junction. The wave exciting force is represented by an *Se* element, the sum of the structural inertia and the infinite-frequency added inertia by an *I* element, the hydrostatic restoring force by a *C* element, the wave radiation force by an *R* element, the external restoring force by a *C* element, and the nonlinear Coulomb and quadratic damping forces each by an *R* element. The *TF* element, representing some transformation relation such as between mechanical rotational and translational domains, connects the body and the PTO (represented by an *R* element). The circle labelled *P* is a power sensor.
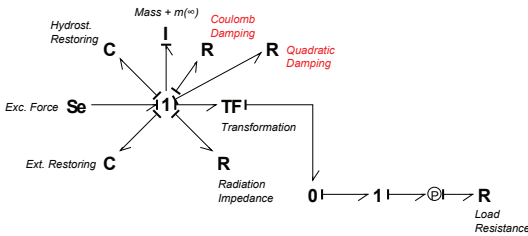

Figure 1. Bond graph model of an oscillating-body WEC reacting against a fixed reference.

If the body moves in a degree of freedom other than the conventional surge, sway, heave, roll, pitch, or yaw (for example, the body slides along a slanted guide), the method of
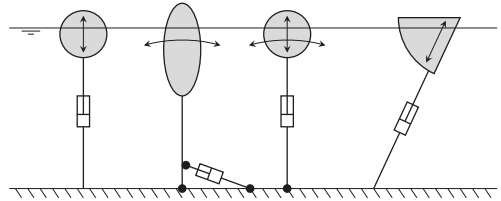

Figure 2. Examples of WECs that may be represented by the bond graph in Fig. 1. Arrows represent degrees of freedom. Dots represent hinges. Attachment points of the guides may alternatively be above the water surface.

generalised modes [12] may be employed to evaluate the generalised forces. One can in principle use the same bond graph as in Fig. 1. If, for a body sliding along a vertical guide, the guide along which the body slides is not fixed, but hinged at one end, an additional degree of freedom (i.e. pitch about this hinge) is introduced. If the body is symmetric in the incident wave direction, however, there is no hydrodynamic coupling between pitch and heave, and so one can still use the bond graph in Fig. 1. Examples of WECs that may be represented by the bond graph in Fig. 1 are shown in Fig. 2.

As a second subcategory, we consider a self-reacting WEC. In self-reacting systems, instead of a fixed reference, the force reaction is provided by a second body which is moving with different phase and/or amplitude from the first body. Power is converted through the relative motion between these bodies.
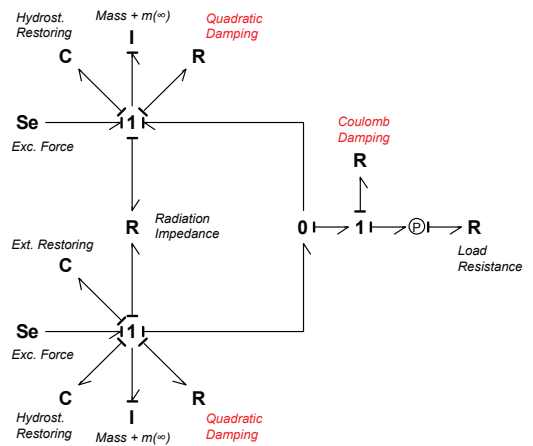

Figure 3. Bond graph model of a two-body self-reacting WEC.

A bond graph model of a self-reacting WEC consisting of two bodies is shown in Fig. 3. Each of the two 1-junctions on the left represents the velocity of each body. Two bonds from
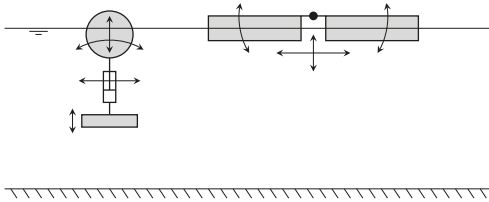
Figure 4. Examples of WECs that may be represented by the bond graph in Fig. 3. Arrows represent degrees of freedom. For the WEC on the right, the PTO is at the hinge (represented by a dot).

Figure 6. Floating and fixed OWCs.

these junctions are connected to a 0-junction which connects to the PTO, signifying the fact that it is the relative motion between the two bodies that is used for power conversion. The hydrodynamic interaction between the two bodies is taken into account by a radiation impedance matrix, represented by an R-field. Normally only one of the bodies is moored; this external restoring force is represented by a C element. This bond graph may represent a system of two bodies where one body is sliding along a guide fixed to the other body, provided the bodies are symmetric in the incident wave direction (for then the vertical motions of the bodies are uncoupled from the horizontal and rotational motions). It may also represent a system of two hinged identical bodies (see Fig. 4).

Using the method of generalised modes, we may represent the system in a more compact vector bond graph form, as shown in Fig. 5, by appropriate selection of the modes, with one mode being the relative motion between the bodies. The same bond graph may represent multiple hinged bodies where the PTO are located at the hinges.
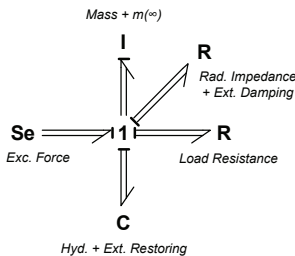

Figure 5. Bond graph model of a self-reacting WEC.

2.2. Oscillating Water Columns

An OWC comprises an air chamber with a submerged opening and an opening to the atmosphere fitted with an air turbine. Upon wave action, the internal water surface rises and falls, resulting in oscillating pressure in the chamber. The difference between pressures inside and outside the air
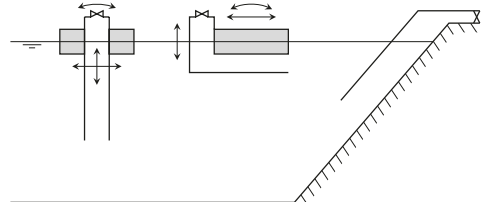
chamber results in an air flow through the turbine, which in turn drives an electric generator. A self-rectifying air turbine, which rotates in one direction regardless of the flow, is usually employed, eliminating the need for rectifying valves. An OWC may be fixed or floating (see Fig. 6).

We first consider a fixed OWC. For a fixed OWC, the chamber is fixed. The equation of motion can be written as

$$Q_e(t) = y(t) * p(t) + Q_v(t) + Q_c(t) + (R_e + 1/R_u) p(t), \quad (2)$$

where $Q_e(t)$ is the excitation volume flow, $p(t)$ is the chamber pressure, $y(t)$ is the radiation admittance IRF, $Q_v(t)$ is the volume flow through the relief valve, $Q_c(t)$ is the volume flow due to air compressibility, R_e is the external damping coefficient, and R_u is the load resistance.

The flow $Q_v(t)$ through the relief valve is governed by the pressure difference across the valve:

$$Q_v(t) = \begin{cases} \dfrac{p(t)}{p_{cl}} Q_{cl} & \text{if } |p(t)| < p_{cl} \\ \operatorname{sgn} p(t) \left[Q_{cl} + \dfrac{|p(t)| - p_{cl}}{p_{op} - p_{cl}} (Q_{op} - Q_{cl}) \right] \\ \qquad\qquad \text{if } p_{cl} \le |p(t)| \le p_{op} \\ C_d A_{\max} \sqrt{\dfrac{2}{\rho_a} |p(t)|} \operatorname{sgn} p(t) & \text{if } |p(t)| > p_{op}, \end{cases}$$

$$(3)$$

where

$$Q_{cl} = C_d A_{\min} \sqrt{\frac{2}{\rho_a} p_{cl}} \quad (4)$$

$$Q_{op} = C_d A_{\max} \sqrt{\frac{2}{\rho_a} p_{op}}. \quad (5)$$

The pressures p_{cl} and p_{op} are reference pressures for the closing and opening of the valve. The valve is closed if $|p| < p_{cl}$, and is fully open if $|p| > p_{op}$. To be realistic, the leakage area $A_{\min}$ is introduced to allow possible leakage when the valve is closed. The fully open flow area is denoted by $A_{\max}$, while ρ_a is the air density, and C_d is the discharge coefficient.

The air compressibility in the chamber follows this nonlinear relationship:

$$p_0 + p = p_0 \left(\frac{V_0}{V_0 - \Delta V} \right)^{\gamma}, \quad (6)$$
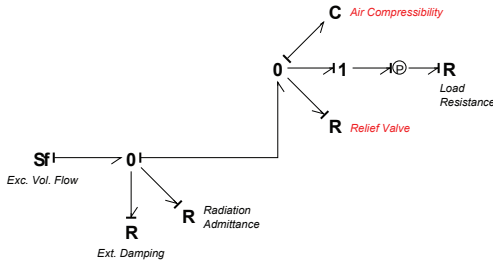
Figure 7. Bond graph model of a fixed OWC.

Figure 8. Bond graph model of a floating OWC whose chamber is free to move in one degree of freedom.

where p_0 is the atmospheric pressure and V_0 is the average air volume in the chamber. The volume change due to compressibility is denoted by $\Delta V = \int_0^t Q_c(t)dt$. The specific heat ratio γ depends on whether the expansion and compression occur rapidly or slowly. The value $\gamma = 1.4$ is usually adopted.

A bond graph model of a fixed OWC is shown in Fig. 7. A 0-junction is used since we are dealing with volume flow balance instead of force balance (cf. Fig. 1). The excitation volume flow is represented by an Sf element, the wave radiation volume flow by an R element, the air compressibility by a C element, and the relief valve by an R element.

For a floating OWC, the chamber is free to move. The coupled equations of motion for a floating OWC whose chamber is free to move in one degree of freedom can be written as

$$
\begin{aligned}
F_e(t) = &[m_m + m(\infty)]\dot{u}(t) + k(t) * u(t) - C(\infty)p(t) \\
&- h(t) * p(t) + (S_b + S)s(t) + R_C \operatorname{sgn} u(t) \\
&+ R_q u(t)|u(t)| - rp(t)
\end{aligned}
\tag{7}
$$

$$
\begin{aligned}
Q_e(t) = &y(t) * p(t) + C(\infty)u(t) + h(t) * u(t) \\
&+ Q_v(t) + Q_c(t) + ru(t) + (R_e + 1/R_u)\,p(t),
\end{aligned}
\tag{8}
$$

where $C(\infty)$ is the infinite-frequency value of the real part of the radiation coupling coefficient (see [13]), and $h(t)$ is the radiation coupling IRF.

A bond graph model of this floating OWC is shown in Fig. 8. One can see that it is a combination of an oscillating body and a fixed OWC, connected by an additional TF element (cf. Figs. 1 and 7). The force balance on the OWC body is represented by the bonds connected to the 1-junction on the upper left. The volume flow balance in the OWC chamber is represented by the bonds connected to the 0-junction on the bottom left. The coupling between the body velocity and the chamber pressure is represented by the TF element connecting the 0-junction to the 1-junction. The TF element to the right of the first 1-junction carries out the transformation between force-velocity and pressure-volume flow. The 0-junction on the right connects 1- and 0-junctions on the left, signifying that the volume flow relative to the body is utilised for power absorption. The nonlinear terms in the model are
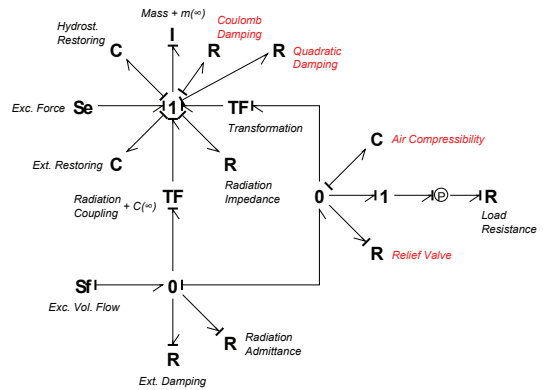
the Coulomb and quadratic damping forces on the body, the volume flow due to air compressibility in the chamber, and the volume flow through the relief valve.

3. RADIATION FORCE MODELS

The traditional representation of the wave radiation force is in the form of a convolution [14]. An alternative is to approximate it by a state-space model [15]. A comparative study of these radiation force models has been presented in [16]. The state-space model, obtained according to the method presented in [17], was shown to be more efficient for time-domain simulation than directly integrating the convolution at every time step, while maintaining the same degree of accuracy.

In the state-space model the convolution term

$$
\mu(t) = k(t) * u(t) = \int_0^t k(t-\tau)u(\tau)d\tau
\tag{9}
$$

is replaced by a set of coupled linear ordinary differential equations, which may be expressed in matrix form (see, e.g. [18]):

$$
\dot{\mathbf{x}}(t) = \hat{\mathbf{A}}\mathbf{x}(t) + \hat{\mathbf{B}}u(t)
\tag{10}
$$

$$
\hat{\mu}(t) = \hat{\mathbf{C}}\mathbf{x}(t)
\tag{11}
$$

where $\mathbf{x}(t)$ is the state vector, the number of components of which corresponds to the *order* of the state-space model, and $\hat{\mathbf{A}}, \hat{\mathbf{B}}, \hat{\mathbf{C}}$ are constant matrices.

We use the frequency-domain identification approach following the algorithm detailed in [17, 19]. The method uses frequency-domain hydrodynamic data for identification. The approach is to fit a rational transfer function

$$
\hat{K}(s) = \frac{P(s)}{Q(s)} = \frac{p_r s^r + p_{r-1}s^{r-1} + \ldots + p_0}{s^n + q_{n-1}s^{n-1} + \ldots + q_0},
\tag{12}
$$

where $s = i\omega$, to the frequency response functions (FRFs) $K(\omega)$, $Y(\omega)$, or $H(\omega)$, depending on the problem considered. Further constraints on the model have been derived in [20] based on the properties of the FRF and its corresponding IRF. A least-squares fitting method is applied to find the coefficients p_i and q_i in (12), and once the coefficients are obtained, the matrices $\hat{\mathbf{A}}$, $\hat{\mathbf{B}}$, and $\hat{\mathbf{C}}$ can be constructed using any of the standard canonical forms.

4. CASE STUDY: BACKWARD-BENT DUCT BUOY

As a case study, we consider a particular type of floating OWC known as the backward-bent duct buoy (BBDB) first proposed by Masuda [21]. A two-dimensional sketch of the device is shown in Fig. 6, centre. The device is interesting in that it utilises coupled resonances of the water column and the device motions in order to broaden the power absorption bandwidth. These multiple resonances are achieved without the introduction of additional bodies, thus making a BBDB a compact device.

The geometry considered is the same as that in [8]. We assume that the device is oriented with its submerged opening in line with the incident wave direction. Thus, the relevant degrees of freedom are surge, heave, and pitch.

A bond graph model has been presented in [8] and is reproduced in Fig. 9. Since we deal with more than one degree of freedom, vector bonds are now connected to the 1-junction representing the body velocities. To the right of this 1-junction, a TF element carries out the transformation required to obtain the vertical velocity of the body at the centre of the mean internal free surface, according to

$$u_b = \mathbf{T}^{\mathrm{T}}\mathbf{u}, \tag{13}$$

where u_b is the vertical velocity of the body at the centre of the mean internal free surface, and $\mathbf{T}$ is the transformation vector given as

$$\mathbf{T} = (0, 0, 1, 0, -x_b, 0)^{\mathrm{T}}, \tag{14}$$

where x_b is the x-coordinate of the centre of the mean internal free surface. To the right of this TF element, another TF element converts the force-velocity pair to pressure-volume flow pair, with the internal mean free surface area as the transformation factor. The R elements labelled 'Ext. Damping' represent losses arising from viscous effects and mooring damping. These losses have the effect of reducing both the body motions and the volume flow available to the turbine. External restoring forces are contributed by moorings, whose contribution is assumed to be a small stiffness in surge.

With state-space models replacing the convolutions for the radiation forces as explained in the previous section,
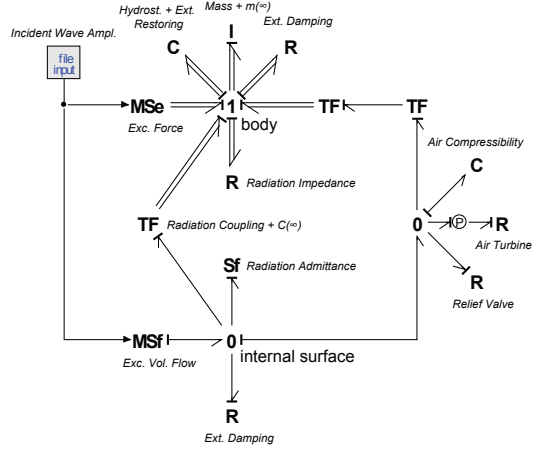
Figure 9. Bond graph model of a backward-bent duct buoy.
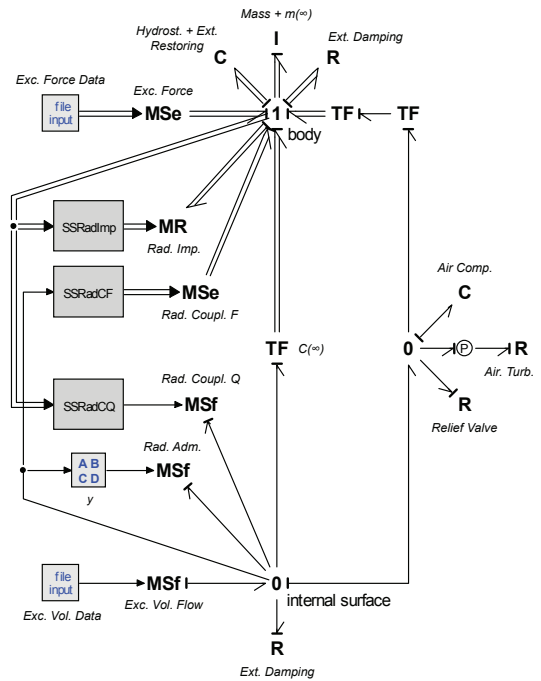
Figure 10. Bond graph model of the backward-bent duct buoy with state-space representations of the radiation forces.

the model becomes as shown in Fig. 10. The rectangles labeled 'SSRadImp,' 'SSRadCF,' and 'SSRadCQ' are submodels each containing a number of state-space models. These
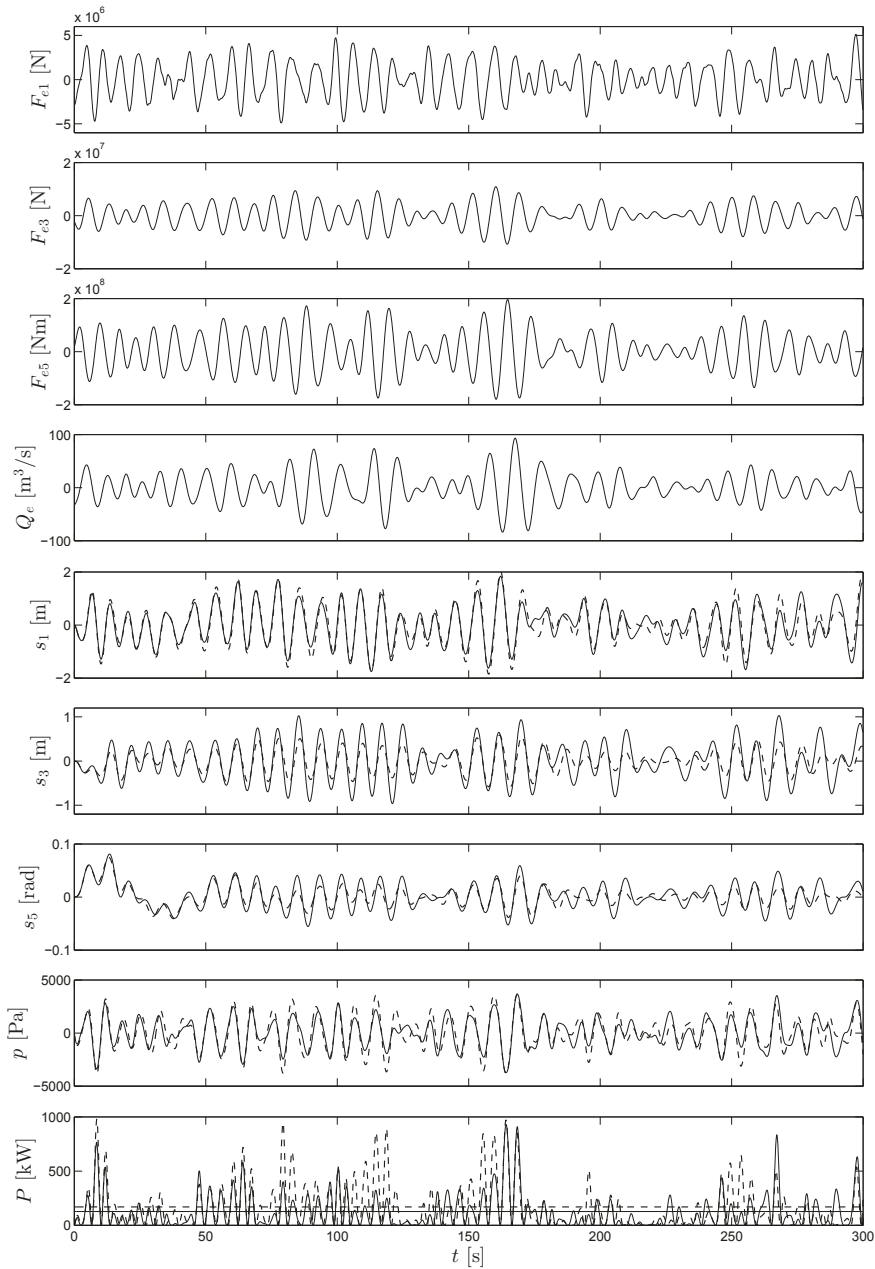
Figure 11. Wave excitation forces, excitation volume flow, body displacements, chamber pressure, and absorbed power of the backward-bent duct buoy, for $T_p = 8$ s and $H_s = 3$ m. Results obtained from the present model (state-space representations of the radiation forces) are plotted in solid lines, while results obtained from direct integration of the convolutions [8] are plotted in dashed lines. Horizontal lines in the absorbed power plot represent the mean values.

take either the body velocities or the chamber pressure as inputs, hence the signal bonds coming from the 1- and 0-junctions into these rectangles. The submodel 'SSRadImp' takes the body velocities as inputs and outputs the wave forces on the body due to its own motions. This submodel contains 9 state-space models, of which 6 are distinct from each other. The submodel 'SSRadCF' takes the chamber pressure as input and outputs the wave forces on the body due to the chamber pressure. This submodel contains 3 distinct state-space models. The submodel 'SSRadCQ' takes the body velocities as inputs and outputs the volume flow through the internal surface due to the body motions. This submodel contains 3 state-space models, which are the same as those in submodel 'SSRadCF'. The square below the submodel 'SSRadCQ' is another state-space model taking the chamber pressure as input and outputs the volume flow through the internal surface due to this pressure. In total, 16 state-space models, of which 10 are distinct from each other, are required for the whole system.

Shown in Fig. 11 is a set of simulation results obtained from irregular incident waves with spectral peak period $T_p = 8$ s and significant wave height $H_s = 3$ m. The simulation is carried out using 20-sim [22]. The excitation force and volume flow time series are generated before the simulation and stored as data files to be read during the simulation (see Fig. 10). A method to generate the time series has been described in [16].

For comparison, results from an earlier work [8] which were obtained by directly integrating the convolutions at every time step are reproduced in the same figure. Fair agreement between the two sets of results is observed. The discrepancies could be due to the number of state-space representations involved. As noted previously, this model contains a total of 16 state-space representations, of which 10 are distinct. An earlier study [16] has shown excellent agreement between results obtained from state-space radiation force models and convolution models for a floating OWC in the form of a simple square box with a square opening, and having only one degree of freedom (heave). This system, however, has only 4 state-space representations, of which 3 are distinct. Furthermore, the present geometry (a BBDB), with only one plane of symmetry, is more complicated than a square box, which has three planes of symmetry. On the other hand, simulation of the present model is significantly faster than that with convolutions, especially for a system with 16 convolutions.

5. CONCLUSION

We have modelled, using the bond graph method, two categories of wave energy converters (WECs), viz. oscillating bodies and oscillating water columns (OWCs). A fixed OWC and an oscillating body have distinct features both in terms of hydrodynamics and the nonlinearities involved. A floating OWC can be seen as a combination of a fixed OWC and an oscillating body, coupled through additional hydrodynamic coupling parameters. This is seen clearly in the bond graph representation.

As a case study, we have modelled a particular type of floating OWC known as the backward-bent duct buoy (BBDB), where the wave radiation forces have been approximated using state-space representations. Some simulation results have been presented and compared to those reported in an earlier work.

The WECs considered in this paper are by no means exhaustive, but the selected examples are intended to be representative of the WEC concepts available to date. It would be interesting to model other categories of WECs, such as those which make use of flexible bodies (e.g. [23]) and overtopping WECs (e.g. [24]). To our knowledge, no bond graph models have been developed for these systems.

Our focus has been on the primary interface and not so much on the power take-off (PTO) system. A comprehensive WEC model would require a more realistic PTO model instead of a linear damper. This PTO model can be built separately and connected to the primary interface model, as illustrated in [9].

Harnessing wave energy in an economical manner is still a dream. It is our hope that this paper would instill some interest in the experienced bond graphers to help make this dream a reality.

ACKNOWLEDGEMENTS

REFERENCES

[1] J. Falnes, "A review of wave-energy extraction," *Marine Structures*, vol. 20, pp. 185–201, 2007.

[2] F. J. M. Farley, "Preface: The peaks and troughs of wave energy, the dreams and the reality," *Philosophical Transactions of the Royal Society A: Mathematical, Physical and Engineering Sciences*, vol. 370, no. 1959, pp. 201–202, 2012.

[3] E. R. Jefferys, "Simulation of wave power devices," *Applied Ocean Research*, vol. 6, no. 1, pp. 31–39, 1984.

[4] G. Nolan, M. O'Catháin, J. Murtagh, and J. V. Ringwood, "Modelling, simulation and validation of the PTO system for a hinge-barge wave-energy converter," in *Proc. 5th European Wave Energy Conf.*, 2003, pp. 1–8.

[5] H. Engja and J. Hals, "Modelling and simulation of sea wave power conversion systems," in *Proceedings of the 7th European Wave and Tidal Energy Conference*, Porto, Portugal, 2007, pp. 1–7.

[6] G. Bacelli, J. C. Gilloteaux, and J. Ringwood, "State space model of a hydraulic power take off unit for wave energy conversion employing bondgraphs," in *Proceedings of World Renewable Energy Conference*, 2008, pp. 1–4.

[7] L. M. Yang, J. Hals, and T. Moan, "A wear model for assessing the reliability of wave energy converter in heave with hydraulic power take-off," in *Proceedings of the 8th European Wave and Tidal Energy Conference*, Uppsala, Sweden, 2009, pp. 874–881.

[8] A. Kurniawan, J. Hals, and T. Moan, "Modelling and simulation of a floating oscillating water column," in *Proceedings of the 30th International Conference on Ocean, Offshore and Arctic Engineering*, Rotterdam, The Netherlands, 2011.

[9] A. Kurniawan, E. Pedersen, and T. Moan, "Bond graph modelling of a wave energy conversion system with hydraulic power take-off," *Renewable Energy*, vol. 38, no. 1, pp. 234–244, 2012.

[10] J. Hals, "Modelling and phase control of wave-energy converters," Ph.D. dissertation, Department of Marine Technology, Norwegian University of Science and Technology, Trondheim, 2010.

[11] WAMIT, WAMIT, Inc., Chestnut Hill, MA, 2008, version 6.4.

[12] J. N. Newman, "Wave effects on deformable bodies," *Applied Ocean Research*, vol. 16, no. 1, pp. 47–59, 1994.

[13] A. C. Fernandes, "Analysis of an axisymmetric pneumatic buoy by reciprocity relations and a ring-source method," Ph.D. dissertation, Department of Ocean Engineering, MIT, Cambridge, Massachusetts, 1983.

[14] W. E. Cummins, "The impulse response function and ship motions," David Taylor Model Basin, Tech. Rep., October 1962.

[15] E. R. Jefferys, "Device characterisation," in *Power from Sea Waves*, 1980, pp. 413–438.

[16] A. Kurniawan, J. Hals, and T. Moan, "Assessment of time-domain models of wave energy conversion systems," in *Proceedings of the 9th European Wave and Tidal Energy Conference*, Southampton, 2011.

[17] T. Perez and T. I. Fossen, "A Matlab Toolbox for Parametric Identification of Radiation-Force Models of Ships and Offshore Structures," *Modeling, Identification and Control*, vol. 30, no. 1, pp. 1–15, 2009.

[18] R. Taghipour, T. Perez, and T. Moan, "Hybrid frequency-time domain models for dynamic response analysis of marine structures," *Ocean Engineering*, vol. 35, no. 7, pp. 685–705, 2008.

[19] T. Perez and T. I. Fossen, "Practical aspects of frequency-domain identification of dynamic models of marine structures from hydrodynamic data," *Ocean Engineering*, vol. 38, no. 2-3, pp. 426–435, 2011.

[20] ——, "Time- vs. Frequency-domain Identification of Parametric Radiation Force Models for Marine Structures at Zero Speed," *Modeling, Identification and Control*, vol. 29, no. 1, pp. 1–19, 2008.

[21] Y. Masuda, T. Yamazaki, Y. Outa, and M. McCormick, "Study of backward bent duct buoy," in *OCEANS '87*, 1987, pp. 384 –389.

[22] 20-sim, Controllab Products B. V., Enschede, The Netherlands, 2009, version 4.1.

[23] F. J. M. Farley, "The free floating clam - a new wave energy converter," in *Proceedings of the 9th European Wave and Tidal Energy Conference*, Southampton, 2011.

[24] J. P. Kofoed, P. Frigaard, E. Friis-Madsen, and H. C. Sørensen, "Prototype testing of the wave energy converter wave dragon," *Renewable Energy*, vol. 31, no. 2, pp. 181–189, 2006.

Previous PhD theses published at the Departement of Marine Technology
(earlier: Faculty of Marine Technology)
NORWEGIAN UNIVERSITY OF SCIENCE AND TECHNOLOGY

Report No.	Author	Title
	Kavlie, Dag	Optimization of Plane Elastic Grillages, 1967
	Hansen, Hans R.	Man-Machine Communication and Data-Storage Methods in Ship Structural Design, 1971
	Gisvold, Kaare M.	A Method for non-linear mixed -integer programming and its Application to Design Problems, 1971
	Lund, Sverre	Tanker Frame Optimalization by means of SUMT-Transformation and Behaviour Models, 1971
	Vinje, Tor	On Vibration of Spherical Shells Interacting with Fluid, 1972
	Lorentz, Jan D.	Tank Arrangement for Crude Oil Carriers in Accordance with the new Anti-Pollution Regulations, 1975
	Carlsen, Carl A.	Computer-Aided Design of Tanker Structures, 1975
	Larsen, Carl M.	Static and Dynamic Analysis of Offshore Pipelines during Installation, 1976
UR-79-01	Brigt Hatlestad, MK	The finite element method used in a fatigue evaluation of fixed offshore platforms. (Dr.Ing. Thesis)
UR-79-02	Erik Pettersen, MK	Analysis and design of cellular structures. (Dr.Ing. Thesis)
UR-79-03	Sverre Valsgård, MK	Finite difference and finite element methods applied to nonlinear analysis of plated structures. (Dr.Ing. Thesis)
UR-79-04	Nils T. Nordsve, MK	Finite element collapse analysis of structural members considering imperfections and stresses due to fabrication. (Dr.Ing. Thesis)
UR-79-05	Ivar J. Fylling, MK	Analysis of towline forces in ocean towing systems. (Dr.Ing. Thesis)
UR-80-06	Nils Sandsmark, MM	Analysis of Stationary and Transient Heat Conduction by the Use of the Finite Element Method. (Dr.Ing. Thesis)
UR-80-09	Sverre Haver, MK	Analysis of uncertainties related to the stochastic modeling of ocean waves. (Dr.Ing. Thesis)
UR-81-15	Odland, Jonas	On the Strength of welded Ring stiffened cylindrical Shells primarily subjected to axial Compression
UR-82-17	Engesvik, Knut	Analysis of Uncertainties in the fatigue Capacity of

Welded Joints

UR-82-18	Rye, Henrik	Ocean wave groups
UR-83-30	Eide, Oddvar Inge	On Cumulative Fatigue Damage in Steel Welded Joints
UR-83-33	Mo, Olav	Stochastic Time Domain Analysis of Slender Offshore Structures
UR-83-34	Amdahl, Jørgen	Energy absorption in Ship-platform impacts
UR-84-37	Mørch, Morten	Motions and mooring forces of semi submersibles as determined by full-scale measurements and theoretical analysis
UR-84-38	Soares, C. Guedes	Probabilistic models for load effects in ship structures
UR-84-39	Aarsnes, Jan V.	Current forces on ships
UR-84-40	Czujko, Jerzy	Collapse Analysis of Plates subjected to Biaxial Compression and Lateral Load
UR-85-46	Alf G. Engseth, MK	Finite element collapse analysis of tubular steel offshore structures. (Dr.Ing. Thesis)
UR-86-47	Dengody Sheshappa, MP	A Computer Design Model for Optimizing Fishing Vessel Designs Based on Techno-Economic Analysis. (Dr.Ing. Thesis)
UR-86-48	Vidar Aanesland, MH	A Theoretical and Numerical Study of Ship Wave Resistance. (Dr.Ing. Thesis)
UR-86-49	Heinz-Joachim Wessel, MK	Fracture Mechanics Analysis of Crack Growth in Plate Girders. (Dr.Ing. Thesis)
UR-86-50	Jon Taby, MK	Ultimate and Post-ultimate Strength of Dented Tubular Members. (Dr.Ing. Thesis)
UR-86-51	Walter Lian, MH	A Numerical Study of Two-Dimensional Separated Flow Past Bluff Bodies at Moderate KC-Numbers. (Dr.Ing. Thesis)
UR-86-52	Bjørn Sortland, MH	Force Measurements in Oscillating Flow on Ship Sections and Circular Cylinders in a U-Tube Water Tank. (Dr.Ing. Thesis)
UR-86-53	Kurt Strand, MM	A System Dynamic Approach to One-dimensional Fluid Flow. (Dr.Ing. Thesis)
UR-86-54	Arne Edvin Løken, MH	Three Dimensional Second Order Hydrodynamic Effects on Ocean Structures in Waves. (Dr.Ing. Thesis)
UR-86-55	Sigurd Falch, MH	A Numerical Study of Slamming of Two-Dimensional Bodies. (Dr.Ing. Thesis)
UR-87-56	Arne Braathen, MH	Application of a Vortex Tracking Method to the Prediction of Roll Damping of a Two-Dimension Floating Body. (Dr.Ing. Thesis)

UR-87-57	Bernt Leira, MK	Gaussian Vector Processes for Reliability Analysis involving Wave-Induced Load Effects. (Dr.Ing. Thesis)
UR-87-58	Magnus Småvik, MM	Thermal Load and Process Characteristics in a Two-Stroke Diesel Engine with Thermal Barriers (in Norwegian). (Dr.Ing. Thesis)
MTA-88-59	Bernt Arild Bremdal, MP	An Investigation of Marine Installation Processes – A Knowledge - Based Planning Approach. (Dr.Ing. Thesis)
MTA-88-60	Xu Jun, MK	Non-linear Dynamic Analysis of Space-framed Offshore Structures. (Dr.Ing. Thesis)
MTA-89-61	Gang Miao, MH	Hydrodynamic Forces and Dynamic Responses of Circular Cylinders in Wave Zones. (Dr.Ing. Thesis)
MTA-89-62	Martin Greenhow, MH	Linear and Non-Linear Studies of Waves and Floating Bodies. Part I and Part II. (Dr.Techn. Thesis)
MTA-89-63	Chang Li, MH	Force Coefficients of Spheres and Cubes in Oscillatory Flow with and without Current. (Dr.Ing. Thesis
MTA-89-64	Hu Ying, MP	A Study of Marketing and Design in Development of Marine Transport Systems. (Dr.Ing. Thesis)
MTA-89-65	Arild Jæger, MH	Seakeeping, Dynamic Stability and Performance of a Wedge Shaped Planing Hull. (Dr.Ing. Thesis)
MTA-89-66	Chan Siu Hung, MM	The dynamic characteristics of tilting-pad bearings
MTA-89-67	Kim Wikstrøm, MP	Analysis av projekteringen for ett offshore projekt. (Licenciat-avhandling)
MTA-89-68	Jiao Guoyang, MK	Reliability Analysis of Crack Growth under Random Loading, considering Model Updating. (Dr.Ing. Thesis)
MTA-89-69	Arnt Olufsen, MK	Uncertainty and Reliability Analysis of Fixed Offshore Structures. (Dr.Ing. Thesis)
MTA-89-70	Wu Yu-Lin, MR	System Reliability Analyses of Offshore Structures using improved Truss and Beam Models. (Dr.Ing. Thesis)
MTA-90-71	Jan Roger Hoff, MH	Three-dimensional Green function of a vessel with forward speed in waves. (Dr.Ing. Thesis)
MTA-90-72	Rong Zhao, MH	Slow-Drift Motions of a Moored Two-Dimensional Body in Irregular Waves. (Dr.Ing. Thesis)
MTA-90-73	Atle Minsaas, MP	Economical Risk Analysis. (Dr.Ing. Thesis)
MTA-90-74	Knut-Aril Farnes, MK	Long-term Statistics of Response in Non-linear Marine Structures. (Dr.Ing. Thesis)
MTA-90-75	Torbjørn Sotberg, MK	Application of Reliability Methods for Safety Assessment of Submarine Pipelines. (Dr.Ing.

Thesis)

MTA-90-76	Zeuthen, Steffen, MP	SEAMAID. A computational model of the design process in a constraint-based logic programming environment. An example from the offshore domain. (Dr.Ing. Thesis)
MTA-91-77	Haagensen, Sven, MM	Fuel Dependant Cyclic Variability in a Spark Ignition Engine - An Optical Approach. (Dr.Ing. Thesis)
MTA-91-78	Løland, Geir, MH	Current forces on and flow through fish farms. (Dr.Ing. Thesis)
MTA-91-79	Hoen, Christopher, MK	System Identification of Structures Excited by Stochastic Load Processes. (Dr.Ing. Thesis)
MTA-91-80	Haugen, Stein, MK	Probabilistic Evaluation of Frequency of Collision between Ships and Offshore Platforms. (Dr.Ing. Thesis)
MTA-91-81	Sødahl, Nils, MK	Methods for Design and Analysis of Flexible Risers. (Dr.Ing. Thesis)
MTA-91-82	Ormberg, Harald, MK	Non-linear Response Analysis of Floating Fish Farm Systems. (Dr.Ing. Thesis)
MTA-91-83	Marley, Mark J., MK	Time Variant Reliability under Fatigue Degradation. (Dr.Ing. Thesis)
MTA-91-84	Krokstad, Jørgen R., MH	Second-order Loads in Multidirectional Seas. (Dr.Ing. Thesis)
MTA-91-85	Molteberg, Gunnar A., MM	The Application of System Identification Techniques to Performance Monitoring of Four Stroke Turbocharged Diesel Engines. (Dr.Ing. Thesis)
MTA-92-86	Mørch, Hans Jørgen Bjelke, MH	Aspects of Hydrofoil Design: with Emphasis on Hydrofoil Interaction in Calm Water. (Dr.Ing. Thesis)
MTA-92-87	Chan Siu Hung, MM	Nonlinear Analysis of Rotordynamic Instabilities in Highspeed Turbomachinery. (Dr.Ing. Thesis)
MTA-92-88	Bessason, Bjarni, MK	Assessment of Earthquake Loading and Response of Seismically Isolated Bridges. (Dr.Ing. Thesis)
MTA-92-89	Langli, Geir, MP	Improving Operational Safety through exploitation of Design Knowledge - an investigation of offshore platform safety. (Dr.Ing. Thesis)
MTA-92-90	Sævik, Svein, MK	On Stresses and Fatigue in Flexible Pipes. (Dr.Ing. Thesis)
MTA-92-91	Ask, Tor Ø., MM	Ignition and Flame Growth in Lean Gas-Air Mixtures. An Experimental Study with a Schlieren System. (Dr.Ing. Thesis)
MTA-86-92	Hessen, Gunnar, MK	Fracture Mechanics Analysis of Stiffened Tubular Members. (Dr.Ing. Thesis)

MTA-93-93	Steinebach, Christian, MM	Knowledge Based Systems for Diagnosis of Rotating Machinery. (Dr.Ing. Thesis)
MTA-93-94	Dalane, Jan Inge, MK	System Reliability in Design and Maintenance of Fixed Offshore Structures. (Dr.Ing. Thesis)
MTA-93-95	Steen, Sverre, MH	Cobblestone Effect on SES. (Dr.Ing. Thesis)
MTA-93-96	Karunakaran, Daniel, MK	Nonlinear Dynamic Response and Reliability Analysis of Drag-dominated Offshore Platforms. (Dr.Ing. Thesis)
MTA-93-97	Hagen, Arnulf, MP	The Framework of a Design Process Language. (Dr.Ing. Thesis)
MTA-93-98	Nordrik, Rune, MM	Investigation of Spark Ignition and Autoignition in Methane and Air Using Computational Fluid Dynamics and Chemical Reaction Kinetics. A Numerical Study of Ignition Processes in Internal Combustion Engines. (Dr.Ing. Thesis)
MTA-94-99	Passano, Elizabeth, MK	Efficient Analysis of Nonlinear Slender Marine Structures. (Dr.Ing. Thesis)
MTA-94-100	Kvålsvold, Jan, MH	Hydroelastic Modelling of Wetdeck Slamming on Multihull Vessels. (Dr.Ing. Thesis)
MTA-94-102	Bech, Sidsel M., MK	Experimental and Numerical Determination of Stiffness and Strength of GRP/PVC Sandwich Structures. (Dr.Ing. Thesis)
MTA-95-103	Paulsen, Hallvard, MM	A Study of Transient Jet and Spray using a Schlieren Method and Digital Image Processing. (Dr.Ing. Thesis)
MTA-95-104	Hovde, Geir Olav, MK	Fatigue and Overload Reliability of Offshore Structural Systems, Considering the Effect of Inspection and Repair. (Dr.Ing. Thesis)
MTA-95-105	Wang, Xiaozhi, MK	Reliability Analysis of Production Ships with Emphasis on Load Combination and Ultimate Strength. (Dr.Ing. Thesis)
MTA-95-106	Ulstein, Tore, MH	Nonlinear Effects of a Flexible Stern Seal Bag on Cobblestone Oscillations of an SES. (Dr.Ing. Thesis)
MTA-95-107	Solaas, Frøydis, MH	Analytical and Numerical Studies of Sloshing in Tanks. (Dr.Ing. Thesis)
MTA-95-108	Hellan, Øyvind, MK	Nonlinear Pushover and Cyclic Analyses in Ultimate Limit State Design and Reassessment of Tubular Steel Offshore Structures. (Dr.Ing. Thesis)
MTA-95-109	Hermundstad, Ole A., MK	Theoretical and Experimental Hydroelastic Analysis of High Speed Vessels. (Dr.Ing. Thesis)
MTA-96-110	Bratland, Anne K., MH	Wave-Current Interaction Effects on Large-Volume Bodies in Water of Finite Depth. (Dr.Ing. Thesis)
MTA-96-111	Herfjord, Kjell, MH	A Study of Two-dimensional Separated Flow by a Combination of the Finite Element Method and

Navier-Stokes Equations. (Dr.Ing. Thesis)

MTA-96-112	Æsøy, Vilmar, MM	Hot Surface Assisted Compression Ignition in a Direct Injection Natural Gas Engine. (Dr.Ing. Thesis)
MTA-96-113	Eknes, Monika L., MK	Escalation Scenarios Initiated by Gas Explosions on Offshore Installations. (Dr.Ing. Thesis)
MTA-96-114	Erikstad, Stein O., MP	A Decision Support Model for Preliminary Ship Design. (Dr.Ing. Thesis)
MTA-96-115	Pedersen, Egil, MH	A Nautical Study of Towed Marine Seismic Streamer Cable Configurations. (Dr.Ing. Thesis)
MTA-97-116	Moksnes, Paul O., MM	Modelling Two-Phase Thermo-Fluid Systems Using Bond Graphs. (Dr.Ing. Thesis)
MTA-97-117	Halse, Karl H., MK	On Vortex Shedding and Prediction of Vortex-Induced Vibrations of Circular Cylinders. (Dr.Ing. Thesis)
MTA-97-118	Igland, Ragnar T., MK	Reliability Analysis of Pipelines during Laying, considering Ultimate Strength under Combined Loads. (Dr.Ing. Thesis)
MTA-97-119	Pedersen, Hans-P., MP	Levendefiskteknologi for fiskefartøy. (Dr.Ing. Thesis)
MTA-98-120	Vikestad, Kyrre, MK	Multi-Frequency Response of a Cylinder Subjected to Vortex Shedding and Support Motions. (Dr.Ing. Thesis)
MTA-98-121	Azadi, Mohammad R. E., MK	Analysis of Static and Dynamic Pile-Soil-Jacket Behaviour. (Dr.Ing. Thesis)
MTA-98-122	Ulltang, Terje, MP	A Communication Model for Product Information. (Dr.Ing. Thesis)
MTA-98-123	Torbergsen, Erik, MM	Impeller/Diffuser Interaction Forces in Centrifugal Pumps. (Dr.Ing. Thesis)
MTA-98-124	Hansen, Edmond, MH	A Discrete Element Model to Study Marginal Ice Zone Dynamics and the Behaviour of Vessels Moored in Broken Ice. (Dr.Ing. Thesis)
MTA-98-125	Videiro, Paulo M., MK	Reliability Based Design of Marine Structures. (Dr.Ing. Thesis)
MTA-99-126	Mainçon, Philippe, MK	Fatigue Reliability of Long Welds Application to Titanium Risers. (Dr.Ing. Thesis)
MTA-99-127	Haugen, Elin M., MH	Hydroelastic Analysis of Slamming on Stiffened Plates with Application to Catamaran Wetdecks. (Dr.Ing. Thesis)
MTA-99-128	Langhelle, Nina K., MK	Experimental Validation and Calibration of Nonlinear Finite Element Models for Use in Design of Aluminium Structures Exposed to Fire. (Dr.Ing. Thesis)
MTA-99-	Berstad, Are J., MK	Calculation of Fatigue Damage in Ship Structures.

129		(Dr.Ing. Thesis)
MTA-99-130	Andersen, Trond M., MM	Short Term Maintenance Planning. (Dr.Ing. Thesis)
MTA-99-131	Tveiten, Bård Wathne, MK	Fatigue Assessment of Welded Aluminium Ship Details. (Dr.Ing. Thesis)
MTA-99-132	Søreide, Fredrik, MP	Applications of underwater technology in deep water archaeology. Principles and practice. (Dr.Ing. Thesis)
MTA-99-133	Tønnessen, Rune, MH	A Finite Element Method Applied to Unsteady Viscous Flow Around 2D Blunt Bodies With Sharp Corners. (Dr.Ing. Thesis)
MTA-99-134	Elvekrok, Dag R., MP	Engineering Integration in Field Development Projects in the Norwegian Oil and Gas Industry. The Supplier Management of Norne. (Dr.Ing. Thesis)
MTA-99-135	Fagerholt, Kjetil, MP	Optimeringsbaserte Metoder for Ruteplanlegging innen skipsfart. (Dr.Ing. Thesis)
MTA-99-136	Bysveen, Marie, MM	Visualization in Two Directions on a Dynamic Combustion Rig for Studies of Fuel Quality. (Dr.Ing. Thesis)
MTA-2000-137	Storteig, Eskild, MM	Dynamic characteristics and leakage performance of liquid annular seals in centrifugal pumps. (Dr.Ing. Thesis)
MTA-2000-138	Sagli, Gro, MK	Model uncertainty and simplified estimates of long term extremes of hull girder loads in ships. (Dr.Ing. Thesis)
MTA-2000-139	Tronstad, Harald, MK	Nonlinear analysis and design of cable net structures like fishing gear based on the finite element method. (Dr.Ing. Thesis)
MTA-2000-140	Kroneberg, André, MP	Innovation in shipping by using scenarios. (Dr.Ing. Thesis)
MTA-2000-141	Haslum, Herbjørn Alf, MH	Simplified methods applied to nonlinear motion of spar platforms. (Dr.Ing. Thesis)
MTA-2001-142	Samdal, Ole Johan, MM	Modelling of Degradation Mechanisms and Stressor Interaction on Static Mechanical Equipment Residual Lifetime. (Dr.Ing. Thesis)
MTA-2001-143	Baarholm, Rolf Jarle, MH	Theoretical and experimental studies of wave impact underneath decks of offshore platforms. (Dr.Ing. Thesis)
MTA-2001-144	Wang, Lihua, MK	Probabilistic Analysis of Nonlinear Wave-induced Loads on Ships. (Dr.Ing. Thesis)
MTA-2001-145	Kristensen, Odd H. Holt, MK	Ultimate Capacity of Aluminium Plates under Multiple Loads, Considering HAZ Properties. (Dr.Ing. Thesis)
MTA-2001-146	Greco, Marilena, MH	A Two-Dimensional Study of Green-Water Loading. (Dr.Ing. Thesis)

MTA-2001-147	Heggelund, Svein E., MK	Calculation of Global Design Loads and Load Effects in Large High Speed Catamarans. (Dr.Ing. Thesis)
MTA-2001-148	Babalola, Olusegun T., MK	Fatigue Strength of Titanium Risers – Defect Sensitivity. (Dr.Ing. Thesis)
MTA-2001-149	Mohammed, Abuu K., MK	Nonlinear Shell Finite Elements for Ultimate Strength and Collapse Analysis of Ship Structures. (Dr.Ing. Thesis)
MTA-2002-150	Holmedal, Lars E., MH	Wave-current interactions in the vicinity of the sea bed. (Dr.Ing. Thesis)
MTA-2002-151	Rognebakke, Olav F., MH	Sloshing in rectangular tanks and interaction with ship motions. (Dr.Ing. Thesis)
MTA-2002-152	Lader, Pål Furset, MH	Geometry and Kinematics of Breaking Waves. (Dr.Ing. Thesis)
MTA-2002-153	Yang, Qinzheng, MH	Wash and wave resistance of ships in finite water depth. (Dr.Ing. Thesis)
MTA-2002-154	Melhus, Øyvin, MM	Utilization of VOC in Diesel Engines. Ignition and combustion of VOC released by crude oil tankers. (Dr.Ing. Thesis)
MTA-2002-155	Ronæss, Marit, MH	Wave Induced Motions of Two Ships Advancing on Parallel Course. (Dr.Ing. Thesis)
MTA-2002-156	Økland, Ole D., MK	Numerical and experimental investigation of whipping in twin hull vessels exposed to severe wet deck slamming. (Dr.Ing. Thesis)
MTA-2002-157	Ge, Chunhua, MK	Global Hydroelastic Response of Catamarans due to Wet Deck Slamming. (Dr.Ing. Thesis)
MTA-2002-158	Byklum, Eirik, MK	Nonlinear Shell Finite Elements for Ultimate Strength and Collapse Analysis of Ship Structures. (Dr.Ing. Thesis)
IMT-2003-1	Chen, Haibo, MK	Probabilistic Evaluation of FPSO-Tanker Collision in Tandem Offloading Operation. (Dr.Ing. Thesis)
IMT-2003-2	Skaugset, Kjetil Bjørn, MK	On the Suppression of Vortex Induced Vibrations of Circular Cylinders by Radial Water Jets. (Dr.Ing. Thesis)
IMT-2003-3	Chezhian, Muthu	Three-Dimensional Analysis of Slamming. (Dr.Ing. Thesis)
IMT-2003-4	Buhaug, Øyvind	Deposit Formation on Cylinder Liner Surfaces in Medium Speed Engines. (Dr.Ing. Thesis)
IMT-2003-5	Tregde, Vidar	Aspects of Ship Design: Optimization of Aft Hull with Inverse Geometry Design. (Dr.Ing. Thesis)
IMT-2003-6	Wist, Hanne Therese	Statistical Properties of Successive Ocean Wave Parameters. (Dr.Ing. Thesis)

IMT-2004-7	Ransau, Samuel	Numerical Methods for Flows with Evolving Interfaces. (Dr.Ing. Thesis)
IMT-2004-8	Soma, Torkel	Blue-Chip or Sub-Standard. A data interrogation approach of identity safety characteristics of shipping organization. (Dr.Ing. Thesis)
IMT-2004-9	Ersdal, Svein	An experimental study of hydrodynamic forces on cylinders and cables in near axial flow. (Dr.Ing. Thesis)
IMT-2005-10	Brodtkorb, Per Andreas	The Probability of Occurrence of Dangerous Wave Situations at Sea. (Dr.Ing. Thesis)
IMT-2005-11	Yttervik, Rune	Ocean current variability in relation to offshore engineering. (Dr.Ing. Thesis)
IMT-2005-12	Fredheim, Arne	Current Forces on Net-Structures. (Dr.Ing. Thesis)
IMT-2005-13	Heggernes, Kjetil	Flow around marine structures. (Dr.Ing. Thesis
IMT-2005-14	Fouques, Sebastien	Lagrangian Modelling of Ocean Surface Waves and Synthetic Aperture Radar Wave Measurements. (Dr.Ing. Thesis)
IMT-2006-15	Holm, Håvard	Numerical calculation of viscous free surface flow around marine structures. (Dr.Ing. Thesis)
IMT-2006-16	Bjørheim, Lars G.	Failure Assessment of Long Through Thickness Fatigue Cracks in Ship Hulls. (Dr.Ing. Thesis)
IMT-2006-17	Hansson, Lisbeth	Safety Management for Prevention of Occupational Accidents. (Dr.Ing. Thesis)
IMT-2006-18	Zhu, Xinying	Application of the CIP Method to Strongly Nonlinear Wave-Body Interaction Problems. (Dr.Ing. Thesis)
IMT-2006-19	Reite, Karl Johan	Modelling and Control of Trawl Systems. (Dr.Ing. Thesis)
IMT-2006-20	Smogeli, Øyvind Notland	Control of Marine Propellers. From Normal to Extreme Conditions. (Dr.Ing. Thesis)
IMT-2007-21	Storhaug, Gaute	Experimental Investigation of Wave Induced Vibrations and Their Effect on the Fatigue Loading of Ships. (Dr.Ing. Thesis)
IMT-2007-22	Sun, Hui	A Boundary Element Method Applied to Strongly Nonlinear Wave-Body Interaction Problems. (PhD Thesis, CeSOS)
IMT-2007-23	Rustad, Anne Marthine	Modelling and Control of Top Tensioned Risers. (PhD Thesis, CeSOS)
IMT-2007-24	Johansen, Vegar	Modelling flexible slender system for real-time simulations and control applications
IMT-2007-25	Wroldsen, Anders Sunde	Modelling and control of tensegrity structures. (PhD Thesis, CeSOS)
IMT-	Aronsen, Kristoffer Høye	An experimental investigation of in-line and

2007-26		combined inline and cross flow vortex induced vibrations. (Dr. avhandling, IMT)
IMT-2007-27	Gao, Zhen	Stochastic Response Analysis of Mooring Systems with Emphasis on Frequency-domain Analysis of Fatigue due to Wide-band Response Processes (PhD Thesis, CeSOS)
IMT-2007-28	Thorstensen, Tom Anders	Lifetime Profit Modelling of Ageing Systems Utilizing Information about Technical Condition. (Dr.ing. thesis, IMT)
IMT-2008-29	Berntsen, Per Ivar B.	Structural Reliability Based Position Mooring. (PhD-Thesis, IMT)
IMT-2008-30	Ye, Naiquan	Fatigue Assessment of Aluminium Welded Box-stiffener Joints in Ships (Dr.ing. thesis, IMT)
IMT-2008-31	Radan, Damir	Integrated Control of Marine Electrical Power Systems. (PhD-Thesis, IMT)
IMT-2008-32	Thomassen, Paul	Methods for Dynamic Response Analysis and Fatigue Life Estimation of Floating Fish Cages. (Dr.ing. thesis, IMT)
IMT-2008-33	Pákozdi, Csaba	A Smoothed Particle Hydrodynamics Study of Two-dimensional Nonlinear Sloshing in Rectangular Tanks. (Dr.ing.thesis, IMT/ CeSOS)
IMT-2007-34	Grytøyr, Guttorm	A Higher-Order Boundary Element Method and Applications to Marine Hydrodynamics. (Dr.ing.thesis, IMT)
IMT-2008-35	Drummen, Ingo	Experimental and Numerical Investigation of Nonlinear Wave-Induced Load Effects in Containerships considering Hydroelasticity. (PhD thesis, CeSOS)
IMT-2008-36	Skejic, Renato	Maneuvering and Seakeeping of a Singel Ship and of Two Ships in Interaction. (PhD-Thesis, CeSOS)
IMT-2008-37	Harlem, Alf	An Age-Based Replacement Model for Repairable Systems with Attention to High-Speed Marine Diesel Engines. (PhD-Thesis, IMT)
IMT-2008-38	Alsos, Hagbart S.	Ship Grounding. Analysis of Ductile Fracture, Bottom Damage and Hull Girder Response. (PhD-thesis, IMT)
IMT-2008-39	Graczyk, Mateusz	Experimental Investigation of Sloshing Loading and Load Effects in Membrane LNG Tanks Subjected to Random Excitation. (PhD-thesis, CeSOS)
IMT-2008-40	Taghipour, Reza	Efficient Prediction of Dynamic Response for Flexible amd Multi-body Marine Structures. (PhD-thesis, CeSOS)
IMT-2008-41	Ruth, Eivind	Propulsion control and thrust allocation on marine vessels. (PhD thesis, CeSOS)
IMT-2008-42	Nystad, Bent Helge	Technical Condition Indexes and Remaining Useful Life of Aggregated Systems. PhD thesis, IMT

IMT-2008-43	Soni, Prashant Kumar	Hydrodynamic Coefficients for Vortex Induced Vibrations of Flexible Beams, PhD thesis, CeSOS
IMT-2009-43	Amlashi, Hadi K.K.	Ultimate Strength and Reliability-based Design of Ship Hulls with Emphasis on Combined Global and Local Loads. PhD Thesis, IMT
IMT-2009-44	Pedersen, Tom Arne	Bond Graph Modelling of Marine Power Systems. PhD Thesis, IMT
IMT-2009-45	Kristiansen, Trygve	Two-Dimensional Numerical and Experimental Studies of Piston-Mode Resonance. PhD-Thesis, CeSOS
IMT-2009-46	Ong, Muk Chen	Applications of a Standard High Reynolds Number Model and a Stochastic Scour Prediction Model for Marine Structures. PhD-thesis, IMT
IMT-2009-47	Hong, Lin	Simplified Analysis and Design of Ships subjected to Collision and Grounding. PhD-thesis, IMT
IMT-2009-48	Koushan, Kamran	Vortex Induced Vibrations of Free Span Pipelines, PhD thesis, IMT
IMT-2009-49	Korsvik, Jarl Eirik	Heuristic Methods for Ship Routing and Scheduling. PhD-thesis, IMT
IMT-2009-50	Lee, Jihoon	Experimental Investigation and Numerical in Analyzing the Ocean Current Displacement of Longlines. Ph.d.-Thesis, IMT.
IMT-2009-51	Vestbøstad, Tone Gran	A Numerical Study of Wave-in-Deck Impact usin a Two-Dimensional Constrained Interpolation Profile Method, Ph.d.thesis, CeSOS.
IMT-2009-52	Bruun, Kristine	Bond Graph Modelling of Fuel Cells for Marine Power Plants. Ph.d.-thesis, IMT
IMT 2009-53	Holstad, Anders	Numerical Investigation of Turbulence in a Sekwed Three-Dimensional Channel Flow, Ph.d.-thesis, IMT.
IMT 2009-54	Ayala-Uraga, Efren	Reliability-Based Assessment of Deteriorating Ship-shaped Offshore Structures, Ph.d.-thesis, IMT
IMT 2009-55	Kong, Xiangjun	A Numerical Study of a Damaged Ship in Beam Sea Waves. Ph.d.-thesis, IMT/CeSOS.
IMT 2010-56	Kristiansen, David	Wave Induced Effects on Floaters of Aquaculture Plants, Ph.d.-thesis, CeSOS.
IMT 2010-57	Ludvigsen, Martin	An ROV-Toolbox for Optical and Acoustic Scientific Seabed Investigation. Ph.d.-thesis IMT.
IMT 2010-58	Hals, Jørgen	Modelling and Phase Control of Wave-Energy Converters. Ph.d.thesis, CeSOS.
IMT 2010- 59	Shu, Zhi	Uncertainty Assessment of Wave Loads and Ultimate Strength of Tankers and Bulk Carriers in a

IMT 2010-60	Shao, Yanlin	Reliability Framework. Ph.d. Thesis, IMT/ CeSOS Numerical Potential-Flow Studies on Weakly-Nonlinear Wave-Body Interactions with/without Small Forward Speed, Ph.d.thesis,CeSOS.
IMT 2010-61	Califano, Andrea	Dynamic Loads on Marine Propellers due to Intermittent Ventilation. Ph.d.thesis, IMT.
IMT 2010-62	El Khoury, George	Numerical Simulations of Massively Separated Turbulent Flows, Ph.d.-thesis, IMT
IMT 2010-63	Seim, Knut Sponheim	Mixing Process in Dense Overflows with Emphasis on the Faroe Bank Channel Overflow. Ph.d.thesis, IMT
IMT 2010-64	Jia, Huirong	Structural Analysis of Intect and Damaged Ships in a Collission Risk Analysis Perspective. Ph.d.thesis CeSoS.
IMT 2010-65	Jiao, Linlin	Wave-Induced Effects on a Pontoon-type Very Large Floating Structures (VLFS). Ph.D.-thesis, CeSOS.
IMT 2010-66	Abrahamsen, Bjørn Christian	Sloshing Induced Tank Roof with Entrapped Air Pocket. Ph.d.thesis, CeSOS.
IMT 2011-67	Karimirad, Madjid	Stochastic Dynamic Response Analysis of Spar-Type Wind Turbines with Catenary or Taut Mooring Systems. Ph.d.-thesis, CeSOS.
IMT - 2011-68	Erlend Meland	Condition Monitoring of Safety Critical Valves. Ph.d.-thesis, IMT.
IMT – 2011-69	Yang, Limin	Stochastic Dynamic System Analysis of Wave Energy Converter with Hydraulic Power Take-Off, with Particular Reference to Wear Damage Analysis, Ph.d. Thesis, CeSOS.
IMT – 2011-70	Visscher, Jan	Application of Particla Image Velocimetry on Turbulent Marine Flows, Ph.d.Thesis, IMT.
IMT – 2011-71	Su, Biao	Numerical Predictions of Global and Local Ice Loads on Ships. Ph.d.Thesis, CeSOS.
IMT – 2011-72	Liu, Zhenhui	Analytical and Numerical Analysis of Iceberg Collision with Ship Structures. Ph.d.Thesis, IMT.
IMT – 2011-73	Aarsæther, Karl Gunnar	Modeling and Analysis of Ship Traffic by Observation and Numerical Simulation. Ph.d.Thesis, IMT.
Imt – 2011-74	Wu, Jie	Hydrodynamic Force Identification from Stochastic Vortex Induced Vibration Experiments with Slender Beams. Ph.d.Thesis, IMT.
Imt – 2011-75	Amini, Hamid	Azimuth Propulsors in Off-design Conditions. Ph.d.Thesis, IMT.
IMT – 2011-76	Nguyen, Tan-Hoi	Toward a System of Real-Time Prediction and Monitoring of Bottom Damage Conditions During

Ship Grounding. Ph.d.thesis, IMT.

IMT-2011-77	Tavakoli, Mohammad T.	Assessment of Oil Spill in Ship Collision and Grounding, Ph.d.thesis, IMT.
IMT-2011-78	Guo, Bingjie	Numerical and Experimental Investigation of Added Resistance in Waves. Ph.d.Thesis, IMT.
IMT-2011-79	Chen, Qiaofeng	Ultimate Strength of Aluminium Panels, considering HAZ Effects, IMT
IMT-2012-80	Kota, Ravikiran S.	Wave Loads on Decks of Offshore Structures in Random Seas. Ph.d.thesis, CeSOS.
IMT-2012-81	Sten, Ronny	Dynamic Simulation of Deep Water Drilling Risers with Heave Compensating Sysetm, IMT
IMT-2012-82	Berle, Øyvind	Risk and resilience in global maritime supply chains, IMT.
IMT-2012-83	Fang, Shaoji	Fault Tolerant Position Mooring Control Based on Structural Reliability, CeSOS.
IMT-2012-84	You, Jikun	Numerical studies on wave forces and moored ship motions in intermediate and shallow water, CeSOS.
IMT-2012-85	Xiang ,Xu	Maneuvering of two interacting ships in waves, CeSOS
IMT-2012-86	Dong, Wenbin	Time-domain fatigueresponse and reliability analysis of offshore wind turbines with emphasis on wlded tubular joints and gear components, CeSOS
IMT-2012-87	Zhu, Suji	Investigation of Wave-Induced Nonlinear Load Effects in Open Ships considering Hull Girder Vibrations in Bending and Torsion, CeSOS
IMT-2012-88	Zhou, Li	Numerical and Experimental Investigation of Station-keeping in Level Ice, CeSOS
IMT-2012-90	Ushakov, Sergey	Particulate matter emission characteristics from diesel enignes operating on conventional and alternative marine fuels, IMT
IMT-2013-1	Yin, Decao	Experimental and Numerical Analysis of Combined In-line and Cross-flow Vortex Induced Vibrations, CeSOS
IMT-2013-2	Kurniawan, Adi	Modelling & geometry optimisation of wave energy converters, CeSOS
IMT-2013-3	Al Ryati, Nabil	Technical condition indexes doe auxiliary marine diesel engines, IMT
IMT-2013-4	Firoozkoohi, Reza	Experimental, numerical and analytical investigation of the effect of screens on sloshing, CeSOS
IMT-2013-5	Ommani, Babak	Potential-Flow Predictions of a Semi-Displacement Vessel Including Applications to Calm Water Broaching, CeSOS